Fall 2009

Simulation of tissues for biomedical applications

Yulia Alexandrovna Skvortsova
University of Iowa

Recommended Citation

Skvortsova, Yulia Alexandrovna. "Simulation of tissues for biomedical applications." PhD (Doctor of Philosophy) thesis, University of Iowa, 2009.
http://ir.uiowa.edu/etd/436.

SIMULATION OF TISSUES FOR BIOMEDICAL APPLICATIONS

by

Yulia Alexandrovna Skvortsova

An Abstract

Of a thesis submitted in partial fulfillment
of the requirements for the Doctor of
Philosophy degree in Chemistry
in the Graduate College of
The University of Iowa

December 2009

Thesis Supervisor: Professor M. Lei Geng

ABSTRACT

Nanoporous particles with hydrophobically-modified surface have found applications in many areas of chemical and biomedical research. The understanding of their interactions with surfactants in aqueous solutions opens the opportunities for using such hydrophobic nanoporous particles in drug delivery, tissue phantom preparation and other biomedical fields.

We investigated surfactant-induced wetting of C18-modified silica gel with aqueous solution by means of fluorescence spectroscopy, confocal fluorescence imaging and multi-photon excitation imaging. Ratiometric imaging with solvatochromic probe Prodan revealed the nanotransport of intact surfactant micelles inside the hydrophobic nanopores. The influence of hydrophobic and electrostatic effects on the distribution of fluorescent probe molecules in the C18-particle-surfactant system was addressed by employing positively and negatively charged water-soluble probes, rhodamine 6G and fluorescein, respectively. The methodology for the preparation of surfactant-decorated particles with retained internal hydrophobicity was evaluated by means of confocal fluorescence imaging.

C18-derivatized nanoporous silica particles were incorporated in the design of semi-solid three-dimensional tissue phantoms. Patient-to-patient differences and complexity of the biochemical environments cause significant variation in the spectral characteristics of cancerous tissues. The use of tissue phantoms with controlled boundaries of optical features can assist in the development of optical biopsy methods. The phantoms were composed of hydrophobic nanoporous silica beads loaded with an endogenous tissue fluorophore, flavin adenine dinucleotide (FAD), and imbedded in 1% agar gel. Uniform 10-micron silica particles serve as perfect imaging objects for testing optical biopsy methods, providing features of known dimensions and shapes.

Efficacies of methods for the analysis of autofluorescence tissue spectra were compared. Evaluated methods included: principle peak ratio (PPR), differential normalized fluorescence (DNF), bivariate DNF (2D-DNF), principal component analysis (PCA) and correlation coefficient mapping (CCM). Comparison was achieved by performing diagnosis in a large simulated tissue-phantom data set. The use of simulation in this study ensured the comparison of methods in nearly the entire sample space, while avoiding environmental and patient-to-patient variation biases. The diagnostic boundaries were established by applying Bayes decision theory, which achieved statistically significant classification of the analyzed samples.

Abstract Approved: ______________________________________

Thesis Supervisor

____

Title and Department

____

Date

SIMULATION OF TISSUES FOR BIOMEDICAL APPLICATIONS

by

Yulia Alexandrovna Skvortsova

A thesis submitted in partial fulfillment
of the requirements for the Doctor of
Philosophy degree in Chemistry
in the Graduate College of
The University of Iowa

December 2009

Thesis Supervisor: Professor M. Lei Geng

Graduate College
The University of Iowa
Iowa City, Iowa

CERTIFICATE OF APPROVAL

PH.D. THESIS

This is to certify that the Ph.D. thesis of

Yulia Alexandrovna Skvortsova

has been approved by the Examining Committee
for the thesis requirement for the Doctor of Philosophy
degree in Chemistry at the December 2009 graduation.

Thesis Committee: _______________________________
M. Lei Geng, Thesis Supervisor

____
Gary W. Small

____
Christopher M. Cheatum

____
James B. Gloer

____
Alan R. Kay

To my beloved Parents.

We usually get what we want, but often a bit later than we wish.

ACKNOWLEDGMENTS

I would like to thank my thesis advisor, Dr. Lei Geng, for his support and trust on all stages of my graduate career at The University of Iowa and beyond. It has been a privilege and a pleasure to be a GGM (Geng Group Member). I benefited greatly from Dr.Geng's scientific guidance and the wealth of knowledge that he was eager to share with all group members. I am also grateful to the other members of my thesis committee: Dr. Gary Small, Dr. Christopher Cheatum, Dr. James Gloer and Dr. Alan Kay, for accommodating my summer defense and for general encouragement.

Many thanks to the past and present GGMs: Gufeng Wang, Jinfu Zhao, Zhenming Zhong, Piyanka De Silva, Edward Crowell, Alice Eck, Anamika Mubayi, Lu Xi, Yi Gao, Chester Duda, Mark Brewer, Reygan Freeney, Ye Li, Rui Zhang, and Claudiu Brumaru, for their friendship, mentorship and scientific cooperation. I had a great time with them all.

Last but not least, I wish to thank my family for their patience, companionship and support during the long and challenging years of the graduate school. I appreciate all the encouragement provided by my mother, Dr. Natalia Skvortsova, and father, Dr. Alexander Skvortsov, who were always confident in my abilities to obtain a Doctorate degree. I am deeply grateful to my husband, SungWan Park, for his endless love, help and sacrifice. I could not have done it without him.

TABLE OF CONTENTS

LIST OF TABLES

LIST OF FIGURES

CHAPTER 1 INTRODUCTION

The work described in this thesis was focused on three areas: spectroscopic detection of cancer, development of tissue phantoms for confocal diagnostic imaging, and investigation of the processes in the hydrophobic nanopores in the presence of surfactant. The uniting point of all three projects is the application of fluorescence in gaining knowledge about biochemical and material systems. Chapter 2 provides theoretical background on the principles of fluorescence, as well as an introduction to confocal and two-photon excitation imaging techniques applied in Chapters 5 through 7.

Due to the increasing population of cancer patients, there is a demand for the development of noninvasive real time detection of pre-cancerous formations in human tissues. Extensive research and clinical studies have shown the capability of fluorescence spectroscopy to provide highly sensitive, specific, and minimally invasive diagnosis of cancers. Analytical methods that allow quantitative differentiation of diseased and non-diseased tissues according to their fluorescence properties range from simple empirical parameters to complicated statistical pattern recognition techniques. The objective of the research project presented in Chapter 3 is the comparison between the methodologies for the analysis of autofluorescence tissue spectra. The methods compared are: principal peak ratio (PPR), differential normalized fluorescence (DNF), bivariate

DNF (2D-DNF), and principal component analysis (PCA). The methodologies are examined with a simulated tissue-phantom data set generated from the spectra of individual tissue chromophores: collagen IV, nicotinamide adenine dinucleotide (NADH), flavin adenine dinucleotide (FAD), and hemoglobin (Hb). The use of simulation in this study ensures the comparison of method performance in the nearly entire sample space, while avoiding environmental and patient-to-patient variation biases.

Currently, the threshold for the differentiation of the tissue spectra is empirically determined. In this study we establish diagnostic boundaries by applying Bayes decision theory, which achieves statistically significant discrimination of the analyzed samples. Moreover, provided probability values associated with the diagnosis are valuable in clinical practice situations. Diagnostic results reported in Chapters 3 and 4 are obtained through probability density function calculation and subsequent application of Bayes theorem.

Statistical correlation coefficient mapping has proven to be a useful technique in tissue classification for cancer diagnosis. Its application for the analysis of a simulated tissue-phantom data set containing 800 spectra is presented in Chapter 4. In the correlation coefficient mapping method, the classification is achieved by comparing the correlation coefficients for an unknown sample to a set of selected tissue samples with known pathological conditions. The correlation coefficients of the sample spectra with the average normal tissue spectrum are calculated and used as diagnostic indices in this chapter. Statistical thresholds are determined by transforming Pearson's correlation coefficients to Fisher's *z*-values and then analyzed with Bayes decision theory. A tissue type is assigned to an unknown sample with a probability value associated with the assignment. The discussed correlation coefficient method provides an excellent contrast between tissue types and requires only the collection of an average normal tissue spectrum for the diagnosis without any *a-priori* information about the samples.

Patient-to-patient differences and complexity of the biochemical environments cause significant variation in the spectral characteristics of cancerous tissues. The use of tissue phantoms with controlled boundaries of optical features can assist in the development of optical biopsy methods. In Chapter 5 we discuss the design of semi-solid three-dimensional tissue phantoms with controlled spectral characteristics. The phantoms are composed of an endogenous tissue fluorophore, flavin adenine dinucleotide (FAD), enclosed in C18-derivatized nanoporous silica beads. To simulate a real tissue matrix, the particles are embedded in 1% agar gel. A straightforward preparation procedure and the non-toxicity of the materials allow fast and easy production of the phantoms in a standard laboratory setting.

Constructed tissue phantoms were imaged with a stage-scanning confocal microscope system built in-house. Fluorescence excitation was provided by a 454-nm line of an argon laser. The use of spherical particles as vesicles for the tissue chromophore allows the simulation of sample inhomogeneities and localization of the areas with different fluorescent properties. Uniform 10-μm silica beads serve as perfect imaging objects for testing optical biopsy methods, providing features of known dimensions and shapes.

The focus of Chapter 6 is the investigation of the interactions between hydrophobically modified nanoporous particles and surfactants in aqueous solution by means of confocal fluorescence imaging. The influence of hydrophobic and electrostatic effects on the distribution of fluorescent probe molecules in the C18-particles-surfactant system is specifically addressed. Confocal imaging is conducted under chromatographic conditions, i.e., the particles are packed inside a quartz microcolumn and the surfactant solution is pumped through, and under unpacked conditions in the bulk surfactant solution. Positively and negatively charged water-soluble fluorescent probes, rhodamine 6G (R6G) and fluorescein (FITC), respectively, are used to trace the interactions between the surfactant and the hydrophobic surface of the nanopores. The methodology for the preparation of surfactant-decorated particles with retained internal hydrophobicity is evaluated by means of confocal fluorescence imaging with R6G. Nanoporous particles with hydrophobically-modified surface have found applications in many areas of chemical and biochemical research. The understanding of their interaction with surfactants opens the opportunities for using such hydrophobic nanoporous particles in drug delivery, tissue phantoms preparation, and various other important areas of research.

Chapter 7 discusses the micropolarity distribution in C18-modified silica gel during the process of its surfactant-induced wetting with aqueous solution. In this chapter we also answer the question of whether intact SDS micelles with a diameter of 44 Å can enter 73 Å hydrophobic nanopores. Polarity-specific information is obtained through ratiometric two-photon excitation imaging with the solvatochromic probe Prodan. It is shown that the surfactant solution front penetrating into the hydrophobic pores has significantly different polarity than the C18-SDS construct that is formed on the inner and outer surfaces of the particles during wetting. A close match between the environmental polarities of the bulk 50-mM SDS solution and the solution front breaking into the pores suggests the nanotransport of Prodan in intact SDS micelles that act as carriers of the fluorescent probe. Some potential directions of future research based on the results presented in this thesis are discussed in Chapter 8.

CHAPTER 2 BACKGROUND

2.1 Introduction to Fluorescence

Fluorescence is the emission of light that occurs within nanoseconds after the absorption of excitation light by a molecule. Molecules that possess the ability to fluoresce are called fluorophores. The energy of light absorbed by such compounds can sometimes move the electrons in a molecule from lower energy to higher energy orbitals thus transitioning the fluorophore from the 'ground state' to the 'excited state'. This transition occurs within femtoseconds. The fluorescent molecule returns to the ground state by losing the absorbed energy mostly through vibrational relaxation and fluorescence emission [1]. When the transition of an electron to a higher orbital is caused by a single photon, special case of multi-photon excitation will be discussed in Section 2.8, the wavelength of the emitted fluorescence light is longer than the wavelength of the excitation light. This difference in wavelengths is known as the Stokes shift and the explanation of its origins can be best provided by referring to the Jablonski diagram (Figure 2.1).

On the diagram, the singlet states of a molecule, in which paired electrons have opposite spins, i.e., +1/2 and -1/2, are labeled "S" and the triplet states are marked with "T". S_0 is the ground state of the molecule. Depending on the energy of the excitation light absorbed by the molecule, an outer electron of the molecule can be promoted into a higher orbital and the molecule then is said to transition into an excited state. S_1 and S_2 are such singlet excited states.

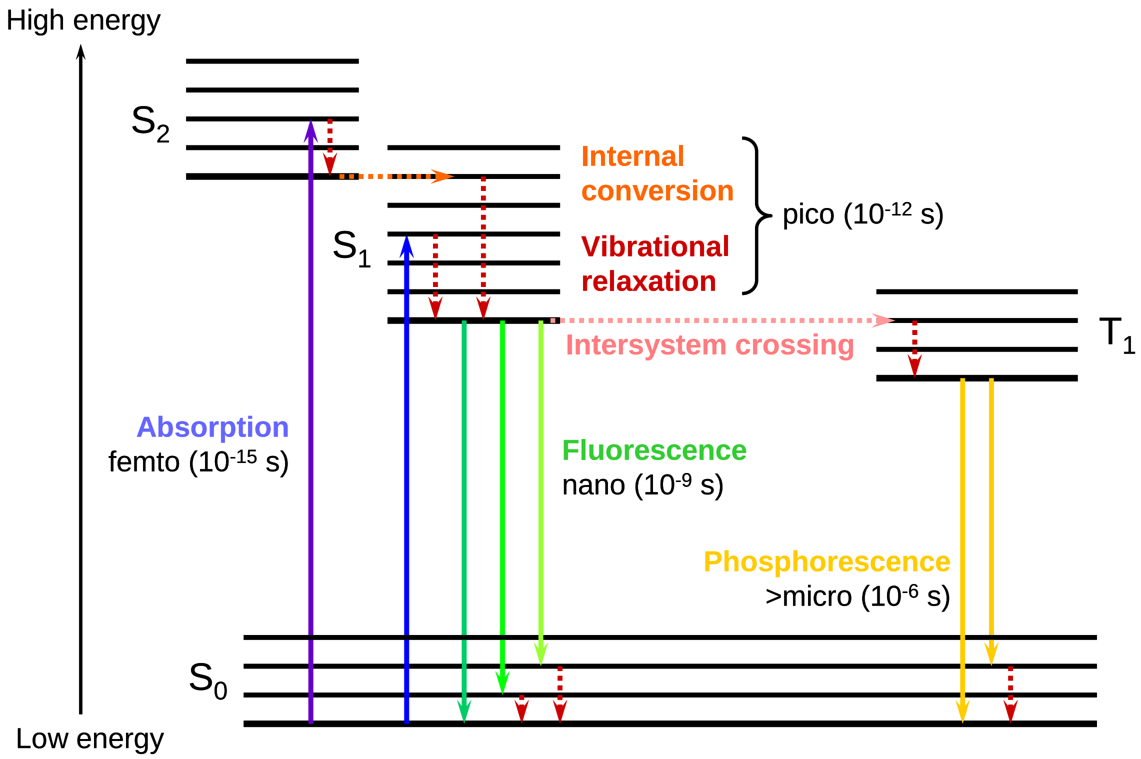

Figure 2.1. Jablonski diagram. S_0 is the ground state, S_1 and S_2 are the excited states.

The energy of the photon absorbed by the molecule is inversely proportional to the wavelength of light, lambda:

$$E = h \cdot C / \lambda \qquad [2.1]$$

where h is Planck's constant, and C is the speed of light in vacuum. Transition of the molecule into an excited state is only possible if the energy of the photon is equal or higher than the energy gap between the ground state and the excited state, i.e. between S_0 and S_1. In the case in which the energy of the photon exceeds the minimum requirement for the transition, the molecule can undergo a change in vibration or rotation, or even move into a higher singlet state S_2. Thus a molecule can be excited by a range of wavelengths, but with different efficiency. Due to the minimal necessary excitation light energy requirement, the right shoulder of the excitation spectrum, corresponding to longer-wavelength-lower-energy excitation light, is usually steeper than the shorter wavelength region of the spectrum.

There are several ways for a molecule at the excited state to lose the absorbed energy and return to the ground state: 'vibrational relaxation', 'intersystem crossing', 'fluorescence', and 'phosphorescence'. In vibrational relaxation the molecule dissipates the excess of vibrational energy through direct interaction with surrounding molecules. In some cases, vibrational relaxation is preceded by the 'internal conversion', a process during which an electron transfers from the low vibrational energy of one electronic state to the high vibrational level of a lower electronic state. In this process no loss of energy occurs, but it can facilitate further vibrational relaxation of the molecule. Both internal crossing and vibrational relaxation happen within picoseconds and as a result usually the molecule reaches the lowest energy level of the excited singlet state S_1.

In the case when the lowest energy level of S_1 overlaps with the vibrational energy levels of the triplet state, a possible pathway for the further loss of the excitation energy is intersystem crossing to the triplet state. This step is usually followed by the nonradiative internal conversion to the lowest energy level of T_1. Further transition of the electron from the triplet excited state to the ground singlet state often takes microseconds, because it requires a change in the spin of the outer electron and is considered a “forbidden” transition in quantum mechanical terms. In most cases this process is accompanied by light emission, termed phosphorescence. Molecules in the triplet state are often reactive and can go through irreversible bleaching, which is highly undesirable in most fluorescence experiments.

An alternative way for a molecule to leave the excited singlet state S_1 is to emit a photon, the energy of which matches the energy gap between the excited singlet state and one of the vibrational or rotational states of the lowest singlet state S_0. This range of acceptable photon energies and wavelengths corresponds to the emission spectrum of the fluorescent molecule. Considering that the fluorophore has experienced prior non-radiative decay of the molecular energy and the emission starts from the lowest vibrational level of S_1, the wavelength of the emitted photons will be mostly longer than the wavelength of the excitation light. This phenomenon is known as the Stokes shift. Fluorophores which exhibit large Stokes shifts are highly desired, because they provide an opportunity to efficiently block the excitation stray light, while collecting the majority of the emission signal in fluorescence spectroscopy and imaging.

The quantum yield of a fluorophore, expressed in Equation 2.2, is a measure of how much light energy a molecule is emitting with respect to the amount of excitation light energy absorbed:

$$Q_{fluorescence} = \frac{E_{emitted}}{E_{absorbed}} \qquad [2.2]$$

In most cases a fluorophore with the quantum yield as close to unity as possible is most desirable. Such widely used, commercially available fluorescent probes as fluorescein and rhodamine 6G that are discussed in Chapter 6 have quantum yields of about 0.9 to 0.95 depending on the solvent [2].

2.2 Introduction to Confocal Microscopy

Confocal optical microscopy has been developed into a powerful imaging technique in recent decades because of its capability of imaging microscopic structures in relatively thick intact samples in three dimensions by acquiring optical sections [3] The continuous interest and advancements in confocal microscopy have been aided by readily available laser sources and powerful computers for image and data processing [3-7].

Confocal microscopy can be conducted in several imaging modes depending on the properties of the sample and research objectives. Reflection mode is broadly used in materials science [8] and can be combined with polarization methods. It is also employed in the electronic industry for the routine quality inspection of circuits. Transmission mode that can be applied with conventional contrasting methods has found applications in biology and medicine [9,10], where it is often combined with another, even more popular, confocal imaging mode: fluorescence confocal microscopy [11-13]. With the progress of biology to the center stage of scientific investigations at the end of the twentieth century, fluorescence confocal microscopy has experienced a burst of advancements. Due to the intrinsic selectivity of fluorescence, the availability of diverse fluorescent probes [2] and the introduction of intrinsically fluorescent gene products, the green fluorescent protein (GFP) being the most widely recognized [14,15], fluorescence confocal imaging became a core research methodology in biology and medicine. Further technical discussion will be focusing specifically on fluorescence confocal microscopy.

2.3 Principles of Confocal Imaging

2.3.1 Confocality

All modern confocal microscopes are based on the principle of confocal imaging described in the 1957 patent by Marvin Minsky. For better understanding of the principles of confocal imaging it is worthwhile to compare it with conventional microscopy. When the samples are imaged with a light microscope, signals from the “out-of-focus” regions of the illumination cone interfere with the signal from the structures in focus. In confocal microscopy, the “out-of-focus” signal is eliminated by the pinhole placed before the detector. Consequently, confocal microscopy provides better resolution than conventional light microscopy. In a wide-field microscope, a large area of the sample is exposed to the light from a mercury or xenon lamp, and the whole image can be viewed directly by eye. In a confocal microscope, illumination of the sample is limited to a tightly focused beam of light, these days usually provided by a laser. A two-dimensional image is created by scanning this light beam across the sample and electronically reconstructing the image from the collected data string. Thus, in confocal microscopy both illumination and detection are considered limited to a point source.

In the original Minsky’s design the illumination light from a zirconium arc source was first passed through a pinhole and then focused by a microscope objective into the sample [6]. The light that passed through the specimen was focused by a second objective lens at a second pinhole, which was confocal to the first, and then delivered to the detector. Minsky has also described the epi-illumination optical configuration (Figure 2.2), in which the excitation and emission light paths overlap and are eventually split with a dichroic mirror. In this approach the microscope objective has a dual role of a condenser that illuminates the specimen and the magnifying and imaging lens that collects the fluorescence emitted by the sample [1]. This is the preferred configuration in modern fluorescent microscopes, because the amount of the excitation light that interferes with the fluorescence signal is dramatically lower than in the transmission configuration.

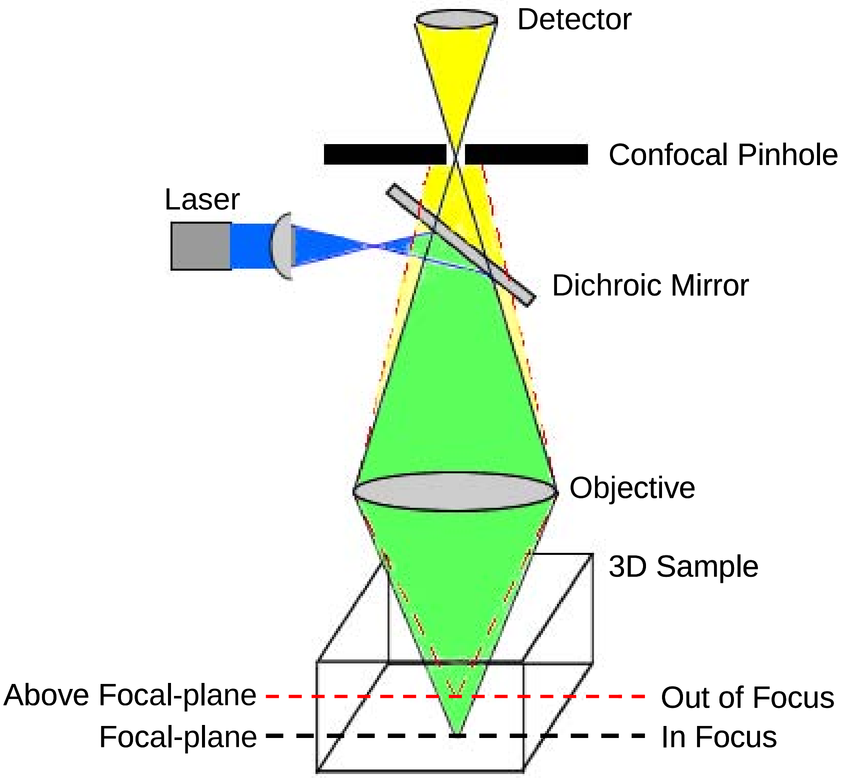

Figure 2.2. Simplified beam paths in a confocal microscope. Excitation light (blue beam) is reflected by the dichroic mirror and focused into the sample. Fluorescence (yellow beam) emitted from the focal point is transmitted through the confocal pinhole while the out-of-focus light (yellow beam with red dashed contour) is mostly blocked by the pinhole, resulting in improved resolution in the axial direction.

While the excitation efficiency of the fluorophore remains the same in both epi- and transmitted microscopes, only excitation light back-scattered by the sample enters the emission channel in the epi-fluorescence system. This back-scattered light is further “filtered out” by the dichroic mirror, which reflects the light of shorter wavelengths (the excitation beam) and allows fluorescence at longer wavelengths to pass through. Most confocal systems are also equipped with a specific band-pass filter or a long-pass barrier filter that further improve the signal to noise ratio of the system. A holographic notch filter can dramatically reduce the back-scattered excitation light, up to a million fold, from the emission signal when a highly scattering sample is imaged.

2.3.2 Construction of a Three-Dimensional Image in Confocal Microscopy

The point excitation and point detection of the signal necessitate scanning of the excitation point across the sample plane to create a two-dimensional image. There are two options available to achieve this goal: rastering the sample/specimen while maintaining the excitation beam focus (stage-scanning method) or scanning the laser beam across the stationary sample (laser-scanning method). The advantages of the first approach include:

1. Comparative simplicity of the optical system, which makes it easier to optimize [16] – this method was applied in the original confocal microscope design by Minsky. The main requirement for the objective lens is the focusing of light into a diffraction-limited spot on the optical plane.

2. Since the off-axis aberrations of the objective are avoided [17], the resolution and contrast of the obtained image are identical across the entire field of view, which produces space-invariant imaging [3].

There are three major drawbacks to the stage-scanning approach:

1. Relatively slow speed of image acquisition (usually a few seconds, depending on the image size and step size);
2. High performance requirements for the sample stage: a stage with nanometer precision and resolution will invariably have limited working distance, while a stage with large working distance is likely to limit system resolving capabilities due to low precision;
3. Movement of the sample, which can distort biological specimens and make any manipulations over the sample while scanning impossible [3,16].

The beam-scanning approach allows faster image acquisition, but requires much more complex optical systems. Beam scanning is usually achieved by using rotating mirror wheels or vibrating galvanometer-driven mirrors [18], or most recently by acoustooptic beam deflectors [19]. In essence, there is no absolute best method of scanning and the choice is usually determined by the application requirements and research objectives. Stage scanning confocal microscopes are traditionally used in materials science, especially in microchip development and imaging [20]. Many commercially available confocal imaging systems, mostly targeting imaging of biological specimens, employ laser-scanning methodology. As will be shown in the following chapters, both stage-scanning and laser-scanning fluorescence microscopy methods can provide high-quality images of tissue phantoms. As will be discussed in the technical sections, the in-house built imaging system used in this work applies the stage-scanning method, while commercial Bio-Rad and LSM 710 confocal microscopes from Zeiss employ laser-scanning of the sample.

Acquisition of three-dimensional images in confocal microscopy is achieved by collecting a series of optical 2D sections at different depth in the specimen - this sequence of images is often called a "z-stack" or "z-series". In both laser-scanning and stage-scanning systems *z*-series are collected by using a computer-controlled stepping motor that moves the stage or the objective up or down by a preset value. With regard to the z-sectioning, it is important to realize that the thickness of each optical section does not depend on the step size of the stepping motor. The 'slice thickness', from which the signal is collected, depends on the objective and the pinhole diameter. The resolution of a fluorescence confocal system is discussed in the next section.

2.4 Resolution in Confocal Microscopy

2.4.1 The Concept of Point Spread Function

Apart from the capabilities of the scanning hardware (either laser-scanning head or a sample-scanning stage), the resolution of the confocal instrument is governed by the wavelength of the excitation light, the objective lens and the properties of the specimen [6]. The highest resolution can be achieved if the illumination light is focused into a diffraction-limited point in the specimen. The resolution of any optical system is defined as the minimum separation between two point objects that allows them to be perceived as distinct entities in the image. However, not even a diffraction limited optical system can image a truly point-like object as a single point. When a point-like light source is imaged through a microscope, the amplitude of the electromagnetic field produced in the image plane can be regarded as the optical system response to the specimen. The strength of this field is related to the amplitude point spread function (PSF), which is a useful reference measure for comparing the performance of optical microscopes [7,21]. Though the amplitude cannot be observed directly, the visible image of the point source formed in a microscope can be visualized through the ocular and recorded by the detector, this is so called intensity point spread function. Intensity PSF corresponds to the squared modulus of the amplitude PSF and describes the system response in real space.

The intensity PSF can be calculated as the product of the amplitude PSF and its complex conjugate:

$$|h(u,\upsilon)|^2 = h(u,\upsilon)\cdot h^*(u,\upsilon) \qquad [2.3]$$

where u and υ are normalized optical units parallel and perpendicular to the optical axis, respectively. With the optical axis in the z direction, υ and u can be expressed as

$$\upsilon = \frac{2\pi nr\sin\alpha}{\lambda},\ u = \frac{2\pi nz\sin^2\alpha}{\lambda} \qquad [2.4]$$

where $r = \sqrt{x^2 + y^2}$ is the lateral distance from the optical axis, λ is the wavelength of the point-like source, α is the opening angle of the objective lens, and n is the refractive index between the objective and the point-object. A more detailed discussion on the theoretical calculation of the three-dimensional PSF is provided by Born and Wolf (1999) [22].

As stated earlier, confocal microscopy uses both pointwise illumination and pointwise detection. Thus, in a confocal fluorescence microscope two point images are generated: one is the projected image of the laser light into the object space, the other is the projection of a point of emitted fluorescence signal into the image space. Only the fluorophores that are in the volume shared by the illumination and detection PSFs have a chance to be both excited and detected. Since the excitation and detection are independent of each other, the total confocal fluorescence PSF can be expressed as the product of the illumination intensity PSF (PSF_{ILL}) and the detection intensity PSF (PSF_{DET}):

$$|h_{confocal}(x, y, z)|^2 = \quad |h_{detection}(x, y, z)|^2 \quad |h_{illumination}(x, y, z)|^2 \quad [2.5]$$

The spread of the illumination intensity PSF is a function of the excitation wavelength and the numerical aperture of the microscope objective, which will be discussed further. It is also influenced by pupil illumination and aberrations in the optical components. PSF_{ILL} is deformed by thick light scattering specimens and the mismatch in the refractive indices of the immersion fluid and the specimen [23]. Matching the refractive indexes is crucial for the diffraction limited performance of the confocal system.

Detection intensity PSF is influenced by all the factors listed above and by the pinhole size. Since the pinhole can never be infinitely small, PSF_{DET} is always larger in dimension than PSF_{ILL}. The smaller the pinhole diameter, the more PSF_{DET} approaches the order of magnitude of PSF_{ILL} [7].

Actual specimens are rarely point sources, but they can be regarded as a superposition of point-like, subresolution objects. The approximate intensity PSF of a microscope can be measured experimentally by imaging a subresolution spherical bead as it is scanned through the focus. Due to aberrations, noise and other technical difficulties in reaching the theoretically expected PSF experimentally, it is generally accepted to use calculated point spread function to evaluate the system performance and compare between different optical arrangements.

2.4.2 Airy Disk

Figure 2.3 shows computer-generated theoretical intensity point spread functions of several point-like objects. The intensity PSF extends in all three dimensions, but for the discussion of the resolution and contrast it is useful to consider the lateral components of the intensity distribution. The top left panel of the Figure 2.3 shows the projection of the 3D-PSF in z direction.

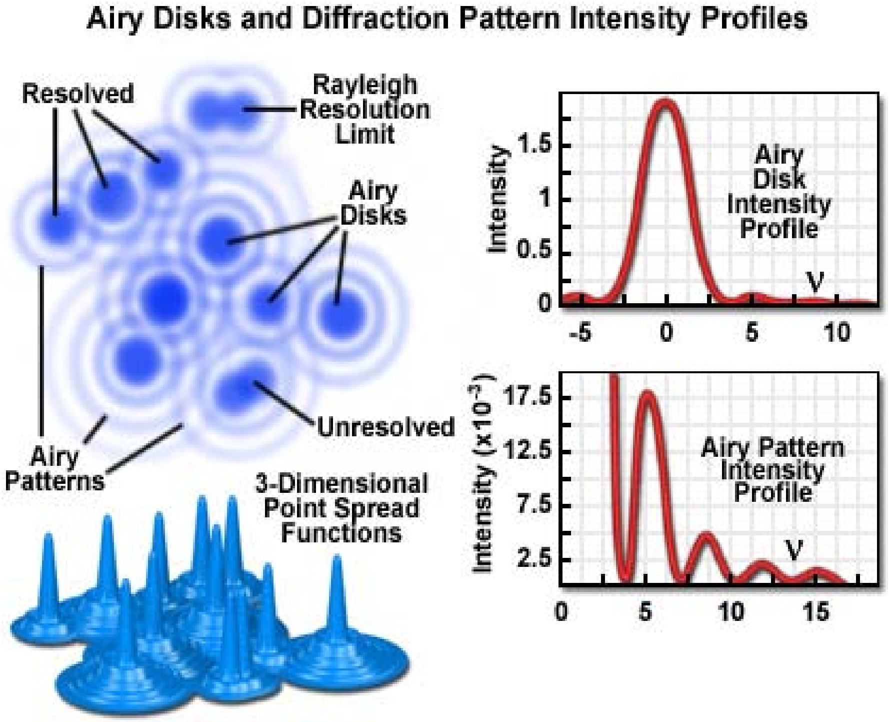

Figure 2.3. Schematic diagram of an Airy disk diffraction pattern and the corresponding three-dimensional point spread functions for image formation in confocal microscopy. Intensity profiles of a single Airy disk, as well as the first and higher order maxima are illustrated in the graphs. Adapted from [29].

To discuss the resolution in confocal systems we should introduce the concept of the Airy disk which is the area of the highest intensity in the diffraction pattern (within the first minimal concentric ring) on the z-projection of the illumination PSF in Figure 2.3. Accordingly, the Airy unit (AU) is defined as:

$$1AU = \frac{1.22 \times \lambda_{ex}}{NA} \qquad [2.6]$$

where λ_{ex} is the excitation laser wavelength, and NA is the numerical aperture of the objective. The airy unit refers to the diameter of the Airy disk [24].

Resolution of an optical system is defined as the minimum distance between two point objects that provides a certain contrast between them, so that they are "sufficiently" distinguished [25]. The Rayleigh criterion is most broadly accepted to define the term "sufficiently" in optical resolution [24,25]. According to this criterion, two point objects are resolved when the first minimum of one Airy disc pattern is aligned with the central maximum of the second Airy disc (Figure 2.4A) [26]. In this case the intensity PSFs of two objects partially overlap displaying two peaks separated by a gap. The larger the depth of the gap between the peaks, the easier it is to distinguish, or resolve, the two objects. It is obvious from this observation that the resolution of the system depends on the widths of the intensity PSFs of the point objects. Microscope resolution is directly related, therefore, to the full width at half maximum (FWHM) of the instrument's intensity point spread function [21,27,28].

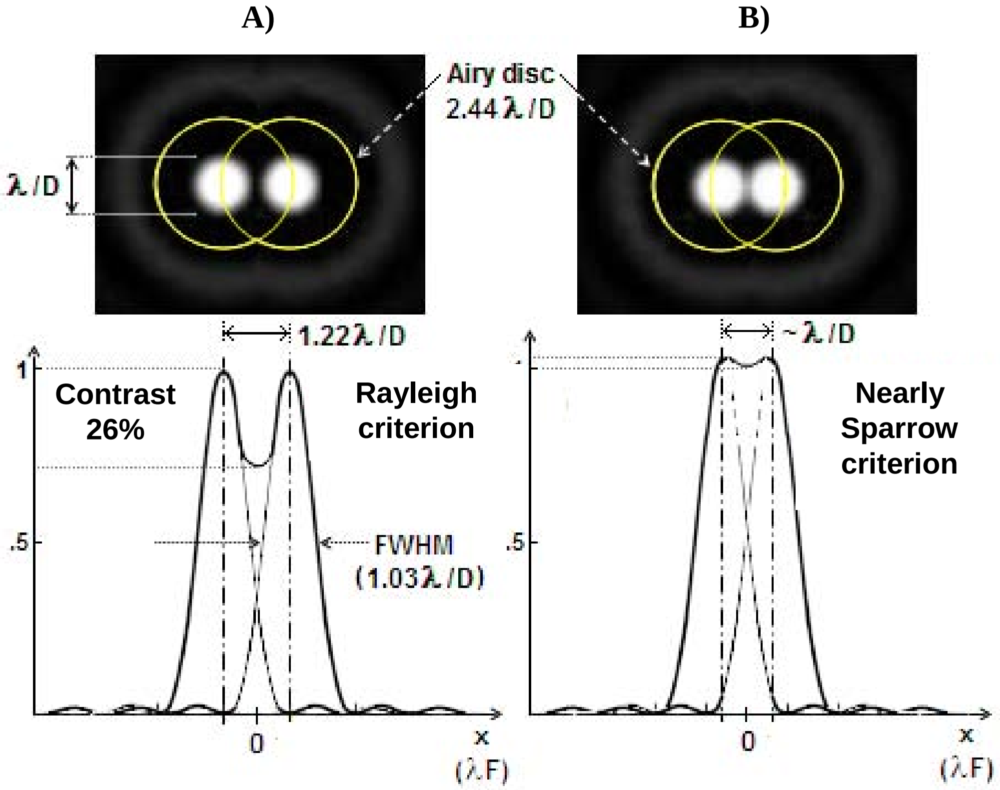

Figure 2.4. Lateral intensity of the single-photon illumination intensity PSF (i.e., the Airy function) for two point objects at two separation distances. (A) The point objects are separated by the distance specified by the Rayleigh criterion, i.e. the radius of the Airy disc, which is equal to $1.22\lambda/D$ (λ is the emission wavelength, D is the aperture diameter or twice the NA of the objective); the achieved contrast is 26%. (B) The point objects, separated by the distance λ/D, provide less than 2% contrast. Reducing the separation to the point at which the intensity between the peaks flattens brings the system to the Sparrow's resolution limit, at which point the contrast is zero. Adapted from [29].

2.4.3 Contrast

To quantify resolution, the concept of contrast can be employed. Contrast is defined as the difference between the maximum intensity of the two objects and the minimum intensity observed between them [25]. Since the maximum intensity of the PSF is normalized to one, the highest achievable contrast is also one [29] and it occurs when the spacing between the two objects is equal to the sum of the two Airy disk radii or more. Defining the resolution in terms of contrast, the Rayleigh criterion corresponds to the distance at which a 26.4% contrast is achieved (Figure 2.4A). The distance at which the dip between two PSF peaks just disappears is referred to as the Sparrow criterion (Figure 2.4B), which defines resolution as the cutoff distance, i.e. the separation below which the contrast becomes zero [25,29,30].

Essentially, any contrast greater than zero can be used to define resolution, but the 26-percent contrast of the Rayleigh criterion is considered reasonable in typical microscopy applications. Under ideal imaging conditions, the lateral resolution of a conventional fluorescence microscope can be defined according to the following equation [25], in which the point separation (r) in the image plane is the distance between the central maximum and the first minimum of the Airy disk:

$$r_{xy} \approx 1.22\, \lambda_{em} / (2 \cdot NA) = 0.6\, \lambda_{em} / NA \qquad [2.7]$$

where λ_{em} is the wavelength of the emitted light and NA is the numerical aperture of the objective.

Since practically it is difficult to gauge the location of an intensity minimum in the Airy disk pattern, to determine the resolution experimentally, it is common to measure the FWHM value of the microscope's PSF [29]. Although, it is good to remember though that the FWHM values are approximately 17% smaller than the resolution calculated using the Rayleigh criterion [25].

For a confocal fluorescence microscope, in which both illumination and detection are limited to a point, so only the fluorophores in the shared volume of the illumination and detection point spread functions are able to be detected, the lateral resolution is about 30% narrower than of the conventional fluorescence microscope. Thus, under ideal imaging conditions, reasonable contrast in a confocal microscope can be achieved if two point-like objects are approximately separated by:

$$r_{xy,\ confocal} \approx 0.4\ \lambda_{em}\ /\ NA \qquad [2.8]$$

As we can see, in both widefield and confocal microscope configurations, the lateral resolution is proportional to the wavelength of the emitted light and inversely proportional to the NA of the microscope objective.

The axial resolution of an optical system can be defined in the same terms as applied for the lateral resolution. Reasonable contrast between two point-like objects lying on the optical axis is achieved when they are separated by the distance between the central maximum and the first minimum of the axial component of the intensity point spread function. Figure 2.5 presents the axial intensity section through the 3D-PSF distributions for a typical widefield and a confocal fluorescence microscopes [29]. There is a dramatic reduction in the side lobes of the confocal PSF as compared to the conventional microscope PSF, meaning that more of the intensity is concentrated at the center of the focal volume [25].

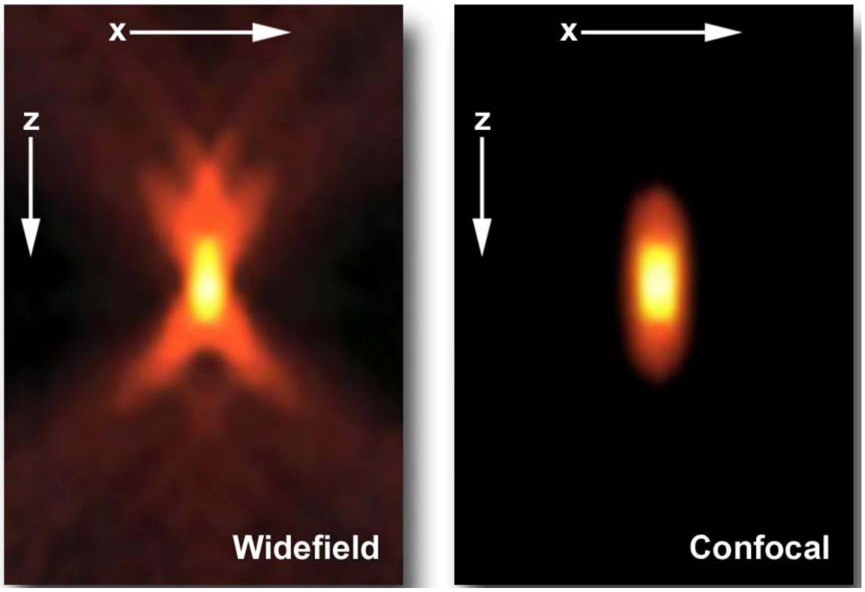

Figure 2.5. Comparison of axial (x-z) projections of the point spread functions for widefield (left) and confocal (right) microscopy. Computed dimensionless representations. Adapted from [29].

Just as the case of lateral resolution, confocal intensity PSF is about 30% narrower in axial extent than widefield intensity PSF, which results in 30% smaller resolution value. The axial resolution of a conventional fluorescence microscope is given by:

$$r_z = 2\,\lambda_{em} \cdot n \,/\, NA^2 \qquad [2.9]$$

where λ_{em} is the wavelength of the emitted light, NA is the numerical aperture of the objective and n is the refractive index of the specimen. The axial resolution for the confocal configuration is:

$$r_{z,confocal} \approx 1.4\, \lambda_{em} \cdot n\, /\, NA^2 \qquad [2.10]$$

The axial resolutions obtained through these calculations are 10% greater than the axial FWHM measurements of the corresponding PSFs [25]. In both microscope arrangements the axial resolution is proportional to the wavelength and refractive index, and inversely proportional to the square of the numerical aperture. Consequently, the numerical aperture of the microscope objective has a much greater effect on axial resolution than does the emission wavelength.

2.5 Optical Sectioning in Confocal Microscopy

Closely related to the concept of the axial resolution is the optical sectioning property of the confocal system, which allows non-destructive sectioning of thick specimens. The ‘slice thickness’ of a confocal system is defined as the distance on either side of the focal plane at which the intensity of the image falls to half maximum [13]. In the ideal case scenario the minimal slice thickness of the confocal system would equal to a half of the FWHM value of the axial component of the intensity PSF. Practically, the optical section of the system can be estimated using the following equation:

$$Z_{1/2} \approx 0.45\, \lambda_{em}\, /\, n\, (1 - \cos a_{max}) \qquad [2.11]$$

where n is the refractive index of the medium between the specimen and the objective (n = 1 for air; n = 1.51 for oil) and a_{max}, the opening angle of the objective lens, is related to the numerical aperture by:

$$NA = n \cdot \sin a_{max} \qquad [2.12]$$

By expressing a_{max} through the numerical aperture and substituting it in equation for the optical section we have:

$$Z_{1/2} \approx 0.45\, \lambda_{em} \,/\, n\,\{1 - \cos\,[\sin^{-1}(NA/n)]\} \qquad [2.13]$$

From the combined equation is it clear that the numerical aperture of the objective strongly influences the optical section thickness as well as the final resolution of a confocal microscope [31]. The higher the NA, the thinner the optical section.

2.6 Improving the Resolution

Two most straightforward approaches to improving the resolution of an optical microscope are optimization of the illumination (and emission) wavelength and adjustment of the numerical aperture of the objective [25]. As was shown in the earlier discussion, both lateral and axial resolutions are proportional to the wavelength of light. Therefore, in single-photon microscopy both resolutions can be improved by using fluorophores that have shorter excitation and emission wavelengths. Conventional microscope optics limit the excitation wavelength to above 350 nm, since UV light has poor transmission through glass. In essence, the nature of the specimen and the experimental design usually determine which excitation and emission wavelengths will be used.

In both widefield and confocal arrangements the lateral resolution of a microscope is inversely proportional to the NA of the objective; and the axial resolution is inversely proportional to the square of the NA. Hence, another efficient way to improve the resolution is to use an objective lens with a higher numerical aperture [25]. NA of an objective is proportional to its angular aperture, which has a practical upper limit of about 72^o [31]. Objective's numerical aperture signifies its light focusing and collection ability. The amount of the excitation light delivered through an objective and the amount of the fluorescence emission collected are both roughly proportional to the squared NA of the objective [1]. Thus, the final signal collected through the fluorescence confocal microscope is roughly proportional to $(NA)^4$. Many objectives with high NA and high magnification are of oil immersion type. They provide an additional benefit of minimizing the light loss due to the reflection and refraction off the coverslip, since the refraction index of the oil matches the one of the coverslip. Unfortunately, the lenses with higher NA are usually those with higher magnification and hence smaller working area and shorter working distance [31]. Also, the use of oil as the medium between the objective and a biological specimen in an aqueous medium might not be optimal due to severe aberrations that degrade the imaging performance, especially at depth beyond 15 μm [17,23]. For imaging thick biological samples a water-immersion lens with a lower NA would provide a better performance than the high NA oil-immersion objective [25].

2.7 Photobleaching

Bleaching is a generic term for all of the processes that cause the fluorescent signal to fade permanently. Theoretically, a fluorophore can cycle between the ground and excited states for an unlimited number of times, but the environmental conditions in which organic fluorophores are usually used limit the number of cycles. For most fluorophores the exact photochemistry of bleaching is not well understood [1], though it is known to be caused by the photon-induced chemical damage and covalent modification [32]. While several recently developed techniques, such as fluorescence recovery after photobleaching (FRAP) [33] and fluorescence loss in photobleaching (FLIP) [34], use photobleaching to their advantage, fading of the specimen caused by the very intense laser light can be a significant problem in confocal fluorescence microscopy. One solution is to select the fluorescent probes that are less sensitive to bleaching [16], such as rhodamine or Alexa Fluor dyes. Another option is the addition of commercially available antifade reagents, but due to the possibility of chemical alterations to the sample environment their use should be highly judicious [29]. Perhaps the best solutions rest in the adjustment of the imaging procedure: limiting the exposure time of fluorophores to illumination and, the concentration and the quantum yield of the fluorophore permitting, reducing the intensity of the excitation beam. The power of the laser light is usually reduced by the introduction of the neutral density filters in the excitation channel.

Neutral density filters are used to attenuate the light equally at all wavelengths. They are specified by the value of optical density, the efficiency to cut down the intensity of light. Neutral density filters are commonly used to adjust or match the intensity of two signals while keeping the optical path and the detector gain the same.

2.8 Two-photon Excitation

2.8.1 Overview

Alongside confocal microscopy, two-photon excitation (TPE) microscopy belongs to the class of imaging techniques that allows observation of biological processes in the specimens at conditions very close to the natural environment [35-37]. Moreover, TPE intrinsically excites the sample in a very small probe volume in the plane of focus, resulting in intrinsic confocality without a confocal pinhole. These attractive features made TPE microscopy one of the most promising and fast-growing optical imaging techniques in biological and medical imaging [7,32,38].

2.8.2 Principles of Nonlinear Fluorescence Excitation

Typically, absorption of a photon of sufficient energy is necessary for the transition of a molecule from the ground state to the excited state. It is also possible that the simultaneous absorption of two photons of lower energy by the molecule can cause a similar transition, if the sum of their energies is enough to span the gap between the excited and ground states (Figure 2.6). This idea was first proposed and demonstrated by Sheppard, Kompfner, Gannaway, and Choudhury, who outlined how such a nonlinear optical phenomenon can be applied in microscopy [39,40].

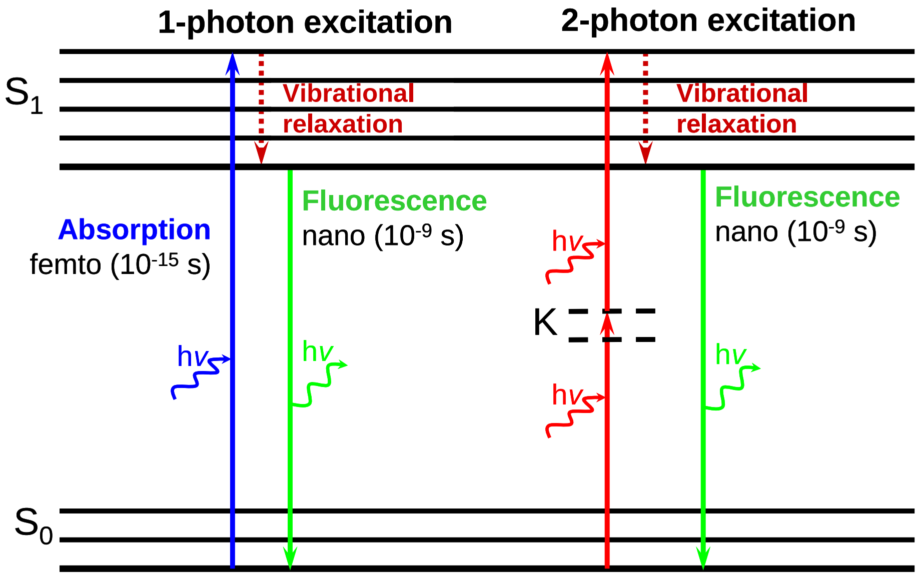

Figure 2.6. Simplified Jablonski diagram comparing the excitation of a fluorescent molecule through one (left) and two (right) photon absorption. S_0 is the ground state, S^* is the excited state, K is a virtual state only permitted for a very short time.

Although the concept of using two-photon excitation in microscopy imaging was conceived in the late seventies, TPE laser scanning microscopy became a practical and widely used technique only in the nineties with the development of ultrafast lasers, providing high-peak-power femto-second pulses with repetition rate of around 100 MHz [41-43].

The requirement for nearly simultaneous absorption of the excitation photons stems from the fact that the molecule’s transition time between the states is very brief, on the order of femtoseconds. Thus, two photons must be within the absorption cross-section of a molecule in the same time frame. The probability of such event is high enough only if the photon flux density is huge, on the order of 10^{30} photons/(s·cm^2) [44]. High illumination flux is achieved through concentrating the photons in time (by pulsing laser radiation) and concentrating them spatially (by tightly focusing laser light through microscope optics) [45]. For example, a Ti:sapphire laser generates picoseconds to 100 femtoseconds pulses of high peak power at a comparatively low repetition rate (~100 MHz, i.e., 10 ns between the pulses) and thus low average power, typically around 10 mW [46]. In commercial instruments a Ti:sapphire laser is generally favored over other mode-locked laser, because it provides greater versatility due to the tunability of its output wavelength: from 720 to 900 nanometers available in commercial models [45]. Even when a sample is illuminated by a short laser pulse of comparatively high intensity, the only area where the photons are “crowded” enough for the “simultaneous” interaction with a single fluorophore molecule is the focal volume. The localization of the excitation to the focal point is the major advantage of the TPE technique over conventional confocal microscopy [47].

As stated earlier, the sum of the energies of two lower-energy photons should be roughly equal to the energy of one photon necessary for the excitation of the molecule. Expressing the energy of light through λ, the wavelength in vacuum:

$$E = \frac{hc}{\lambda} \qquad [2.14]$$

where $h = 6.626 \cdot 10^{-34}$ J·s is Plank's constant and $c = 2.9979 \cdot 10^{8}$ m/s is the speed of light in vacuum, we can establish the relationship between the wavelengths of the single-photon and two-photon excitation illuminations as:

$$E_{1-photon} = E_{photonA} + E_{photonB} \qquad [2.15]$$

$$\lambda_{1-photon} = \left(\frac{1}{\lambda_{photonA}} + \frac{1}{\lambda_{photonB}} \right)^{-1} \qquad [2.16]$$

In principle, two photons necessary to excite one molecule do not have to be identical [44], but for practical reasons using a single pulsed laser as an excitation source is more common. In this case,

$$\lambda_{photonA} = \lambda_{photonB} = 2\lambda_{1-photon} \qquad [2.17]$$

Unfortunately, the quantum-mechanical selection rules for TPE differ from those for one-photon excitation [7,32]. This means that the excitation cross-section, i.e. the propensity to absorb photons having a certain energy or wavelength, for multi-photon excitation microscopy cannot be derived from the knowledge of one-photon cross-sections and must be measured. A “rule of thumb” based on Equation 2.15 states that one may expect the TPE cross-section to peak in the vicinity of twice the wavelength with respect to one-photon excitation, especially in symmetric molecules [47].

2.8.3 Resolution in Two-photon Excitation Microscopy

In a two-photon microscope, the fluorescence emission intensity is proportional to the probability of simultaneous absorption of two photons by one molecule. Since the absorption of each photon is an independent event, the probability of such simultaneous event is proportional to the square of the excitation intensity. Due to the intrinsic confocality of two-photon microscopy, i.e., only molecules in the plane of focus have an appreciable chance to absorb two photons simultaneously, a large-area detector can be used without the confocal pinhole. In this case, the intensity PSF of a two-photon microscope is equal to the illumination intensity PSF [7]:

$$|h_{two\text{-}photon}(x, y, z)|^2 = [|h_{illumination}(x, y, z)|^2]^2 \qquad [2.18]$$

On the other hand, adding a pinhole to the detection path, if the signal intensity permits, can further improve the extent of the two-photon microscope intensity PSF. In this case, the two-photon confocal intensity point spread function is expressed as:

$$|h_{2p\text{-}confocal}(x, y, z)|^2 = [|h_{illumination}(x, y, z)|^2]^2 \, |h_{detection}(x, y, z)|^2 \quad [2.19]$$

Addition of the pinhole in the emission channel can improve the axial resolution of a two-photon microscope by approximately 40% [7]. Nevertheless, compared even to this “pinhole-enhanced” configuration of a two-photon microscope, conventional microscopy usually provides better resolution, both laterally and axially. In fact, two-photon microscopy has 15% broader FWHM of the intensity PSF than conventional (non-confocal) fluorescence PSF [25]. Lateral and axial two-photon resolution can be calculated according to the following formulae:

$$r_{xy,2-photon} \approx \frac{0.7\lambda_{em}}{NA} \qquad [2.20]$$

$$r_{z,2-photon} \approx \frac{2.3\lambda_{em} n}{NA^2} \qquad [2.21]$$

where λ_{em} is the wavelength of emitted light, n is the refractive index between the objective and the focal plane, and NA is the numerical aperture of the objective lens.

Thus, the optical sectioning performance of a two-photon microscope is worse than that of a comparable confocal microscope. Other drawbacks of TPE microscopy include: broad two-photon excitation cross-sections of many dyes, which limits the signal resolution from a multiply labeled specimen, and higher photobleaching in the focal plane than in the confocal case [38,48], though surely in TPE it is confined to the focal volume and overall photobleaching is reduced.

2.8.4 Advantages and Applications of TPE

Two-photon excitation microscopy excels at imaging living cells [44,47,49], intact tissues such as brain slices [37,50,51], embryos, whole organs, and even entire alive animals [51-54]. The following list of the TPE advantages is the explanation for its popularity in imaging biological samples:

1. Deeper imaging capabilities: since the Rayleigh scattering is inversely proportional to λ^4, the excitation light of longer wavelength has a chance to penetrate deeper into the highly scattering biological tissues than ultraviolet-visible wavelengths used for conventional excitation [51].
2. Large-area detectors, which collect photons more efficiently than point detectors, can be used, because emitted fluorescent photons stem from the confined illumination volume, thus providing intrinsic confocality [47].
3. Reduction in background fluorescence, since only molecules in the focal volume are excited, partially compensates for the reduction in spatial resolution due to the wavelength [44,55].
4. Photobleaching and photodamage are confined to the focal volume, which improves thick specimen viability during image acquisition [56].
5. Imaging of a UV-excited probe with single-photon excitation requires the use of expensive UV optics, while TPE can be coupled with a conventional microscope, though this advantage can be somewhat offset by the high cost of femtorsecond laser sources [47,57].

6. In one-photon excitation microscopy, care should be taken to separate any scattered excitation light from the emission signal, which can be challenging due to their comparative wavelength proximity (about 50-200 nm between peaks). In TPE, fluorescence occurs at substantially shorter wavelength than excitation and thus can be easily detected without interefernce from the scattered excitation [7].

The applications of TPE microscopy for the analysis of non-biological objects are not as prominent in literature, but it can provide certain advantages when imaging a UV-excited fluorophores with regular, non-UV, optical system is desired. It is always worthwhile to first carry out experiments with a confocal microscope and with single-photon excitation. Preliminary confocal imaging is advisable to ensure the structural features of the sample can be sufficiently resolved, since the image resolution with two-photon excitation is often worse than that achieved in a well-aligned confocal microscope [45].

The intrinsic property of TPE to interact with the specimen only in a very small region of the order of 0.1 femtoliter makes it suitable for interactive experimentation methods, such as chemical uncaging [58] and light-induced isomerization. In the study of model lipid bilayer membranes [59] two-photon absorption photoinduced the flip-flop of stilbazolium markers, which caused transient perforation of the membrane. An additional benefit of two-photon excitation utilized by the researchers was direct monitoring of the process by concomitant TPE fluorescence and second-harmonic generation (SHG) signals. Both uncaging and photoisomerization applications of TPE promise the possibility of using it for microscale localized and targeted controlled drug delivery in deep tissue [46].

CHAPTER 3 STATISTICAL SIMULATION OF TISSUE SPECTRA FOR COMPARISON OF SPECTRAL ANALYSIS METHODS

3.1 Introduction

3.1.1 Cancer Diagnosis

Cancers remain one of the most pressing health-care issues worldwide for the significant number of new cases diagnosed each year and the low success rate of treatment, if the cancer reaches a late stage [60]. The survival rate of cancer patients greatly depends on the stage of the disease at the time of diagnosis. Current cancer therapies are quite effective at early stages of cancer; the 5-year survival rate of patients with no spread of the disease for most cancers is over 90% [60]. However, according to American Cancer Society, currently only a limited fraction of cancer cases is diagnosed in the early stage before the disease spreads to nearby organs. For example, only 39% of colorectal cancer patients are diagnosed when the disease is still localized [60]. Thus, detection of cancers at their early stages is the key to timely treatment and improved survival rate of the patients.

The gold standard for cancer diagnosis in clinical practice is histopathology of tissue obtained through biopsy, i.e., removal of small samples at suspicious locations. After excision, collected tissues are prepared for histopathological analysis, which takes at least several hours. In addition, biopsy carries a certain risk of complications due to its invasive nature. Most importantly, the decision of whether the tissue should be sampled or not is based only on its visual impact during physical examination. This decision can be especially difficult in case of gastrointestinal cancer diagnosis. Since the screening relies solely on the physical appearance of polyps, dysplasia and early-stage cancer are frequently overlooked [61]. The challenge of an accurate judgment lays in differentiation of malignant abnormal from benign abnormal tissue conditions.

Taking colonic cancer as an example, the clinical tissue conditions are divided into four pathological stages: normal, hyperplastic, adenomatous, and cancerous [62-64]. Hyperplastic tissue conditions are characterized by the abnormal multiplication of normal cells in normal arrangements. Since hyperplastic polyps are not spreading, they are treated as benign abnormals and usually do not require medical treatment. Adenomatous tissues are a form of epithelial tumor that does not invade the surrounding tissues or metastasize to other parts of the body. Nevertheless, statistics show that over 90% of colon cancers originate from adenomas, so adenoma is considered to be a pre-cancerous stage and, if possible, should be removed. The fact that adenomatous tumors usually do not return after surgical excision makes the diagnosis of adenomatous conditions particularly desirable [65]. Development of minimally invasive, fast screening routines along with quantitative diagnostic thresholds between the benign abnormals, i.e., hyperplastic polyps, and malignant abnormals, i.e., adenomatous polyps and cancerous tumors, is of vital importance in the early diagnosis and prevention of gastrointestinal cancers.

3.1.2 Optical Diagnosis

Optical spectroscopy offers a particularly promising solution in the pursuit of noninvasive methods for early cancer diagnosis [62,63,66]. Its advantage of noninvasiveness comes from the capability of delivering the illumination light and collecting tissue signal though fiber optics. A spectroscopic optical probe is often incorporated into a standard white-light endoscopy system [67-70], thus, collected and instantaneously analyzed spectral information can provide real-time feedback on the condition of the tissue during endoscopic examination. Aside from the low cost, high speed and noninvasiveness, optical spectroscopy provides quantitative results that can greatly enhance the objectivity of diagnosis.

The biochemical and morphological changes in the tissue during the development of cancer manifest themselves in the optical characteristics of the tissue, including absorption, scattering, and autofluorescence. It was demonstrated in many studies that tissue fluorescence spectra are related to the tissue clinical condition [63,66,67,71]. Due to the intrinsic sensitivity and selectivity of autofluorescence spectroscopy, it has been a highly active area in cancer diagnosis research [66,71-76]. A general trend of decreased autofluorescence intensity has been observed during tissue progression from normal to cancerous condition [67,75,77-80]. The differences in the fluorescence emission spectra of normal and cancerous tissues might be caused by changes in the molecular composition specific to dysplasia or the tissue morphology [72]. Based on the spectroscopic differences between tissue types, various spectral analysis methods have been proposed to quantitatively differentiate diseased from non-diseased tissues [67,68,75-77,81-88]. These methods range from simple empirical parameters to complicated statistical pattern recognition techniques.

This study was aimed at comparison of methods for the analysis of tissue autofluorescence spectra for the purpose of cancer diagnosis. The methods compared were: principal peak ratio (PPR), differential normalized fluorescence (DNF), bivariate DNF (2D-DNF), and principal component analysis (PCA). The use of simulation in this study allowed us to conduct the evaluation of methods in the nearly entire sample space. For statistically meaningful comparison, the classification boundary in each method was determined according to the Bayes decision theory [76,89]. The efficacies of the methods were then evaluated with the five generally used statistical criteria: sensitivity, specificity, predictive value positive (PVP), predictive value negative (PVN), and false alarm rate [75].

3.2 Experimental

3.2.1 Chemicals and Materials

Collagen type IV (type VI according to Sigma classification), nicotinamide adenine dinucleotide in reduced form (NADH), flavin adenine dinucleotide (FAD), and hemoglobin (Hb) were obtained at the highest purity from Sigma-Aldrich (St. Louis, MO) and used as received. Individual spectra of tissue chromophores were collected from solutions prepared in phosphate buffer saline (PBS, pH 7.4, 150 mM) and are displayed in Figure 3.1. Ultra pure Milli-Q (Millipore, Bedford, MA) water was used to prepare the buffer solutions. Fluorescence emission spectra excited at 325 nm by a HeCd laser were recorded from 350 nm to 650 nm with 1-nm step with an SLM48000MHF (Jobin Yvon, Edison, NJ) spectrofluorometer with a photomultiplier tube (PMT) detector. Fluorescence emission spectrum of collagen was collected with a 345-nm long-pass filter in the detection channel to reduce the scattered excitation light and match the optical conditions for the acquisition of real tissue fluorescence spectra [75]. The blank PBS buffer served as the control to correct the solvent Raman scattering. The absorption spectrum of hemoglobin was collected on a Cary 3.0 UV-Vis spectrometer.

3.2.2. Simulation of Tissue-Phantom Spectra

Fluorescence spectra of colonic tissues in different clinical conditions were constructed from the individual spectra of tissue chromophores. Three major tissue fluorophores, collagen IV, NADH and FAD, contribute to tissue autofluorescence under experimental conditions in our lab [75,90]. The Soret band of hemoglobin absorption overlaps with collagen and NADH fluorescence and produces a dip in the overall tissue spectrum.

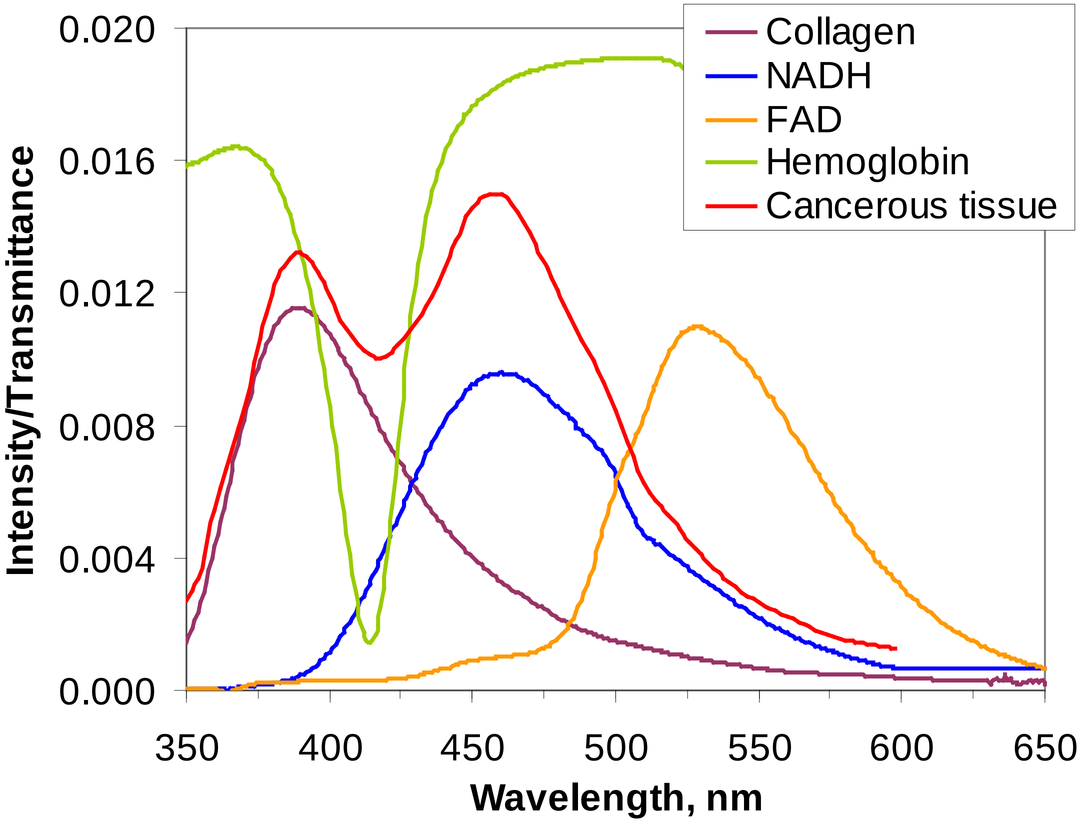

Figure 3.1. Individual spectra of tissue chromophores and a selected cancerous tissue spectrum. Spectra of collagen, NADH and FAD are normalized to the integrated area of one; hemoglobin transmittance spectrum is off-set for clarity. The excitation wavelength was 325 nm for all fluorescence spectra.

Twenty thousand simulated spectra of tissues in different clinical conditions were constructed in Matlab (MathWorks, Natick, MA). Contributions of the four tissue chromophores were assumed normally distributed and were randomly generated in MatLab within three standard deviations of the mean value. Listed in Table 3.1 are the means and standard deviations of the distributions that were adapted from a clinical study by Schomacker et al. [67]. This study reported on 177 fluorescence spectra collected *in vivo* during routine colonoscopy and included 86, 35, 49, and 7 spectra of normal, hyperplastic, adenomatous and adenocarcenomatous specimens, respectively.

Table 3.1. Contributions of individual tissue chromophores to the tissue fluorescence intensity.

Tissue type	N	Collagen %	NADH %	FAD %	Hemoglobin %
Normal	86	87.4 +/- 1.4	11.6 +/- 1.3	1.0 +/- 0.2	22.0 +/- 0.5
Hyperplastic	35	64.4 +/- 3.3	32.6 +/- 3.1	3.1 +/- 0.5	22.8 +/- 1.1
Adenomatous	49	49.1 +/- 3.6	47.9 +/- 3.5	3.0 +/- 1.5	26.3 +/- 1.4
Cancerous	7	42.8 +/- 6.8	53.8 +/- 7.0	4.7 +/- 2.1	35.7 +/- 6.0

Note: N - number of samples.

Source: Schomacker, K. T., J. K. Frisoli, C. C. Compton, T. J. Flotte, J. M. Richter, N. S. Nishioka, and T. F. Deutsch. "Ultraviolet Laser-Induced Fluorescence of Colonic Tissue - Basic Biology and Diagnostic Potential." *Lasers in Surgery and Medicine* 12, no. 1 (1992): 63-78.

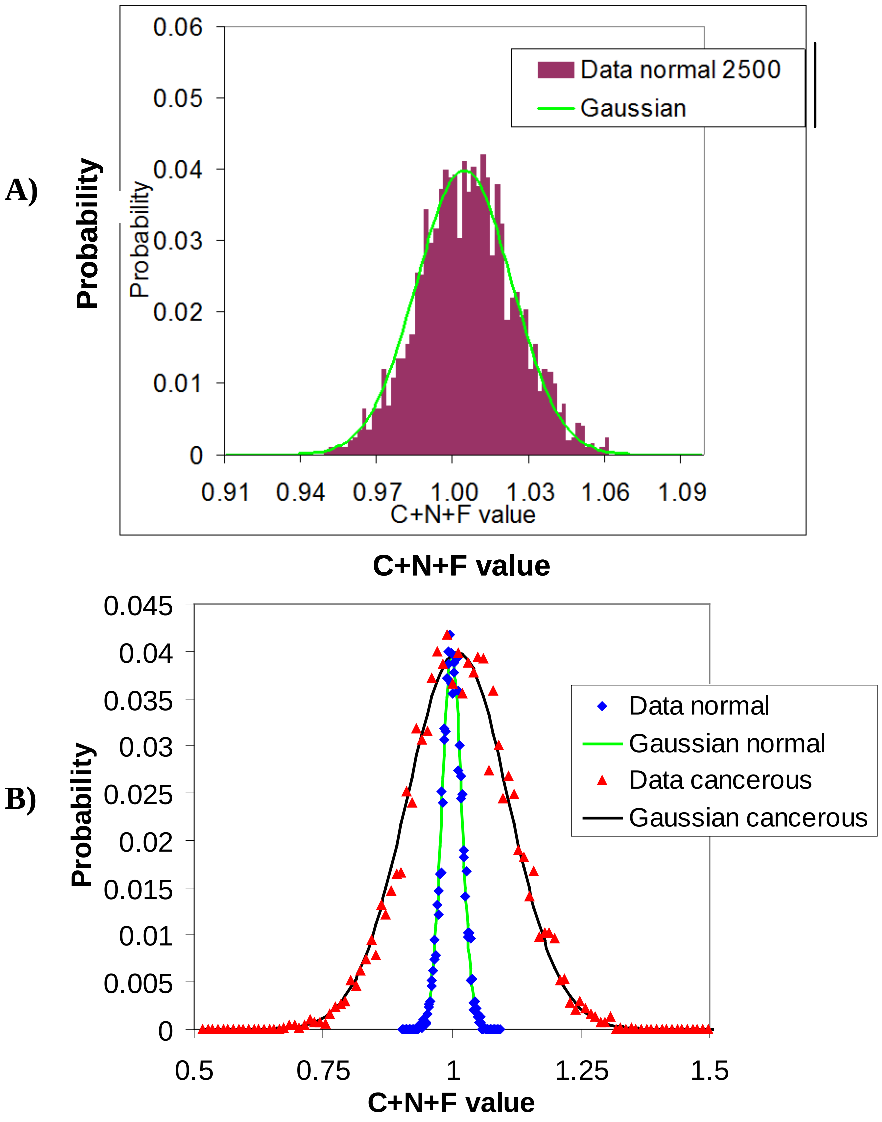

Figure 3.2. Probability distribution of the integrated simulated spectral intensity before hemoglobin absorption is accounted for. (A) Probability distribution of the normal tissues from the training set (2500 spectra). (B) Comparison of the normal and cancerous tissues distributions.

Prior to the simulation, each component spectrum was normalized to the integrated area of one. The maximum of the collagen spectrum was centered to 390 nm to account for experimental and instrumental differences between Schomacker's report and the spectroscopic data used in this work. The intensity of simulated spectrum I at each wavelength λ was calculated according to:

$$I(\lambda) = I_C(\lambda)\alpha_C + I_N(\lambda)\alpha_N + I_F(\lambda)\alpha_F \qquad [3.1]$$

where I_C, I_N and I_F are the spectral intensities and $\alpha_C, \alpha_N, \alpha_F$ are the fractional intensity contributions of collagen, NADH and FAD, respectively. Integrated fluorescence intensities of the spectra simulated according to equation [3.1] have normal distribution (Figure 3.2). Absorption of hemoglobin was taken into account according to Schomacker et al. [67]. The 20,000 simulated spectra were randomly divided into a training set and a prediction set, each containing 2500 normal, 2500 hyperplastic, 2500 adenomatous and 2500 cancerous tissue spectra (Figure 3.3).

3.2.3. Evaluation of Methods

Fluorescence spectra of the training set were analyzed with principal peak ratio, differential normalized fluorescence, bivariate DNF, and principal component analysis statistical methods using programs written in Matlab. Diagnostic boundaries were determined by applying Bayes decision theory. Determined threshold values were further tested for the discrimination of tissue conditions within the prediction set. The comparison of methods was made on the basis of achieved sensitivity (SE), specificity (SP), predictive value positive (VP), predictive value negative (VN), and false alarm rate (FAR), five evaluative parameters that are used in clinical applications [91].

Sensitivity, the conditional probability of the technique providing a positive diagnosis to a diseased sample, is calculated as the ratio of true positive results to all analyzed diseased samples (diagnosed as true positives or false negatives). Specificity is the conditional probability of the technique yielding a negative diagnosis of a normal tissue, which is determined by obtaining the ratio of true negative results to all non-diseased samples. Predictive value positive, the probability that a positive result is truly positive, is calculated by taking the ratio of true positives to all positive results (true and false). Similarly, predictive value negative is the probability that a negative result is truly negative and calculated as the ratio of true negatives to all negative results (true and false). In statistical notations, sensitivity, specificity, predictive value positive and predictive value negative of diagnosis between two conditions, for example normal (N) and diseased (D), can be defined as $P(+|D)$, $P(-|N)$, $P(D|+)$, and $P(N|-)$, respectively. In the definitions, '+' and '-' denote positive and negative diagnosis. The false alarm rate represents the probability of incorrect diagnosis of normal tissue as diseased and is found as the ratio of the false positives to all positive diagnosis (true and false).

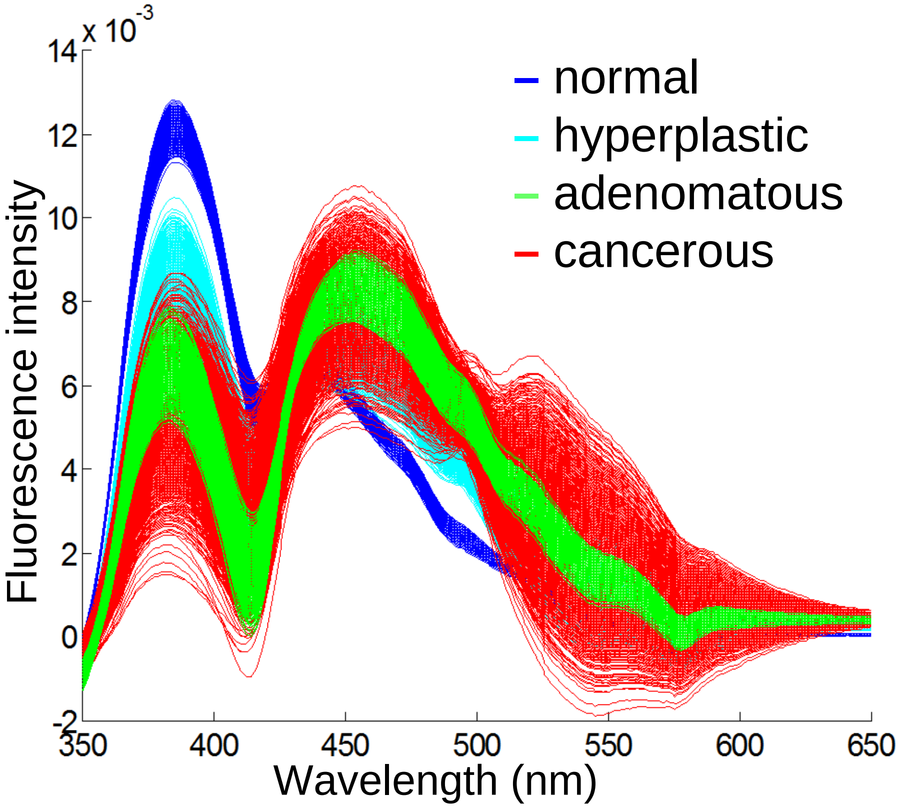

Figure 3.3. Generated tissue-phantom spectra of the training set.

3.3 Results and Discussion

3.3.1. Visual Analysis of the Simulated Tissue Spectra

The fluorescence spectra of three major tissue fluorophores and a representative cancerous tissue spectrum collected in our lab are plotted in Figure 3.1. The emission peaks of collagen and NADH qualitatively match the two main peaks present in the tissue spectrum. The third fluorophore, FAD, contributes only a small fraction (less than 5% for most tissue conditions) to the tissue fluorescence. The transmittance spectrum of hemoglobin displays maximum absorption at 415 nm, qualitatively matching the dip in the tissue spectrum.

The averaged spectra of each tissue type derived from the simulation training set are presented in Figure 3.1. All tissue types have two major emission bands in their emission spectra: one at ~380 nm and the other at ~460 nm, corresponding to collagen and NADH emission regions, respectively.

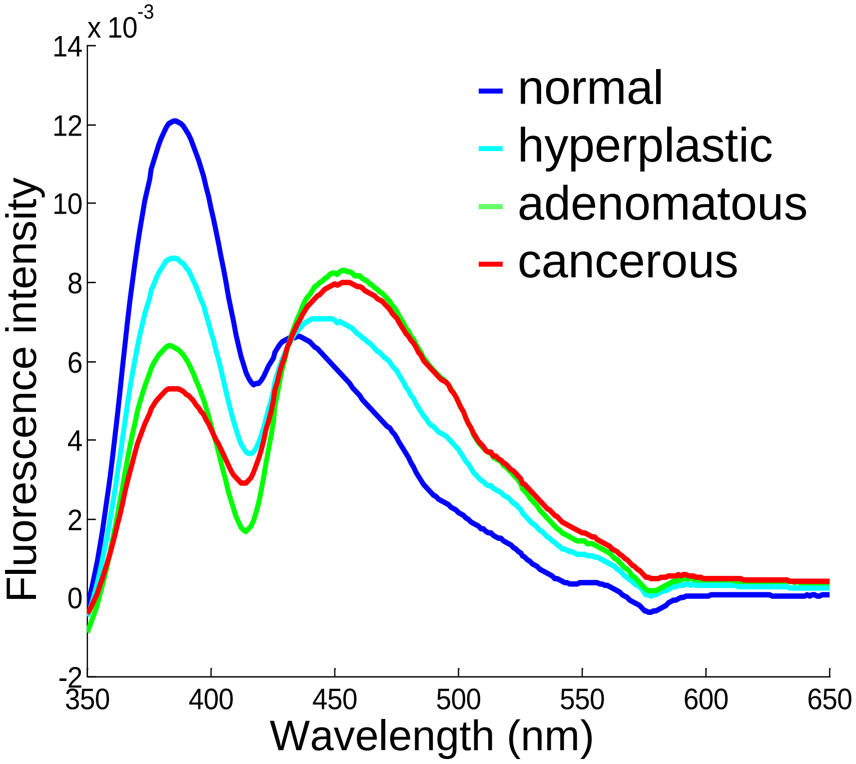

Figure 3.4. Average simulated fluorescence spectra of the training set.

The simulated normal tissue spectra have the highest intensities in the collagen region among all tissue types, consistent with spectra collected from real tissues. During the advancement of disease, the peak ratio between collagen region and NADH region decreases from normal, through hyperplastic, to adenomatous and finally cancerous tissue conditions. This is also consistent with known tissue fluorescence spectra [67,68,75].

Due to a large variation in the morphologies of the cancerous polyps and comparatively small sample number of adenocarcenomas, the standard deviations of the component contributions determined for the cancerous tissue type are about twice as large as those of other tissues. This results in a very broad variation of the spectral properties among the simulated cancerous tissue spectra. In addition to the variations in spectral shapes, the integrated fluorescence intensities of cancerous tissue spectra are broadly distributed compared to the normal (Figure 3.2B). There is a strong overlap of the spectra for adenomatous and adenocarcenomatous tissues (Figure 3.3). A feature of simulated tissue fluorescence spectra is that the difference between adenomatous and cancerous tissue spectra is relatively small, especially at the 460 nm region (Figure 3.4). This is because the intensity contributions of tissue fluorophores in these two tissue types are not significantly different (Table 3.1). Since the clinical difficulty lies in the differentiation between "benign abnormals" (i.e. hyperplastic) from "malignant abnormals" (i.e. adenomatous and cancerous), the adenomatous and cancerous spectra were treated as a single group of the diseased type in this study.

3.3.2. Principal Peak Ratio (PPR)

Successful differentiation between normal and cancerous colorectal tissues by means of a two-peak ratio algorithm applied for the analysis of autofluorescence spectra was reported by Wang et al. [84]. On Figure 3.4 we can see that non-diseased tissue spectra maximize at 384 nm, while cancerous tissue spectra have a maximum at 462 nm. This observation correlates well with the spectral shapes of real colonic tissues analyzed in our lab [75,91]. The PPR for each sample was obtained by dividing its intensity at 384 nm peak by the spectral intensity at 462 nm. Calculated peak intensity ratios of the training set are displayed in Figure 3.2 and were used as statistical indices for the differentiation between the tissue conditions.

Bayes decision theory was applied to determine the threshold PPR value for discrimination between the tissue types [68,92]. In the Bayes decision theory, the conditional probability densities for the sample indices are assumed to be multivariate normal [76]. For differentiation of tissues based on a univariate parameter, such as PPR, the probability density function of diagnostic index x for each clinical condition j was calculated as:

$$F_j(x) = \frac{1}{\sqrt{2\pi\sigma_{j,x}^2}} \exp[-\frac{(x - x_{j,ave})^2}{2\sigma_{j,x}^2}], \qquad [3.2]$$

where $x_{j,ave}$ is the mean and $\sigma_{j,x}$ is the standard deviation of the diagnostic index for a tissue type j.

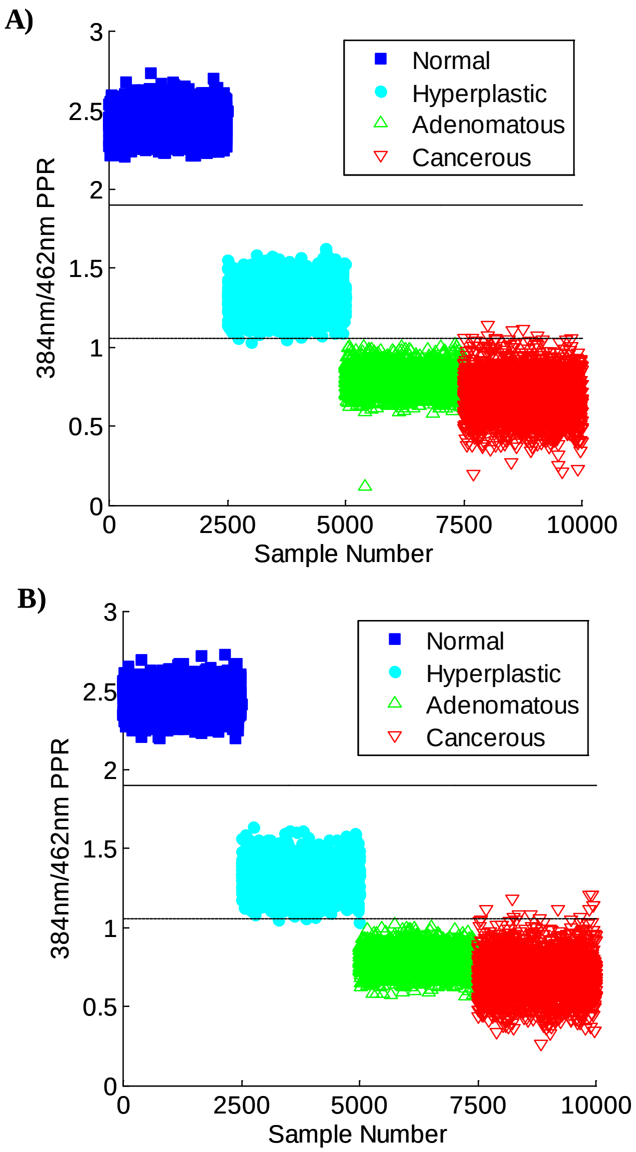

Figure 3.5. Principal Peak Ratio scores of all samples in (A) the training and (B) the prediction set. The solid lines are the probability 0.5 thresholds between normal and hyperplastic condition, the dashed lines are the probability 0.5 thresholds between hyperplastic and adenomatous/cancerous state.

Further, the probability of an individual sample to belong to the tissue type *j* was calculated by means of the Bayes theorem:

$$P_j(x) = \frac{p_j F_j(x)}{\sum_j p_j F_j(x)} \qquad [3.3]$$

where p_j is the probability of finding a tissue type *j* in the sample population, which in this study was identical for all tissue types, because spectra of all four clinical conditions were simulated in the same number.

Samples in the prediction set were treated as unknown and their probabilities of belonging to normal, hyperplastic, and diseased-state calculated according to Equation 3.3 were used for the classification (Figure 3.1). All normal tissues were correctly assigned without any ambiguity since they all have high probabilities close to 1 of belonging to the normal tissue type (Figure 3.6A). The other three types of tissue were clearly differentiated from the normal, displaying probabilities close to zero.

Figure 3.6B shows the probability of all samples belonging to the hyperplastic tissue type. Two hyperplastic samples from the prediction set were misclassified as diseased and ten adenomatous/cancerous samples were misdiagnosed as hyperplastic. The larger number of misclassified diseased samples reflects the large spread in the cancerous tissue indices. Figure 3.6C shows that most samples from 5001 to 10000 have very high probabilities of belonging to the diseased state except for seven cancerous tissue spectra. Five hyperplastic samples in Figure 3.6C were misclassified as diseased according to their probability values, thus the total count of errors is 12, the same as when the probability of tissues being hyperplastic was calculated (Figure 3.6B).

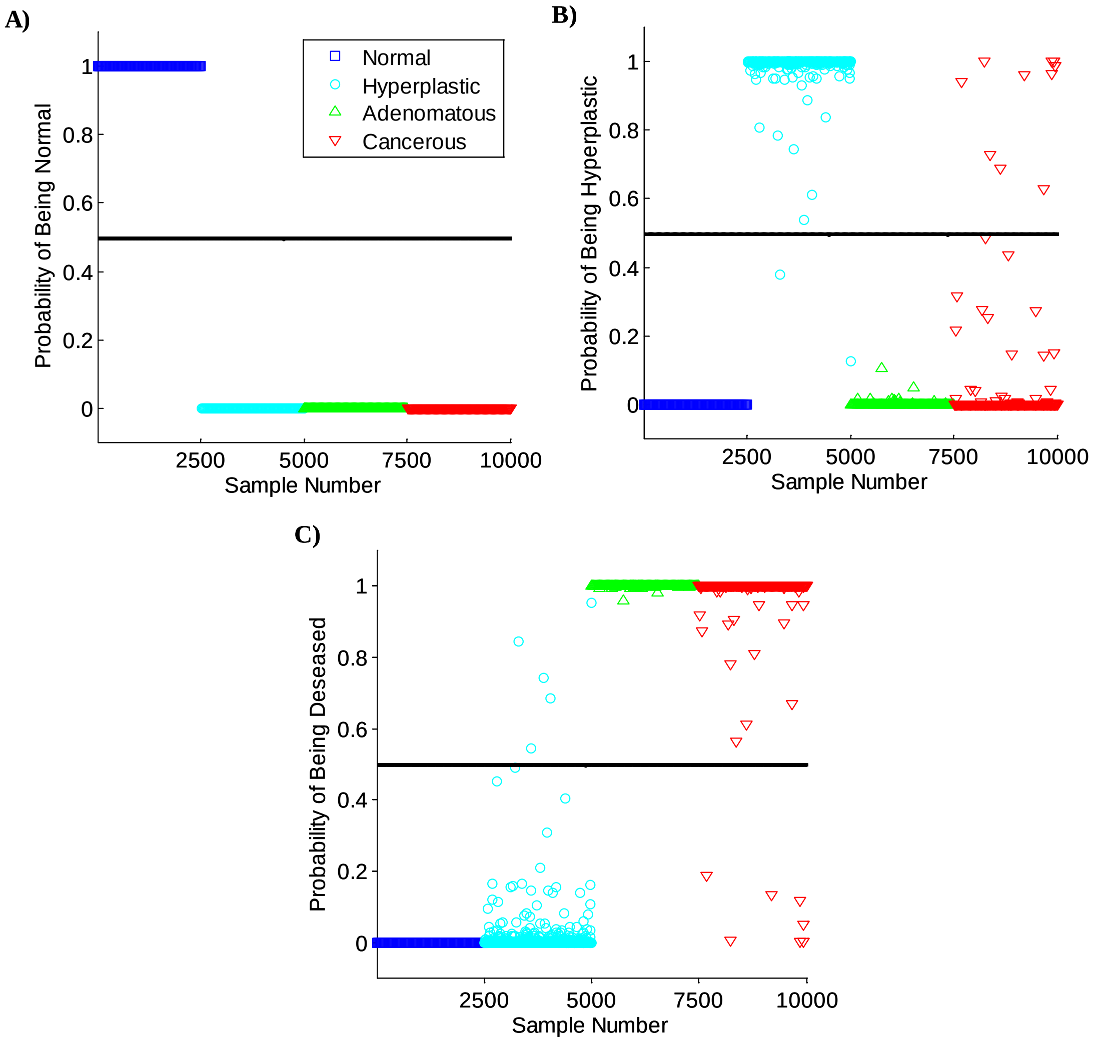

Figure 3.6. Probabilities of all simulated spectra in the prediction set belonging to (A) normal tissue type; (B) hyperplastic tissue type and (C) adenomatous/cancerous (diseased) tissue type. The solid lines are the probability 0.5 threshold values.

Considering the clinically useful classification between the hyperplastic and diseased (adenomatous and cancerous) tissue conditions, the resulting sensitivity of 99.9%, specificity of 100%, predictive value positive of 100%, predictive value negative of 99.7% , and false alarm rate of 0.04% were obtained for PPR method (Table 3.2).

In an alternative approach, the threshold boundaries between tissue types are determined and used in classification directly. The threshold *x*-value is decided so that a sample having this index value would have equal probabilities of belonging to either of two discriminated tissue types. For example, an index value that has equal probabilities of 0.5 for both hyperplastic and diseased tissue types was determined to be 1.06 on the PPR scale (Figures 3.5A and 3.5B). Using the same protocol, the threshold of the PPR values between normal and hyperplastic tissue types was determined to be 1.91, which is closer to the normal tissue values reflecting the narrower variation distribution in this tissue type. Obtained threshold values can be used directly to classify tissue spectra, if no probability information is required. With application of the 1.06 threshold value, the diagnostic results for the prediction set were: 99.9% sensitivity, 99.5% specificity, 99.8% predictive value positive and predictive value negative, and 0.24% false alarm rate (Table 3.2).

Table 3.2. Diagnostic results of all applied methods using Bayes analysis.

Method and modality		Mis-assigned		Evaluation Parameters					E
		HP	AD/ CA	***SE***	***SP***	***PVP***	***PVN***	***FAR***	
PPR	**P of HP**	2	10	0.998	0.999	1.00	0.996	0.0004	12
	P of AD/CA	5	7	0.999	0.998	0.999	0.997	0.001	12
	0.5 P line	12	6	0.999	0.995	0.998	0.998	0.002	18
DNF	**386 nm**	25	35	0.993	0.990	0.995	0.986	0.005	60
	485 nm	53	117	0.977	0.979	0.989	0.954	0.01	170
	386/485 nm	6	4	0.999	0.998	0.999	0.998	0.001	10
PCA	**PC1**	51	56	0.989	0.980	0.990	0.978	0.01	107
	PC1/PC2	10	14	0.997	0.996	0.998	0.994	0.002	24
	PC1/PC3	13	7	0.998	0.995	0.997	0.997	0.003	20

Note: Discrimination between 2500 hyperplastic and 5000 diseased simulated tissue spectra reported. Methods: PPR, principal peak ratio; DNF, differential normalized fluorescence; PCA, principal component analysis. Tissue types: HP, hyperplastic; AD, adenomatous; CA, cancerous. Evaluation parameters: SE, sensitivity, SP, specificity, PVP, predictive value positive; PVN, predictive value negative; FAR, false alarm rate. E: total number of misdiagnosed samples.

3.3.3. Single Peak Differential Normalized Fluorescence (DNF) Intensity Analysis

The use of differential normalized fluorescence (DNF) indices was introduced in 1995 by Tuan Vo-Dihn in the esophageal cancer study [82]. It was demonstrated by Wang et al. [76] that DNF is equally effective for the analysis of the colon tissue spectra for the purpose of cancer diagnosis. In addition, Wang et al. has introduced a new method of probability-based DNF bivariate analysis, which will be discussed in section 3.3.4.

In the DNF method, the difference between each spectrum and the average normal spectrum is calculated [93]. Practically, the averaged spectrum of all normal samples in the training set was subtracted from the spectra of each sample in both the training and the prediction sets.

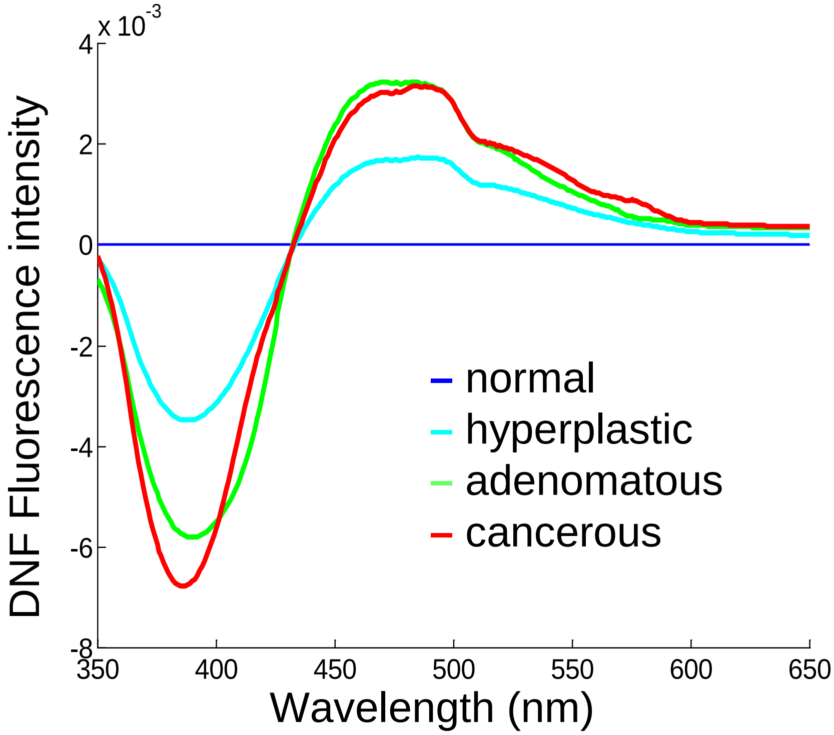

Figure 3.7. Average differential normalized fluorescence spectra.

Figure 3.2 shows the average DNF curves for hyperplasic, adenomatous, and cancerous samples of the training set, or the difference between the average spectrum of a specific tissue condition and the average normal spectrum. As expected, the DNF values for the average normal tissue are zero. The average DNF curves show two features of significance: a negative peak, minimized at 386 nm, and a positive peak, maximized at 485 nm. The differences in the DNF values between the tissue types are largest at these two peak locations. This suggests that DNF intensities at 386 nm and 485 nm are good candidates for diagnostic indices in cancer diagnosis.

The DNF intensity at 386 nm as an index to differentiate the diseased and non-diseased tissues was tested first (Figure 3.3). All normal samples, as predicted, had DNF index at 386 nm close to zero. Similar to the PPR method, threshold between the clinical conditions was determined by means of the Bayes decision theory. Mean values and standard deviations of the DNF indices for normal, hyperplastic and diseased clinical conditions were determined and applied in the calculation of the probability density functions using Equation 3.2. Established statistically significant threshold was applied for the discrimination of samples in the prediction set and yielded 99.3% sensitivity and 99.0% specificity (Table 3.2). Using an empirical threshold might yield better diagnostic results, however for the comparison of methods Bayes decision theory provides results of higher statistical importance. The empirically-established threshold is tailored for the data set and could perform worse in the prediction of unknown sample.

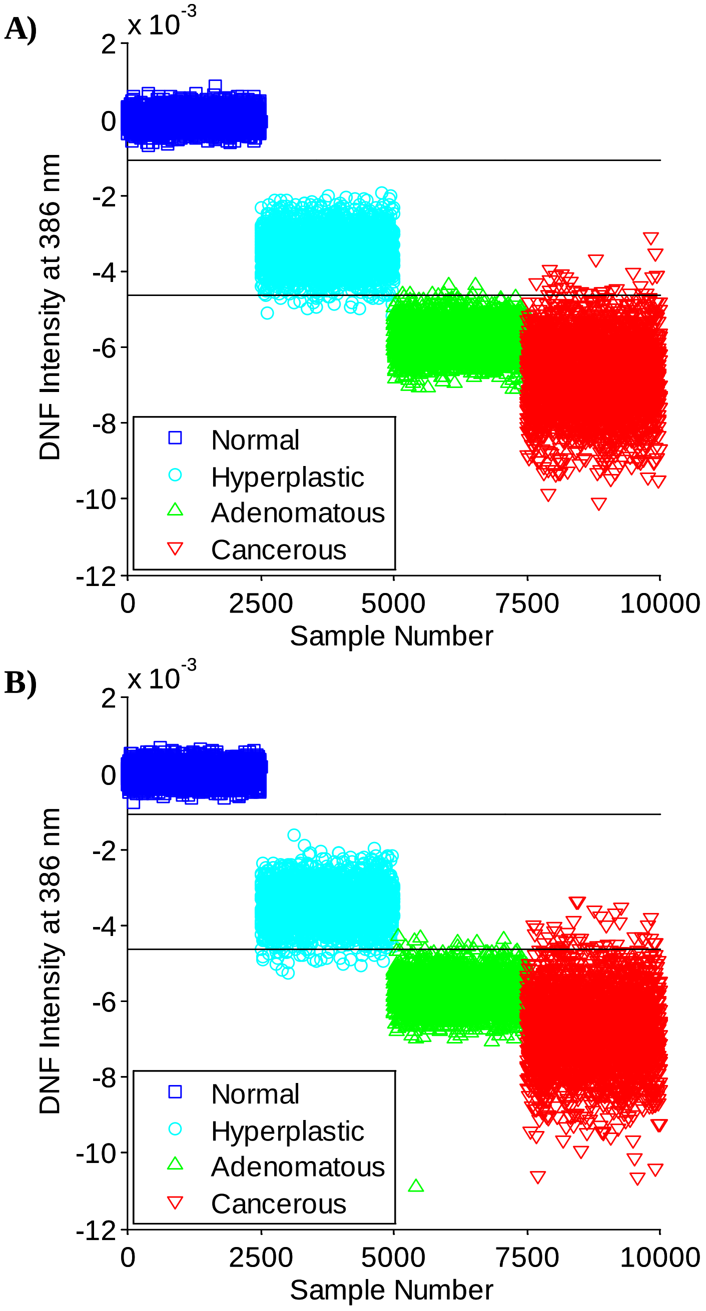

Figure 3.8. Differential normalized fluorescence intensity values at 386 nm for all spectra in (A) the training and (B) the prediction set. The solid lines are the probability 0.5 threshold values.

The DNF intensities at 485 nm were used for the discrimination of simulated tissue spectra next (Figure 3.4). The sensitivity and specificity obtained by using only 485 nm DNF value were 97.7% and 97.9% respectively (Table 3.2).

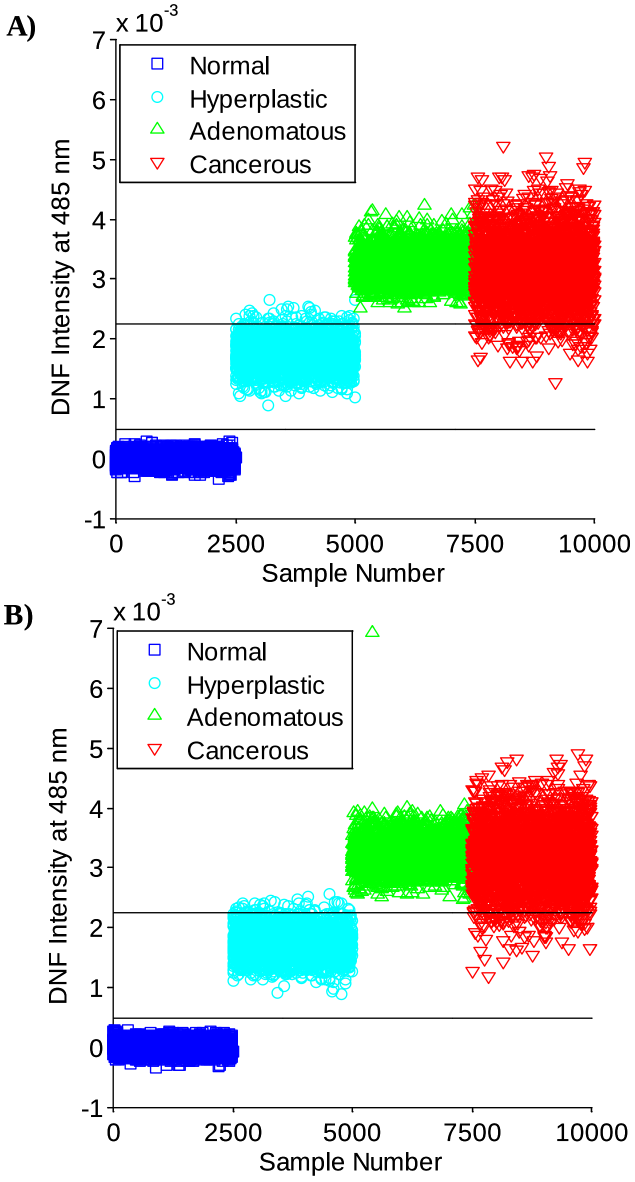

Figure 3.9. Differential normalized fluorescence intensity values at 485 nm for all spectra in (A) the training and (B) the prediction set. The solid lines are the probabilities 0.5 threshold values.

As expected from the plot of average DNF curves (Figure 3.7), the results of diagnosis using 485-nm DNF indices was worse than when DNF intensity at 386 nm was used. This is also reflected in the original spectra (Figure 3.3) that showed better distinction between the hyperplastic and adenomatous/ adenocarcenomatous tissues at the 386-nm band than the 485-nm band.

3.3.4. Bivariate Differential Normalized Fluorescence (2D-DNF) Method

While the use of 485-nm DNF value alone did not improve the diagnostic potential of the method, the application of both DNF peak values simultaneously might actually yield better results since the two wavelengths carry different information [91]. Approach suggested by Wang et al. [76] incorporates examining DNF intensities at 386 nm and 485 nm in a bivariate analysis. In the bivariate scatter plot in Figure 3.10, we chose to plot 386-nm DNF values on the x-axis and 485-nm DNF values on the y-axis. Interestingly, the indices corresponding to the cancerous and hyperplastic samples are distributed evenly, while points for the normal and adenomatous tissues are orientated along the diagonal.

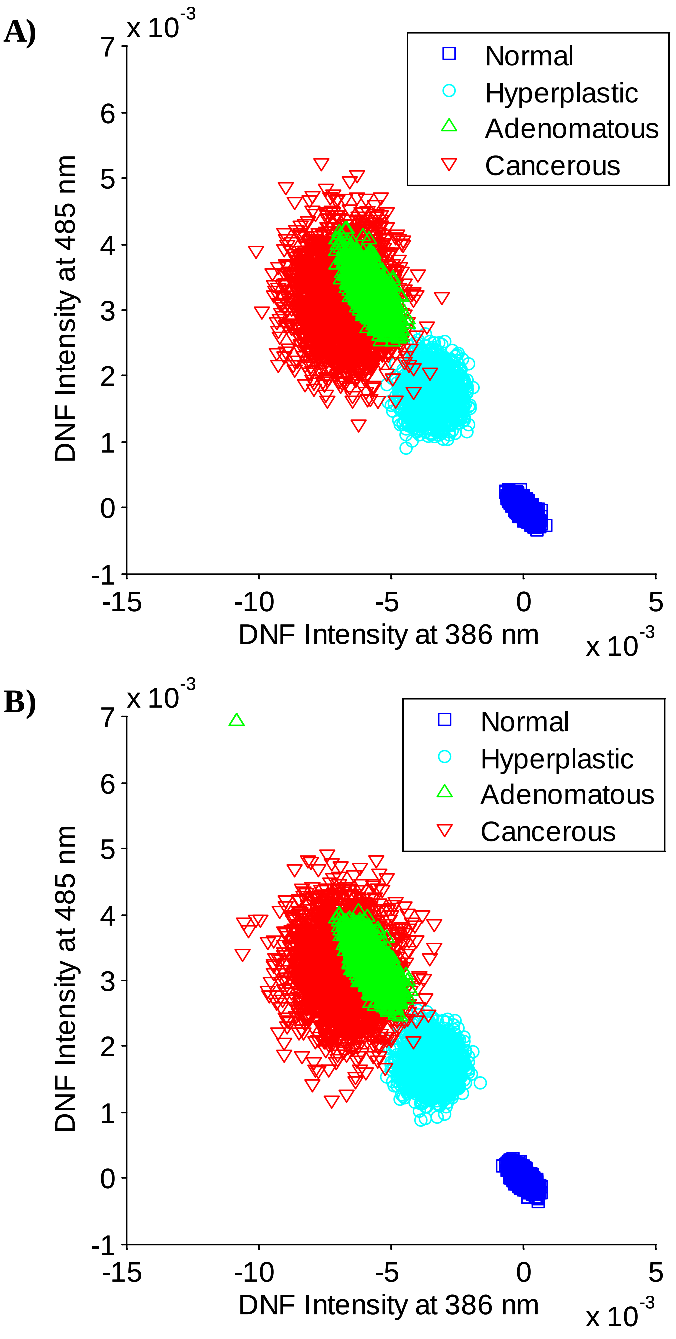

Figure 3.10. Bivariate scatter plots of (A) the training set and (B) the prediction set.

Simulated spectra of all tissue types were generated according to the same protocol and all tissue types demonstrated normal distribution of their integrated fluorescence intensity. While much larger variation in the cancerous tissues (Figure 3.2B) might explain its difference from the distribution of the normal tissue indices in the bivariate DNF plot, the standard deviations in chromophores contributions for adenomatous and hyperplastic conditions (Table 3.1) are quite similar. The diagonal trend might indicate that the DNF 386 nm intensities are to some extent correlated with the DNF 485 nm intensities, but the question why this feature was observed only for the normal and adenomatous samples remains open.

To apply Bayes decision theory with this method, bivariate normal density functions for all tissue types were calculated as:

$$F_j(x,y)=\frac{1}{2\pi\sigma_{j,x}\sigma_{j,y}\sqrt{1-\rho_j^{\,2}}}\exp[-\frac{1}{2(1-\rho_j^{\,2})}(\frac{w_x^2}{\sigma_{j,x}^2}-\frac{2\rho_j w_x w_y}{\sigma_{j,x}\sigma_{j,y}}+\frac{w_y^2}{\sigma_{j,y}^2})] \quad [3.4]$$

where $w_x = x - x_{j,ave}$ and $w_y = y - y_{j,ave}$, x and y are DNF indices at 386 nm and 485 nm respectively, $x_{j,ave}$ and $y_{j,ave}$ are the means, and $\sigma_{j,x}$ and $\sigma_{j,y}$ are the standard deviations of the tissue-type-specific DNF values. The correlation coefficient between x and y of a tissue type j is calculated as:

$$\rho_j = 1/(n-1)\sum_{i=1}^{n}(x_i - x_{j,ave})(y_i - y_{j,ave})/\sigma_{j,x}\sigma_{j,y} \quad [3.5]$$

Similar to the probability calculation for measured single indices, bivariate form of Bayes theorem is expressed:

$$P_j(x,y) = \frac{p_j F_j(x,y)}{\sum_j p_j F_j(x,y)} \qquad [3.6]$$

Figure 3.11 shows the probability surface between the hyperplastic and adenomatous conditions (normal and cancerous tissues are excluded from this consideration), as an example to demonstrate the methodology of tissue classification.

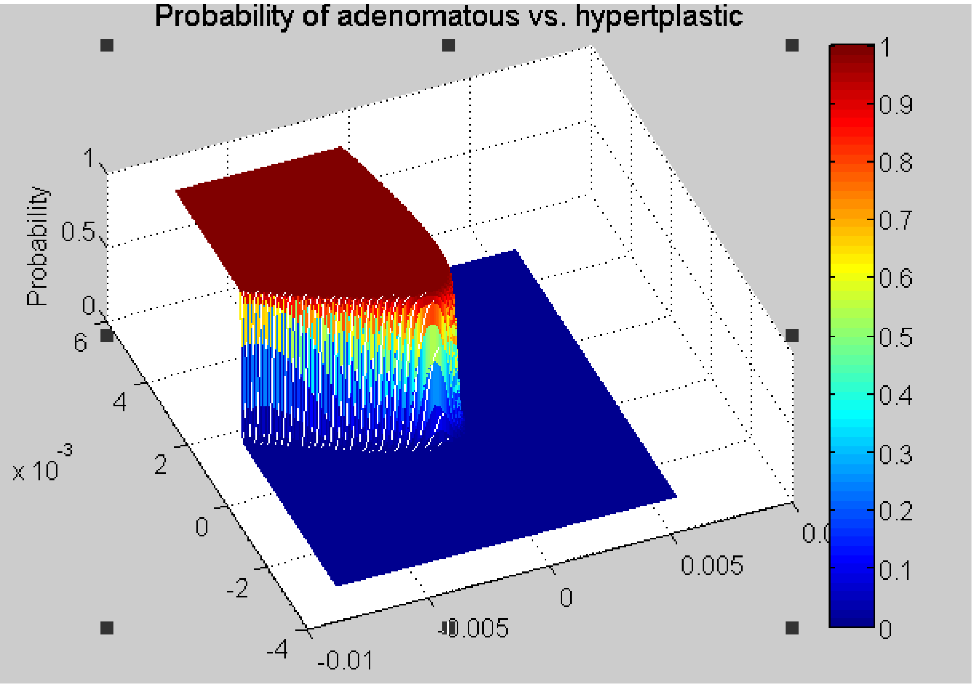

Figure 3.11. Probability surface between adenomatous and hyperplastic tissues of the training set calculated on the basis of bivariate DNF indices.

The probability density functions were first evaluated for each data point according to Equation 3.4 to form matrices for each tissue condition. The probability matrix was then calculated from the probability density functions of the adenomatous (F_A) and hyperplastic (F_H) tissues. Since the number of samples of each tissue type is the same, the probability surface was obtained as:

$$P_{A-H} = \frac{F_A}{F_H + F_A} \qquad [3.7]$$

The probability surface in Figure 3.11 shows that tissue samples falling into the blue region in the bivariate DNF plot have basically close-to-zero probability of being adenomatous, while the tissue samples in the dark red region of the probability surface have near statistical certainty to be adenomatous. The transitional region is where the hyperplastic and adenomatous tissues overlap in practical clinical settings and is the region where tissue classification is made. The contour of the probability surface at desired probability value applied on the DNF bivariate scatter plot provides the threshold line for discrimination between the tissue types. Figure 3.12A shows the 0.5 probability contour of the P_{A-H} surface from Figure 3.11. Tissues corresponding to data points on this contour line would have equal statistical probabilities of belonging to the hyperplastic or the adenomatous classes. According to this threshold, all tissue samples on the upper left side of the curve in the plot are classified as adenomatous while all other samples are diagnosed as hyperplastic. It should noted that the normal and cancerous tissues are excluded from the statistical calculation and the classification.

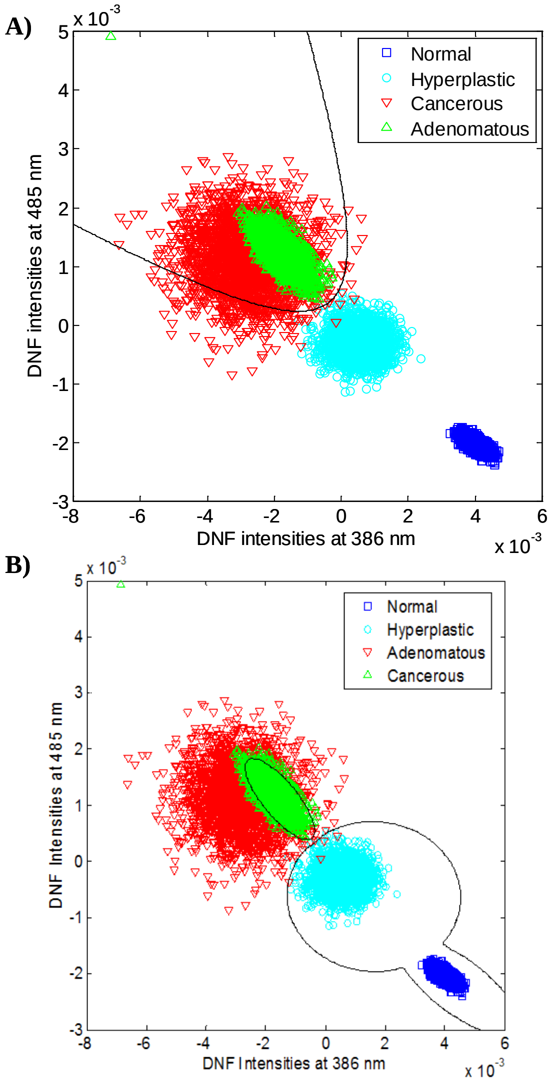

Figure 3.12. Differentiation of tissue types in the prediction set using DNF indices at both 386 nm and 485 nm. (A) The equal probability curve between hyperplastic and adenomatous tissue types. Samples corresponding to the data points on this curve would have equal probabilities of belonging to the hyperplastic or the adenomatous classes. (B) The equal probability curve between adenomatous and cancerous tissues (ellipsoid) and the equal probability curve between normal/hyperplastic (non-diseased) and adenomatous/cancerous (diseased) states.

More practical and all-inclusive diagnostic threshold line between all diseased (adenomatous and cancerous) and all non-diseased (normal and hyperplastic) conditions was calculated as:

$$P_{AC-NH} = \frac{F_A + F_C}{F_N + F_H + F_A + F_C} = 0.5 \qquad [3.7]$$

Discrimination using this statistically determined threshold (Figure 3.12B) demonstrated significant improvement over diagnosis with either of the two single peak DNF values. Applying the bivariate DNF method only 6 out of 2500 hyperplastic condition spectra were misclassified as diseased and only 4 out of 5000 diseased samples received false negative diagnosis. This resulted in the false alarm rate of 0.12%, sensitivity of 99.9% and specificity of 99.8%.

3.3.5. Principal Component Analysis (PCA)

PCA is a powerful classification method and has been applied in combination with fluorescence spectroscopy for the diagnosis of different types of cancer [63,83,89]. Principal component analysis is a way to express the data in such a way that will highlight the differences and similarities between the samples. Another advantage of PCA is its intrinsic capability to compress the data by reducing the number of dimensions, without much loss of information.

Analysis of the simulated tissue spectra with PCA in MatLab showed three major principal components (Figure 3.1), further referred to as PC1, PC2 and PC3, accounting for 91.1%, 7.0% and 1.9% variance respectively (Table 3.3).

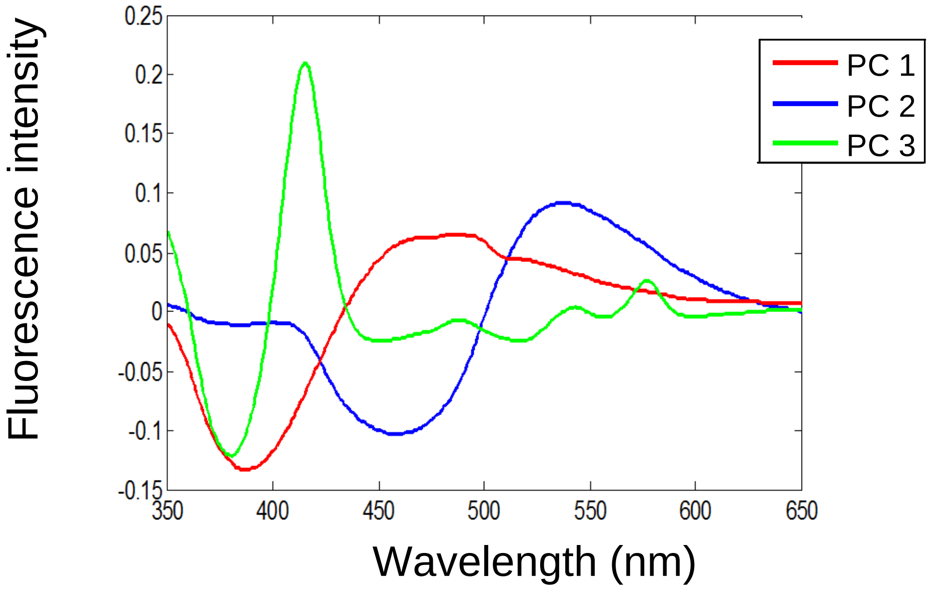

Figure 3.13. Principal Component spectra of the training set.

Table 3.3. Statistical parameters of the first four Principal Components (PC).

PC	Variance (%)	Average score for NR	Average score for HP	Average score for AD	Average score for CA
1	91.1	-0.030	-0.0037	0.016	0.018
2	7.01	$9\cdot10^{-4}$	$8\cdot10^{-4}$	$-9\cdot10^{-4}$	$2\cdot10^{-4}$
3	1.85	$8\cdot10^{-5}$	$-4\cdot10^{-4}$	$-3\cdot10^{-3}$	$4\cdot10^{-3}$
4	$6\cdot10^{-17}$	$-9\cdot10^{-13}$	$2\cdot10^{-12}$	$-3\cdot10^{-13}$	$-1\cdot10^{-12}$

Tissue types: NR, normal; HP, hyperplastic; AD, adenomatous; CA, cancerous.

It is of interest to note that the shape of the fist PC very much resembles the average DNF curves shown in Figure 3.7. In other words, PC1 carries the spectral information best differentiating between the tissue classes. Scores on PC1 of all simulated spectra of the training set are plotted in Figure 3.2A. Using univariate form of the Bayes decision theory the threshold lines between the normal and hyperplastic and between the diseased and hyperplastic tissue types were calculated and applied for discrimination in the prediction set (Figure 3.14B). Clear differentiation between the normal and hyperplastic samples was achieved. The diagnosis between hyperplastic and diseased tissues yielded a sensitivity of 98.9% and a specificity of 98.0%. Scores on the second and third principal components individually, displayed in Figure 3.35, did not promise much diagnostic potential alone.

Applying prior knowledge of discrimination on the basis of bivariate information, we conducted the analysis of tissue spectra using sample scores on PC1 and sample scores on PC2 simultaneously (Figure 3.46A). Bivariate normal density functions were calculated for all four tissue types according to Equation 3.4.

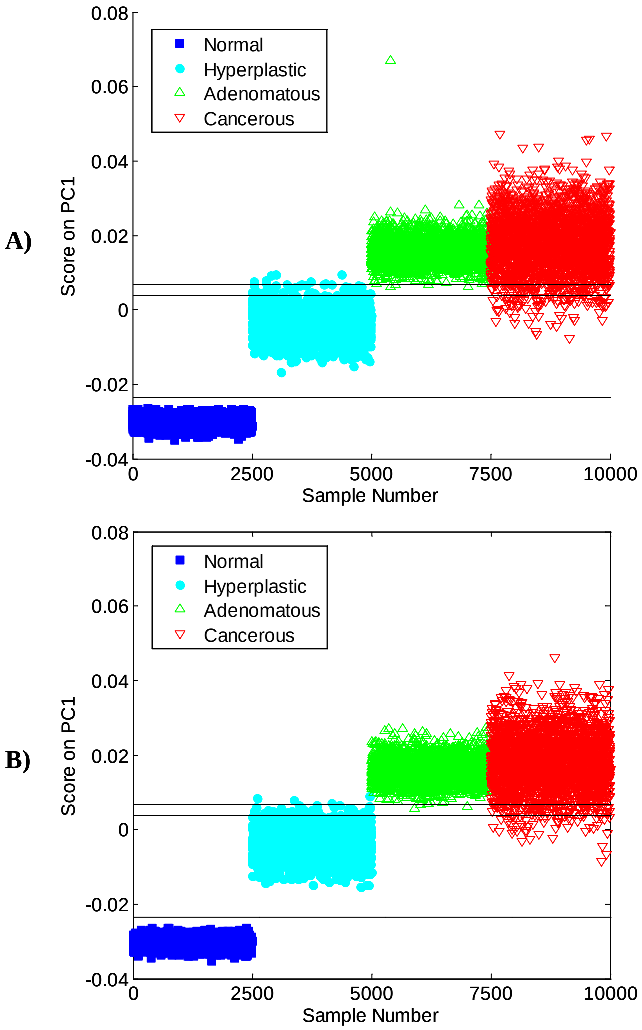

Figure 3.14. Scores on the first PC of (A) the training set and (B) the prediction set. The solid lines correspond to the equal probability threshold between hyperplastic and normal, and between hyperplastic and adenomatous tissues. The dashed lines correspond to the equal probability threshold between hyperplastic and diseased (adenomatous/cancerous) classes.

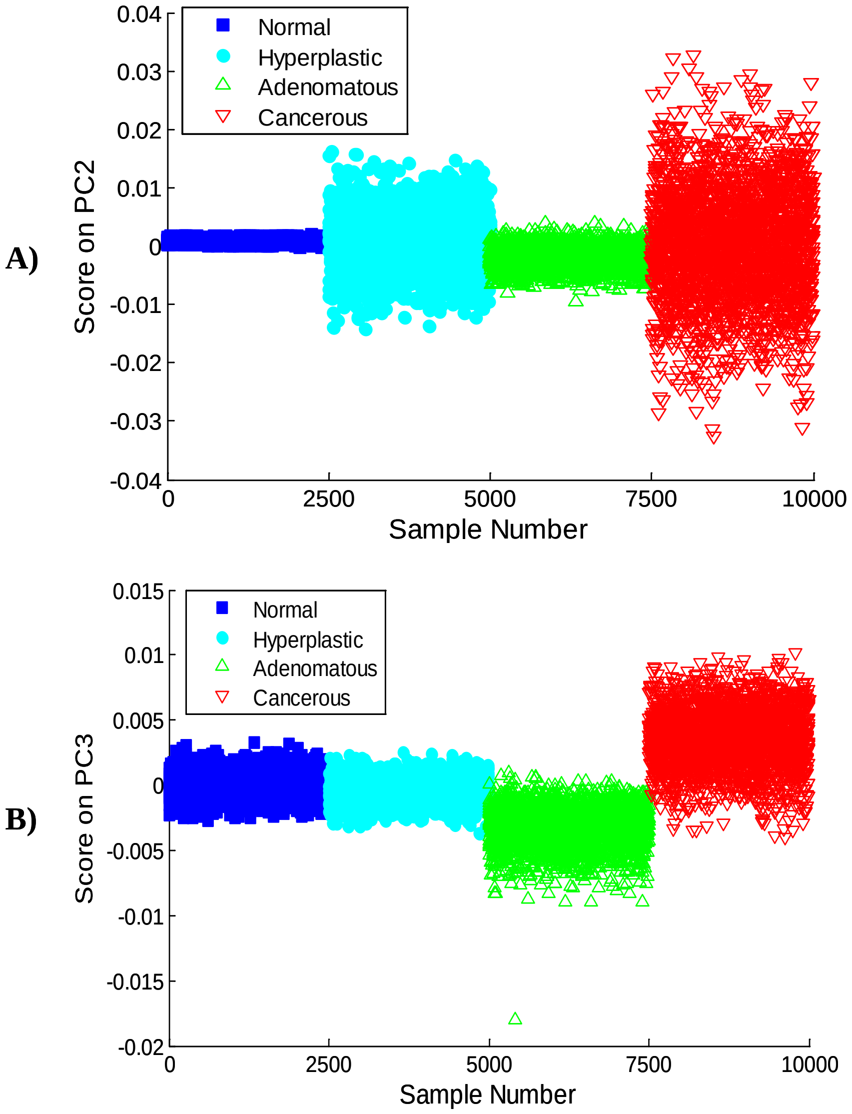

Figure 3.15. Scores on (A) the second PC and (B) the third PC of the spectra in the prediction set.

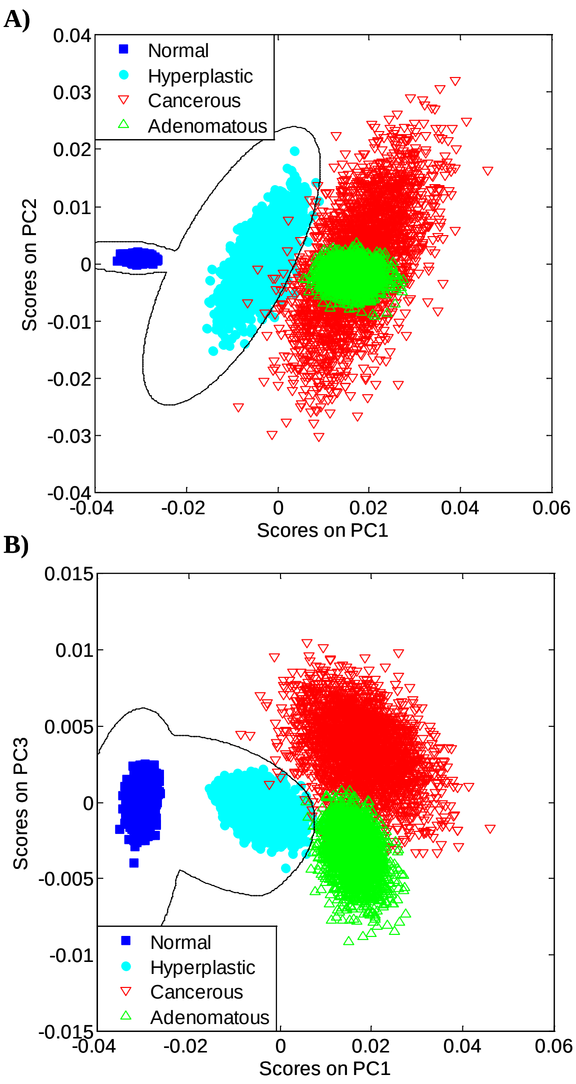

Figure 3.16. The bivariate scatter plot of the scores on (A) the second PC and the first PC; (B) the third PC and the first PC of the prediction set spectra. The solid lines correspond to the equal probability threshold between normal/hyperplastic (non-diseased) and adenomatous/cancerous (diseased) states.

The plot of the probability surface between the non-diseased and diseased conditions, obtained through equation 3.7, is shown in Figure 3.5A. Corresponding 0.5 probability threshold line was applied for discrimination within the prediction set and can be seem as black border-line in Figure 3.16A.

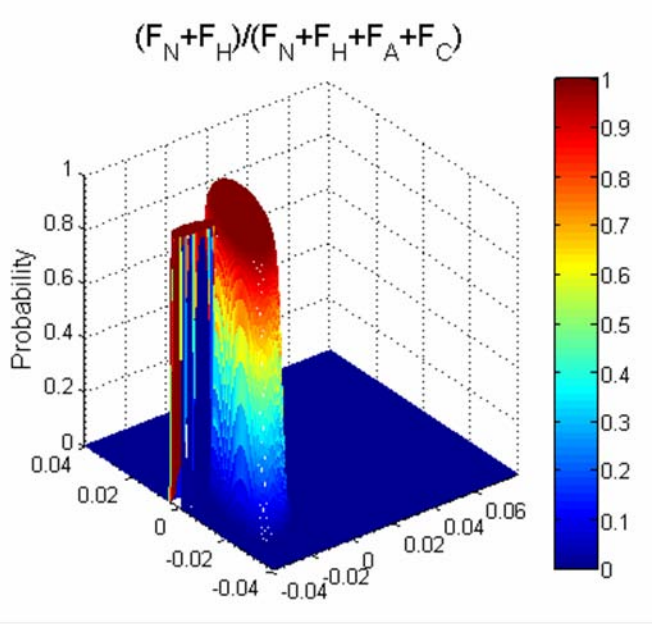

Figure 3.17. The probability surface between normal/hyperplastic (non-diseased) and adenomatous/cancerous (diseased) states of the prediction set spectra according to their scores on the PC1 and PC2.

Similarly calculated threshold line for the case when scores on PC1 are applied with scores on PC3 is displayed on the bivariate scatter plot of PC3 scores vs. PC1 scores (Figure 3.16B). In both cases of bivariate analysis of the scores on the principal components the statistical performance of the method improved. When scores on PC1 were applied in conjunction with scores on PC2, the number of misclassified hyperplastic samples was 10 and 14 diseased tissues were overlooked as hyperplastic. When scores on PC1 were used together with scores on PC3, the number of missed hyperplastic tissues increased to 13, but fewer cancerous and adenomatous samples, i.e. 7, received false diagnosis, which resulted in the sensitivity of 99.8% and specificity of 99.5% (Table 3.2).

Interestingly, while bivariate analysis of scores on PC3 versus scores on PC2 did not produce very impressive diagnosis between the diseased and non-diseased tissue states, it showed reasonable discrimination between the adenomatous and cancerous conditions (Figure 3.68), which was almost impossible to achieve by using other methodologies. Speculatively, the positive peak of the PC3 spectrum is quite close in wavelength to the hemoglobin's Soret band. As shown in Table 3.1, the spectral compositions of adenocarcenomatous tissue contain fairly similar levels of fluorophore contributions to those of the adenomatous tissue but there is a significant difference between their levels of hemoglobin absorption. As a consequence, PC3 can effectively help to pull the adenomatous tissue samples out of the distribution of cancerous tissues. Without doubt this observation of the PC3 role in discrimination between the diseased samples deserves further investigation as it can potentially provide means for quantification of disease progression. Comparison of diagnostic performances of three discussed bivariate PC methods (PC1+PC2, PC1+PC3, PC3+PC2) in discrimination between adenomatous and cancerous tissues is presented in Table 3.4.

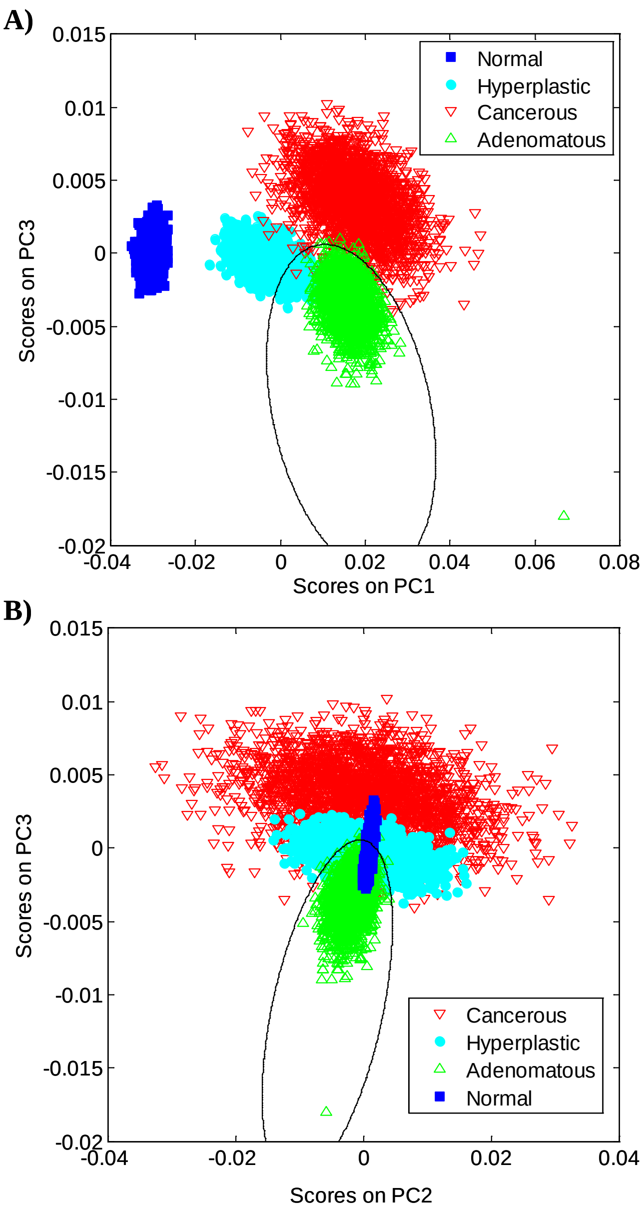

Figure 3.18. The bivariate scatter plot of the prediction set scores on (A) the third PC and the first PC; (B) the third PC and the second PC. The solid lines correspond to the equal probability threshold between adenomatous and cancerous states.

Table 3.4. Results of discrimination between 2500 adenomatous (AD) and 2500 cancerous (CA) simulated tissue spectra by means of bivariate principal component analysis (PCA).

Modality of bivariate PCA	Mis-assigned		Evaluation Parameters					E
	AD	CA	*SE*	*SP*	*PVP*	*PVN*	*FAR*	
PC2/PC1	151	531	0.788	0.937	0.929	0.816	0.07	682
PC3/PC1	12	63	0.975	0.995	0.995	0.975	0.005	75
PC3/PC2	9	47	0.981	0.996	0.996	0.982	0.004	56

Note: PC1, PC2 and PC3 are first, second and third principle components, respectively. Evaluation parameters: SE, sensitivity, SP, specificity, PVP, predictive value positive; PVN, predictive value negative; FAR, false alarm rate. E: total number of misdiagnosed samples.

3.4 Conclusions

With an appropriate development of endoscopic instrumentation for “optical biopsy” and reliable methods for the analysis of collected spectroscopic data, autofluorescence has a chance to become an effective tissue diagnostic modality, because it does not require administration of exogenous probe molecules to the patient and provides quantitative information on the tissue condition. For clinical applications, the classification method needs to be simple and robust. In addition, since the number of tissue samples that can be used for the training set is always limited and the application of the diagnostic methodology is desired immediately, transportability of method between laboratories would be highly desirable. Collection of the fluorescent components spectra with following simulation of a statistically significant spectral database for training of the diagnostic methods and establishing threshold values might be a promising solution to the lab-to-lab method transportability challenge.

The threshold determination with the Bayes decision theory allowed us to avoid the bias of empirically established discrimination boundaries and achieve objective method comparison. Differentiation within the non-diseased states, i.e., between the normal and hyperplastic conditions, was readily achieved by all methods used in this study. Discrimination results between the diseased and non-diseased tissue condition were satisfactory, but the isolation of the adenomatous samples from the cancerous represents a challenge for most methods.

Reporting on the analysis of nearly the entire spectral sample space with principal peak ratio, differential normalized fluorescence, bivariate DNF, and principal component analysis methods we can conclude that the increased complexity of data processing does not always yield improved diagnostic success. Empirical principal peak ratio method is mathematically the simplest method. Superior diagnostic results achieved with the principal peak ratio method and bivariate differential normalized fluorescence indicate that the majority of the spectral information pertinent to the cancer diagnosis is concentrated in two bands: one at ~380 nm and the other at ~460 nm. The potential for reduction of the collected data from 300-nm long spectra to just a few fluorescence bands can lead to much faster data acquisition and tissue imaging, which is crucial for successful applications of fluorescence spectroscopy for *in vivo* screening.

CHAPTER 4 STATISTICAL TWO-DIMENSIONAL CORRELATION COEFFICIENT MAPPING OF SIMULATED TISSUE PHANTOM DATA. BOUNDARY DETERMINATION IN TISSUE CLASSIFICATION FOR CANCER DIAGNOSIS

4.1. Introduction

Statistical correlation coefficient mapping is one type of recently developed two-dimensional correlation spectroscopy (2D COS) methods that is used to enhance spectral resolution and to visualize inherent correlations between spectral bands [94-96]. Unlike the widely applied generalized 2D correlation spectroscopy [97], it is solely based on statistical parameters and the evaluation of correlation coefficients does not require specific ordering of the spectral data. Because of this property, correlation coefficient mapping is ideal for cancer diagnosis where the tissue spectra are usually randomly collected for analysis [94-96]. Recently, Crowell et al. proposed to apply statistical correlation coefficient mapping in the classification of tissue autofluorescence spectra for cancer diagnosis [75]. In Crowell's study, correlation coefficient mapping demonstrates that four tissue components are mainly responsible for the fluorescence signals without any prior assumptions as needed in the analysis of 1D spectra. When applied to tissue classification, it proves to be a simple and fast data analysis method to reveal similarities between sample spectra. The diagnostic sensitivity and specificity based on correlation coefficient mapping are found to be similar to, or higher than current classification methods in the literature [75].

Currently an empirical correlation coefficient threshold is used to classify tissue spectra. In this study, we determined the statistical threshold for tissue classification by transforming correlation coefficients between samples to Fisher's z-variables [68,76]. The apparent mean and standard deviation of the z-variables for each tissue type were then analyzed with Bayes decision theory. Statistically significant boundaries between tissue types were determined. Furthermore, a probability was provided in assigning clinical tissue conditions to each sample. Fisher's z-transformation has been applied together with the 2D correlation coefficient mapping to study tunnel ionization mechanism of heavy water molecules [98]. The classical statistical theory was used to test the null hypothesis (true correlation coefficient value to be zero) of the correlation coefficient between two ionization species. In this work, Fisher's *z*-transformation of the correlation coefficients was used in combination with Bayesian analysis to determine the statistical threshold and to predict the classification probability. The improved method was tested with a simulated tissue-phantom data set and satisfactory diagnostic results were yielded. The use of simulated data allowed us to assess the methodology with an expanded spectra set, and to explore the entire range of the sample space.

4.2. Experimental and Data Analysis

4.2.1. Simulation of Tissue Spectra

Fluorescence spectra of colonic tissues in different clinical conditions were constructed from the individual spectra of tissue chromophores. Three major tissue fluorophores - collagen, nicotinamide adenine dinucleotide in reduced form (NADH) and flavin adenine dinucleotide (FAD) - contribute to the tissue autofluorescence under experimental conditions in our lab. Hemoglobin is a strong absorber that produces a dip in the overall tissue spectrum. Individual spectra of tissue chromophores were collected from solutions prepared in phosphate buffer saline (PBS, pH 7.4). Collagen (type IV), NADH, FAD and hemoglobin were obtained at the highest purity and used as received. Fluorescence emission spectra excited at 325 nm by a HeCd laser were recorded from 350 nm to 650 nm on an SLM48000MHF (Jobin Yvon, Edison, NJ) spectrofluorometer. Blank PBS buffer served as the control to correct the solvent Raman scattering. The absorption spectrum of hemoglobin was collected on a Cary 3.0 UV-Vis spectrometer.

Eight hundred simulated spectra of tissues in different clinical conditions were generated in MatLab (MathWorks, Natick, MA). Contributions of the four tissue chromophores were assumed normally distributed. The means and standard deviations of the distributions were adapted from a clinical study by Schomacker and are listed in Table 3.1 [67]. Prior to the simulation, each component spectrum was normalized to a total area of one. The maximum of the collagen spectrum was centered to 390 nm to account for the instrumental differences between

Schomacker report and the spectrofluorometer used in this work. The intensity of simulated spectrum I at each wavelength λ was calculated according to:

$$I(\lambda) = I_C(\lambda)\alpha_C + I_N(\lambda)\alpha_N + I_F(\lambda)\alpha_F \qquad [4.1]$$

where I_C, I_N and I_F are the spectral intensities of collagen, NADH and FAD, and $\alpha_C, \alpha_N, \alpha_F$ are their fractional intensity contributions, respectively. Absorption of hemoglobin was taken into account according to Schomaker. The 800 simulated spectra were randomly divided into a training set and a prediction set, each containing 100 normal, 100 hyperplastic, 100 adenomatous and 100 adenocarcenomatous tissue spectra.

4.2.2. Correlation Coefficient Mapping

Fluorescence spectra were analyzed with statistical correlation coefficient mapping method [75,94-96]. This approach allows the analysis of a randomized set of data, unlike the generalized 2D correlation method, which requires controlled perturbation of the system and specific data ordering [97]. For a series of dynamic spectra collected under different conditions with *m* measurements at *n* variables, the *correlation coefficient* between each pair of samples s_1 and s_2 is defined as:

$$r(s_1, s_2) = \frac{1}{n-1} \sum_{i=1}^{n} \frac{[y_i(s_1) - y_{avg}(s_1)]}{\sigma(s_1)} \frac{[y_i(s_2) - y_{avg}(s_2)]}{\sigma(s_2)} \qquad [4.2]$$

where *n* is the number of wavelengths in each spectrum, *y* is the spectral intensity, $y_{avg}(s_j)$ is the mean and $\sigma(s_j)$ is the standard deviation of the *j*th sample. A two-dimensional contour plot of the correlation coefficients with respect to two sample axes is termed a sample-sample *correlation coefficient map*. A correlation coefficient map illustrates the similarity between samples. Classification of sample spectra can be achieved through a quantitative analysis on the correlation coefficients within the data set [75].

4.2.3. Fisher's *z*-transformation of the Correlation Coefficients

Correlation coefficients are bounded between +1 and -1, where +1 indicates perfect correlation or similarity and -1 indicates perfect antisimilarity or negatively perfect similarity between two sample spectra, and a value of 0 indicates no similarity. Any value in between is a measure of the extent of similarity.

Unfortunately, generally the sampling distribution of correlation coefficients is not normal. The distribution of the correlation coefficients depends on the sampling size n and the true value of the correlation coefficient. For example, when there is no correlation between two measurements, corresponding to a true correlation coefficient value of 0, the sampling distribution of correlation coefficients is symmetric about 0. As the sample size n increases, the sampling distribution becomes more normal in shape. When the true value of a correlation coefficient increases from zero (becomes more positive), the sampling distribution becomes negatively skewed, and vice versa. As the true value of correlation coefficient approaches +1 or -1, the sampling variance decreases and the distribution becomes narrower (approaching 0) and increasingly skewed.

Fisher's z-transformation is an ideal method to expand Pearson's correlation coefficient to an approximately normally distributed variable z [99,100]. The z-transformation essentially expands the short tails of the distribution of correlation coefficients and makes it symmetric according to equation:

$$z = 0.5\ln\frac{1+r}{1-r} \qquad [4.3]$$

where r is the correlation coefficient defined by Equation 4.2. The distribution of z-variable is perfectly symmetric for the correlation coefficient between variable pairs that are bivariate normally distributed. As the sampling number n increases, the distribution tends to become perfect normal quickly.

For the correlation coefficients between two spectra belonging to different types, the transformed z values show a distribution that is symmetric and close to normal in shape. The apparent mean and standard deviation of the z-variables were then used in the following Bayesian analysis.

4.2.4. Bayesian Analysis

After the Fisher's z transformation, a threshold that differentiates clinical conditions of the tissue can be determined by applying the Bayes decision theory on the correlation coefficients between the simulated tissue spectra [68,76,92]. Practically, the averaged spectrum of all normal samples in the training set is calculated. Correlation coefficients of all samples in the prediction set with the averaged normal spectrum are evaluated using Equation 4.2 and then transformed to the z-values using Equation 4.3. Since the z variable is approximately normally distributed, Bayes decision theory can be applied for further probability analysis. The probability density function of z for each clinical condition (tissue type) j is evaluated for each sample spectrum:

$$F_j(z) = \frac{1}{\sqrt{2\pi\sigma_{j,z}^2}} \exp[-\frac{(z - z_{j,ave})^2}{2\sigma_{j,z}^2}] \qquad [4.4]$$

where $z_{j,ave}$ is the mean and $\sigma_{j,z}$ is the standard deviation of the z variables for a tissue type j. The probability of an unknown sample belonging to a tissue type j can be calculated by means of the Bayes theorem:

$$P_j(x,y) = \frac{p_j F_j(x,y)}{\sum_j p_j F_j(x,y)} \qquad [4.5]$$

where p_j is the prior probability that stands for the probability of finding a tissue type j in the sample population. The sample is then assigned to the tissue type that gives the largest probability. Or, alternatively, a threshold *z*-value that differentiates two tissue types with equal probabilities is determined. The corresponding correlation coefficient threshold can be calculated using Equation 4.3 and used directly in tissue classification.

4.3. Results and Discussion

4.3.1. General Description of the Simulated Tissue Spectra

The fluorescence spectra of three major tissue fluorophores and a selected cancerous tissue spectrum collected in our lab are plotted in Figure 3.1. The emission peaks of collagen and NADH qualitatively match the two peaks presented in the tissue spectrum. The third fluorophore, FAD contributes only a small fraction of the tissue fluorescence. The transmittance spectrum of hemoglobin displays maximum absorption at 415 nm, qualitatively matching the dip in the tissue spectrum.

Fluorescence spectra of tissues in different clinical conditions were simulated with the individual chromophore spectra. Intensity contributions of the tissue components were randomly generated to form the normal distributions according to the parameters in Table 3.1. The averaged tissue spectra of each type derived from the simulation are presented in Figure 3.4. All tissue types have two major emission bands in their emission spectra: one at ~ 380 nm and the other at ~ 460 nm, corresponding to collagen and NADH emission regions, respectively. The simulated normal tissue spectra have the highest intensities in the collagen region among all tissue types, consistent with spectra collected from real tissues. With the advance of disease states, the peak ratio between collagen region and NADH region decreases from normal, through hyperplastic to adenomatous, and finally cancerous tissue conditions. This is also consistent with known tissue fluorescence spectra [67,75].

A feature of tissue fluorescence spectra is that the difference between adenomatous and cancerous tissue spectra is relatively small, especially at the 460 nm region (Figure 3.4). This is because the intensity contributions of tissue fluorophores in these two tissue types are not significantly different. Since the clinical difficulty lies in the differentiation between "benign abnormals" (i.e., hyperplastic) from “malignant abnormals” (i.e., adenomatous and cancerous), the adenomatous and cancerous were treated as a single group of the diseased in this study.

4.3.2 Correlation Coefficient Mapping

The simulated spectra were analyzed with statistical correlation coefficient mapping. For clarity in presentation, all spectra in the training set and prediction set were merged into one matrix and analyzed. Figure 4.1 shows the correlation coefficient map of all 800 spectra from the training and the prediction sets. Samples 1-100, 101-200, 201-300 and 301-400 are the simulated normal, hyperplastic, adenomatous and cancerous tissue spectra in the training set, respectively. Similarly, samples 401-500, 501-600, 601-700 and 701-800 are the simulated normal, hyperplastic, adenomatous and cancerous tissue spectra in the prediction set, respectively.

A few features are immediately apparent in the 2D correlation map. The first feature we observe is that spectra of the same tissue type correlate to each other with high correlation coefficients close to unity.

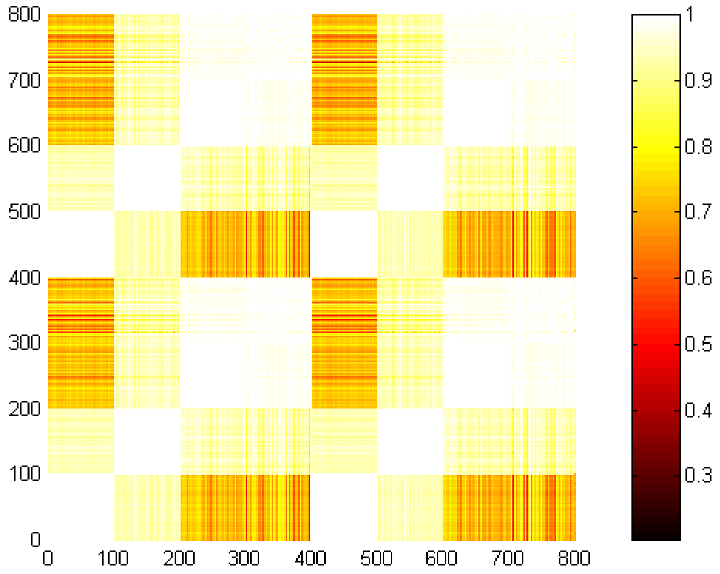

Figure 4.1. Two-dimensional sample-sample correlation coefficient map of all spectra in the training and the prediction sets. Spectra 1-400 belong to the training set and spectra 401-800 to the prediction set. In each set: the first 100 spectra are normal; the second 100 spectra are hyperplastic; the third 100 spectra are adenomatous; and the last 100 spectra are cancerous.

For example, samples 1-100 are simulated normal tissue spectra in the training set. They correlate to each other with high correlation coefficients and generate a white block in the 2D map. They also show high correlation coefficients with samples 401-500, the normal tissue spectra in the prediction set. A white block is shown in the 2D map between sample blocks of 1-100 and 401-500. All other samples have relatively low correlation coefficients with samples 1-100, indicating that they belong to different tissue types. Secondly, the simulated adenomatous and cancerous tissue spectra are similar to each other displaying high cross correlation coefficients close to unity. For example, a white block in the 2D map is shown between samples 201-300 (adenomatous in the training set) and samples 301-400 (cancerous in training set), indicating that the two tissue types are very similar in spectral features. Similarly, all adenomatous samples (samples 201-300 and 601-700) correlate well with all cancerous samples (samples 301-400 and 701-800) in both the training and the prediction sets. Thirdly, the correlation coefficients show the extent of similarity between samples. For example, hyperplastic tissues show higher similarities with the normal tissues than adenomatous/cancerous ones do, consistent with their benign classification. The numerical value of the correlation coefficients is in the vicinity of 0.9 between hyperplastic and normal tissues while is only around 0.6 between hyperplastic and adenomatous/cancerous tissue spectra.

The correlation coefficients between samples can serve as a diagnostic criterion in tissue classification. In Crowell's report, the averaged correlation coefficient of each sample with all normal samples in the data set were calculated and then used in the differentiation of tissue types [75]. In this work, we proposed to use a reference spectrum to simplify this procedure. The correlation coefficients of all samples with this reference spectrum were calculated and analyzed for the purpose of tissue classification. Practically, the averaged spectrum of all normal tissues in the training set was used as the reference. Indeed, when this reference spectrum is used, the method is identical to Crowell's report and gives an excellent contrast between tissue types.

Figure 4.2 shows the correlation coefficients of all samples with the averaged normal tissue spectrum. Samples in the training set are plotted in Figure 4.2A, and samples in the prediction set are plotted in Figure 4.2B. In both data sets, samples 1-100 show correlation coefficients very close to unity, indicating that they are very similar in shape with the averaged normal spectrum. Samples 101-200 have correlation coefficients around 0.90, illustrating that hyperplastic tissues possess a certain degree of similarity with the averaged normal conditions. Both adenomatous and cancerous tissues show relatively low correlation coefficients with the averaged normal, indicating they bear the least resemblance in spectral shape to the normal tissues. The cancerous tissues were more spread than the adenomatous tissues. This reflects the data used in simulation, where the standard deviations of the component contributions of cancerous tissues were much larger than those of adenomatous tissues. Judging from the correlation coefficients in Figure 4.2, the adenomatous tissues were enclosed in the cancerous tissue type.

The correlation coefficients of all normal tissues were very close to unity and show the least variance. This property is known for the Pearson's correlation coefficient, where the variance approaches 0 when *r*-value approaches 1. The correlation coefficients of the same tissue type were grouped together and separated between tissue types, which was the foundation of using correlation coefficients for sample classification. The tissue type of a specific sample can be determined directly by setting up an empirical threshold between tissue classes, as demonstrated by Crowell [75]. However, the empirical threshold is not statistically important and does not provide uncertainty information in classification.

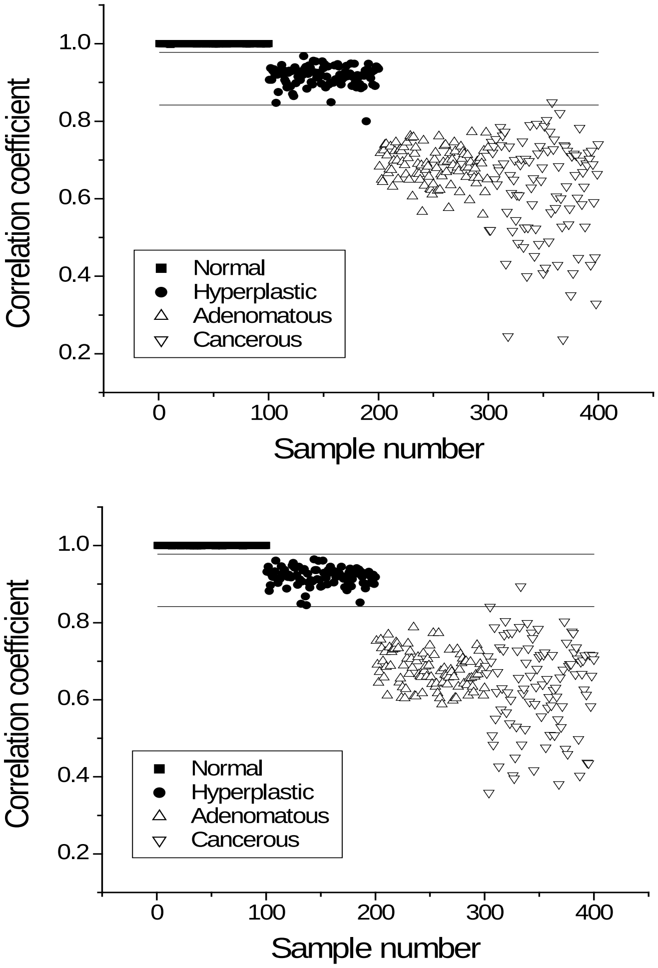

Figure 4.2. Correlation coefficient of each sample spectrum in (A) the training set and (B) the prediction set with the averaged normal spectrum in the training set. Upper line: statistical threshold between normal and hyperplastic tissues. Lower line: statistical threshold between hyperplastic and adenomatous/cancerous tissues. The thresholds are calculated with Bayesian analysis applied on the asymmetrically expanded correlation coefficients.

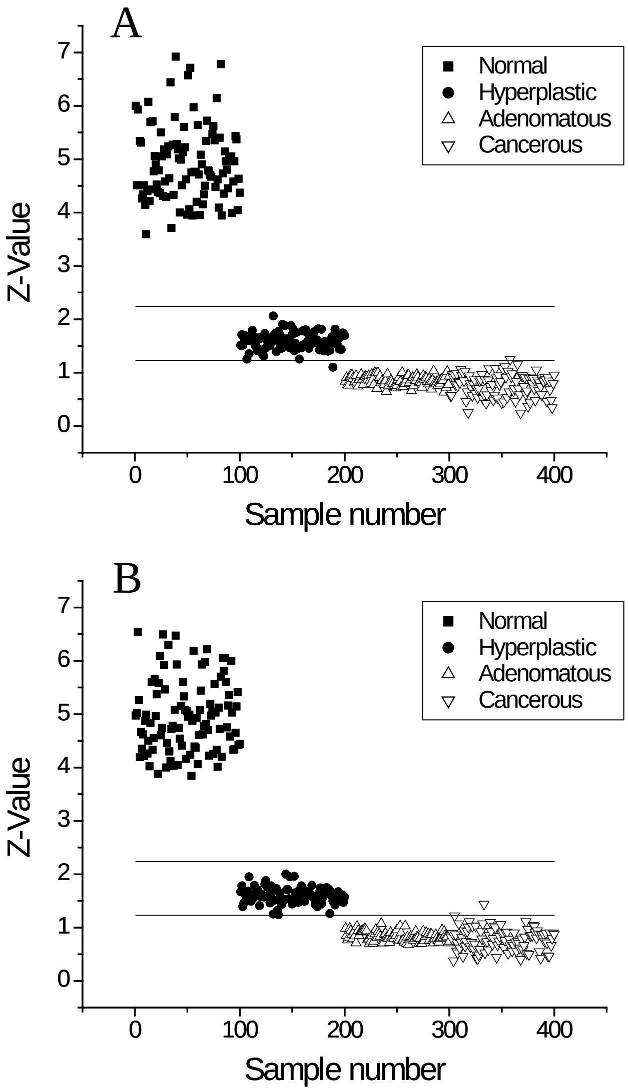

Figure 4.3. Z values of the spectrum of each sample in (A) the training set and (B) the prediction set with the averaged normal spectrum in the training set. Upper line: statistical threshold between normal and hyperplastic tissues. Lower line: statistical threshold between hyperplastic and adenomatous/cancerous tissues.

4.3.3 Fisher’s Transformation of the Correlation Coefficients

In order to obtain the probability information in classification, the correlation coefficients were transformed to Fisher’s z values according to Equation 4.3. The transformation essentially expanded the short tail of the distribution of correlation coefficients. Figure 4.3 shows the distribution of the corresponding z values of correlation coefficients presented in Figure 4.2. The normal tissues are symmetrically spread out with an average of 4.9 and an apparent standard deviation of 0.70. The hyperplastic tissues have a center value of 1.6. The adenomatous and cancerous tissues are treated as a same group of the diseased and have an average of 0.80. The apparent means and standard deviations of the z-variables for each tissue type were used in the following Bayesian analysis.

4.3.4. Bayesian Analysis and Diagnostic Results

Bayes decision theory was applied on the z values in order to classify the simulated tissue spectra statistically. The apparent mean and standard deviation of the *z*-variables for each tissue type were inserted into Equation 4.4 to calculate the probability density functions. The probabilities of all samples belonging to normal, hyperplastic, and diseased-state were evaluated and used in the classification (Figure 4.4). All normal tissues were correctly assigned without any ambiguity since they all have high probabilities close to 1 of belonging to the normal tissue type (Figure 4.4A). This can also be viewed from the *r*-plot (Figure 4.2) or the *z*-plot (Figure 4.3) that normal tissues are well separated from other groups.

Figure 4.4B shows the probability of all samples belonging to the hyperplastic tissue type. All hyperplastic samples were correctly assigned, with a few samples having marginal probabilities. There is a single cancerous tissue mis-classified as the hyperplastic tissue (sample 333). This abnormality discloses the fluctuation nature of the simulated spectra. Figure 4.4C shows that all samples from 201 to 400 have very high probabilities belonging to the diseased state except sample 333, which is mis-assigned to the hyperplastic tissue type in Figure 4.4B.

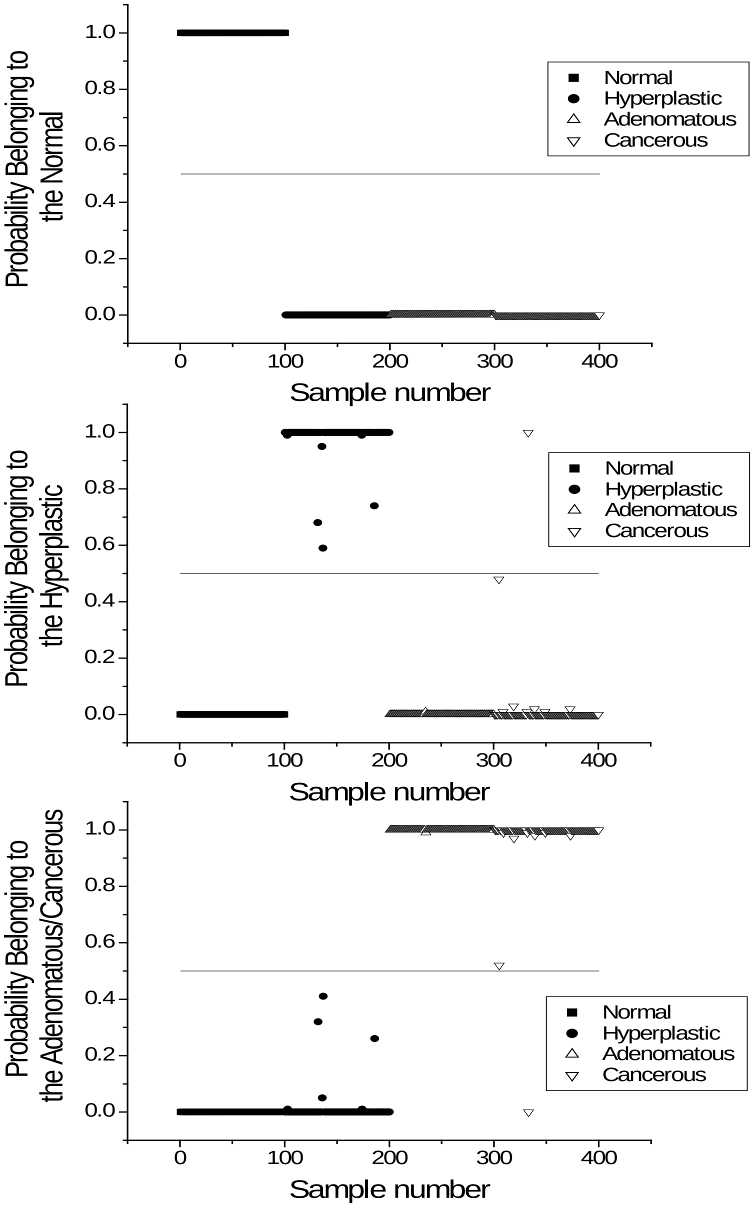

Figure 4.4. Probabilities of all simulated spectra in the prediction set belonging to (A) normal tissue type; (B) hyperplastic tissue type and (C) adenomatous/cancerous tissue type.

The clinically useful classification is between the hyperplastic and diseased (adenomatous and cancerous) tissue conditions. With the combined use of Bayes decision theory and the *z*-transformation, the classification yields only one error count out of 400 samples in the prediction set (Figure 4.4). The resulted sensitivity and specificity are 99% and 100%, respectively (Table 4.1). If we apply the same analysis on the training set, only 1 hyperplastic and 1 diseased tissue are mis-classified. This leads to a sensitivity of 99% and a specificity of 99%, respectively (Table 4.1). Both results are satisfactory. The diagnostic performance is presented as sensitivity (SE), specificity (SP), predictive value positive (PVP), predictive value negative (PVN), and false alarm rate (FAR). Their corresponding values are listed in Table 4.1.

Table 4.1. Diagnostic results using Bayes analysis on the asymmetrically expanded correlation coefficients of all samples with the average of normal samples.

Data set	**HP mis-assigned**	**AD/CA mis-assigned**	**SE**	**SP**	**PVP**	**PVN**	**FAR**
Training	1	1	0.99	0.99	0.99	0.99	0.01
Prediction	0	1	0.99	1.00	1.00	0.99	0.01

HP: hyperplastic tissues; AD: adenomatous tissues; CA: cancerous tissues; SE: sensitivity; SP: specificity; PVP: predictive value positive; PVN: predictive value negative; FAR: false alarm rate.

In an alternative approach, the boundary between tissue types were determined and used in classification directly. The threshold was obtained by assuming a z-value that has equal probabilities belonging to the two neighboring tissue types. For example, a z-value that has equal probabilities of 0.5 for both hyperplastic and diseased tissue types was determined to be 1.23 (Figures 4.3A and 4.3B). At this z-value, the probability of it belonging to the normal tissue type is very close to zero. Using Equation 4.3, the corresponding correlation coefficient that differentiates hyperplastic and adenomatous/cancerous tissue types was calculated to be 0.84 (Figures 4.2A and 4.2B). Using the same procedures, the threshold of the z and r values between normal and hyperplastic tissue types were determined to be 2.24 and 0.98, respectively. These values can be used directly to classify tissue spectra if no probability information is required. The same diagnostic results for the training set and the prediction set were obtained.

4.4 Conclusions

The method of using statistical correlation coefficient mapping to classify spectra was improved. Correlation coefficients reveal inherent correlation among samples and provide good criteria in sample classification. However, correlation coefficients are not normally distributed, which hampers further statistical analysis of the correlation coefficients in sample classification. In this study, Pearson's correlation coefficients were transformed to Fisher's z-values. The transformation allows the application of the Bayes decision theory on the correlation coefficients between tissue samples. Statistically significant boundaries between tissue types were established with the combined use of Fisher's z-transformation and Bayes decision theory. Moreover, tissue types were resolved with a probability value associated with the classification, which is appreciable in clinical practices.

The improved methodology was examined with simulated tissue-phantom data sets. The use of simulated data allowed the possibility of analyzing the entire sample space with large sample density that is impossible in clinical studies. The samples were classified as three clinical conditions: normal, hyperplastic and diseased (adenomatous/cancerous). Discrimination of the simulated spectra was achieved with high sensitivity, selectivity, predictive value positive and predictive value negative scores. In the course of this investigation, it was proven that the diagnosis between the benign abnormal and diseased tissue conditions by the improved statistical correlation coefficient method was successful.

CHAPTER 5 DESIGN OF TISSUE PHANTOMS USING NANOPOROUS MATERIALS

5.1 Introduction

5.1.1 Tissue Phantoms

Design and analysis of tissue phantoms have proven to be a useful tool in understanding spectrochemical properties of tissues and ultimately optimizing diagnostic methods based on optical biopsy [101-105]. There are several other reasons for the development and commercialization of tissue phantoms. First of all, patient-to-patient and site-to-site variations [106] make standardization and comparison of analytical methodologies challenging without the “reference sample”. Second, ex-vivo tissues have low stability and shelf life and thus are not suitable as “reference samples”. Third, the optical properties of tissues are bound to alter drastically upon excision, due to the changes in the levels of blood, oxygen and associated concentrations of NADH, NADPH and FAD. Fourth, involvement of human or animal subjects in the development of novel diagnostic methodologies is often unsafe and expensive. Finally, the use of artificial tissue-simulating structures instead of the animal models is highly desirable due to the ethical and humanitarian reasons that are usually backed by strong public support.

Tissue phantoms, formally defined as synthetically created materials, whose properties mimic the parameters of a target tissue, are successfully used for a number of purposes:

1. fitting and deconvolution of tissue spectral signatures;
2. designing and optimizing diagnostic and photodynamic therapy systems;
3. routine quality control of system performance;
4. comparison between different diagnostic methodologies and
5. facilitating lab-to-lab method transferability.

The properties and structure of the phantom are determined by its intended use. Thus, the phantoms intended to simulate the response of the tissue to the photodynamic therapy or cosmetic treatments are likely to differ drastically from the phantoms intended for routine instrument calibration in optical coherence tomography (OCT). Nevertheless, there are certain parameters that are desirable in all tissue phantoms' designs:

1. optical properties of the phantom exhibit wavelength dependence similar to the real tissues;
2. absorption and scattering coefficients, as well as refractive index of the phantom are close to those of the tissues;
3. biochemical molecules of interest can be easily incorporated and would respond to the optical stimuli in a fashion similar to the intact tissue;

4. inhomogeneities can be included in the phantom matrix and optical properties of the phantom can be varied to simulate the tissues at different clinical conditions;
5. thermal, mechanical and diffusion properties are similar to the tissue;
6. stability at ambient environmental conditions and within a reasonable time frame;
7. inexpensive and comparatively easy to produce – these two last parameters provide competitive advantage of the tissue phantoms over the animal models.

One of first areas of clinical research that adopted the use of tissue phantoms in early 1980s was near-infrared imaging for breast cancer diagnosis [107,108]. Later development of photodynamic therapy for the treatment of cancers created a new wave of interest in tissue phantom development due to the necessity to accurately estimate the therapeutic doses of light [109-112]. Development of spatially resolved, time-resolved and frequency-domain spectroscopy and tissue imaging in 1990s produced a plethora of new tissue phantoms mimicking the response of tissues to these analytical modalities [101,113-115]. Recent progress in minimally-invasive methods of diagnosis and adaptation of these techniques in the clinical practice keep the development of tissue phantoms one of the top priority topics in biomedicine. Tissue phantoms continue playing an important role in the development, optimization and comparison studies in such analytical techniques as OCT,[116-119], near-infrared imaging [120-122] and photodynamic therapy dosimetry [113,123].

There is an increasing interest in developing micrometer and nanometer domains with well-defined biochemical compositions and spectroscopic properties [124]. These small domains can be used to mimic cells in a biological matrix or the initial formation of disease in tissue. They are valuable in the studies of cell functions [125] and in the development of imaging modalities for noninvasive disease diagnosis [105,126,127]. The biomedical applications impose a few requirements on these small domains:

1. they should be conveniently formed, without the need of extensive chemical synthesis;
2. the biochemical composition and spectroscopic properties could be tuned with ease;
3. a clear boundary is maintained when the domains are imbedded into an aqueous biological matrix.

The last requirement is especially critical in the preparation of tissue phantoms in the field of optical biopsy. The validation of diagnostic imaging methods depends on the demonstration that domains of distinctive spectral properties can be clearly differentiated in three-dimensional imaging. A clear boundary of the domains needs to be maintained in the phantom preparation and during optical imaging.

At macroscopic dimensions, phantom domains can be prepared as stacked layers [105,123,127] or suspended optical cells [102,127-129]. At microscopic and nanoscopic dimensions these approaches are not easily implemented or practical. Novel designs are desired to generate microscopic and nanoscopic domains in a phantom matrix.

5.1.2 Design of Phantoms for Confocal Imaging

Due to the prominence of fluorescence spectroscopy and imaging in the early detection of cancer, there is a significant interest in the development of biologically relevant tissue phantoms that contain tissue chromophores, such as hemoglobin and melanin, collagen and elastin, cofactors (flavin adenine dinucleotide (FAD) and nicotinamide adenine dinucleotide (NADH)), porphyrins, lipids and vitamins. The necessity of including these biological molecules drives the design of tissue phantoms from the nonorganic polymer matrixes [129,130] to more biologically compatible media, such as agar [51,102,119], gelatin [126,131], and collagen gel [104,105,127]. The biological molecules also demand mild conditions for the phantom preparation. Collagen matrix is desirable in the tissue phantoms for fluorescence based optical biopsy, because it is one of the major extracellular endogenous fluorophores. Unfortunately, collagen is a fairly expensive component and the methodology for the preparation of consistent semisolid and relatively thick collagen gels requires precise control of the experimental conditions. Agar and gelatin matrices, while being more cost-efficient and easier to prepare than collagen gel, allow the inclusion of biological molecules, as well as layers of intact cells, and provide semisolid phantom matrixes that can be cut into a variety of shapes. In this chapter, agar-based tissue phantoms with spherical FAD-carrying particles as localized fluorescent domains are described.

Spherical particles, mostly polystyrene microspheres, are broadly used in the design of tissue phantoms to adjust the scattering coefficient to the levels of biological tissues [101,103,126,127,132-134]. Polymer microspheres are often preferred scattering components for the tissue phantoms over lipid emulsions [101,119,128] or suspensions of white metal oxides [130], because the scattering properties of the spherical objects can be accurately predicted using Mie scattering theory [135], which is an attractive feature for method validation.

The potential of using mesoporous particles as femtoliter containers/carriers for the purpose of drug and contrast agent delivery has been shown in many studies [136-138]. High surface-to-volume ratio, robustness and commercial availability of a variety of sizes and surface modifications of silica particles make them attractive candidates as fluorophore-loaded components of tissue phantoms. In the pursuit of creating distinct spectral domains within the three-dimensional tissue phantom, we proposed imbedding hydrophobically-modified nanoporous silica particles within water-based agar matrix. The key principle of this design is the nonwettability of the hydrophobic nanoparticles by an aqueous solution [139]. The particles are preloaded with the desired composition of biological molecules. A clear biological/optical boundary is achieved when the particles are dispersed into the matrix to make tissue phantoms, because the aqueous solution cannot wet the hydrophobic nanopores, thus the loaded biological molecules will stay inside the pores to maintain a well-defined domain boundary. Uniform silica beads 10 μm in diameter serve as perfect imaging objects for testing optical methods for cancer imaging. In addition, they provide features of known shapes and dimensions comparable to eukaryotic cells.

5.2 Experimental

5.2.1 Chemicals and Materials

The nanoporous silica particles used in this study were highly uniform and microscopically smooth LUNA® C18 beads, obtained from Phenomenex (Torrance, CA). The particles have an average diameter of 10 μm, a nominal pore size of 100 Å and a surface area of 400 m^2/g. The surface of the silica is covered with an organic monolayer of C18, rendering the pores hydrophobic. Flavin adenine dinucleotide (FAD) was purchased at the highest purity from Sigma-Aldrich (St. Louis, MO). Acid soluble collagen from human placenta, type IV according to Bornstein and Traub, (type VI according to Sigma classification) was obtained in powder form from Sigma-Aldrich (St. Louis, MO) as well. All solutions were prepared using deionized water purified with a MilliQ system (Millipore, Bedford, MA), unless otherwise specified. HPLC-quality acetonitrile was purchased from Fisher Scientific (Fair Lawn, NJ). Phosphate Buffer Saline (PBS) was prepared from sodium phosphate, sodium biphosphate and sodium chloride using standard protocol; the pH of the solution was adjusted to 7.4 with sodium hydroxide solution. Neither the beads, nor chemicals were subjected to any pre-treatment before the phantom preparation.

A highly purified agar powder was obtained from Sigma-Aldrich (USA) and dissolved in deionized water for a final concentration of 1% by mass. To facilitate the dissolution of agar powder, the mixture was heated to 85^{o}C, the melting point of agar, in a water bath. In preparation of agar solution, the use of a standard heater is not recommended, because direct heat can cause slight burning of agar, which will result in a detectable increase of its absorption coefficient.

The hydrophobic silica beads were loaded with an endogenous tissue fluorophore, flavin adenine dinucleotide (FAD, Figure 5.1), which is one of the major fluorophores responsible for the laser-induced fluorescence of the colon tissue as mentioned earlier, in Chapter 3 [67,75]. First, the particles were wetted with acetonitrile; this wetting step allows the subsequent loading of biological fluorophores. Then the beads were separated from the solution by centrifugation and mixed with a 0.5 mM stock solution of FAD in PBS buffer. The particles, now loaded with FAD, were separated from the solution in the second round of centrifugation and dried in the oven at 40°C overnight to completely remove the solvent from the nanopores.

A)

B)

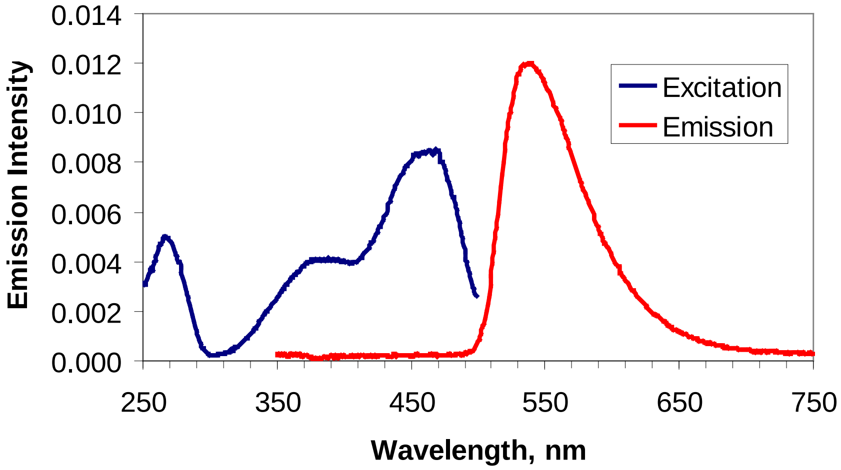

Figure 5.1. Chemical structure (A) and fluorescence excitation/emission spectra (B) of flavin adenine dinucleotide (FAD).

To test the complete dryness of the pores, a small sample of the silica gel was placed between two tightly fixed microscope coverslips and observed under the microscope as a 20-μL drop of PBS solution was placed at the edge of the top coverslip and allowed to disperse around the particles. No indications of the solution penetrating inside the pores were observed; the intensity and thus the concentration distribution of FAD remain unchanged before and after the solvent placement. Another sample of the FAD-loaded and dried silica gel was fixed between two coverslips and observed under the microscope as the particles were first wetted with 20 μL of pure acetonitrile and then mixed with 20 μL of PBS. In the second sample, the distribution of FAD inside the beads changed remarkably and the results of this re-wetting experiment are discussed in section 5.3.3.

Pre-loaded with FAD then dried C18 beads were added into an aqueous solution of agar (1% by mass) at 50°C. The solution was sonicated immediately for 2 minutes to disperse the particles in the agar gel. Due to the hydrophobicity of the particles, they tend to cluster in the aqueous solutions. The sonication step also facilitated the disruption of particle aggregates. The resulting suspension of particles in agar gel was then poured into a mold and allowed to set at 5°C for several hours to form the tissue phantom.

Attempt was made to image fluorescence of collagen gel with blank (unloaded) silica beads distributed inside the matrix. Procedure for collagen gel preparation was adopted from [105] with minor modifications. Lyophilized collagen type IV was mixed with 0.2 % acetic acid and allowed to dissolve overnight without stirring at room temperature to produce 3 mg/ml solution (~24 μM). To prepare collagen gel, 7 parts of the collagen in 0.2 % acetic acid solution were mixed with 0.89 parts of 150 mM PBS and 1 part 0.2 M HEPES, pH 7.3. The pH of the mixture was adjusted to 7.4 with 1 M NaOH. One milliliter (1 part) of the resulting solution was mixed with 1.11 parts of PBS buffer and 0.03 g of 10 μm Luna® C18 silica particles. Collagen-particles mixture was poured into a mold and allowed to gel in the oven at 40°C to produce a semi-solid phantom.

5.2.2 Instrumentation and Measurement

The images of the beads at each step of the phantom preparation were collected with the stage scanning confocal fluorescence microscope system built in-house and described earlier [140]. The schematic of the optical path is presented in Figure 5.2. In brief, the excitation light at 454 nm, provided by an air-cooled argon laser (Model: 35-LAP-431-220, Melles Griot, Carlsbad, CA), was focused into a diffraction-limited spot within the sample using a 100X oil-immersion objective (1.45 NA). This wavelength provides optimum excitation of FAD fluorescence (Figure 5.1B). The three-dimensional movement of the focal point across the tissue phantom was achieved by using a piezoelectric objective stepper and an xy-piezo flexure stage (Physik Instrumente, Germany) with sub-nanometer resolution. The movements of the stage were controlled with LabView programs written in house. Emitted fluorescence was collected by the same objective and passed through a 455 nm dichroic mirror, while scattered excitation light was reflected by the mirror. Out-of-focus signals were efficiently rejected by a confocal 50-μm pinhole and the fluorescence signal from the focal plane was directed to an avalanche photodiode detector (APD, model SPCM-AQ, PerkinElmer Optoelectronics).

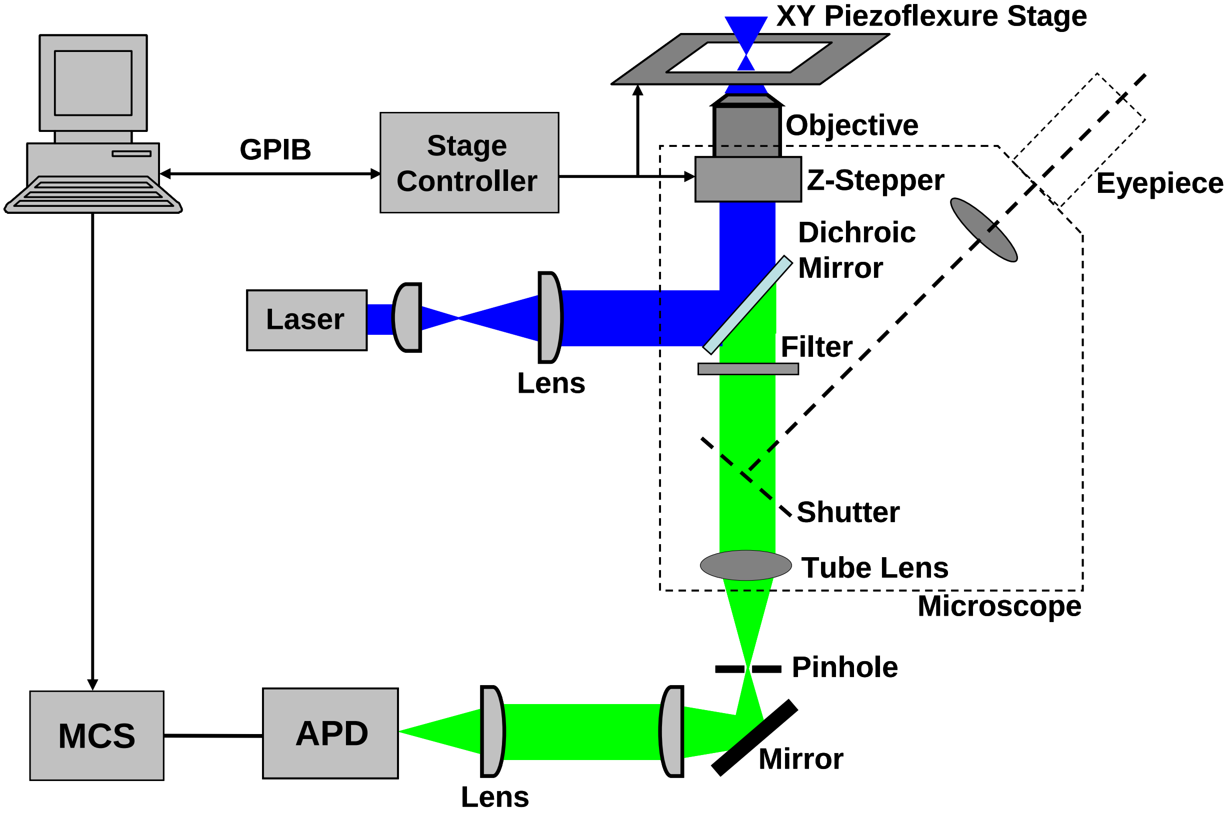

Figure 5.2. Schematic diagram of the home-built system for confocal imaging and single molecule detection (GPIB – general purpose interface bus, APD - avalanche photodiode; MCS - multichannel scaler). Adapted from [141].

The confocal volume achieved by this optical configuration is ~250 nm in lateral resolution and ~1 μm in axial resolution. To further improve the signal-to-noise ratio and effectively reject scattered excitation light, a 475-nm long-pass filter and a 530-nm band-pass filter with 55-nm bandwidth were used in the emission channel. Space-dependent data was acquired by collecting the fluorescence photon counts using a multichannel scaler (MCS) while the laser spot was translated in three dimensions in the sample. Intensity traces as a function of the stage movements experimentally collected were processed in MatLab (Mathworks Inc., Natick, MA) to construct the images.

Excitation lines provided by argon laser are not optimal for collagen IV excitation. Spectral properties of collagen suggest that laser with shorter wavelength, such as a Helium-Cadmium laser, providing 325-nm excitation, should be used to excite collagen fluorescence. Optical confocal set-up described earlier is built around an inverted microscope (Eclipse TE2000-U, Nikon), whose optics are not suitable for transmitting UV light. Thus, images of the collagen matrix were obtained using another in-house built optical system. This system was designed for the spectrally-resolved fluorescence correlation spectroscopy experiments in frequency domain, thus it contains several components which were not utilized in the confocal microscopy imaging of the collagen gel.

Simplified schematic of the set up, including only components directly involved in the imaging experiments discussed here, is shown in Figure 5.3. In essence, the laser light was directed through a periscope, a polarizing cube and a series of mirrors to the 325 nm dichroic mirror.

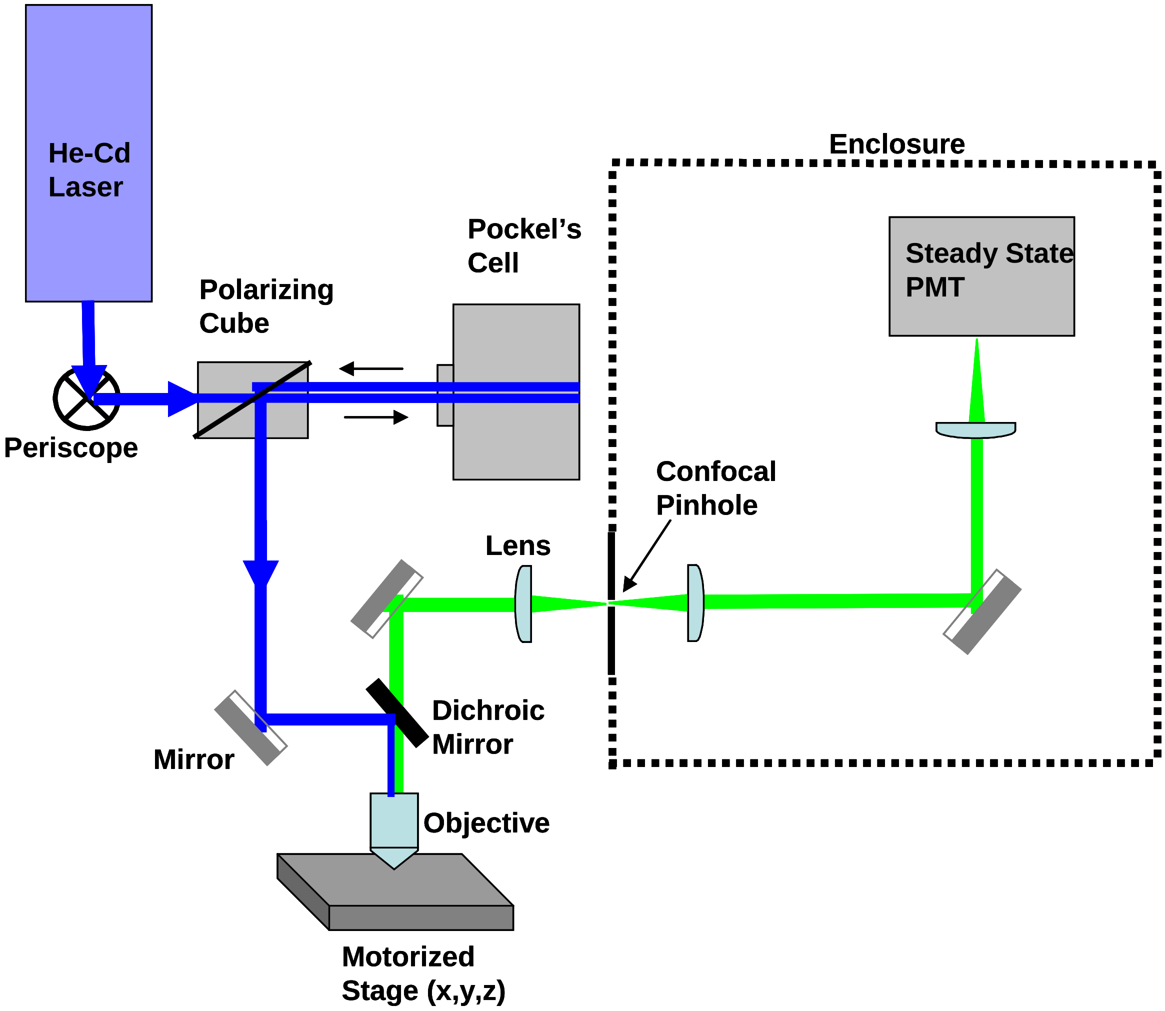

Figure 5.3. Part of confocal microscopy set-up used for imaging collagen gel. Excitation provided by a HeCd laser at 325 nm (PMT – photomultiplier tube).

The Pockel's cell, which would modulate the laser light in correlation spectroscopy experiments, was switched off and acted as a mirror in the steady state experiments. Reflected by the dichroic mirror laser light was focused into the sample by a 40X objective with anti-reflectance coating for the 335-500 nm region (OFR, Thorlabs, Newton, NJ). Emitted fluorescence signal was collected by the same objective, passed through the dichroic mirror and the 150-μm confocal pinhole, and then focused into the steady state PMT detector located inside the detector enclosure. The signal-to-noise ratio of the system was further improved by placing a 345-nm long-pass filter in the emission channel, which minimized the scattered excitation light from reaching the detector.

The scanning of the sample was achieved by an xyz translational stage (Thorlabs, Newton, NJ) with 1-inch working distance in all three directions. Since the system was intended for the analysis of biopsy samples, in the selection of the stage large travel distance was one of the main criteria. Possessing the travel distance of one inch in all three directions, this stage has naturally lower precision than the piezoelectric two-dimensional stage discussed earlier, thus the images of the particles might appear less resolved. The advantage of using spherical beads as a part of tissue phantom becomes apparent when optimization of the instrument performance without the eyepiece is considered.

5.3 Results and Discussion

5.3.1 Loading C18 Silica Particles with Endogeneous Fluorophores

The presence of fluorescent impurities in nanoporous silica was detected in prior single molecule experiments [141]. Multiple pre-washing of the beads was necessary for such ultrasensitive experiments. The images of blank C18 beads (Figure 5.4A) show minimal background signal, about 800 times lower than the intensity of the fluorescence from FAD-loaded particles (Figure 5.4B). It was concluded that for the tissue phantom preparation the background fluorescence of the particles is negligible.

FAD partitions into the nanopores of the beads when the solvent composition is optimal for the wetting of the pores. FAD is readily soluble in phosphate buffer, but the beads are not wetted with aqueous solutions due to the nonpolar C18 coating on the silica surface of the nanopores. The loading of FAD into the pores is achieved by prior wetting of the beads with a less-polar solvent, such as acetonitrile or ethanol, and further addition of the fluorophore solution in aqueous buffer. Fluorescence images of the beads soaked in stock FAD solution show relatively homogeneous distribution of FAD throughout individual beads (Figure 5.4B).

5.3.2 Restoration of Internal Hydrophobicity of Fluorescent Domains

The next step in the phantom preparation is the recovery of the hydrophobic environment of the pores, which is achieved by drying the beads. The drying step causes the dewetting of the pores and redistribution of the fluorophore molecules inside the beads (Figure 5.4C). Apparently, the solvent evaporation starts at the openings and gradually proceeds into the pores. Water-soluble FAD relocates deeper into the core of the silica particles following the receding solvent front.

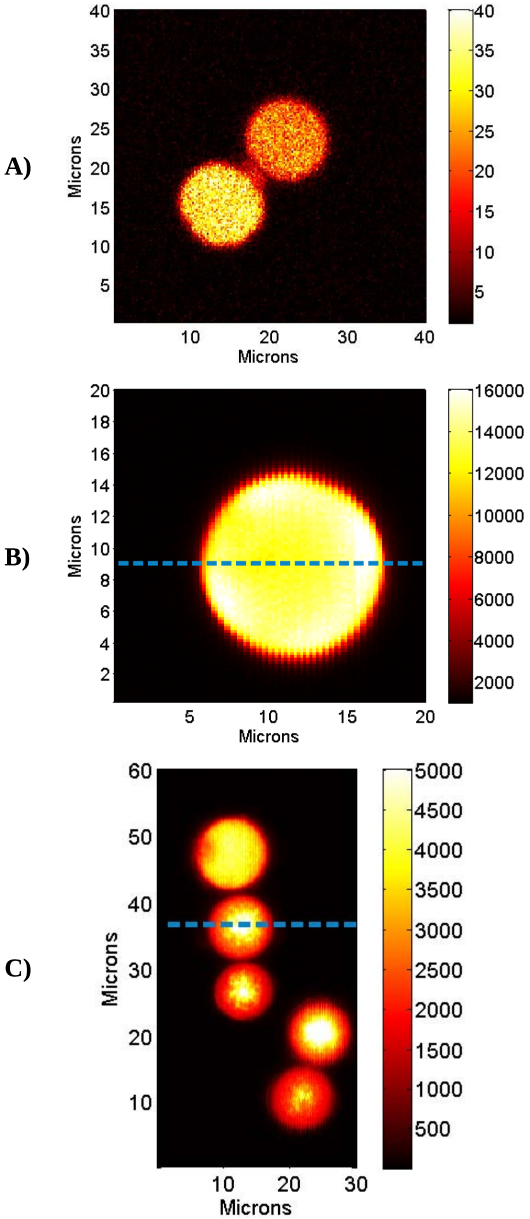

Figure 5.4. Confocal fluorescence images of silica beads. (A) Blank C18 silica beads in 1% agar gel, ND filter OD 2; (B) a bead pre-wetted with acetonitrile and loaded with FAD, ND filters OD 2 and 0.3; (C) beads loaded with FAD and dried in the oven, no ND filters. Excitation wavelength 454 nm, laser power 0.42 mW. Fluorescence intensity is in units of photon counts.

It is noteworthy to mention that the fluorescence intensity of FAD in dry particles is about 400 to 480 times lower than fluorescence signal from wetted FAD-filled beads (Figure 5.5).

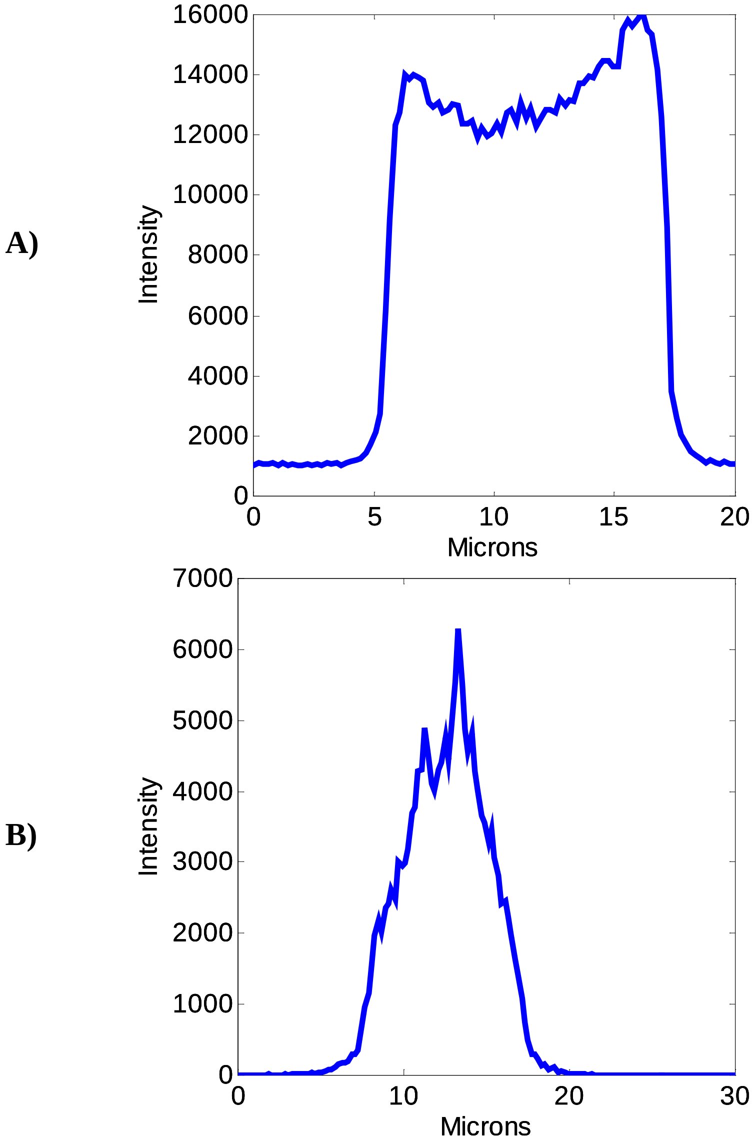

Figure 5.5. Intensity cross-sections of the particle images indicated by the blue dashed lines in Figure 4.5. (A) Cross-section of a bead pre-wetted with acetonitrile and loaded with FAD, ND filters OD 2 and 0.3; (B) cross-section of a bead loaded with FAD and dried in the oven overnight, no ND filters.

Considering that image in Figure 5.4B was acquired with two neutral density filters OD 2 and OD 0.3 in the excitation channel and image shown in Figure 5.4C was obtained without any filters we need to calculate the actual intensity of the wetted particles for adequate comparison. Assuming the apparent fluorescence intensity in Figure 5.4B to be 13000, the intensity without the filters would be:

$$I_0 = \frac{I}{10^{-2.3}} = \frac{13000}{10^{-2.3}} \approx 2600000$$

which is approximately 500 times higher than the fluorescence intensity of the dry particles.

There are three possible causes for this intensity drop. First, larger difference in the refractive index between the silica and air in the dry nanopores causes more scattering of the laser light, thus, the excitation of the fluorophore inside dry particles is less efficient. Second, FAD, as many other fluorophores, could be sensitive to the polarity of its microenvironment, which changes significantly in the process of particle drying. Third, the concentration of FAD in the nanopores after drying could be so high that fluorescence intensity decreases through concentration quenching. Intensity of the FAD fluorescence can be restored by rewetting the pores of the particles, which proves that FAD was retained in the pores during the drying process.

5.3.3 Re-wetting of Nanoporous Particles with Restored Hydrophobicity

Non-wettability of the dried beads with aqueous solution, combined with the absence of any change in the distribution of the fluorophore inside the pores of the beads, indicated restored hydrophobicity of the nanopores, which prevented the penetration of aqueous solution into the core of the silica gel. To prove the assumption of the hydrophobicity-controlled non-wettability of the particles, a small sample of the pre-loaded and dried silica gel was fixed between two coverslips and observed under the microscope. Addition of pure acetonitrile to the hydrophobic FAD-loaded beads effectively solubilized the particles, but did not change the fluorescence intensity and the distribution of FAD (Figure 5.6), because FAD is poorly soluble in nonpolar solvents. Subsequent addition of PBS solution to the acetonitrile-prewetted beads caused immediate dissolution of FAD, restoring its even distribution throughout the particles. Fluorescence intensity increased a hundred folds compared to ACN-wetted particles, as can be seen in Figure 5.7.

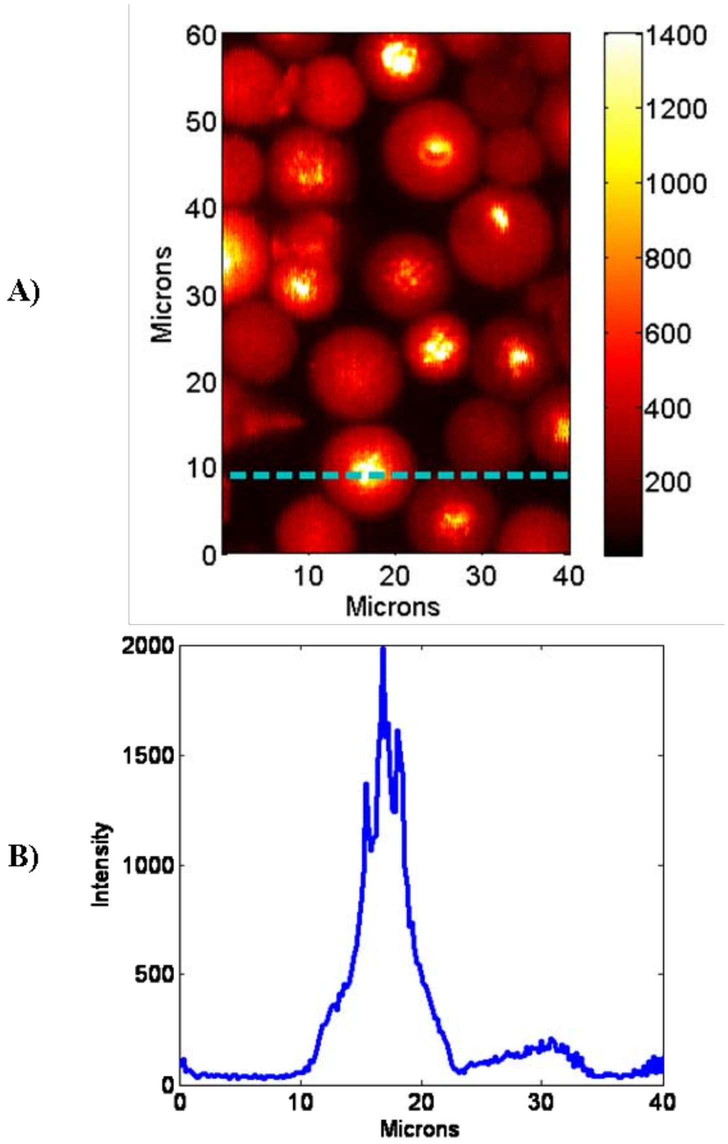

Figure 5.6. Wetting of C18 silica particles preloaded with FAD and dried overnight with pure acetonitrile. (A) Particles wetted with acetonitrile were applied on the coverslip and imaged without ND filter; (B) intensity profile along the dashed blue line in the image above. Excitation wavelength 454 nm, laser power 0.42 mW.

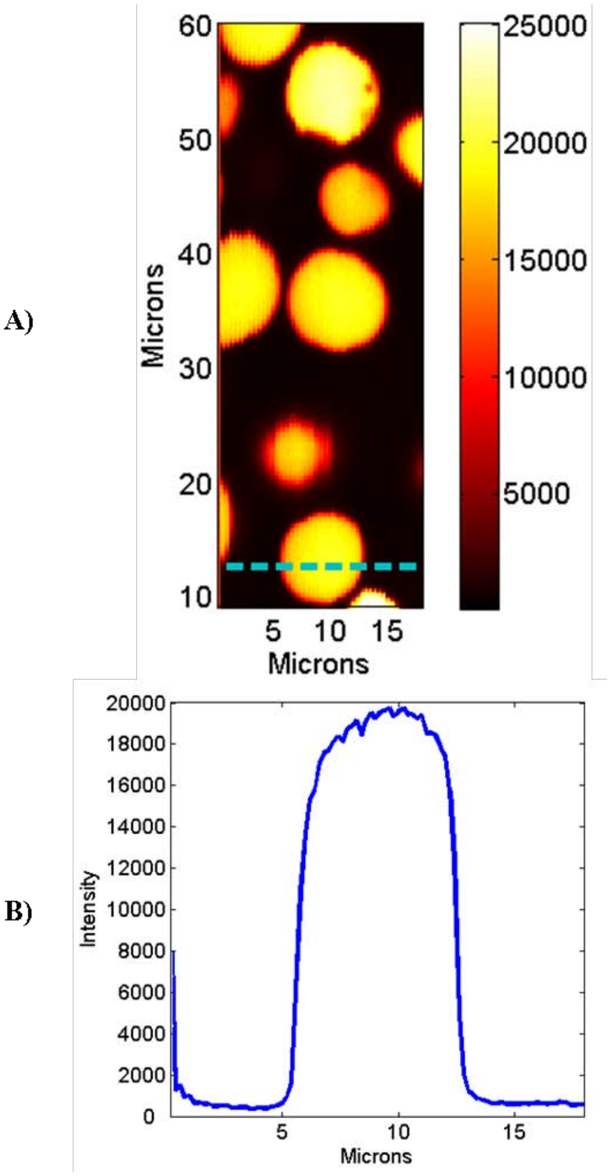

Figure 5.7. Wetting of C18 silica particles preloaded with FAD with acetonitrile and PBS. (A) C18 silica particles preloaded with FAD and dried overnight were placed on the coverslip and then directly wetted with a drop of acetonitrile, followed by a drop of PBS (pH 7.4); (B) intensity profile along the dashed blue line in the image above. Excitation wavelength 454 nm, laser power 0.42 mW, ND filter OD 1.

5.3.4 Dispersion of Hydrophobic Nanoporous Particles in Hydrophilic Matrices

To mimic a real tissue matrix, the beads were embedded in 1% agar gel [128]. Restored hydrophobicity of the nanopores ensures the embedding of the beads in aqueous agar gel without “leakage” of the fluorophore into the surrounding matrix. Clear boundaries are maintained for these 10-μm optical domains inside the tissue phantom matrix. Optical slices in the three-dimensional confocal image of the tissue phantom (Figure 5.8) show spherical boundaries of the FAD composed silica particles. The fluorophore molecules adsorbed on the outer surface of the beads can be removed by washing the beads with water. Since the exterior surface of the porous particles is negligible compared to the total surface area, the amount of FAD deposited on the outer surface is minor and this extra washing step was determined to be unessential in the phantom preparation. The hydrophobic silica particles have a natural tendency to aggregate in the aqueous matrix to minimize the total energy of the system. Sonication of the warm agar upon the addition of the beads helped dispersion of the particles in all three dimensions. The particles loaded with endogenous fluorophore, FAD, and imbedded in the agar matrix form a three-dimensional nontoxic tissue phantom. The use of spherical beads to localize the endogenous fluorescent tissue components allows the simulation of the sample inhomogeneities. To prepare complete tissue phantoms, mimicking spectral characteristics of the human tissues, other endogenous fluorophores, such as NADH, will be loaded into the nanopores. Particles pre-loaded with co-factors will be dispersed in collagen gel, simulating extracellular matrix.

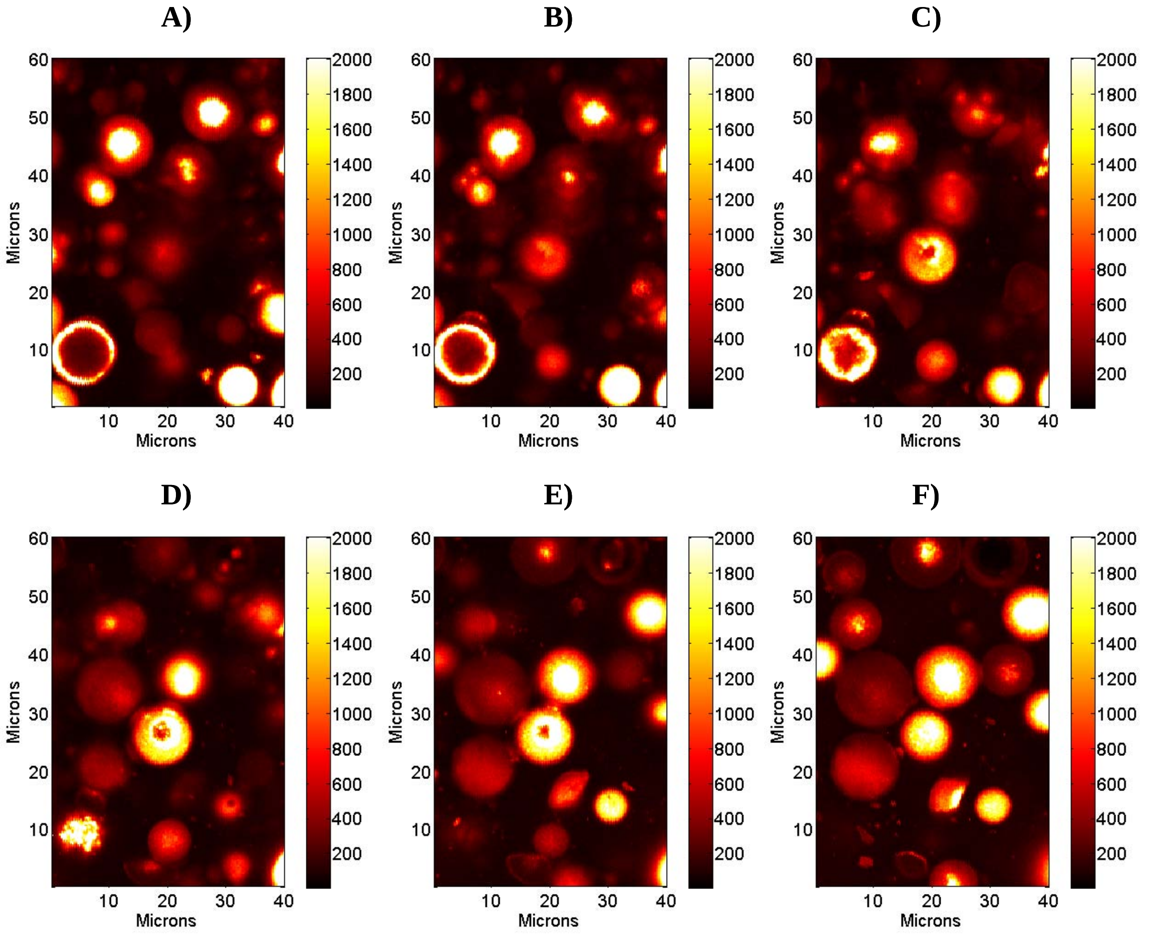

Figure 5.8. Z-sections of the three-dimensional tissue phantom composed of FAD-loaded silica particles dispersed in 1% agar gel. Z-slices were taken at 2 μm increments. Relative z positions: (A) 0 μm; (B) 2 μm; (C) 4 μm; (D) 6 μm; (E) 8 μm and (F) 10 μm. Excitation: 454 nm, step size in x-y directions: 0.2 μm.

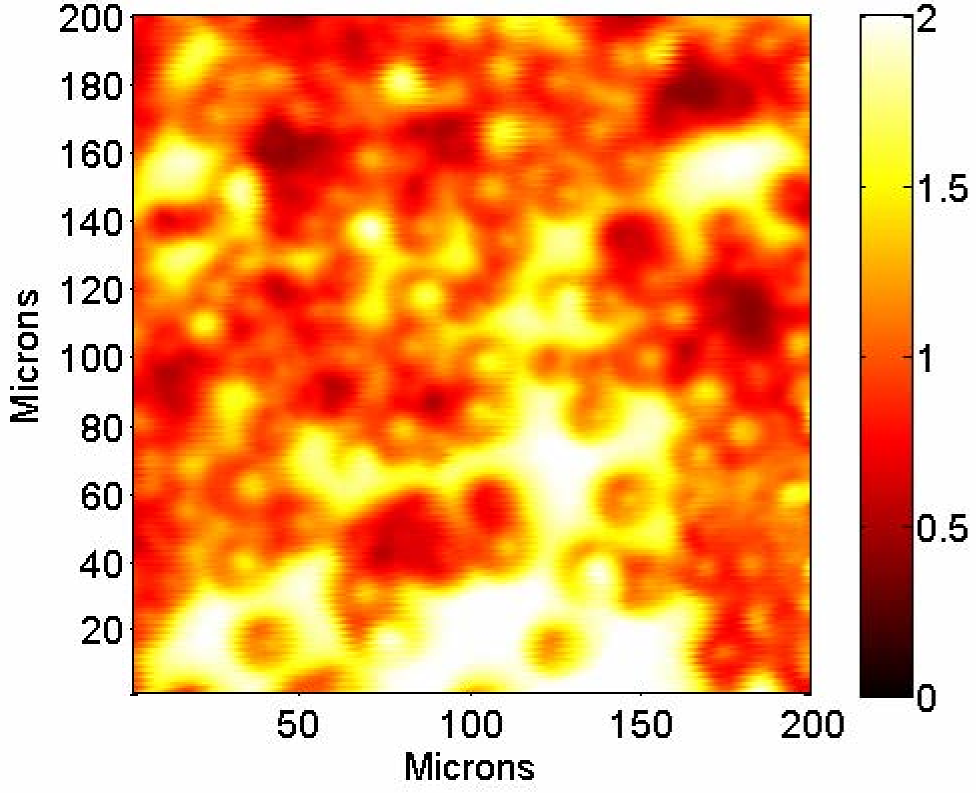

Figure 5.9. Tissue phantom composed of blank (unloaded) C18 silica particles dispersed in collagen IV gel. Excitation: 325 nm, 40X objective, step size in x-y directions: 1 μm.

5.3.5 Imaging of Collagen IV Matrix with Blank Particles

Imaging of collagen IV matrix with newly built confocal set-up providing 325-nm excitation revealed two important points for future tissue phantom design. First, semi-solid collagen gel emitted bright fluorescence under 325-nm laser light excitation. This observation signifies the formation of the collagen-specific lysine-derived cross-links within the protein molecules, which resulted in the fluorescence of the gel at wavelength above 345 nm. Fluorescence of aromatic amino acids is expected to have a very minor contribution to the final signal, because of the long excitation wavelength used in our imaging. Second, the ability of the system to resolve the non-fluorescent 10-μm silica particles embedded in the fluorescent collagen gel was clearly demonstrated (Figure 5.9). Both of these observations indicate the suitability of the collagen gel, prepared though the acid-dissolution method, for the tissue phantom matrix that would simulate the extracellular fluorescence of the tissues.

5.4. Conclusions

Uniform 10-μm silica beads serve as perfect imaging objects for testing optical biopsy methods, providing features of known dimensions and shapes. We have developed and described the procedure for loading hydrophobic nanoporous silica particles with an endogenous fluorescent molecule. Suggested protocol is simple and gentle enough, so that biological molecules retain their ability to fluoresce and at the same time remain inside the hydrophobic pores of the silica gel, even when the particles are placed into the aqueous medium of agar gel. Though the uniform distribution of hydrophobic fluorescent domains within the hydrophilic phantom matrix presents some technical challenges, the possibility of surfactant-assisted dispersion is being explored in our group and will be discussed in the following chapter. Another area of future work is the combination of all three major tissue fluorophores used in cancer diagnosis (collagen, NADH and FAD) in one tissue phantom and spectrally-resolved imaging of such system. Successful imaging of the collagen gel with 325-nm excitation was demonstrated already and imaging of the NADH-loaded particles with the same optical system has been achieved in preliminary studies. The designed phantoms are model systems for the analysis of the effects of tissue optical properties, physiological fluorophore compositions, and the optical geometry on diagnostic imaging. Understanding of the microscopic origins of the observed spectral signatures could promote the development of new methodologies for spectral acquisition and analysis, and enhance the effectiveness of the diagnostic protocols.

CHAPTER 6 SURFACTANT-ASSISTED WETTING OF HYDROPHOBIC NANOPOROUS SILICA. ELECTROSTATIC EFFECTS IN THE DISTRIBUTION OF FLUORESCENT PROBES IN THE PARTICLE-SURFACTANT SYSTEM

6.1 Introduction

6.1.1 Nanoporous Silica

The International Union of Pure and Applied Chemistry (IUPAC) classifies nanoporous materials by pore size into microporous, mesoporous, and macroporous types, with pore sizes < 2 nm, 2-50 nm, and > 50 nm, respectively [142]. There are many kinds of nanoporous materials such as silica, alumina, carbon nanotubes, zirconia, and zeolites [143]. Due to their unique structures and attractive properties, nanoporous materials have found applications in many fields, including chemistry, biology, medicine, and environmental sciences. Firstly, their porous structures result in a high surface-area-to-volume ratio, which in turn provides a large number of interaction sites highly desirable in such areas as chemical catalysis [144], and environmental sensing, cleanup, and remediation [145]. Secondly, this large surface area can be modified with functional groups, which will alter the surface properties and cause specific interactions with the target molecules. A perfect example of function-targeted nanoporous surface modification can be found in the area of chromatography [146,147]. Thirdly, the nanoporous particles can function as delivery vehicles with volumes in the femto- and attoliter range, which can be applied in drug and contrast agent delivery [136-138,148].

In addition to the structural advantages outlined above, mesoporous silica materials possess high mechanical rigidity, chemical robustness, and biocompatibility combined with comparatively simple and inexpensive manufacturing methodology [137], which contributed to their popularity in many areas of science. Mesoporous silica particles, silica nanotubes, hollow mesoporous spheres, and silicate films have been featured as solid supports in analytical and materials science, particularly in the areas of chromatography [149,150], heterogeneous catalysis [143], chemical sensing [151], and biomedical delivery [137,152-154]. Since spherical silica particles are the most commonly used column packing material in high performance liquid chromatography (HPLC), their synthesis and surface derivatization has been extensively studied and optimized. A wide range of particle sizes with different pore diameters and narrow polydispersity are available commercially.

Many chemical and biological applications of nanoporous silica particles require hydrophobic modification of the particle and its pore surface. The hydrophobically-derivatized particles have been used as the pseudostationary phase in chemical separations, especially at the nanometer dimensions [149]. They provide well-defined spectral domains in tissue phantoms that can be used for the development of noninvasive methods for cancer detection [155]. A challenge in their applications is the incompatibility of the hydrophobic surface of the particles with the aqueous environment these applications are carried out in. In this study, we proposed the use of surfactant to effectively solubilize hydrophobic C18 silica particles in aqueous solution.

6.1.2 Hydrophobic Interactions

The significance of hydrophobicity in molecular organization was first recognized more than 70 years ago [156]. Hydrophobic interactions provide the driving force for the self-assembly of micelles, vesicles, and lipid bilayers, for interactions between biomacromolecules, and for protein folding. Surface active agents, or surfactants, are amphipathic molecules possessing both hydrophobic and hydrophilic portions. When dissolved in aqueous solution, it is energetically favorable for the surfactant to migrate to any available hydrophobic interface and orient itself with its hydrophobic portion toward the interface and its hydrophilic portion exposed to the aqueous solution [157,158]. In cases where the concentration of surfactant in the solution is high enough, e.g., beyond the critical micellar concentration (cmc), surfactant molecules aggregate to form micelles and thus reduce the exposure of their lyophilic portions to the aqueous solution. Clearly, when a surfactant solution with a concentration higher than the cmc is brought in contact with a hydrophobic surface, the extent of surfactant adsorption on this surface will be governed by the competition between the thermodynamic benefits of the hydrophobic interactions with the surface versus micellar organization. Other factors, such as electrostatic interactions between the surfactant and the surface, hydrogen bonding, temperature, and the properties of the bulk fluid phase will also contribute to the adsorption equilibrium [157,159].

According to the proposed hypothesis, upon addition of the surfactant solution to the C18 silica gel, the hydrophobic force causes self-organization of the nonpolar surfactant tails toward the carbon chains on the surface of the particles, rendering polar surfactant heads exposed to the solution as shown in Figure 6.1. Oriented in this way, a layer of surfactant molecules acts as a hydrophilic “coat” covering the outer surfaces of the particles and effectively solubilizing them in the aqueous solution. Constructs, formed by the interaction between C18-modified nanoporous silica particles and surfactant, were investigated with fluorescence spectroscopy and confocal imaging. To answer the question if the surfactant migrates into the pores of the particles and carries aqueous solution with it, fluorescent probes, rhodamine 6G and fluorescein, were added to the solution to monitor the wetting process. R6G and fluorescein have remarkably high photostability [160], quantum yield close to unity, and fluorescence emission peak in the aqueous solution of 50 mM SDS at 553 nm and 512 nm, respectively (Figure 6.2).

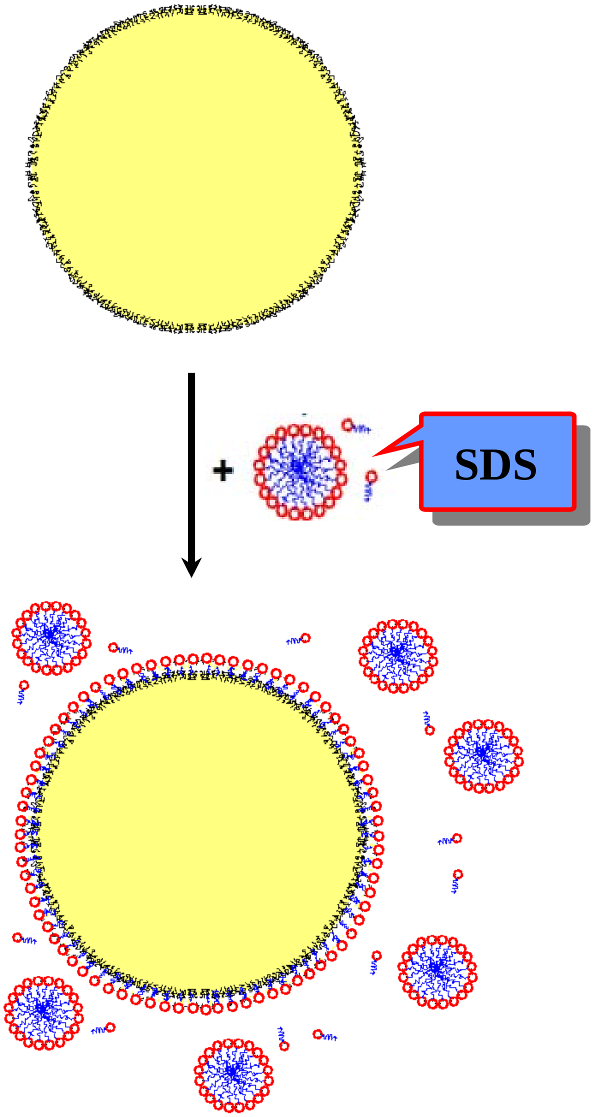

Figure 6.1. Schematic representation of the SDS surfactant interaction with a C18-derivatized silica particle. Silica bead is shown in cross-section and nanoporous network is not depicted for clarity of presentation. Surfactant molecules, micelles and C18 chains are enlarged to communicate the concept.

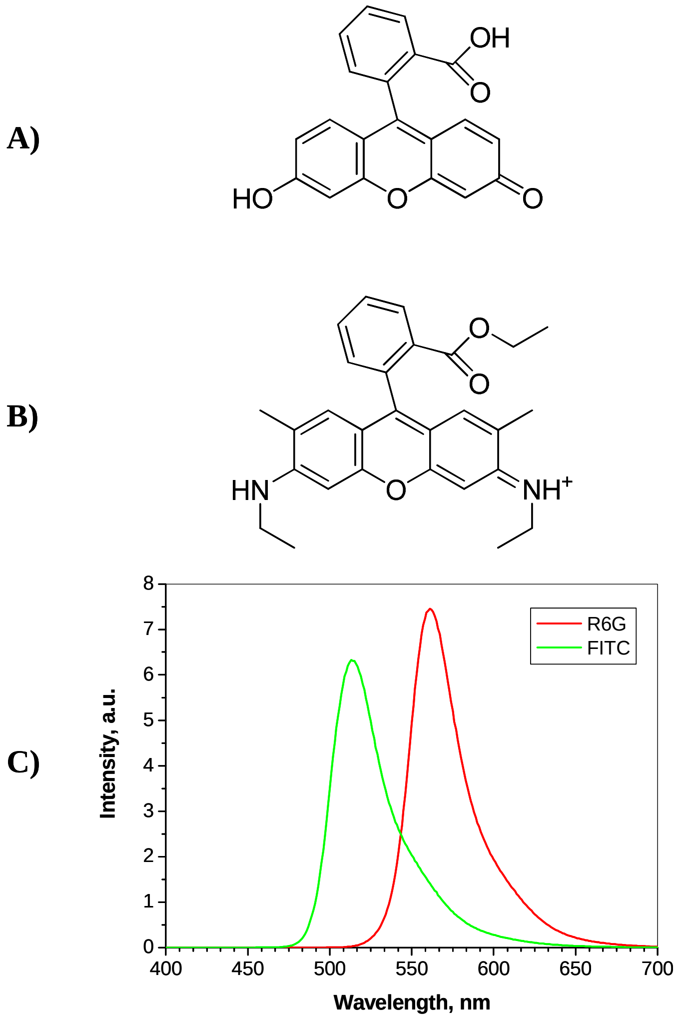

Figure 6.2. Fluorescent probes used for imaging. (A) Chemical structure of Fluorescein (FITC); (B) chemical structure of Rhodamine 6G (R6G); (C) original fluorescence emission spectra of the fluorescent probes. Spectra obtained using 10 μM solutions in 50 mM aqueous SDS.

The focus of this work was to investigate the interaction between the hydrophobically modified nanoporous particles and surfactants in aqueous solution. To understand and visualize the structure of the particle-surfactant system, water-soluble fluorescent probes were used to trace the interactions observed by confocal fluorescence imaging.

Confocal microscopy provides superior resolution and the capability of real-time optical sectioning, which allowed us to image the process of surfactant-assisted wetting inside the nanoporous core of the hydrophobic silica gel. To evaluate the influence of electrostatic effects on the silica-surfactant-dye system formation we employed positively charged (rhodamine 6G) and negatively charged (fluorescein) fluorescent probes.

6.2 Experimental

6.2.1 Chemicals and Materials

Nanoporous silica particles used in this study had a nominal diameter of 10 µm, an average pore size of 100 Å and a surface area of 400 m^2/g. Both the outer surface and the pore surface of the particles were covered with a monolayer of C18 chains. The particles were obtained from Phenomenex (Torrance, CA) and used in all experiments without any pre-treatment. Precise specifications of the Luna® C18 particles batch used in this study can be found in Table 5.1. Sodium dodecyl sulfate (SDS), a surfactant with negatively charged sulfate head group and a nonpolar tail of twelve carbons, was obtained from Fisher Scientific (Pittsburgh, PA). In all experiments the concentration of SDS in the solution was kept at 50 mM, well beyond the critical micellar concentration (8.2 mM), to ensure that a sufficient amount of surfactant was available for the coverage of the total surface area of the silica particles (detailed calculations are included in Chapter 7).

All solutions were prepared using deionized water purified with a MilliQ system (MilliQ-Plus, Millipore, Bedford, MA). Fluorescent dyes rhodamine 6G (R6G) and fluorescein (FITC) were purchased from Sigma-Aldrich (Milwaukee, WI). Stock solutions of fluorescent probes were prepared in HPLC grade ethanol. An aliquot of the stock solution was introduced into the sample vial and the solvent was evaporated by nitrogen flow. The fluorescent probe was then resuspended in 50 mM aqueous SDS solution or deionized water for the resulting 10 µM concentration. Polyimide-coated capillaries (50-µm i.d. and 360-µm o.d.) and quartz cells (400-µm i.d. and 550-µm o.d.), used in the micro-column preparation, were acquired from Polymicro Technologies (Phoenix, AZ).

6.2.2 Instrumentation and Measurement

Pore wetting and solution migration in the core of the hydrophobic particles as the particle-surfactant system is formed have been visualized with confocal fluorescence imaging. Experiments were conducted at the University of Iowa Central Microscopy Research Facility using an upright laser-scanning confocal microscope (Bio-Rad Radience 2100MP) fitted with a 60X oil lens. The schematic of the optical path is presented in Figure 6.3.

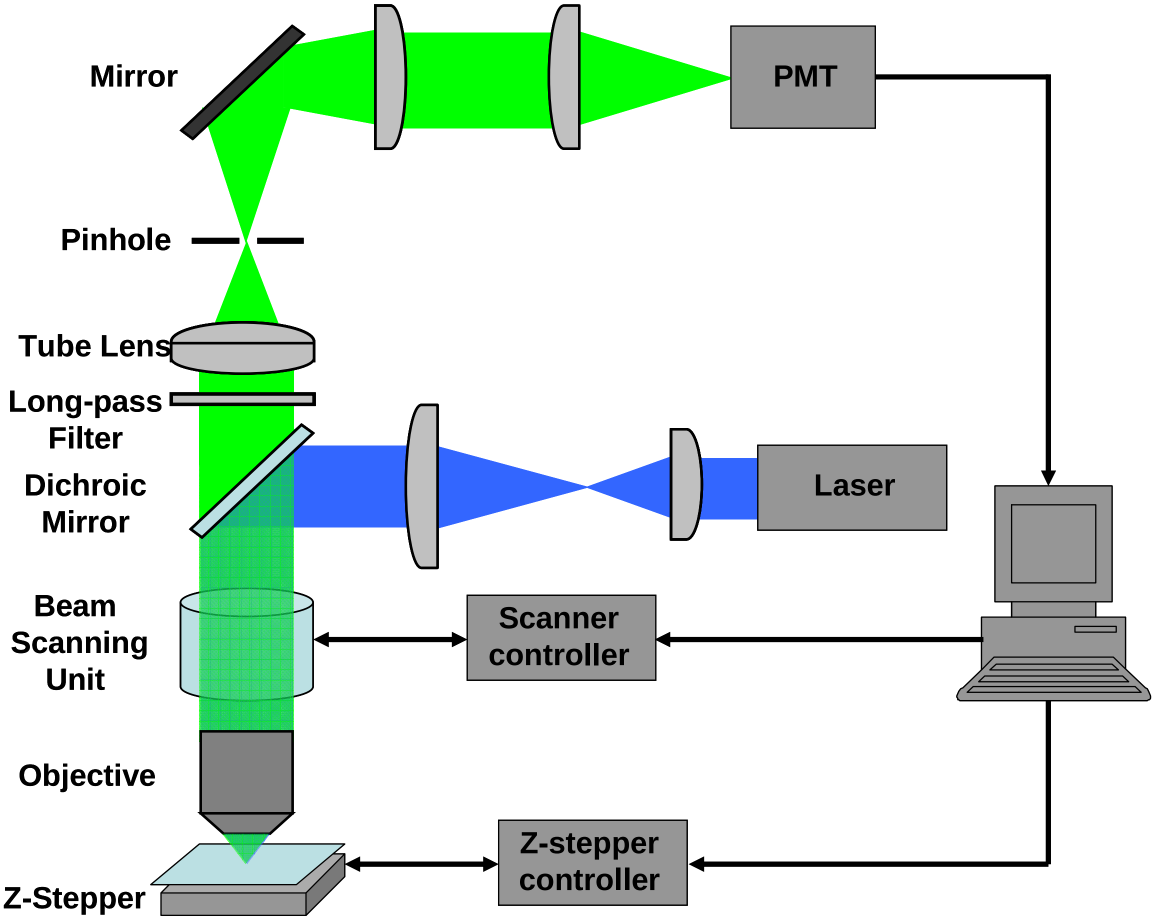

Figure 6.3. Schematic diagram of the confocal laser-scanning optical set up with single channel detection (PMT: photomultiplier tube).

Excitation was provided by an air-cooled argon laser. For the fluorescein and rhodamine 6G excitation 488 nm and 514.5 nm lines of the laser were used, respectively. The excitation light was reflected by a dichroic beam splitter and focused into the packed column by the microscope objective. The fluorescence emission was collected by the same objective and transmitted through the dichroic beam splitter. The dichroic mirror was selected automatically by the computer to match the requirements for the optimal excitation/emission separation. To minimize scattered excitation light that might have passed through the dichroic mirror, a long-pass filter was placed in the emission channel. For the imaging with R6G 530-nm long-pass filter was used, and with FITC - 500-nm long-pass filter was employed. A photomultiplier tube (PMT) was used for the fluorescence detection in both confocal and spectroscopic experiments. Obtained fluorescence intensity data were analyzed and plotted in ImageJ (Research Services Branch, NIH).

6.2.3 Imaging under Chromatographic Conditions

The images of C18 silica particles interacting with surfactant molecules were taken under both packed and unpacked conditions. The particles imaged under packed conditions were not pre-treated in any way. The procedure for micro-column preparation, described in detail previously [161], was adopted in this study with minor modifications. Schematic representation of the packed microcolumn is depicted in Figure 6.4. Commercially available Luna® C18 silica gel was packed into a short quartz column, 400-μm i.d. The particles were held inside the quartz cell by two polyimide-coated capillaries (360-μm o.d.) with fritted ends. The frit at one end of each capillary was prepared by sintering C18 silica particles wetted with ethanol. The fritted end of one capillary was then inserted into the quartz cell and glued to the inner wall of the cell by a nonfluorescent adhesive from Norland Products Inc. (New

Brunswick, NJ). C18 silica particles were packed into the quartz cell using a vacuum pump before the second fritted capillary was glued to the other end of the quartz cell. The packed column was then glued to a microscope slide; the zone selected for imaging was submerged in the immersion oil and covered with a cover slip. Solutions were pumped through the column using a syringe pump (Model: 341, Sage Instruments).

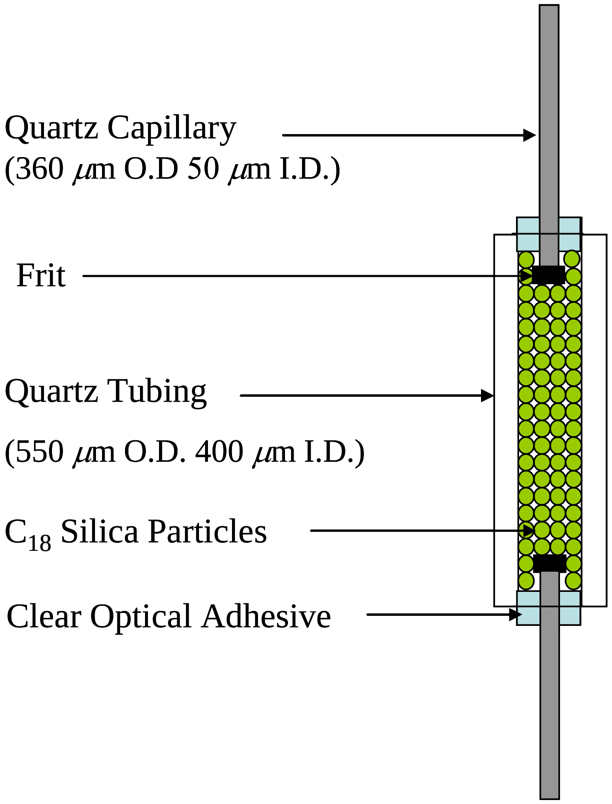

Figure 6.4. Schematic diagram of packed C18 silica gel column. Adapted from [161].

6.2.4 “Vortexing” Procedure and Imaging under Unpacked Conditions

Imaging of unpacked silica particles was done on the sample subjected to the “vortexing procedure” [162,163]. The rational for employing the “vortexing procedure” was to create particles that would retain hydrophobicity on the inside while becoming hydrophilic on the surface due to the created surfactant shell. Such particles would be able to disperse in the aqueous solution, but at the same time would retain unwetted core that would contain a target molecule. As shown in Figure 6.5, the “vortexing procedure” incorporated vigorous vortexing of the C18 particles in 50 mM SDS solution for 19 hours, followed by 24-hour rest in ambient conditions [164]. Particles prepared in this fashion separated into three fractions, dubbed as “bottom”, “middle” and “top”. A sample vial with three fractions is shown in Figure 6.6. The “bottom” fraction was composed of the particles that “precipitated” to the bottom of the vial, the “middle” fraction represented particles dispersed in the solution and the “top” fraction was formed by very stable “foam” containing the majority of particles. These three fractions were carefully separated using pipettes and cotton swabs, so as to minimize their cross-contamination, stained with 10 µM R6G solution and then imaged individually.

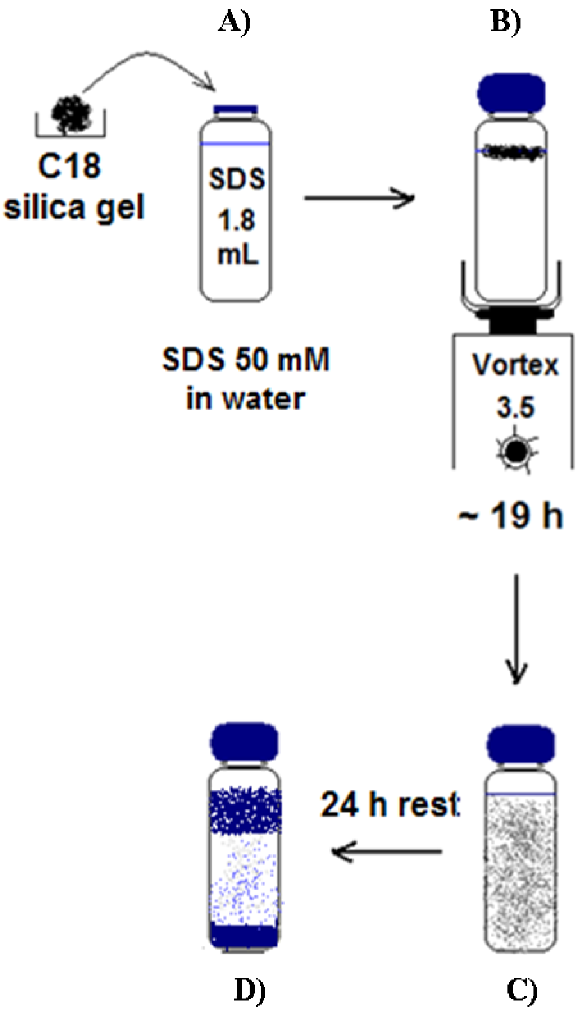

Figure 6.5. Preparation steps of the “vortexing” procedure: (A) addition of weighed C18 silica particles to the SDS solution; (B) vigorous vortexing of the sample vial; (C) solution with evenly dispersed particles; (D) a vial with three distinct fractions of particles formed during the 24-hour rest period. Adapted from [164].

For the imaging, 20 μL of suspension consisting of silica particles, surfactant, and R6G were deposited onto the surface of a 2-inX4-in microscope slide. A coverslip of the matching size was placed immediately on top of the solution. The use of extra large slides and coverslips ensured a slower evaporation rate. To obtain 3D images of the particles from the “top” fraction we intentionally allowed the sample to dry, which effectively immobilized the particles on the surface of the microscope slide. Z-sections of the sample were obtained using a vertical stepper and laser-scanning of each optical plane in x-y direction.

Figure 6.6. Photograph of a sample that was subjected to the “vortexing procedure”. Three distinct fractions of silica C18 particles in SDS solution are clearly distinguishable. Image was adapted from [163].

6.3 Results and Discussion

6.3.1 Observation of Surfactant-Induced Wetting of Hydrophobic Nanopores

This work offers structural understanding of surfactant-induced pore wetting and solubilization of hydrophobic nanoporous particles in aqueous solution. In the preliminary studies on tissue phantom preparation, we have established that the addition of surfactant to the aqueous solution will cause solubilization of the hydrophobic particles [155]. Nevertheless, the question of pore-wetting remained unresolved. Will the surfactant molecules penetrate into the nanopores of the particles and cause wetting of the particles' core? To answer this question, a 50 mM SDS solution containing 10 µM R6G probe was pumped through the column packed with C18-particles. Confocal fluorescence images of the packing were collected over time to follow the interaction between the SDS solution and the particles. At first, as the solution was introduced into the column, the particles appeared as bright loops as shown in Figure 6.7A. Apparently, surfactant molecules interact with the outer hydrophobic surface of the particles with the nonpolar tails, forming C18-C12 construct. Rhodamine 6G, which has octanol/water partition coefficient of 2.69 [165], preferentially partitions into this construct, which causes high fluorescence intensity signal from the outer surface of the particles.

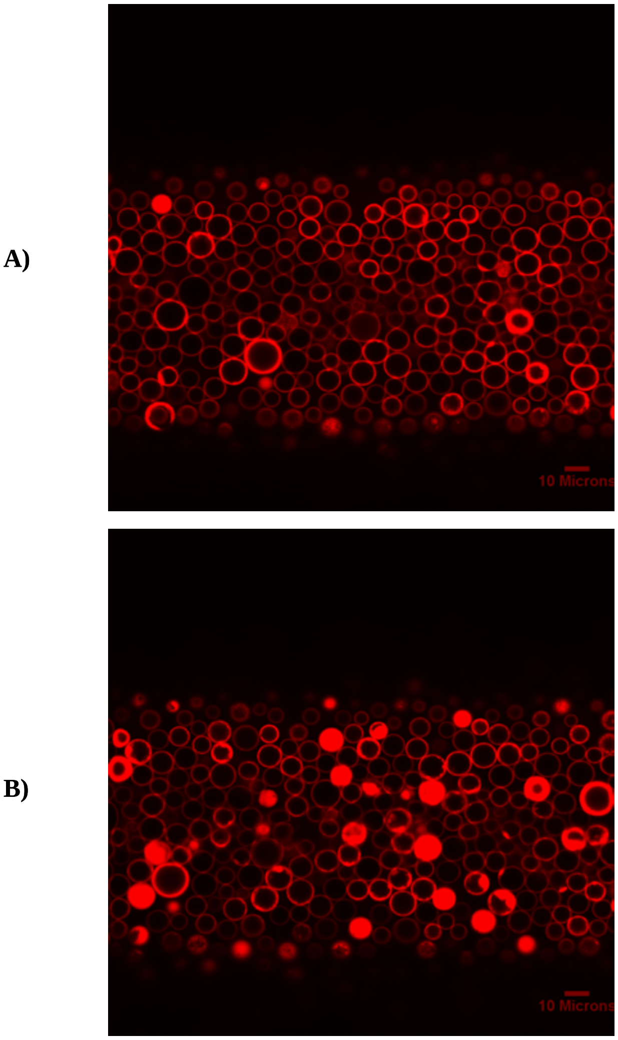

Figure 6.7. Confocal fluorescence images of a column packed with C18 particles. A 10-μM R6G in 50 mM SDS solution was pumped through the column. (A) Start time (t = 0); (B) t = 2.5 minutes. Excitation wavelength: 514 nm.

The large partition coefficient results in a high contrast in the confocal images, with bright loops formed by the C18-C12 construct on the particle surface and low fluorescence intensity from the solution. The formation of this C18-C12 construct occurs rather quickly, within the collection time of the first image. As more solution was pumped through the column, we observed gradual filling of the particles with the fluorophore (Figure 6.7B). The loops become thicker as the solution migrates into the core of the particles radially. In the wetting process, we hypothesize that SDS surfactant molecules move into the pores to form a C18-C12 construct on the wall surface of the nanopores, rendering the pore surface hydrophilic by lining the wall with the charged head groups. This newly created surface induces nanopore wetting by the aqueous solution. After 2.5 minutes of solution pumping, some particles are completely wetted (Figure 6.7B), while others are at different stages of wetting. The fluorescence intensity of the filled particles becomes brighter as solution pumping provides more probe molecules to reach high concentration inside the hydrophobic region as dictated by the partition coefficient.

In the processes of pore wetting, we observed the differences between the particles and heterogeneities within each individual silica particle. The wetting rates differed significantly from particle to particle. Clearly, some particles were filled earlier than others, some were filled only partially, some, though very few, were not filled at all – the latter represent a small fraction of particles that have solid nonporous core. It has been estimated that less than 2% of studied C18 silica particles have this type of “nonporous core” structure [161]. Due to the presence of heterogeneities in the C18 coverage of the particles [141] some of the particles were filled from the side opposite to the solution flow. This is consistent with our earlier observation of heterogeneity in nanopore wetting with mixed solvents of acetonitrile and water [141]. It is anticipated that, unlike mixed solvents, SDS-induced wetting of nanopores will show a pore size effect due to the finite size of the surfactant molecules that will determine the dimension of the structure that the surfactant molecule forms on the pore surface. This point is currently under investigation.

In previous experiments, we have observed the migration of hydrophobic fluorescent probe Nile red into nanopores without pore wetting [141]. In this case, the C18 monolayer on the wall surface of the nanopores acts as a pseudo-liquid phase to solubilize Nile Red molecules and allow them to diffuse into the cores of the particles without solvent wetting. To rule out the possibility of R6G migration into the core of the particles through the pseudo-liquid C18 phase, a control experiment without surfactant was performed. In this experiment a 10 μM R6G solution in water was pumped through a C18-particle-packed column. In the images obtained in this experiment, particles appeared as dark circles surrounded by the bright background (Figure 6.8). As the solution was pumped through the column over time, none of the beads was filled with the fluorophore. Clearly, the fluorescent probe's penetration inside the pores depends on the wetting of the particles' interior surface. This observation proves the critical role of surfactant in the pore wetting process.

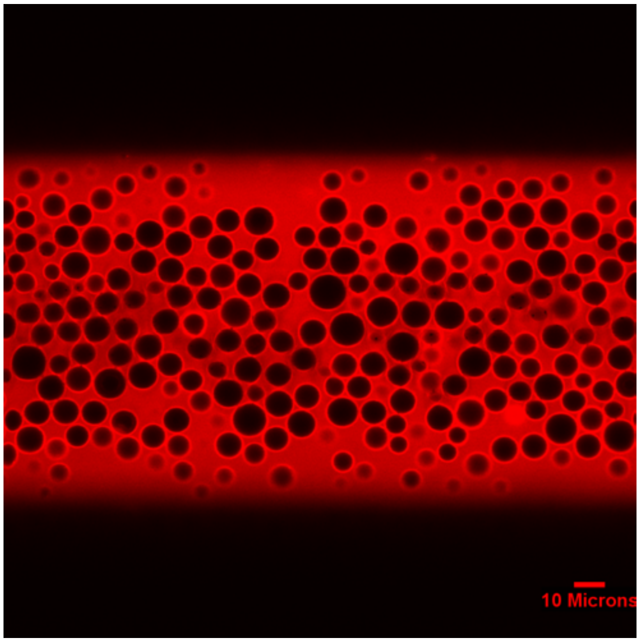

Figure 6.8. Control experiment: 10 μM R6G dissolved in deionized water pumped through the C18-silica-gel-packed column, no surfactant present. Excitation wavelength: 514 nm.

Detailed analysis of the images obtained in the control experiment, in which solution of R6G in water was pumped through the column, further demonstrates that the pores remain unwetted (Figure 6.9A). The aqueous medium surrounding the particles display a reasonable fluorescence intensity determined by the R6G concentration in the solution. The core of the particle shows much lower and flat intensity signal, corresponding to background scattering. Interestingly, we observed the presence of bright loops around the dark particles (Figure 6.9A). This feature signifies partitioning of R6G in the C18 phase on the outer surface of the particles, which is in agreement with reported high

1-octanol-water partition coefficient of R6G [165]. Gaussian fit of the intensity profile of the loops yielded a loop thickness of 470 nm to 695 nm, consistent with the spatial resolution of our confocal imaging, illustrating that R6G partitions only into the C18 layer on the outer surface of the particles.

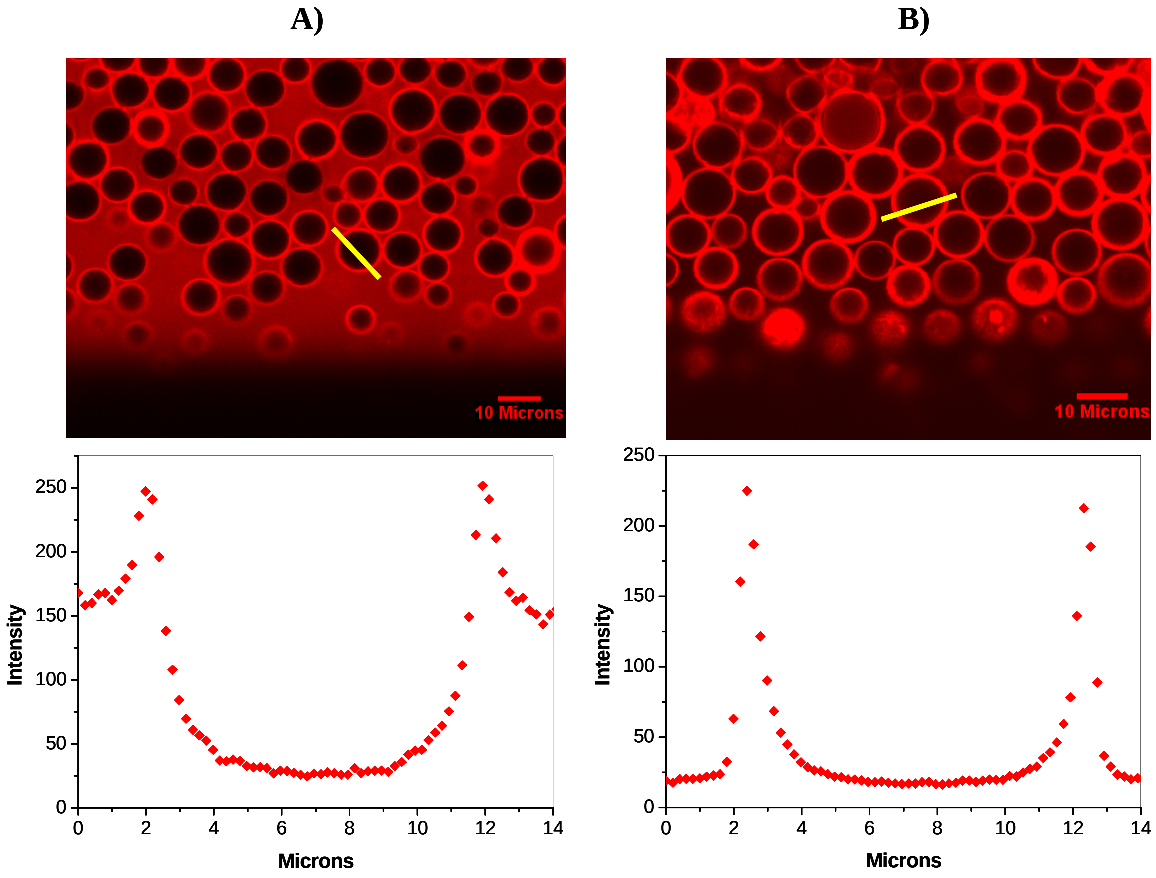

Figure 6.9. C18-silica particles in (A) 10 µM R6G in water, no surfactant present; and (B) 10 µM R6G in 50 mM SDS solution. Upper panels: images of the packed columns. Lower panels: intensity cross sections through the particles along the yellow lines in the upper panels. Excitation wavelength: 514 nm.

In pure water, the bright rims were clearly distinguishable from the bulk solution surrounding the particles, but a remarkable observation is that the intensity difference between the rims and the solution was much smaller than when SDS was present in the system. In case when fluorophore was introduced in the column in the pure water the intensity of the rims was 40% higher than the intensity of the bulk solution. When SDS surfactant was present, before the particles were wetted, the rims around the particles were 8 to 10 times brighter than the solution around (Figure 6.9B). This means that R6G preferentially partitions in the C18 phase when the surfactant is present. As SDS forms construct with C18 on the surface of the particles, partitioning of R6G in this construct is enhanced by the electrostatic interaction between the negatively charged sulfate groups of SDS and positively charged amine groups of the dye. This conclusion was further proven by imaging the system with a negatively charged dye, FITC.

6.3.2 Effects of Hydrophobic and Electrostatic Interactions in the Surfactant-Probe-C18 System; Imaging with Negatively Charged Fluorescent Probe

To explore the significance of electrostatic interaction on our investigation of nanopore wetting, a negatively charged dye, FITC, was used as a probe. When FITC was introduced into the column in aqueous solution the distribution of the dye between the bulk solution and C18 phase on the surface of the particles was very similar to R6G distribution. We observed bright rims around the particles as organic dye FITC partitioned into the C18 layer as shown in Figure 6.10A. These rims, just as in the case of R6G, are about 40% brighter than the bulk solution around the silica gel. In this case, the partitioning of the probe is mainly determined by the hydrophobic interactions between the hydrophobic moiety of the probe molecule and the C18 layer.

When SDS surfactant was added to the system, FITC behavior differentiated from R6G drastically (Figure 6.10B). First, the intensity of the bulk solution stayed very similar to the intensity of the FITC solution without SDS. In addition, bright rims around the particles were no longer prominent. As hydrophobic particles were filled with the solution with the aid of surfactant, FITC was brought inside the particles along with the aqueous phase, but intensity of the fluorophore detected inside the particles was about 20% lower than the intensity of the bulk solution (Figure 6.10B).

Clearly, negatively charged fluorescein did not exhibit preferential partitioning in the C18-SDS construct like did R6G. As the process of particle wetting progressed, fluorescence intensity in some wetted particles reached the level of the bulk solution (Figure 6.11 - panels b and c), but in all of them we observed a rim of 1.5-2 μm which maintained 20-25% lower intensity than the bulk solution. We suspect that electrostatic repulsion between the negatively charged FITC and the monolayer of sulfate head groups of SDS caused relatively low concentration of FITC on the surface of the particles. To fully explain this phenomenon and comment on the difference in the surfactant distribution inside the hydrophobic pores and on the surface of the particles further experiments should be conducted.

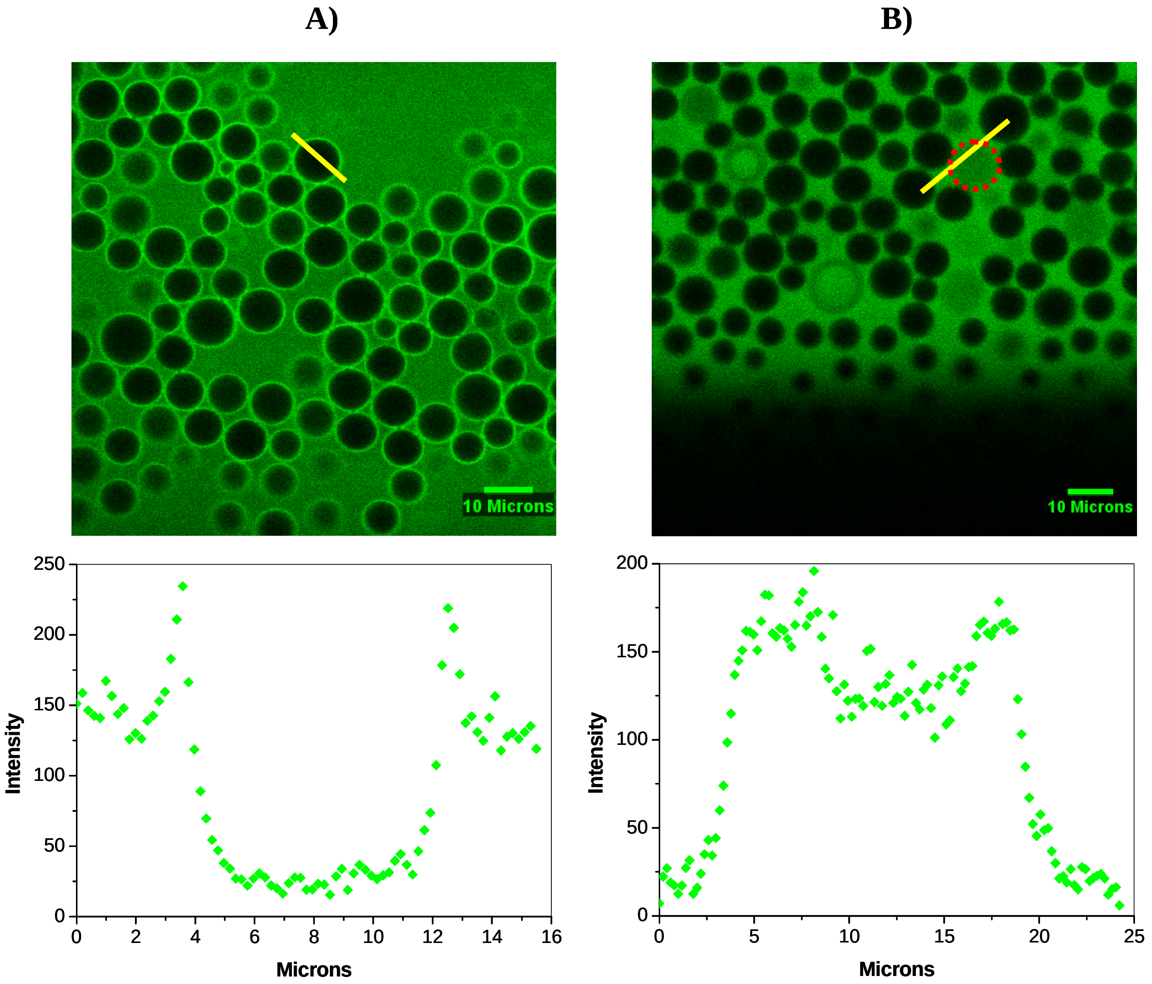

Figure 6.10. C18-silica particles in (A) 10 μM FITC in water, no surfactant present; and (B) 10 μM FITC in 50 mM SDS solution. Upper panels: images of the packed columns. Lower panels: intensity cross sections through the particles along the yellow lines in the upper panels. Excitation wavelength: 488 nm.

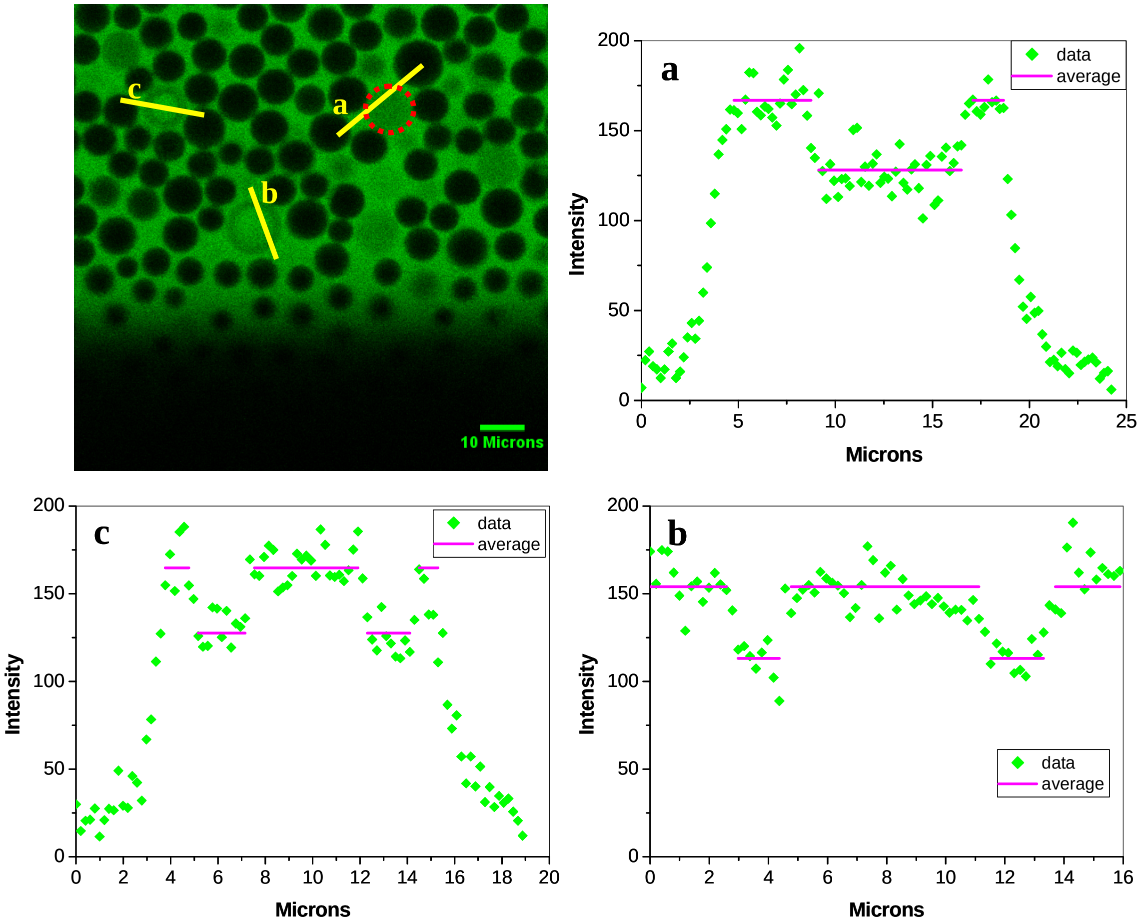

Figure 6.11. Representative cross-sections through the C18 silica particles wetted with 10 μM FITC in 50 mM aqueous SDS solution. Intensity cross-sections correspond to the yellow lines in the image and are labeled accordingly. Magenta lines in the cross-section plots show calculated average fluorescence signal for the particular areas. Excitation wavelength: 488 nm.

6.3.3 Revealing the Nature of “Vortexed” Sample Fractions through Fluorescence Confocal Microscopy

Analyzing the three fractions obtained through the “vortexing procedure” we have to acknowledge that it was impossible to achieve their ideal separation from one another, so we should pay attention to the statistical majority of the particles present in each fraction rather than individual particles. Another interesting aspect of imaging these samples lies in the fact that the glass slide and the cover slip were not pressed tightly enough to generate a gap of ~ 10 μm – the dimension of a silica particle. Thus, the particles trapped between the glass slide and the coverslip were not pressed into a monolayer, but were freely floating in the solution volume with depth of about 20 μm. Imaging the "bottom" fraction in z-direction, starting from the coverslip and moving down to the glass slide, we observed that even within this small volume the particles distributed into layers according to their average density due to the gravitational force. The particles that were not filled with the solution and still contained air in their pores stayed in the upper layer of the imaged volume, close to the coverslip. As we moved down into the sample, we observed more and more partially and completely filled particles. Finally, on the surface of the slide the absolute majority of particles appeared as bright filled circles (Figure 6.82A), which indicated that their pores were wetted. The average density of the wetted particles is higher than the density of the aqueous solution, so they "sink", which is observed on both macro (in the vial) and micro (between the glass slides) scale.

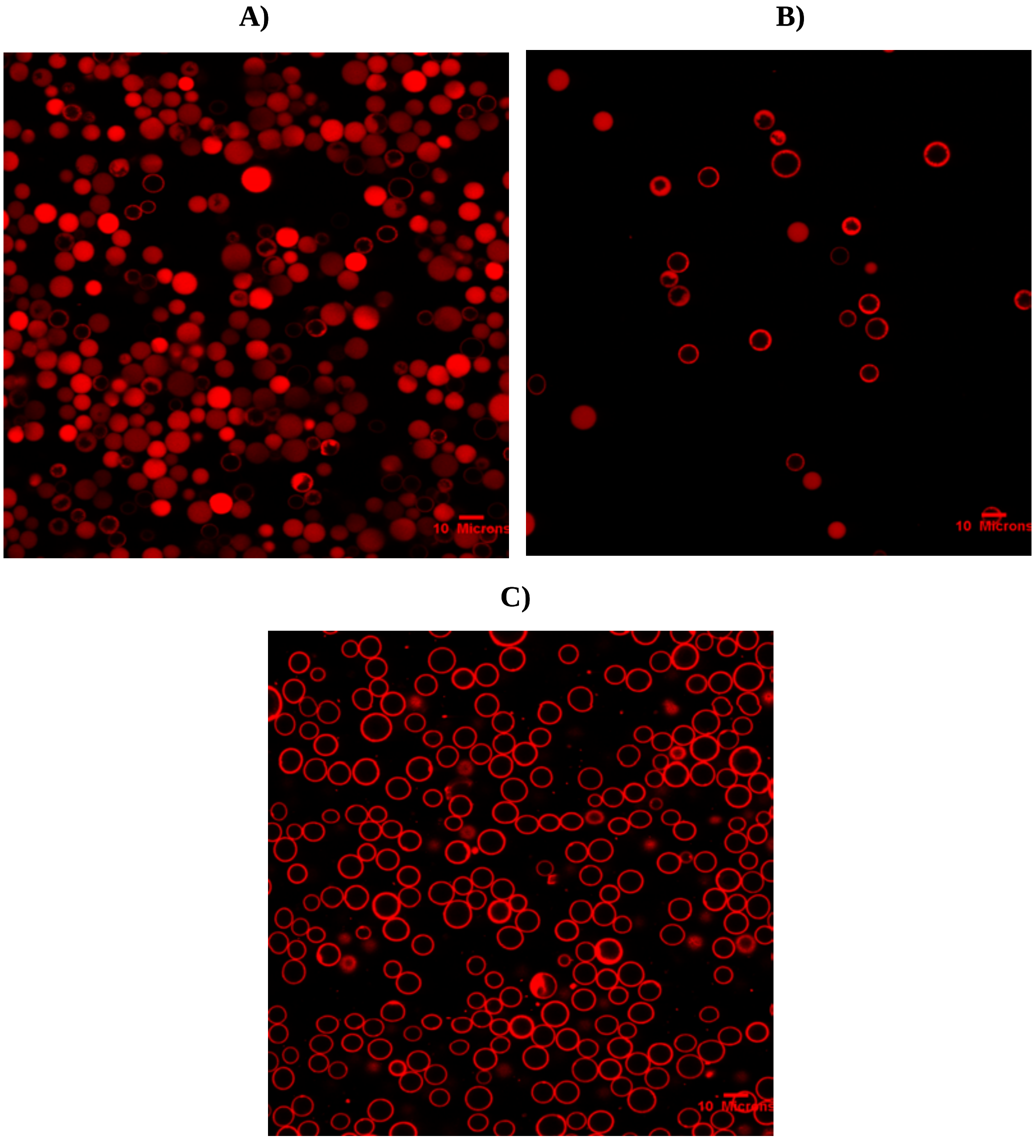

Figure 6.12. Three separate fractions of the vortexed sample: (A) “bottom” fraction, particles are filled with R6G solution; (B) “middle” fraction, partially filled particles with expected contamination from two other fractions; (C) “top” fraction, particles that dry and hydrophobic inside carry hydrophilic shells of surfactant on the exterior surface; R6G partitioned into the C18-SDS construct. Excitation wavelength: 514 nm.

A)

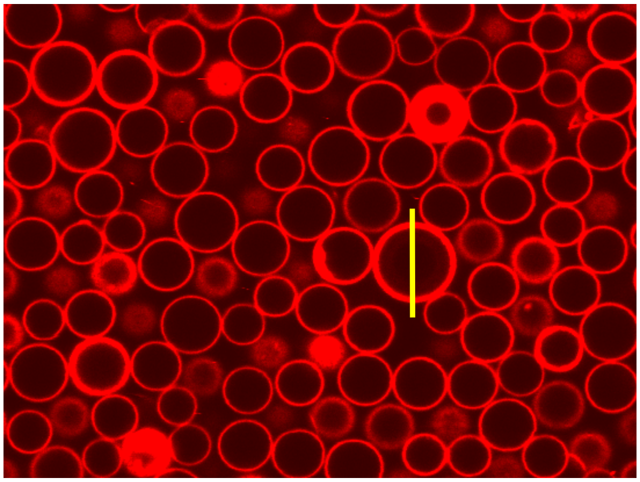

B)

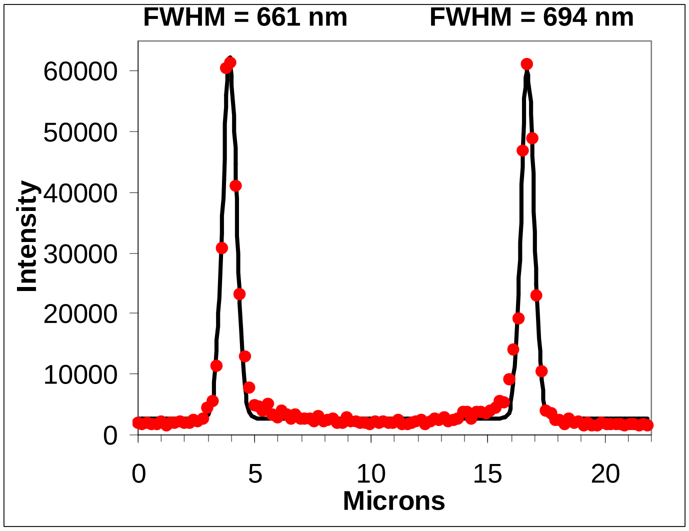

Figure 6.13. Analysis of the "top fraction". (A) Confocal image of C18 particles stained with 10 μM R6G. (B) Double-peak Gaussian curve fitting of the particle intensity profile corresponding to the section along the yellow line in panel (A). Excitation wavelength: 514 nm.

The "middle" fraction of the sample contained comparatively small fraction of the particles, its image can be seen in Figure 6.12B. This observation is quite expected, because for the particle to be suspended in the 50 mM SDS solution its density should closely match the density of the solution. This means that the majority of the particles in this fraction should be partially filled with air and partially with the solution. We suppose that the particles that were not internally wetted during the "vortexing procedure" had their pores clogged by microbubbles that were formed in the process of vigorous vortexing. Since the porous channels in the particles present an interconnected network of channels, it is reasonable to suggest that if at least some pores were not clogged with the bubbles the particle would have been completely wetted unless it possessed some internal obstacles in the pore meshwork. We know that only a few percent of the total particle population have solid nonporous core [161], thus only a small portion of particles should be present in the "middle" fraction of the sample.

Earlier described "vortexing procedure" is amazingly efficient in retaining the internal hydrophobicity in the majority of the particles, which formed the "top" fraction of the sample (Figure 6.12C). These particles obtained a shell of surfactant molecules on their surface, with polar surfactant head groups extended into the solution, which allowed these particles to freely solubilize in aqueous solution upon agitation. At the same time, they retained the air inside the pores, thus, due to their density being lower than the density of the solution, they floated to the surface of the sample and formed a layer of highly stable "foam" when left at rest. Utilizing this procedure C18-derivitized particles, pre-loaded with biological fluorophores, can be easily incorporated in the water-based tissue phantoms and serve as localized spectral domains for the development and evaluation of noninvasive diagnostic methods.

Majority of the particles composing the “top” fraction of the sample appeared as bright loops or shells, which was confirmed as the sample was allowed to dry on the slide (Figure 6.93A) and optical sections in axial direction were obtained. Fitting of a dry-bead cross-section intensity profile with Gaussian curve is shown in Figure 6.13B. It convinces us that there was a monolayer of the fluorophore molecules that formed this bright shell. The conclusion is based on the fact that the 650-700 nm Full–Width-at-Half-Maximum (FWHM) of the fitted Gaussian curves is close to the optical resolution of the confocal instrument with 514.5 nm excitation.

6.4. Conclusions

The interaction and wetting of the C18 modified stationary phase with surfactant solution was probed with confocal imaging using two fluorescent probe molecules. It is noteworthy to remark that the understanding of the polarity trends and the mechanisms of surfactant interaction with C18 silica particles creates opportunities for using such hydrophobic particles as drug delivery vehicles and in tissue phantoms.

Uniform silica particles 10 μm in diameter serve as perfect imaging objects for testing optical methods for cancer imaging. Pre-loading these particles with biological fluorophores, restoring their hydrophobicity and then dispersing them in the aqueous solution or gel using surfactants creates spectroscopic domains with controlled and well-defined boundaries. As can be clearly seen from our experiments, direct addition of surfactant in aqueous solution to the hydrophobic nanoporous particles causes rapid wetting of the particles' cores and would not allow the retention of any water-soluble load inside the particles. Fortunately, addition of a simple vortexing step in the preparation procedure allows decoration of the external surface of all particles with a hydrophilic "coat" of the surfactant while rendering the majority of particles dry and hydrophobic on the inside. Such spherical particles, pre-loaded with biological fluorophores and decorated with surfactant shell, will become a key feature of novel tissue phantoms that can be used for testing the methods of non-invasive cancer diagnosis.

On the other hand, the observation of particle "loading" with the water-soluble fluorophore in the presence of surfactant molecules provides an insight in the possibility of using this methodology for the preparation of drug delivery vehicles. It was demonstrated in literature that the affinity between the loaded guest molecules and the surfaces of the mesoporous material can have a significant effect on both the loading and release kinetics [166-168]. Adjustment of the surface properties in nanoporous materials with surfactant molecules can provide a new route for boosting the system's drug delivery potential. As we could see, when the charge of the surfactant is opposite to the charge of the fluorescent load molecule, electrostatic effects enhance partitioning of the probe into the hydrophobic particles wetted with surfactant solution. This observation should prompt further exploration in the area of surfactant-target matching in drug delivery systems based on solid particles as well as multi-component liposomes.

CHAPTER 7 SPECTROSCOPY AND RATIOMETRIC IMAGING OF WETTING DYNAMICS AND NANOTRANSPORT IN HYDROPHOBIC NANOPORES

7.1 Introduction

7.1.1 Micelle-mediated Drug Delivery

Targeted controlled drug delivery, i.e. directly supplying a therapeutic agent to the affected organ or tissue in desired amount, is an active area of research striving to achieve selectively high drug concentration at the target sites with no adverse effects on the normal tissue, improving administration methods and efficacy of the treatment [169]. Micelle-mediated transport of drugs through nanopores is of interest in controlled-release applications [170-172]. Micelles can significantly increase solubility of compounds poorly soluble in aqueous solutions, but they are usually larger than the target solute. The enhancement in solubility and decrease in mobility [173], resulting from the larger size of micelles compared to the drug alone, are the basis for the technique of micelle-assisted controlled drug delivery [174].

Microreservoir-type systems, such as liposomes (mainly, for water-soluble drugs) and micelles (mainly for water-insoluble drugs) have a number of advantages over other drug delivery systems, including high drug loads, easily adjusted composition and size, and a small required quantity of the targeting component, because just a few targeting moieties can carry multiple drug moieties [169]. Micelles of tailored compositions can also improve the stability of the drug en route to the target tissue, while effectively reducing the toxicity to the nontarget organs. Due to their small sizes compared to other delivery vehicles, micelles exhibit spontaneous penetration into the intersitium of the body compartments with leaky vasculature (such as tumors) thus demonstrating a form of selective delivery termed “passive targeting” [169]. In cases when cell membranes are intact, the physicochemical aspects of micelle penetration through the cell nanopores remain to be addressed. To this end, applications of fluorescence imaging technology in the medical and pharmaceutical fields have demonstrated the capability for real-time quantitative measurements of the dynamic processes in the biological systems [175].

It was established in Chapter 6 that the hydrophobic nanopores of C18 silica gel could be wetted by an aqueous solution with the aid of a surfactant, such as SDS. In the imaging experiments described in this chapter, we explore the mechanism of micelle-induced wetting of the nanopores. Aspects we investigated include the possibility of intact SDS micelles migrating into the hydrophobic pores along with SDS monomers, the process of micelle intercalating into the C18 layer, and the structure formed by the SDS molecules and the C18 chains. A deciding factor of the wetting mechanism is the dimension of a micelle.

Calculation of the dimension of the SDS micelle, the pore size of the particles, and the thickness of the C18 layer have been established in our group [176] and will be briefly discussed here. To calculate the diameter of an SDS micelle we should consider its two structural components: an inner hydrophobic core formed by hydrocarbon chains and an outer hydrophilic shell formed by anionic sulfate head-groups (Figure 7.1A). Thus, the diameter of a micelle can be expressed as a sum of the hydrophobic core diameter (D_{core}) and diameters of two anionic head-groups ($D_{sulfate}$):

$$D_{micelle} = D_{core} + 2D_{sulfate} \qquad [7.1]$$

The volume of the hydrophobic core can be calculated from the volume occupied by the individual alkyl chains, which is according to Tanford [177]:

$$\upsilon_{chain} = 27.4 + 26.9n_C \qquad [7.2]$$

where n_C is the number of carbons in the hydrocarbon chain. Consequently, for a micelle with an aggregation number m, the volume of the core is obtained in Å^3 as:

$$V_{core} = \upsilon_{chain} m = (27.4 + 26.9n_C)m \qquad [7.3]$$

In the concentration range used in our experiments, the shape of the SDS micelle is spherical. Thus, the volume of the core can also be expressed as:

$$V_{core} = \frac{4}{3}\pi r_{core}^3 \qquad [7.4]$$

Therefore, the radius of the hydrophobic core is:

$$r_{core} = \sqrt[3]{\frac{3m(27.4 + 26.9n_C)}{4\pi}} \qquad [7.5]$$

According to this equation, for an SDS micelle with an aggregation number of 62, the core radius was 17.3 Å.

The diameter of the anionic head group can be estimated from the simulation data of a system containing 60 SDS monomers and 7579 water molecules published by Bruce et al. [178]. The distance from the sulfur atom in the hydrophilic shell of an SDS micelle to the nearby water oxygen was reported to be 3.8 Å; subtracting the radius of water (1.4 Å) from this value, one obtains the radius of the sulfate head group or:

$$D_{sulfate} = 2r_{sulfate} = 2\cdot(l_{S\text{-}O} - r_{water}) = 2\cdot(3.8-1.4) = 4.8\ \text{Å} \qquad [7.6]$$

Adding up the diameter of the core and two diameters of the anionic head group together, we obtain the diameter of an SDS micelle to be 44.2 Å, which is in reasonable agreement with the value acquired experimentally through X-ray scattering: 44.6 Å [179].

The silica particles used in this study had a nominal pore diameter of 100 Å; the value reported for the particular batch used in the experiments was 93 Å. This pore diameter was reported by the manufacturer for native, underivatized silica nanopores. The actual pore opening after C18 derivatization can be calculated from the surface area and the pore volume of derivatized particles. These values were obtained through theoretical calculations by Brumaru et al. [163] as 256 m^2/g and 0.47 ml/g for the surface area and the pore volume, respectively (experimental confirmation of these parameters is now in progress). Approximating the shape of the pore as a cylinder, we obtained the diameter of the pore opening after C18-derivatization using the following equations:

$$A_{pore} = 2\pi R_{pore} H \qquad [7.7]$$

$$V_{pore} = \pi R_{pore}{}^{2} H \qquad [7.8]$$

$$\Rightarrow A_{pore} = \frac{2V_{pore}}{R_{pore}} \qquad [7.9]$$

$$\Rightarrow D_{pore} = \frac{4V_{pore}}{A_{pore}} \qquad [7.10]$$

where A_{pore} is the area and V_{pore} is the volume of a cylinder-like pore, H is the pore length, R_{pore} is the radius and D_{pore} is the diameter of the pore opening. With appropriate unit conversions, the diameter of the C18-derivatized pore was calculated to be 73 Å versus 93 Å of underivatized silica gel [176].

When hydrophobic nanopores are wetted with a surfactant solution, according to the proposed wetting mechanism (Figure 7.1), C18 chains will extend into the solution, stabilized by the hydrophobic interactions with hydrocarbon tails of SDS. The “decoration” of C18 surface with either a SDS monolayer or SDS hemimicelles, in the absence of intercalation of the SDS tails into the C18 layer, would further reduce the open pore diameter down to about 29 Å, smaller than the diameter of an intact SDS micelle.

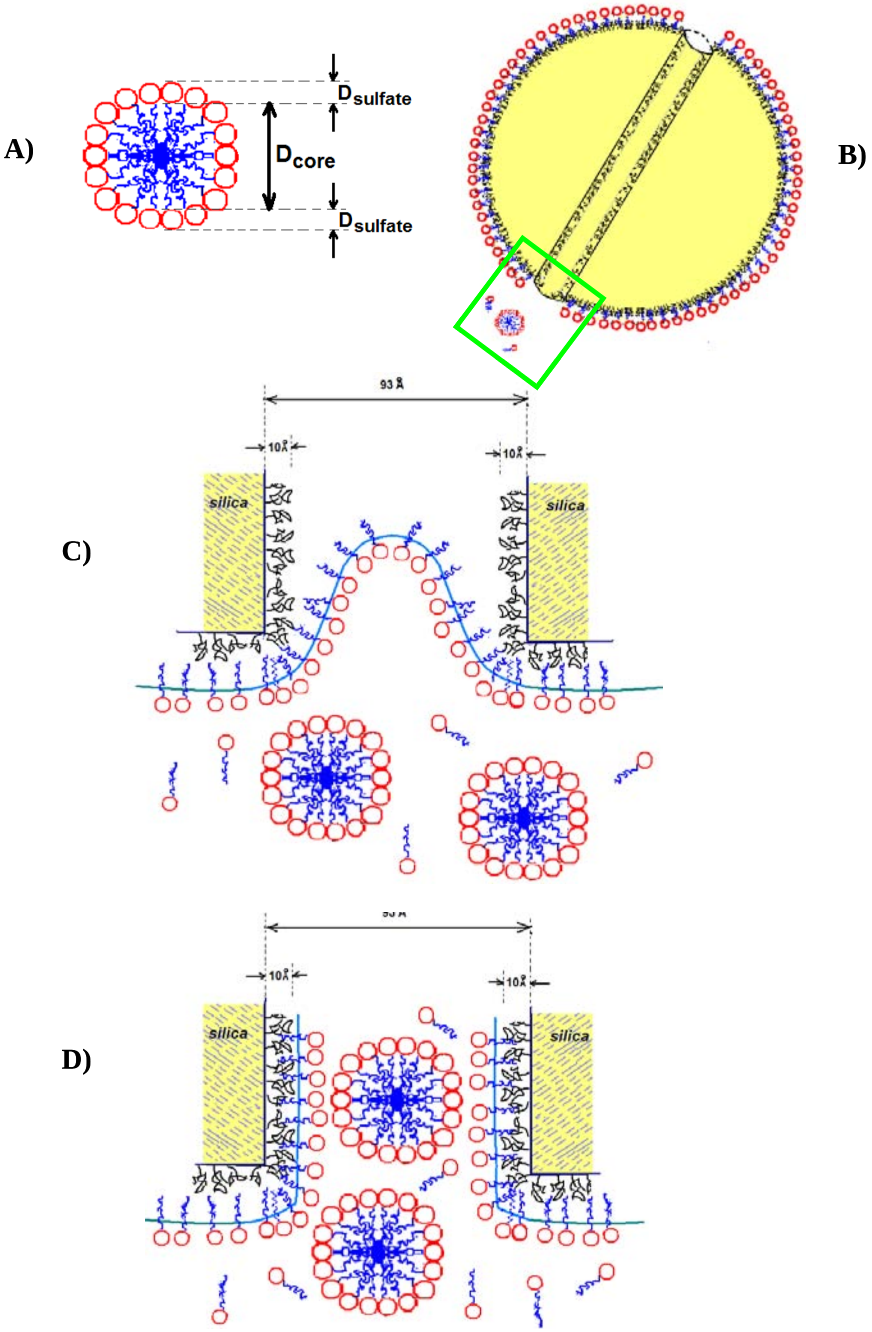

Figure 7.1. Schematic representation of the surfactant-assisted wetting of C18 particles. (A) Simplified view of a micelle structure in cross-section, arrows indicate the diameters of the hydrophobic core and hydrophilic head groups. (B) Surfactant-assisted hydrophobic particle wetting; (C) and (D) expansion of green box area in panel (B) in the process of pore wetting. Adapted from [176].

Considering the diameter of the SDS-wetted nanopores under these conditions, spatial restriction would not allow the diffusion of intact micelles into the pores. However, it is quite possible that the SDS molecules will partially insert their hydrocarbon chains into the C18 layer forming the C18-SDS construct. With these considerations, it is not obvious if SDS migrates into the silica gel core as monomers or intact micelles.

We investigated the process of nanotransport of the fluorescent target inside the hydrophobic pores with the aid of surfactants by means of fluorescence spectroscopy and two-photon excitation (TPE) microscopy. Ratiometric TPE microscopy was employed to image the change in the micropolarity of the environment during the pore wetting of the hydrophobic silica gel. The ability of confocal and two-photon microscopy to optically section the sample [7] and to directly visualize the distribution of fluorescent molecules in real time makes these techniques ideal for studies of relatively slow molecular and micellar transport within the nanopores [136,168,180,181].

An additional interest in the development of the imaging methodology that would allow real-time monitoring of the micellar migration through the hydrophobic pores lies in the applications of surfactants for transdermal drug delivery. Because of skin's barrier function, for drugs of large molecular weight it is hard to achieve an effective systemic effect upon simple topical application or even using a potential gradient, such as applied in transdermal iontophoresis [171,182,183].

The anionic surfactant SDS has long been recognized as a skin penetration enhancer for many pharmaceutical substances [184-187]. Micellar and liposomal enhancement of drug delivery through the skin barrier has been proven by conducting delivery experiments with *ex vivo* epidermis in flow-cell or diffusion-cell arrangements [188]. Efforts were made to visualize the penetration of intact micelles and liposomes into the skin layer [189,190] by means of CLSM [181,191,192], TPE microscopy [193] and transmission electron microscopy (TEM) [194], but, to our knowledge, none of the published studies reported the monitoring of the transdermal migration of the vesicles in real-time. In most referenced imaging experiments, several skin samples (or live animals) were treated with preparation solution in parallel, then sectioned and imaged at different time points to allow for tracking of the drug delivery progress [189,191,195]. Speculations that intact vesicles penetrate the skin barrier are based on indirect evidence – the colocalization of fluorescent probes incorporated into the liposomes prior to the application on the skin [196] and the detection of vesicular bodies in the images [193]. Imaging methodology that would allow visualizing vesicular penetration through the skin barrier in real time would provide a definite resolution to the disputed intactness of vesicles [197] en route through the skin barrier.

7.1.2 Solvatochromic Fluorescent Probes

Solvent polarity and the local environment can have significant effects on the emission spectra of fluorophores. These effects are complex, and there is no single theory that accounts for all of them [32]. One of the most commonly observed effects is fluorescence spectral shift to longer wavelength with increasing solvent polarity. As was discussed in Chapter 2, in the case of one-photon excitation, emission from the fluorophore generally occurs at wavelengths longer than the excitation wavelength. This loss of energy is due to a variety of dynamic processes, such as internal conversion and vibrational relaxation. Solvent effects can shift the emission to even lower energy due to stabilization of the excited state by the polar solvent molecules. Typically, the fluorophore has a larger dipole moment in the excited state than in the ground state. Following the fluorophore excitation, the solvent dipoles can reorient around the excited state dipole, lowering the energy of the excited state. This effect of the excited state stabilization becomes larger as the polarity of the solvent is increased (Figure 7.2). In general, nonpolar fluorescent molecules are minimally susceptible to the solvent polarity. The red shift in fluorescence emission with increasing solvent polarity is most often observed in polar molecules that have large excited-state dipole moments. Some representative solvatochromic fluorophores include polycyclic aromatic compounds, such as pyrene, Nile Red and Anilinonaphthalenesulfonate (ANS), and aminonaphthalenes, such as

Prodan, Laurdan, Badan and Dansyl, which are all effective probes of environmental polarity. Fluorescence spectroscopy with solvatochromic probes have proven to be a useful tool to elucidate interactions between species in the solutions and at the solid-liquid interface [198,199].

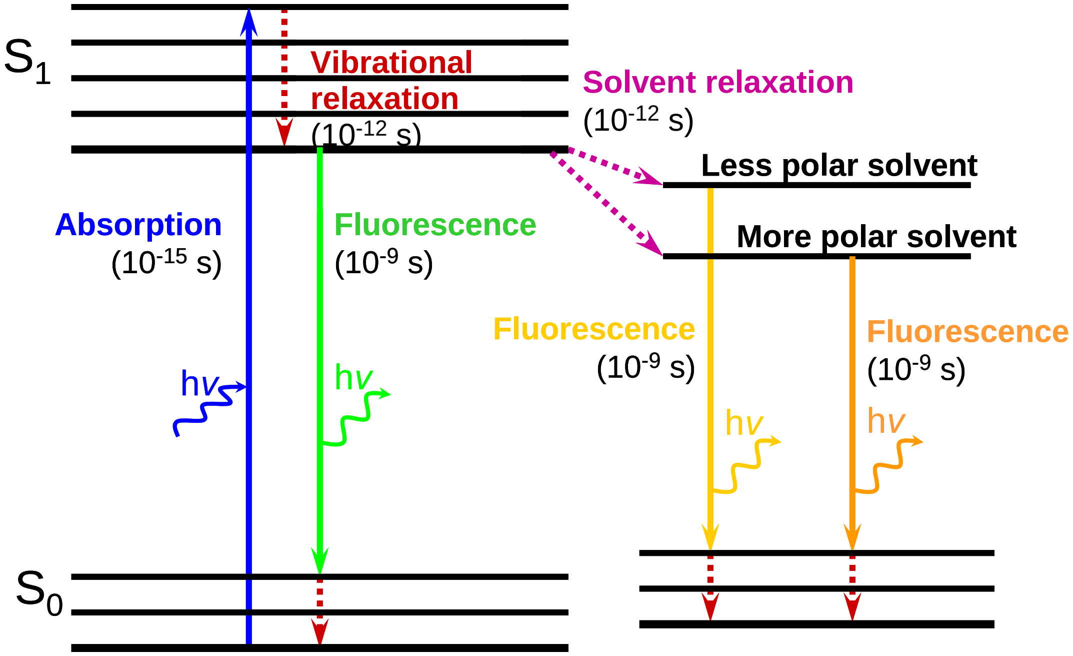

Figure 7.2. Modified Jablonski diagram showing the effect of solvent polarity on the fluorescence of a solvatochromic compound.

7.1.3 Pyrene

Pyrene is one of the few condensed aromatic hydrocarbons which shows fine structure (vibronic bands) in its fluorescence spectra in solution (Figure 7.3). Fluorescence emission spectrum of pyrene monomer contains five predominant peaks, matching five well-established vibronic bands. It has been accepted for a while [200] to refer to the peaks in pyrene spectrum using Roman numerals (I-V) with peak I corresponding to the 0-0 transition.

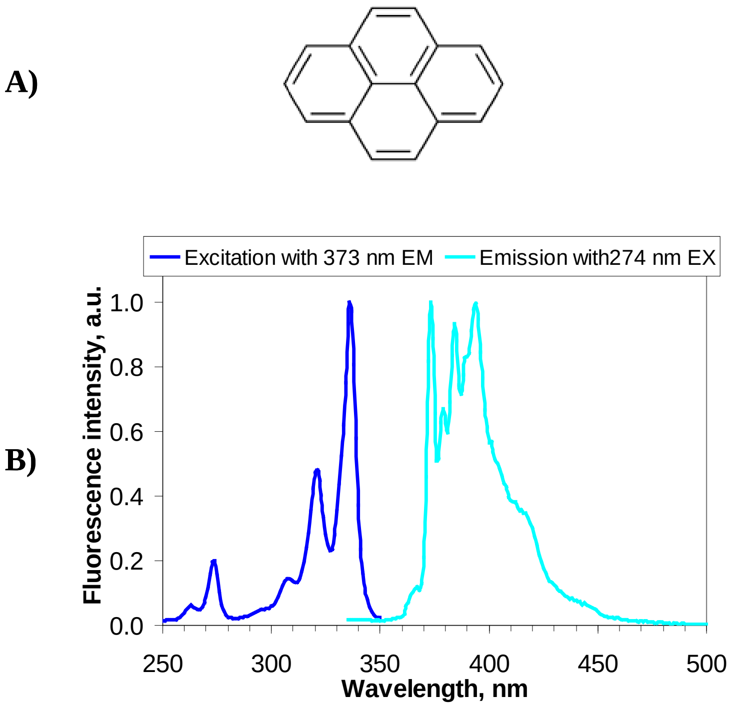

Figure 7.3. Chemical structure (A) and fluorescence excitation/emission spectra (B) of Pyrene. Spectra obtained using 0.5 µM solution of Pyrene in 50 mM aqueous SDS.

The solvatochromic properties of pyrene were first investigated by Nakajima [201-203]. He reported that the relative intensities of the pyrene emission peaks were found to show strong dependence on the environmental polarity with an enhancement of the 0-0 band intensity in the presence of polar solvents. The gold standard in the applications of pyrene for the environmental polarity measurements was set by Kalyanasundaram and Thomas [200]. In this work, it was noted that peak III of pyrene emission spectrum shows maximum variations in intensity relative to the 0-0 band. The relative intensity of peak III to peak I, referred to as the III/I (or 3/1) ratio, was proposed as a measure for the environmental effects on pyrene monomer fluorescence. Since then, pyrene has been extensively used for the study of microheterogenious systems, such as micellar solutions [204-206] and the “III/I peak ratio” of pyrene fluorescence has become a common measure of microenvironmental polarity.

A)

B)

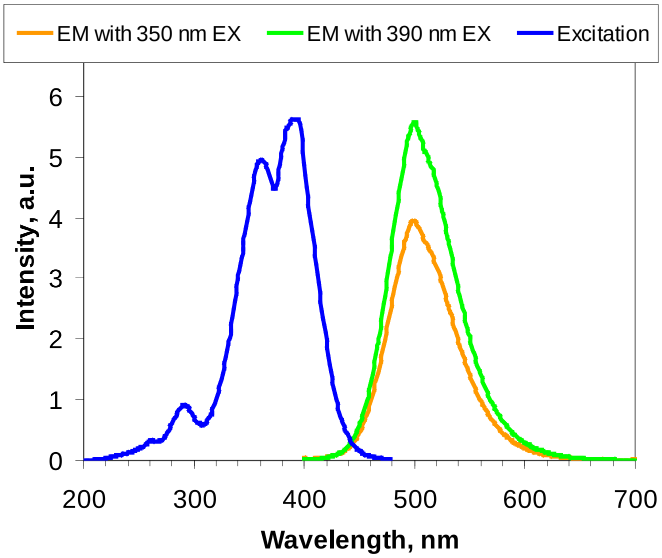

Figure 7.4. Chemical structure (A) and fluorescence excitation/emission spectra (B) of Prodan (6-propionyl-2-dimethylaminonaphthalene). Spectra obtained using 3 µM solution of Prodan in 50 mM aqueous SDS.

7.1.4 Prodan

Ratiometric imaging described in this chapter was achieved by using Prodan (6-propionyl-2-dimethylaminonaphthalene) fluorescent probe, one of the most solvatochromic fluorophores (Figure 7.4). Prodan was first prepared and characterized in 1979 by Weber and Farris [207]. Since then it has been widely used to study the structure of model and natural membranes [208-212], protein binding domains [213] and ionic liquids [214], to list just a few applications.

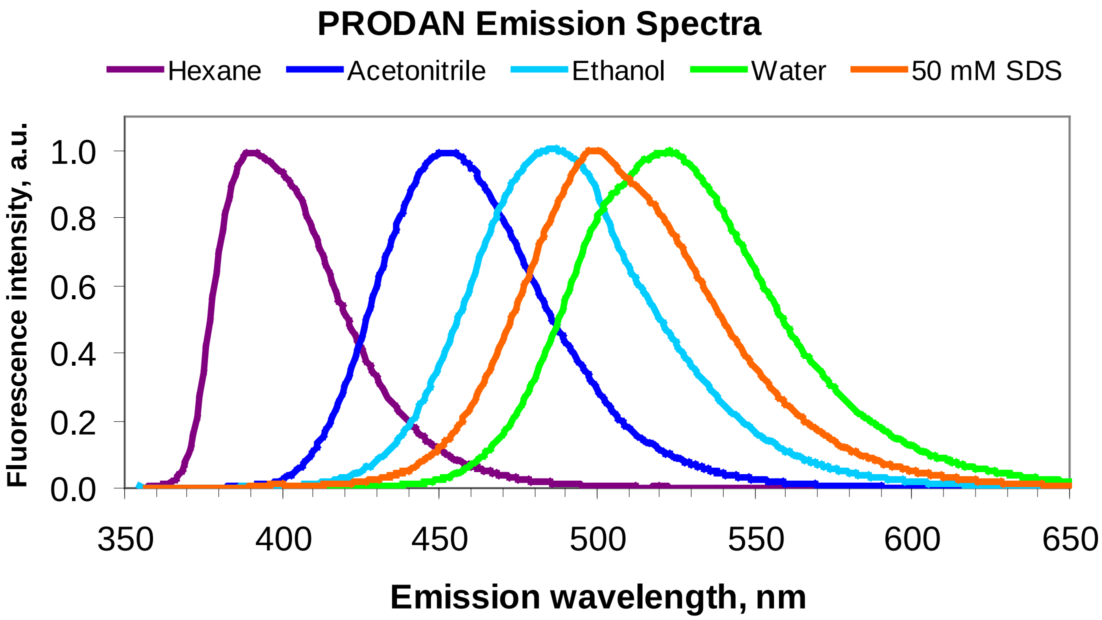

Figure 7.5. Fluorescence emission spectra of 3 μM Prodan in different solvents.

Location of the fluorescence peak of Prodan is highly dependent on the polarity of its environment. For example, in acetonitrile Prodan's emission peak is close to 450 nm, while in water it is around 520 nm

(Figure 7.5). Prodan is especially suitable for characterization of micelle systems, because it is soluble in an extensive range of media, suggesting the possibility of its simultaneous partitioning into all regions of the micelle [215]. It is well known that in an aqueous solution of surfactant beyond the critical micellar concentration Prodan would be preferentially located inside the micelles [216]. It is anticipated that when hydrophobic C18-derivatized particles are introduced into the solution, the surfactant molecules interact with the C18 chains on the particles' surface and Prodan redistributes from the SDS micelles into the more hydrophobic C18-C12 construct. The change in the polarity of Prodan's environment results in the spectral shift of its fluorescence spectrum. This feature combined with submicron spatial resolution of the confocal imaging allowed us to monitor the polarity dynamics of the surfactant solution migration inside the hydrophobic pores of the beads and the formation of the C18-SDS construct inside the nanopores.

7.2 Experimental

7.2.1 Chemicals and Materials

The 10-µm Luna® C_{18}-modified silica beads were obtained from Phenomenex (Torrance, CA). According to the manufacturer's specifications, this batch of particles had an average diameter of 8.54 µm and an average pore size of 93 Å, a carbon loading of 17.5%, calculated bonded phase coverage of 3.00 mol/m^2, and a surface area of 426 m^2/g before C18 derivatization. The particles and surfactant sodium dodecyl sulfate (SDS), obtained from Fisher Scientific (Pittsburgh, PA), were used without any pre-treatment. All aqueous solutions were prepared using 18.2 MΩ ultrapure water obtained from a MilliQ-Plus water filtration system (Millipore, Bedford, MA). HPLC grade acetonitrile, dimethyl formamide, ethanol, and hexane were acquired from Fisher Scientific (Fair Lawn, NJ). Polyimide-coated capillaries, i.d. 50-µm, o.d. 360-µm, and quartz cells with 400-µm i.d. and 550-µm o.d., necessary for the assembly of the UV-transparent microcolumns, were acquired from Polymicro Technologies (Phoenix, AZ).

Prodan was purchased from Molecular Probes (Eugene, OR) and used directly, without purification. The fluorophore stock solution with concentration 1.50 mM was prepared in HPLC grade ethanol. To prepare dilute solutions of Prodan in different solvents, small aliquots of the stock solution were introduced into the dry sample vials and the solvent was evaporated by nitrogen flow. The fluorescent probe was then resuspended in 50 mM aqueous SDS solution or pure water, or other pure solvent. Pyrene was obtained from Sigma-Aldrich (Milwaukee, WI) and used for the preparation of the 0.158 mM stock solution in ethanol as is. For the polarity-probing fluorescence spectroscopy experiments 1 µM pyrene solutions were prepared according to the same aliquot-evaporation protocol as Prodan.

7.2.2 Concentration of the Surfactant Solution

In all experiments, concentration of SDS in the solution was kept at 50 mM, which is well beyond the critical micellar concentration (8.2 mM). High SDS concentration was necessary to ensure sufficient amount of surfactant for the complete coverage of the beads inside and out and the presence of the ample amount of micelles remaining in the solution afterwards. The following calculations offer theoretical support for the choice of the concentration.

We considered two cases of particle surface coverage with SDS: adsorption of individual SDS molecules in the form of a monolayer and formation of hemimicelles on the C18-derivatized surface of the beads. As stated earlier, the surface area of silica particles in this particular batch was reported to be 256 m^2/g by Brumaru et al. [163]. Assuming uniform cylindrical shape of the SDS molecule we can approximate the area occupied by one SDS molecule as a circle with the diameter of 5 Å. In the extreme case of hexagonal close packing (HCP) of SDS molecules in the monolayer, 90.7% of the total surface is covered by SDS. From this, the concentration of the surfactant necessary for the monolayer coverage of the silica surface with individual SDS molecules was calculated as:

$$C_{SDS} = \frac{0.907 \cdot A \cdot m}{\pi \cdot {r_{SDS}}^2 \cdot N_A \cdot V} \qquad [7.11]$$

where A is the surface area of the particles, m is the mass of the silica gel added to SDS solution of volume V, r_{SDS} is the radius of the sulfate head-group in the SDS molecule and N_A is Avogadro's number. In case when wetting of 0.05 g of particles in 3 ml of SDS solution is considered, the necessary concentration of SDS solution is 33 mM.

Since we are considering a relatively high concentration of surfactant, it is more likely that the hemimicellar structure would be formed on the hydrophobic surface of the particles [159,217-219]. Considering hexagonal close packing of the hemimicelles on the surface, the SDS solution concentration is then obtained as:

$$C_{SDS} = \frac{0.907 \cdot A \cdot m}{\pi \cdot r_{hm}^{2} \cdot n_{hm} \cdot N_A \cdot V} \qquad [7.12]$$

where n_{hm} is the aggregation number for an SDS hemimicelle, i.e., 31, and r_{hm} is the radius of an SDS hemimicelle, which is equal to the radius of a micelle, assuming a hemimicelle is an ideal hemisphere. Applying the diameter of the SDS micelle calculated earlier, 44 Å, and assuming no intercalation of SDS tails into the C18 layer, we obtain the value of the solution concentration necessary for the complete coverage of the particles' surface with tightly packed hemimicelles to be 13 mM. Though the second case scenario is more probable, it is still an extreme approximation. Due to the negative charge of the sulfate groups, hemimicelles cannot be tightly packed. The presence of "uncovered" spaces between the micelles was confirmed multiple times by AFM imaging of surfactants adsorbed on different surfaces [220-223]. Thus, 50 mM concentration of SDS used in the experiments was sufficient to ensure an abundance of micelles in the solution after complete coverage of the hydrophobic surface of the silica gel with surfactant.

7.2.3 Fluorescence Spectroscopy with Pyrene

Steady state fluorescence spectra were obtained using AMINCO-Bowman Series2 Luminescence Spectrometer, Model FA-354 (Thermo Electron, Waltham, MA) and standard 10-mm optical path quartz cuvettes. Excitation wavelength, varied depending on the fluorescent probe used, was provided by a Xenon lamp and both excitation and emission monochromators were set to a bandpass of 2 nm. For pyrene excitation we chose to use 274 nm wavelength and the emission spectra were recorded from 335 to 500 nm. Using procedure outlined in section 6.2.1, 1 µM solution of pyrene in 50 mM SDS was prepared in a vial and then transferred to a cuvette. Fluorescence spectrum of pyrene prior to the addition of the particles was obtained. Weighed C18 silica particles (usually 0.03 to 0.05 g) were added directly to the cuvette. The sample was gently shaken by hand to bring all silica beads in contact with the solution. In earlier experiments, we tried using stir-bar to mix the particles into the surfactant solution, but the microbar that is recommended for the use with a standard 10-mm cuvette does not provide enough agitation to break the particle/solution interface that is stabilized by the hydrophobic interactions between the surfactant and C18 chains on the surface of the particles. Thus, if the stir-bar is added to the cuvette before the beads, minimal interaction between the particles and the surfactant occurs and majority of the beads stay dry on the surface of the solution even after 120 hours of continuous stirring (experimental data not shown here). Addition of the particles to the vial with consequent transfer to the cuvette was not favored either, because hydrophobic beads tend to adsorb on the surface of the glass and no quantitative control over the loss of the material is feasible. Clearly, vortexing and sonication of the quartz cuvette to achieve the integration of the hydrophobic particles in the surfactant solution cannot be recommended either.

In Experiment I, 0.0293 g of 10-μm Luna C18 silica particles were added directly to the cuvette containing 3 ml of 50 mM SDS solution. Upon the initial shaking of the cuvette and the acquisition of the emission spectra, the solution was left in the instrument without agitation for 70 hours. To monitor the dynamics of the polarity change in the solution as the particles wetted with the surfactant precipitated, fluorescence spectra were obtained periodically, specifically at 18, 24, 42, 48 and 70 hours. At the end of the experiment the sample was gently shaken again, which caused re-suspension of all precipitated beads. The final acquisition of the fluorescence spectra followed immediately. Fluorescence data at each time point was collected in triple replicates with the scan rate 1 nm/s.

In Experiment II, C18-derivatized silica beads were added to the vial containing 3 milliliters of 50 mM aqueous SDS solution. The vial was shaken thoroughly, after which two milliliters of the solution with wetted particles was “decanted” by a pipette into a cuvette. A small fraction of the hydrophobic silica gel that was not wetted by the surfactant solution was left behind in the vial. Micro-size stir-bar was place into the cuvette to keep the sample agitated at all times between the measurements. Instrument capabilities did not allow us to stir the sample during the spectral acquisition, so the cuvettes were kept on the stir-plate and moved into the instrument compartment for fluorescence measurements. The experiment was performed in double replicate. In the first trial 0.0495 g of 10-μm C18-derivatized silica particles were added to the surfactant solution, in the second trial – 0.0503 g of the particles from the same batch were used. The surfactant solution was identical in both experiments. Consistency in the sample handling procedure was the paramount goal in this experiment, though we acknowledge the inevitable variations that the “decanting” step and the manual positioning of the sample in and out of the cuvette holder introduce. The total length of the experiment was 96 hours. At each time point, two fluorescence spectra were collected in consecutive manner with brief sample agitation in between. The scan rate was 1 nm/s, which resulted in approximately 3-minute acquisition time per spectrum.

Spectra of the particle-containing solutions were baseline adjusted to account for the strong scattering of the particles. Among the Lorentzian, Gaussian, and linear functions, the former one provided the best fit, so it was used for the analysis of all spectra in Experiments I and II. After the baseline adjustment through the subtraction of Lorentzian function, spectra were normalized to unity at the first fluorescence peak, consequently, the intensity of the third peak corresponded to the III/I pyrene peak ratio and was used as the polarity indicator.

7.2.4 Fluorescence Spectroscopy with Prodan

For the acquisition of fluorescence spectra in different solvents 3 μM solutions of Prodan in acetonitrile, dimethylformamide, ethanol, hexane, deionized water and 50 mM aqueous SDS were prepared according to the aliquot-evaporation method described in section 7.2.1. Prodan fluorescence was excited at 350 nm and the emission spectra were collected in 300 to 700 nm range. To obtain the spectrum of Prodan fluorescence in the presence of C18 silica beads, 0.03 g of silica particles were added to 3 ml of 10 μM Prodan in 50 mM SDS solution. The cuvette was gently shaken for a few minutes until all particles were wetted with the surfactant solution. The fluorescence spectra were collected before the particle addition, immediately after all added beads were wetted and the next day, when the majority of the particles precipitated to the bottom of the cuvette due to the gravitational forces. Fluorescence was recorded with both 360 and 390 nm excitation wavelengths, which correspond to the maxima in the single-photon excitation spectrum of Prodan (Figure 7.4).

7.2.5 Two-photon Excitation Microscopy

To obtain polarity-specific information during the process of wetting C18 silica particles with SDS solution two-channel ratiometric imaging was conducted using an upright laser-scanning Bio-Rad Radience 2100MP Multiphoton/Confocal Microscope at the University of Iowa Central Microscopy Research Facility. Since the peak excitation of Prodan lies in the UV region, we employed two-photon excitation to overcome poor transparency of the microscope optics to the UV light. Pulsed infrared Titanium-Sapphire laser with tunable range of 710 to 920 nm and the capability to generate 100 fs pulses at frequency 80 MHz was employed as the excitation source in the imaging experiments. A two-photon excitation spectrum of Prodan (Figure 7.6) was built by acquiring images of a capillary filled with Prodan solution. The excitation wavelength was varied from 710 nm to 875 nm in 5 nm steps. The average intensity of the fluorescent area in each image was calculated using a built-in ImageJ function. The “raw” constructed fluorescence spectrum was calibrated by the output laser power by dividing the TPE fluorescence intensity by laser power squared. Figure 7.7 shows the calibrated two-photon excitation spectrum of Prodan in comparison with its single photon excitation spectrum. For the imaging experiments with Prodan probe 770-nm excitation wavelength was chosen.

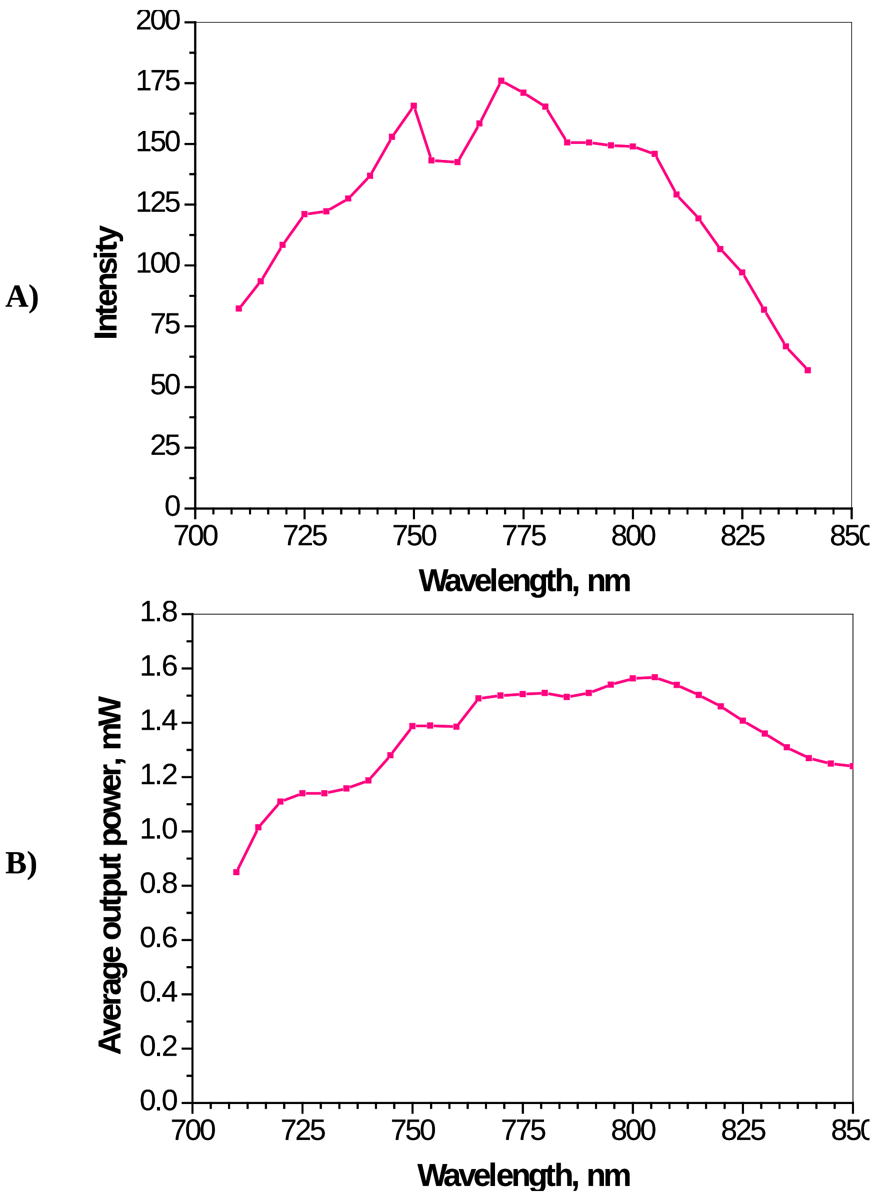

Figure 7.6. Two-photon excitation spectrum of Prodan. (A) Spectrum built point by point by calculating the average intensity of the area in the image of Prodan-filled capillary; (B) average output laser power at different wavelengths.

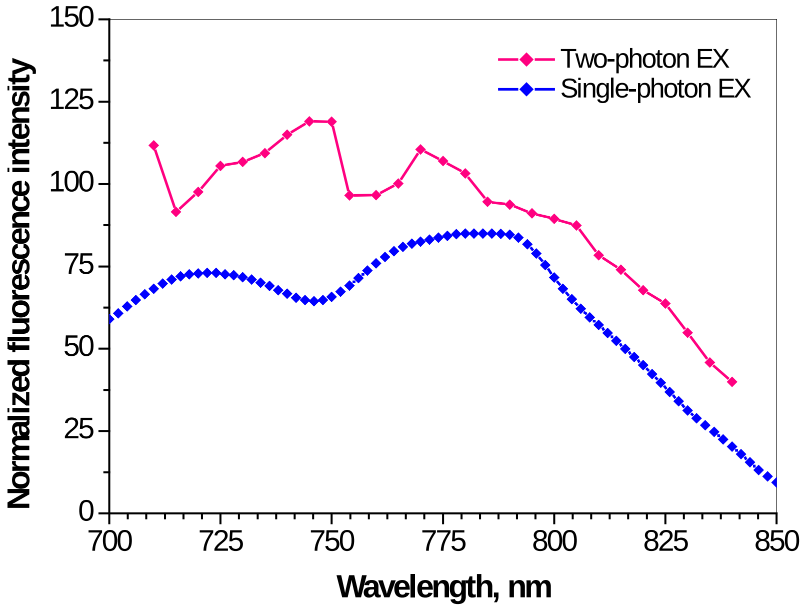

Figure 7.7. Two-photon excitation spectrum of Prodan normalized to the output laser power squared, and compared to the single photon excitation spectrum, which was intentionally off-set.

As most commercial confocal systems, Bio-Rad Radience 2100MP operates in the laser-scanning mode. The schematic of the optical path is presented in Figure 7.8. Upon passing through the laser-scanning head, the excitation light was focused by a 60X oil objective into the sample. Fluorescence emitted by Prodan was collected by the same objective and passed through the dichroic mirror. As was discussed in Chapter 2, two-photon excitation mode provides intrinsic confocality, so no pinhole was necessary to obtain the optical sectioning of the sample. The fluorescence signal was separated into two channels by the dichroic beam splitter.

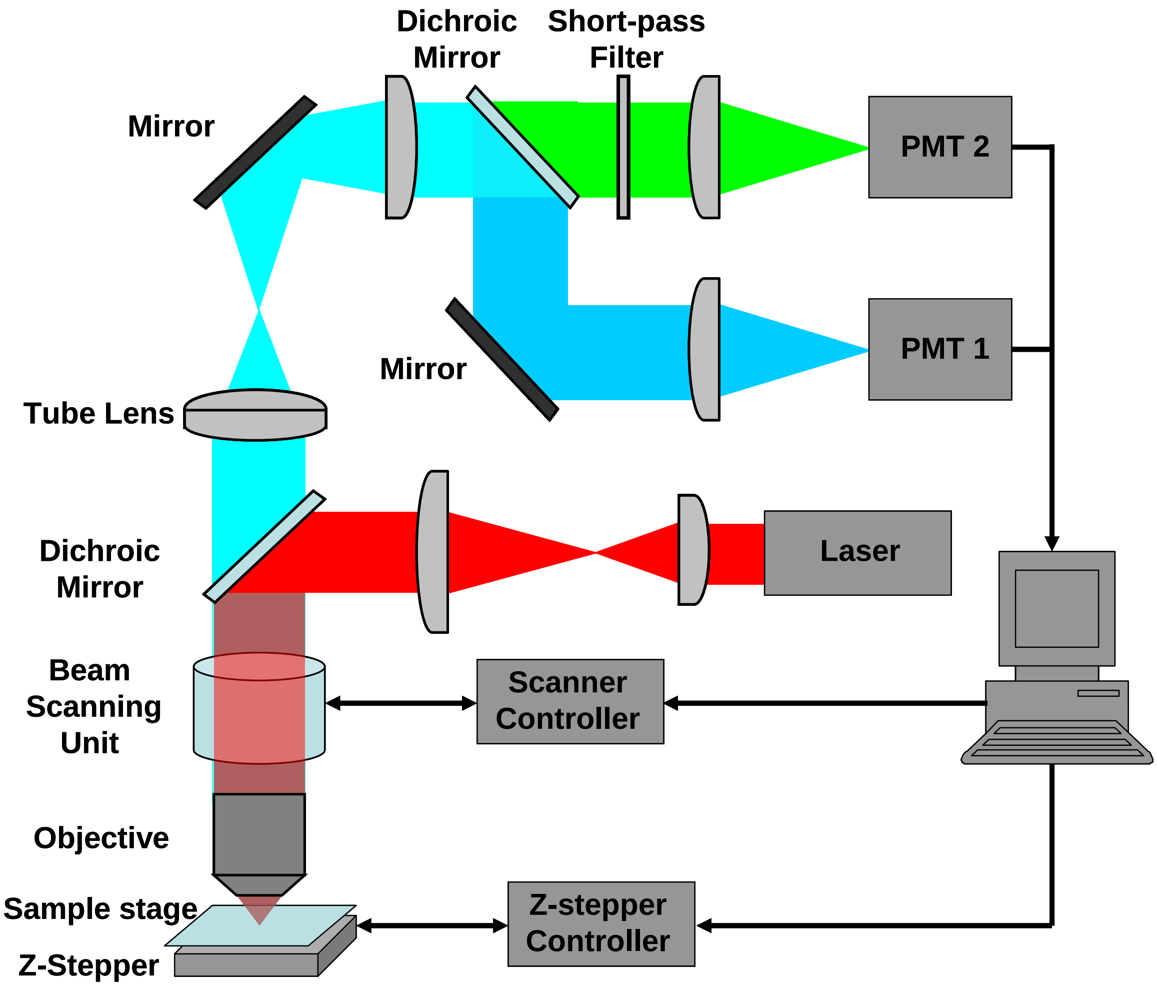

Figure 7.8. Schematic diagram of the commercial two-photon excitation laser scanning optical system with dual channel detection. PMT1: photomultiplier tube for “blue”/shorter wavelength channel, PMT2: photomultiplier tube for “green”/longer wavelength channel.

Based on the results of the steady state fluorescence experiments, discussed in detail in the section 7.3.2, we decided to use a 440-nm dichroic mirror to separate the fluorescence signal of Prodan in SDS micelles from the signal of Prodan located in the particles-SDS construct. Short wavelength fluorescence was reflected by the dichroic mirror to the PMT 1 detector (“blue channel”). Transmitted through dichroic mirror longer-wavelength fluorescence light was passed through a 610-nm short-pass filter, to reject any scattered 770-nm excitation light, and was focused into the PMT 2 (“green channel”). The ratiometric image characteristic of the microenvironment polarity was obtained by dividing the intensity of the “green” channel by the intensity of the “blue” channel, which was done using ImageJ software (Research Services Branch, NIH). The background signals from both the stationary phase and the mobile phase were negligible when compared to fluorescence signals.

To facilitate the imaging of the surfactant-assisted wetting of C18 silica beads and especially visualize the migration of the solution front inside the hydrophobic pores, the particles were packed into a quartz microcolumn and held in place by two capillaries with fritted ends [161]. Specifically, a frit at one end of each 50-µm i.d. capillary was prepared by sintering C18 silica beads wetted with ethanol. The fritted end of one capillary was then inserted into a 15-mm long piece of quartz tubing, 400-µm i.d., and glued to the inner wall of it by a nonfluorescent adhesive from Norland Products Inc. (New Brunswick, NJ). C18 silica beads were packed into the quartz column using vacuum before the second fritted capillary was glued to the other end of the quartz tubing.

Several columns with packed zone about 5 mm in length were prepared in this fashion.

For imaging, the packed column was glued on a microscope slide alongside with two “spacers” made of the quartz tubing of the same outer diameter. Spacers ensured that the quartz cover slip placed over the microcolumn was located in parallel to the microscope slide. Since the imaging was done using an oil-immersion objective, the space around the column, between the slide and the coverslip, was filled with the same immersion oil as was used for the objective (Figure 7.9). Close match in the refractive index of the immersion oil and the quartz ensured minimization of the light refraction at the interfaces and thus improved the quality of the images.

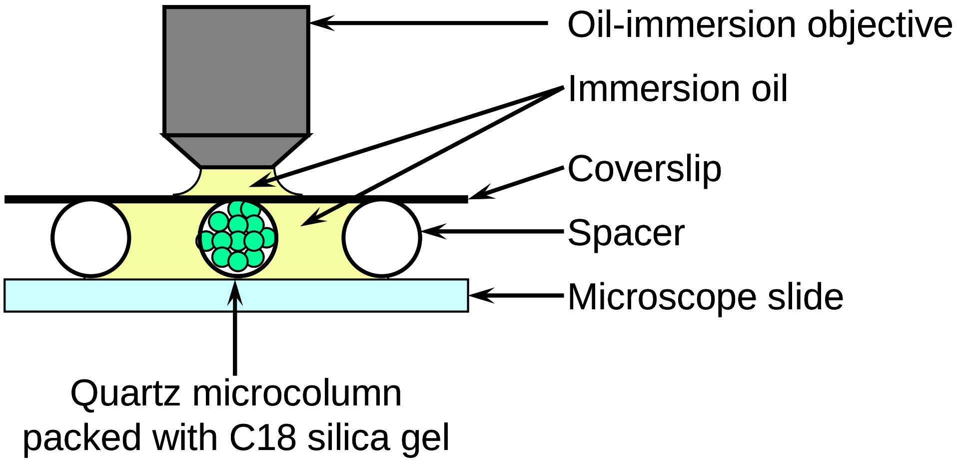

Figure 7.9. Schematic of the sample slide and oil-immersion objective showing the strategic placement of the immersion oil for best imaging results.

The wetting solution containing 10 µM concentration of Prodan in 50 mM aqueous solution of SDS was pumped through the column by a syringe pump (Model: 341, Sage Instruments).

7.3 Results and Discussion

7.3.1 Spectroscopic Study of C18 Silica-surfactant System with Pyrene Fluorescent Probe

The pyrene III/I intensity ratio, obtained from the intensity at 384 nm and 373 nm, in 50 mM aqueous SDS solution was calculated to be 0.935 ± 0.007. The value was obtained by analyzing spectra from four independent solution samples scanned on different days. In both Experiment I and Experiment II, upon the addition of the C18-derivatized silica particles to the solution, significant decrease in fluorescence intensity accompanied with an increase in the III/I peak ratio was observed (Figure 7.10). Figure 7.10A shows the absolute intensity values recorded, while in Figure 7.10B spectra were normalized to unity at 373-nm peak to highlight the difference in the III/I peak ratio. The drop in the integrated spectral intensity was explained by strong scattering from the beads introduced to the solution. The increase in the III/I peak ratio indicates the formation of less polar environment, most likely the C18-SDS construct on the surfaces of the particles, which is less polar than

SDS micelles. Immediate change in the pyrene peak ratio indicates fast kinetics of the C18-SDS construct formation.

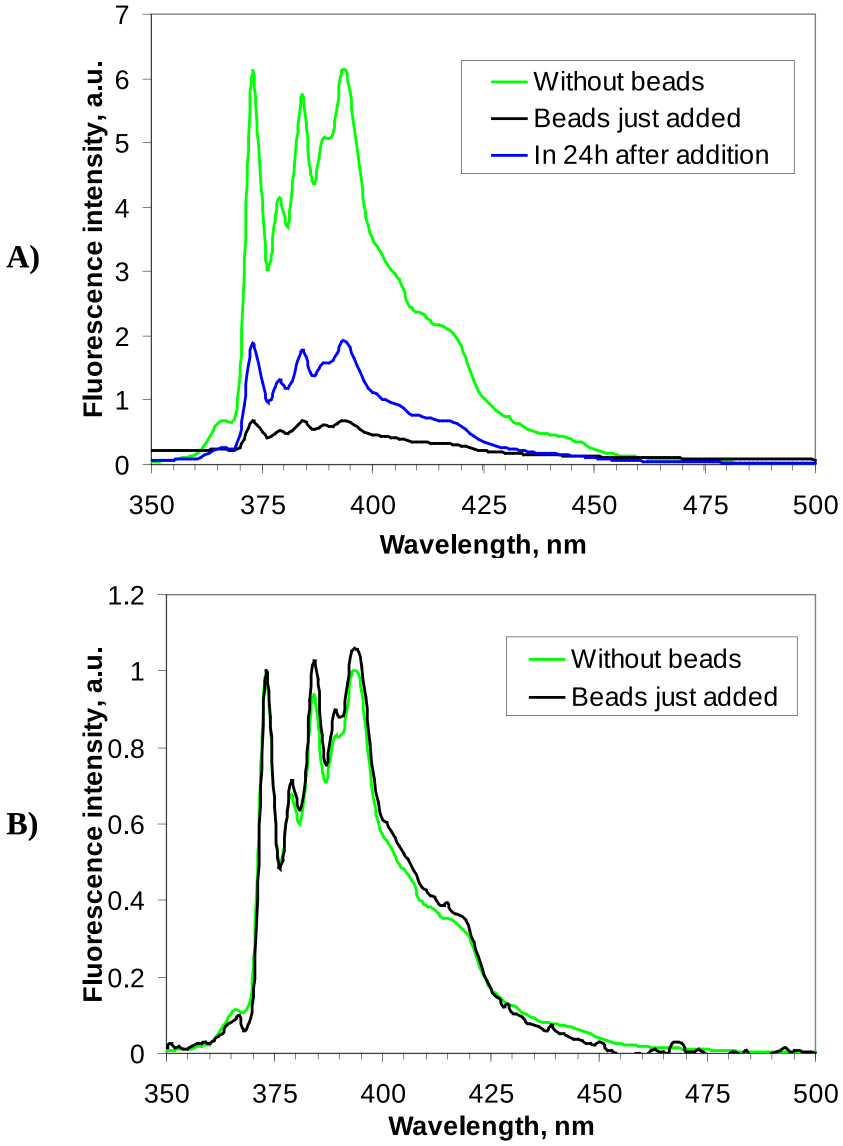

Figure 7.10. Fluorescence spectra of Pyrene collected in Experiment I. (A) Original spectra showing the decrease in fluorescence intensity upon the addition of the particles to the solution; (B) normalized to unity at 373 nm fluorescence spectra highlighting the change in the III/I Pyrene peak ratio.

It is important to mention at this point that at time zero (right after the addition of the beads) the polarity ratios in Experiment I and Experiment II were slightly different: 1.03 ± 0.03 and 1.10 ± 0.03 respectively. Since the original volume of the SDS solution in both experiments was identical (3 ml), but the amount of particles used in Experiment II was larger, we expect that the final concentration of the beads suspended in the solution was higher in Experiment II. Consequently, the contribution to the pyrene fluorescence spectrum from the more non-polar C18-SDS environment was higher in this experiment, which resulted in overall higher polarity ratio.

In Experiment I, after the solution was allowed to settle for 18 hours a significant decrease in III/I peak ratio was registered, after which the ratio changed minimally approaching closer and closer the polarity ratio of pure SDS solution without beads (Figure 7.11). At the same time, incremental increase in the integrated spectral intensity was recorded, accompanied with, and most likely caused by, the reduction in scattering. This indicated the presence of some beads suspended in the solution even after 18 hours of dormancy. Their "sedimentation" overtime decreased scattering and increased apparent fluorescence signal.

In 24 hours, the III/I pyrene peak ratio was within two standard deviations from the ratio in the pure 50 mM SDS solution without the particles. Nevertheless, the integrated spectral intensity continued increasing and the background signal continued decreasing beyond this point (Figure 7.12).

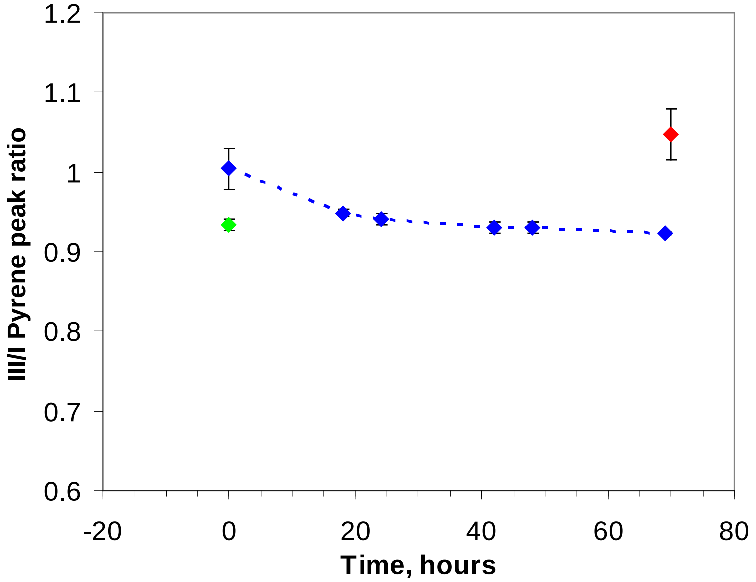

Figure 7.11. Change in Pyrene III/I peak ratio over time observed in Experiment I. Green point corresponds to the polarity value of the SDS solution before the addition of the beads, red – to the polarity of the solution agitated at the end of the experiment.

In 42 hours, the background signal reached the level within one standard deviation of the original SDS solution background before the addition of the beads. The background signals at 48 hours and 69 hours can be considered identical to the signal at 42-hours mark. From that point the III/I peak ratio remained constant as well (within one standard deviation of the calculated point values). Most of the beads “precipitated” and the major contributor to the fluorescence signal was pyrene present in SDS micelles.

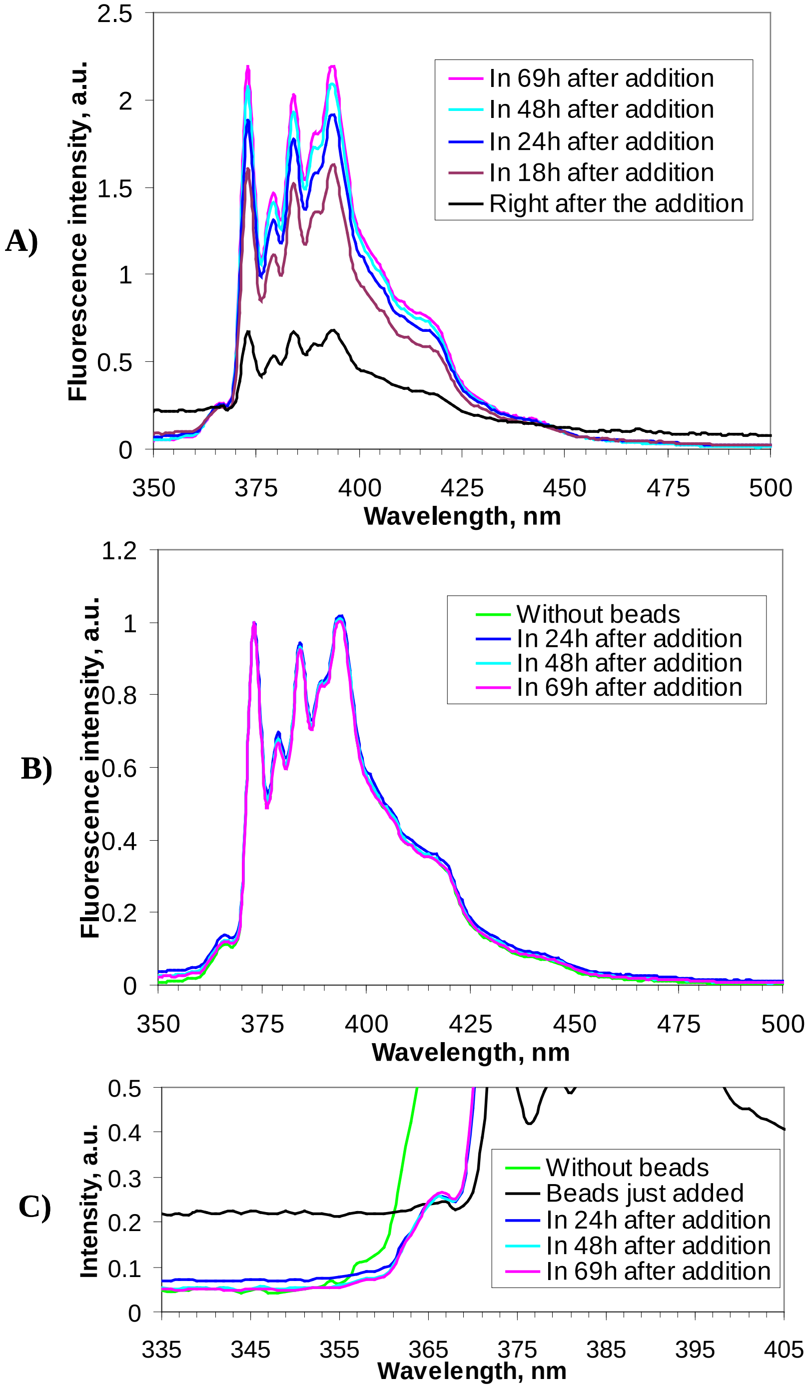

Figure 7.12. Fluorescence spectra of Pyrene obtained in the course of Experiment I. (A) Original spectra; (B) spectra in panel (A) normalized to unity at 373 nm and baseline-adjusted; (C) close up of the shorter wavelength region of original spectra.

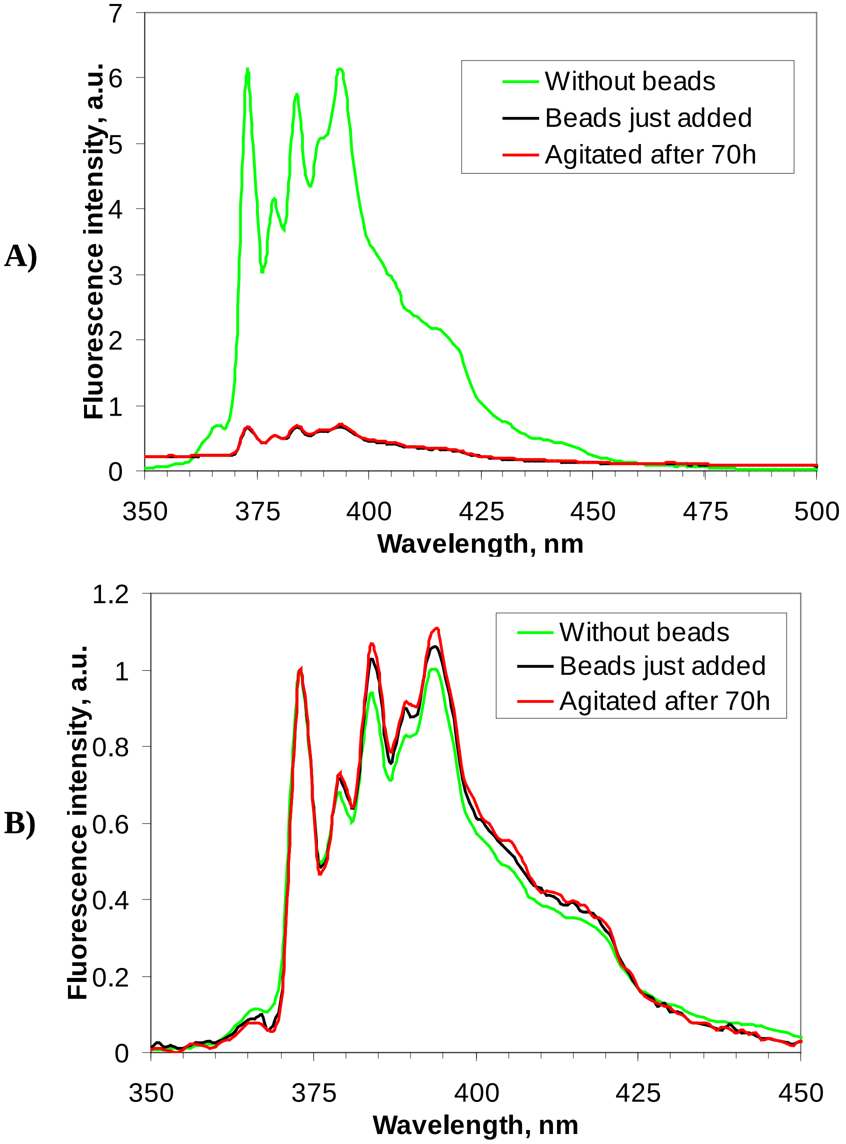

Figure 7.13. Comparison of solution fluorescence in Experiment I before addition of the beads, right after, and in 70 hours, when the sample was agitated. (A) Original fluorescence spectra; (B) spectra in panel (A) baseline-adjusted and normalized to unity at first fluorescence peak.

Upon solution agitation at the end of the Experiment I, the background signal of the solution was slightly higher than when the beads were just added (Figure 7.13). We can speculate that some silica particles that remained dry in the upper part of the cuvette were eventually wetted and brought into the solution. Interestingly, the polarity ratio increased beyond the III/I peak ratio of freshly mixed particle-containing solution (Table 7.1).

Table 7.1. Polarity trend observed in Experiment I.

HOURS AFTER ADDITION OF SILICA C18 BEADS	**AVERAGE III/I PYRENE PEAK RATIO**	**STANDARD DEVIATION IN THE AVERAGE III/I PYRENE PEAK RATIO**
N/A (before the addition)	0.9384	0.0075
0	1.029	0.026
18	0.9528	0.0047
24	0.9427	0.0069
42	0.9325	0.0071
48	0.9304	0.0072
69	0.9246	0.0022
70 (agitated)	1.069	0.032

The increase in the polarity ratio after solution agitation can be caused by two factors. First, since the concentration of the particles in the solution increased, which was indicated by the increase in scattering, there was larger contribution of the pyrene present in more non-polar environment of C18-SDS construct to the apparent fluorescence signal.

Second, over the 70 hours that the particles remained wetted with the surfactant solution, more SDS-decorated C18 phase became available for pyrene to partition into due to the diffusion process. Thus, a larger fraction of pyrene redistributed from the SDS micelles into more hydrophobic C18 phase and into the C18-SDS constructs on the surfaces of the silica gel. We believe both factors contributed to the apparent polarity ratio increase, though Experiment II adds some more weight to the first cause.

<u>In Experiment II,</u> upon the initial mixing of the particles into the 50 mM SDS solution, 2 ml of the suspension was "decanted" from the unwetted particles on the surface of the solution with a pipette. "Decantation" of the sample eliminated the first aforementioned factor of polarity ratio increase at the end of Experiment I. In addition, it improved the homogeneity of the polarity distribution between the particles, which resulted in minimal increase in the polarity ratio (within 3 standard deviations) from the moment when the beads were added to the solution and for the following 90 hours (Table 7.2).

Immediately after the addition of the silica beads to the solution, III/I pyrene peak ratio increased to the level higher than the final polarity ratio at time zero recorded in Experiment I (Figure 7.14). Although some undefined amount of particles was lost in the decantation process, most likely the average concentration of the C18-derivatized silica was higher in Experiment II as suggested earlier. Larger amount of highly scattering particles and constant agitation of the solution in this experiment also resulted in higher levels of noise in the spectra.

Table 7.2. Polarity trend observed in Experiment II.

HOURS AFTER ADDITION OF SILICA C18 BEADS	AVERAGE III/I PYRENE PEAK RATIO IN TWO TRIALS	STANDARD DEVIATION IN THE AVERAGE III/I PYRENE PEAK RATIO
N/A (before the addition)	0.9352	0.0066
0	1.078	0.023
23	1.118	0.025
44	1.124	0.024
48	1.132	0.017
67	1.134	0.025
71	1.151	0.016
95	1.126	0.025
96 (agitated)	1.109	0.013

Just as in Experiment I, though to a lesser extent, the integrated intensity of the sample increased due to partial precipitation of the particles overtime (Figure 7.15). This spectroscopic observation supported visual estimation of the limited agitation capabilities of the micro stir-bar placed in a cuvette.

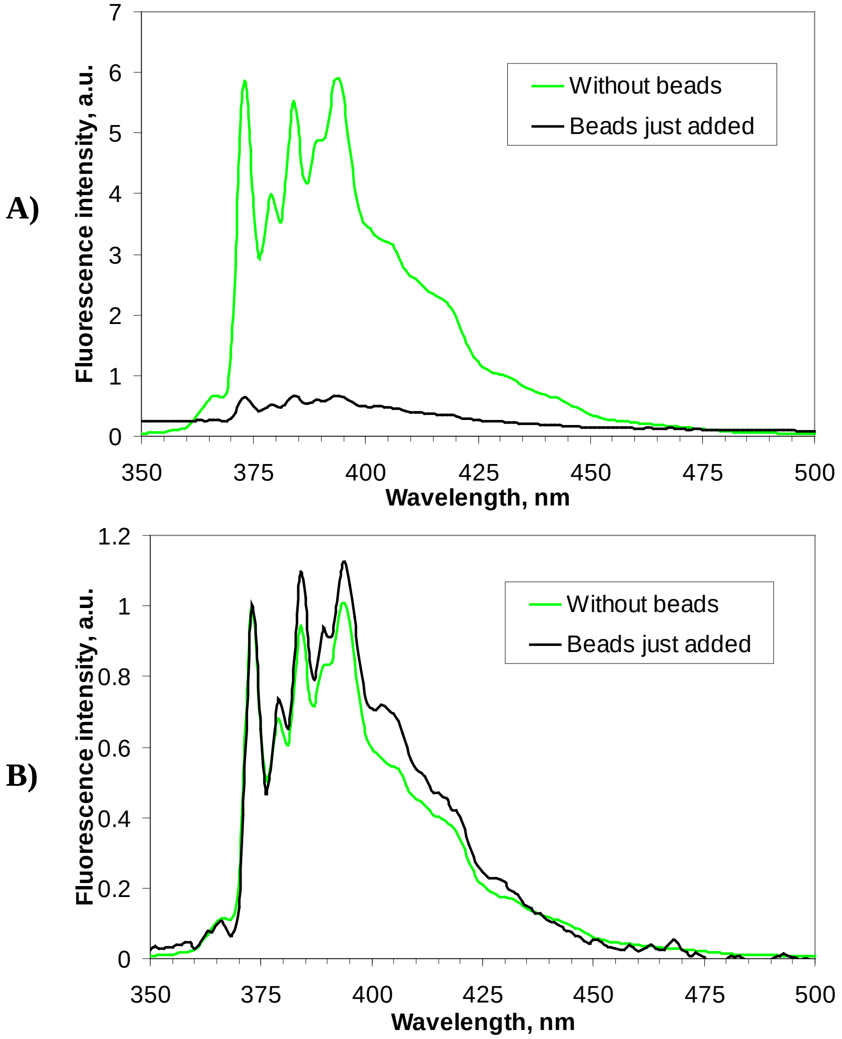

Figure 7.14. Fluorescence spectra of Pyrene collected in Experiment II. (A) Original spectra showing the decrease in fluorescence intensity upon the addition of the beads; (B) baseline-adjusted and normalized to unity at 373 nm fluorescence spectra.

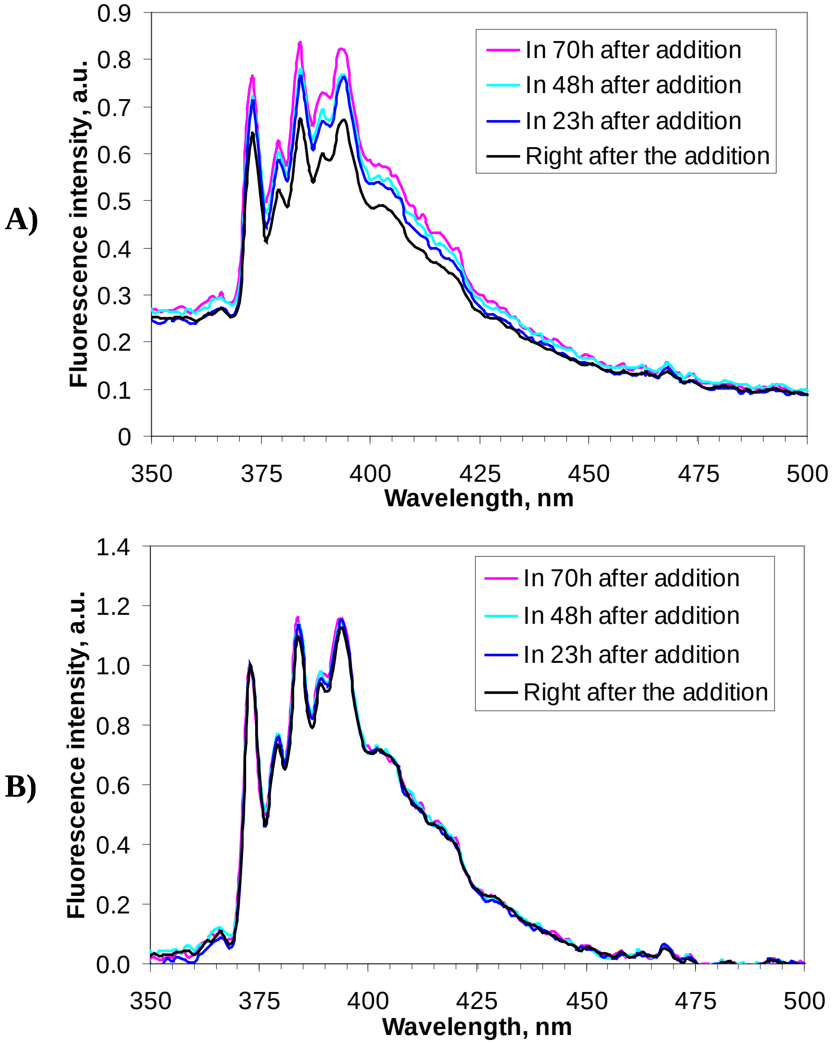

Figure 7.15. Spectra of Pyrene obtained in the course of Experiment II. (A) Original fluorescence spectra indicating increase in spectral intensity overtime; (B) spectra in panel (A) normalized to unity at 373 nm and baseline-adjusted.

At the end of the experiment, solution was gently shaken to ensure all particles are suspended. Thought the beads were left in the solution of surfactant even longer than in the Experiment I (90 hours vs. 70 hours), upon agitation of the sample there was no increase in the III/I pyrene peak ratio (Figure 7.16). On the contrary, slight drop (within two standard deviations) in the polarity was detected.

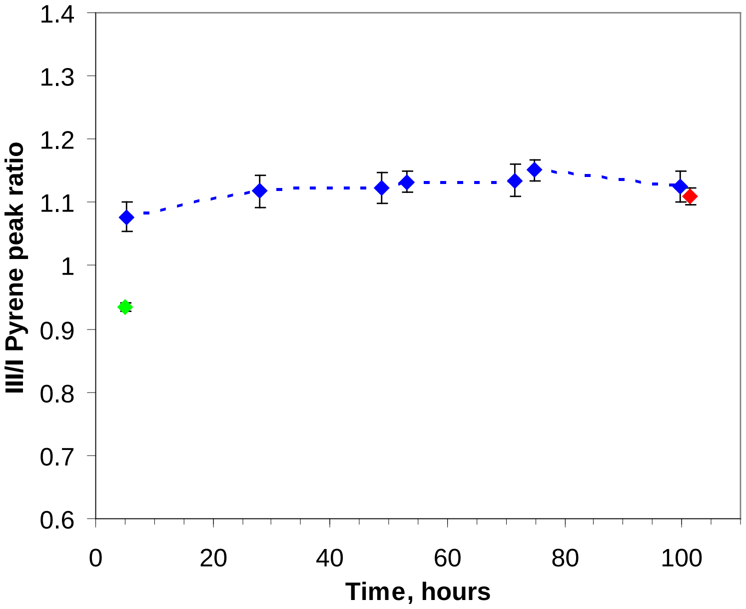

Figure 7.16. Change in Pyrene III/I peak ratio over time observed in Experiment II. Green point corresponds to the polarity value of the SDS solution before the addition of the beads, red – to the polarity of the solution agitated at the end of the experiment.

Since the values of the III/I peak ratio reported in this experiment (Table 7.2) represent the average of two trials conducted in parallel, reported standard deviations for the polarity ratio are higher than in Experiment I. Remarkably, though there was a significant discrepancy in the integrated spectral intensity between the trials, due to uncontrolled loss of particles in the decantation step, and difference in the III/I peak ratio at each time point was within two standard deviations in the polarity ratio (± 0.02). This last observation clearly indicates the advantages of polarity measurement through ratiometric spectroscopy with a single solvatochromic probe.

In the bulk solution, the polarity reading will be always a combination of several signals: from the solvatochromic probe in the micelles and in the more non-polar environment of the C18-SDS construct, in our case. To distinguish between these two components of the fluorescence signal we decided to resort to the imaging techniques to continue the exploration of the interactions between the hydrophobic particles and the surfactant. The ability of confocal and two-photon microscopies to optically section the sample collecting the signal only from a small probe volume provided us with unsurpassed capabilities to differentiate between the hydrophobic surface and micellar environment of the fluorescent probe molecule.

7.3.2 Fluorescence Spectroscopy of Prodan in C18-SDS Construct. Implications for the Optical Design in the TPE Imaging Experiment

To gauge the microenvironmental polarity of SDS micelles and develop an optimal optical configuration for the ratiometric imaging we first examined solvatochromic characteristics of Prodan in several solvents with varying polarity. The peak of the Prodan fluorescence emission in hexane, acetonitrile, dimethylformamide, ethanol, and water was located at 400 nm, 453 nm, 453 nm, 486 and 523 nm respectively (Figure 7.5). As can be seen from the steady state fluorescence spectra, the polarity of 50 mM SDS solution falls between that of ethanol and that of water, since the emission peak of Prodan in SDS is observed at 500 nm. Table 7.3 summarizes the observed maxima of the excitation and emission spectra in each solvent, including 50 mM SDS. The observed peak locations are consistent with those reported in the literature [207,215,224].

Table 7.3. First peak wavelengths of the Prodan excitation and emission spectra in different solvents.

SOLVENT	EX I, NM	EM I, NM
Hexane	346	400
Acetonitrile	356	453
DMF	356	453
Ethanol	358	486
SDS	360	500
Water	356	523

Considering the peak wavelength of Prodan in 50 mM SDS solution, it would seem natural to use 500-nm dichroic mirror in ratiometric imaging experiments to split the fluorescence signal of Prodan in the more polar and the less polar environments. Detailed steady state fluorescence spectroscopy study of SDS solution incorporating Prodan and silica gel suggested that 440-nm dichroic would provide superior contrast. Using Xenon lamp excitation at 390 nm we obtained emission spectra of Prodan in aqueous 50 mM SDS before and after the addition of C18 silica beads into the solution (Figure 7.17). As expected, introduction of the silica particles significantly increased scattering of the sample (Figure 7.17A). Due to the increased solution scattering, the intensity of Prodan fluorescence decreased 6-fold, but the fluorescence maximum did not shift appreciably. Normalization of spectra confirmed overlapping of fluorescence maxima at 500 nm (Figure 7.17B). Striving to resolve the left shoulder of the fluorescence spectrum from the Prodan solution with C18 beads convoluted by the strong scattering signal, we shifted excitation to a shorter wavelength of 360 nm. Normalization of fluorescence spectra obtained with 360-nm excitation revealed the presence of an additional fluorescence band at 420 nm for the solution carrying silica particles (Figure 7.18C). Solvatochromic property of Prodan dictates that the fluorescence at shorter wavelength originates from the probe molecule in a less polar environment. Thus, we suggested that the fluorescence band at 420 nm is characteristic of the Prodan located in the C18-SDS construct on the surface of silica.

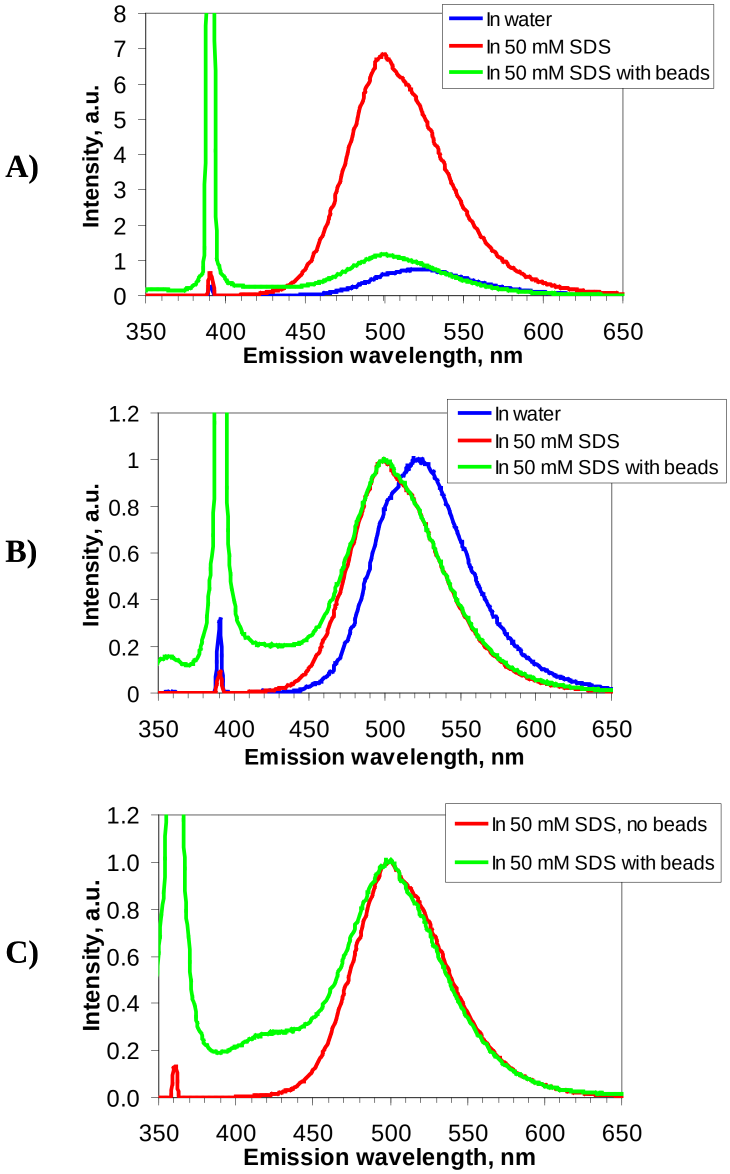

Figure 7.17. Fluorescence emission spectra of 10 µM Prodan in water, 50 mM pure SDS solution and 50 mM SDS solution containing C18 silica beads. (A) Original fluorescence spectra obtained with 390 nm excitation; (B) spectra in panel (A) normalized at the fluorescence peaks; (C) normalized fluorescence spectra obtained with 360 nm excitation.

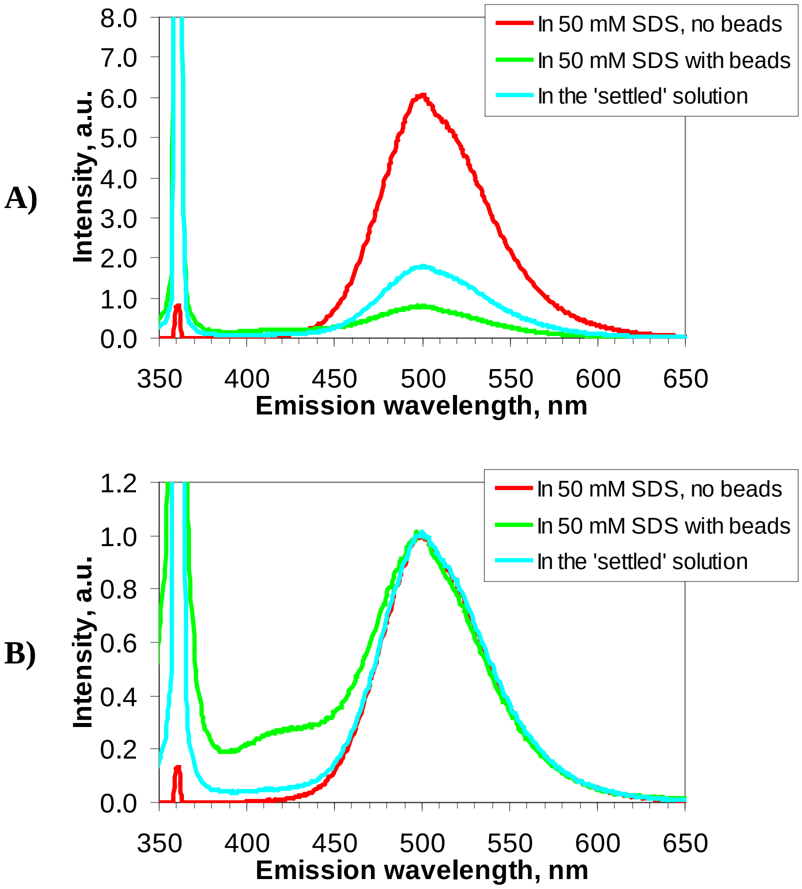

Figure 7.18. Fluorescence emission spectra of 10 µM Prodan in 50 mM SDS solution with and without C18 silica beads, and in 24 hours of rest upon the addition of the particles. (A) Original fluorescence spectra obtained with 360 nm excitation; (B) spectra in panel (A) normalized to unity at the fluorescence peaks.

To test this hypothesis, the particles in the solution were allowed to naturally precipitate overnight due to gravitational forces and the fluorescence of the solution over the precipitate was obtained. As depicted in Figure 7.18, there were three major changes in the fluorescence spectrum upon the particle precipitation. First, the fluorescence intensity of Prodan increased (Figure 7.18A), though it was still significantly lower than in the solution without the beads. Second, the scattering of the sample decreased somewhat, though again not to the levels of the particle-free SDS solution. Both of these spectral changes indicated the presence of a fraction of particles that were wetted partially and remained suspended in the solution due to close match of their density to the density of the bulk solution. Finally, the fluorescence band at 420 nm reduced significantly and became undistinguishable from the baseline (Figure 7.18B). Altogether, these observations confirmed the origins of the signal at 420 nm from the Prodan on the surfaces of the particles decorated with SDS surfactant.

The presence of the so-called blue-edge shoulder (between 420 and 450 nm) in the aqueous solutions of Prodan was observed by several researchers. We find it necessary to address the close proximity of this blue-edge shoulder and the 420-nm band scrutinized in our experiments. As illustrated in Figure 7.19, the aforementioned shoulder is significantly (about 6 times) smaller than the band observed in our system when the spectra are normalized at the peak wavelengths.

Bunker et al. assigned the origins of the blue-edge shoulder to the presence of water-soluble impurities in the Prodan sample [225]. A few years later, Sun et al. argued with this hypothesis by thoroughly investigating the dependence of the blue-edge shoulder fluorescence on the solution freshness, the preparation procedure and solvent composition [224]. In the study conducted by Sun et al., 10 μM Prodan solutions were prepared by two methods: “wet”, the addition of an aliquot of the stock solution directly to the cuvette with the desired solvent, and “dry”, identical to the protocol applied in our experiments, aliquot-evaporation with subsequent addition of the solvent.

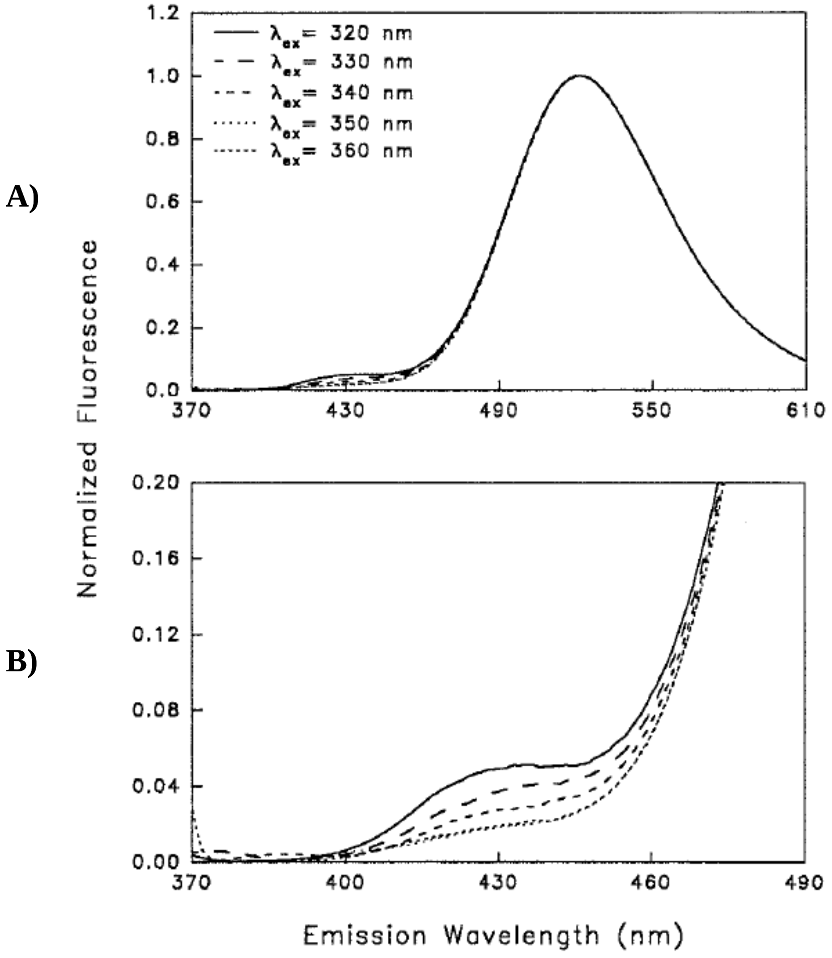

Figure 7.19. Fluorescence spectra of 10 µM aqueous solution of Prodan prepared from a stock ethanolic solution using “wet” method. (A) Normalized excitation-wavelength-dependent emission spectra of a 2-h-old sample; (B) expansion of the spectral region centered at 430 nm. Plots are obtained from reference [224].

It was concluded by Sun at al. that the shorter-wavelength emission shoulder in freshly prepared 10 μM water solution of Prodan was a result of Prodan aggregates and n-mers formation, because the solubility limit of Prodan in water (~3.5 μM) was exceeded [207]. It was emphasized that this blue-edge shoulder fluorescence was only apparent in the freshly prepared solutions and its intensity reached the maximum between 100 and 300 min following sample preparation. In addition, the intensity of the shoulder was more apparent when the stock solution of Prodan was prepared in acetonitrile and much less prominent, when ethanol was the solvent for the stock solution. Regardless of the solvent choice, samples prepared by the "dry" method exhibited almost no blue-edge shoulder.

The blue-edge shoulder discussed by Sun and coworkers was not observed in any of our spectra. The fact that our samples were prepared by the "dry" method and from the ethanolic stock solution correlates well with the lack of the shorter wavelength shoulder and observations of Sun et al. It is important to point out that although the Prodan concentration of 10 μM exceeds its solubility in aqueous solution, Prodan was expected to completely dissolve into the 50 mM micellar solution eliminating the possibility of crystal formation. We conclude that the 420-nm band, believed to have originated from the Prodan located in the less-polar environment of C18-SDS construct, is unlikely to be convoluted by the blue-edge fluorescence shoulder discussed in the literature.

Considering the results of the fluorescence spectroscopy experiments, we decided to use 440-nm dichroic mirror to accentuate the differentiation between the more polar microenvironment of SDS micelles (fluorescence peak of Prodan at 500 nm) and the less polar environment of C18-SDS construct on the external and internal surfaces of the silica particles (fluorescence peak of Prodan at 420 nm).

7.3.3 Ratiometric Imaging with Two-Photon Excitation

Based on the imaging system setup described in section 7.2.4, the ratio that served as a polarity indicator in the particle-surfactant system is defined as the fluorescence signal collected by detector PMT 2 (“green” channel - emission above 440 nm) divided by that collected by PMT 1 (“blue” channel - emission below 440 nm). Representative images from the two channels of the silica-C18-packed column in the process of being wetted with SDS solution are shown in Figure 7.20. Solvatochromic dye Prodan displays large red shifts in the emission maxima when exposed to more polar media. Thus, the “green” to “blue” signal ratio increases with an increase in the polarity of the microenvironment in which Prodan is located, and in the ratiometric images more polar areas appear brighter (Figure 7.191).

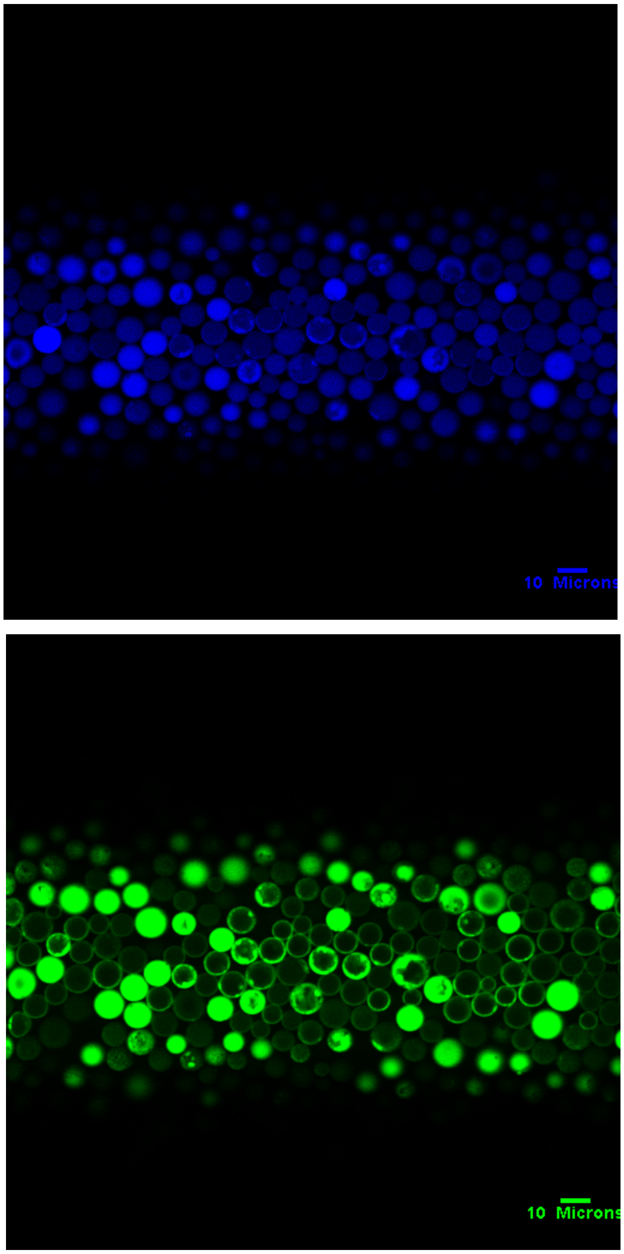

Figure 7.20. Dual channel two-photon excitation images of Luna-C18-packed microcolumn wetted with 10 μM solution of Prodan in 50 mM SDS. Fluorescence signal was split into two channels by a 440-nm dichroic beam splitter. Upper and lower panels are fluorescence images in the short and long wavelengths regions, respectively. Excitation wavelength: 770 nm.

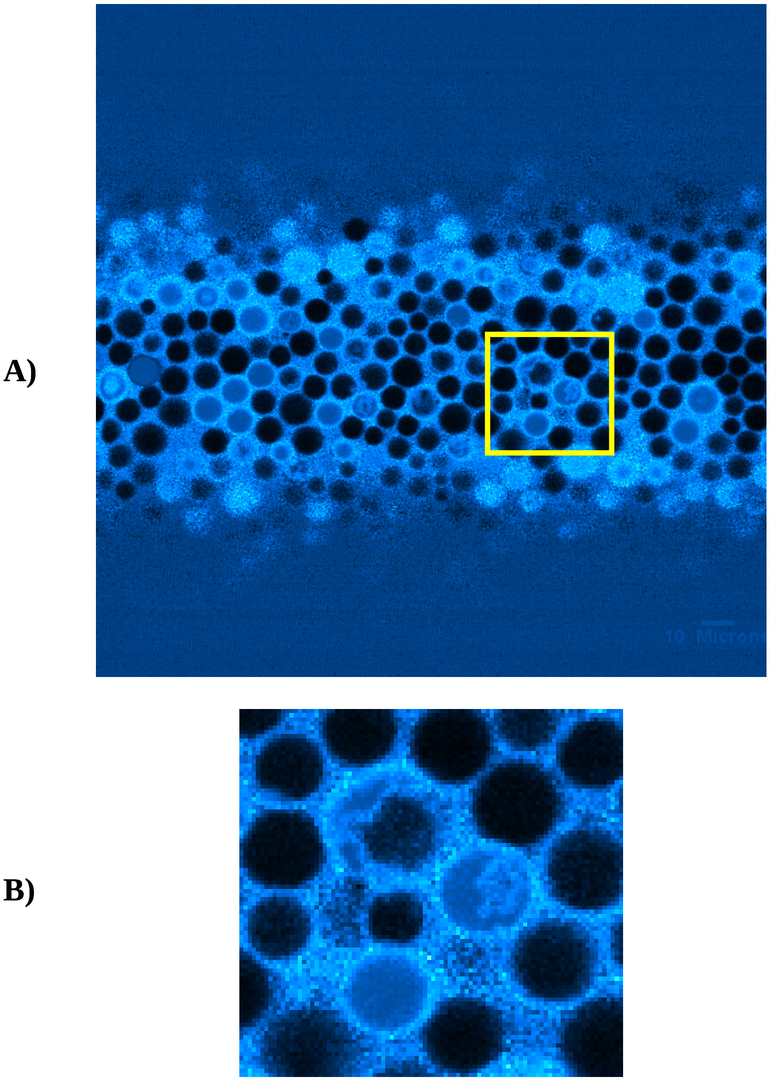

Figure 7.21. Ratiometric image of Luna-C18-packed microcolumn wetted with 10 μM solution of Prodan in 50 mM SDS obtained by pixel-by-pixel division of the green channel by the blue channel shown in Figure 7.20. (A) Image of the entire microcolumn; (B) expansion of the image area marked by the yellow box in panel (A).

It is well known that in the surfactant solution above the critical micellar concentration Prodan will be mostly present inside the micelles. On the close-up in Figure 7.21 we can see that in the particles that were completely wetted with SDS solution Prodan fluorescence ratio (“green”/“blue” ratio) is lower than the fluorescence ratio of the surrounding solution containing micelles. The decrease in the longer-wavelength fluorescence signal confirms the transition of Prodan from SDS micelles into the more non-polar environment of C18-SDS construct. The drop in microenvironment polarity of the solvatochromic probe results in the decrease of the ratiometric intensity.

A few particles in Figure 7.21 were observed in the midst of the wetting process, during which the solvent front penetrating inside the beads can be clearly distinguished due to its relatively high ratiometric fluorescence intensity. On the close-up image (Figure 7.21B) the polarity distribution within one bead partially wetted with the surfactant solution is even more apparent. Figure 7.20 shows a time-series montage of the area from Figure 7.21B; three hydrophobic nanoporous silica particles in the process of wetting can be observed. As we can see, the solvent front has higher polarity intensity ratio than already wetted areas of the bead, in which surfactant-C18 constructs have already been formed. The “green”/“blue” fluorescence ratio of the solution front inside the nanopores closely matches the ratio of the bulk micelle-rich solution. This fact confirms the presence of intact micelles in the aqueous solution front carried into the pores.

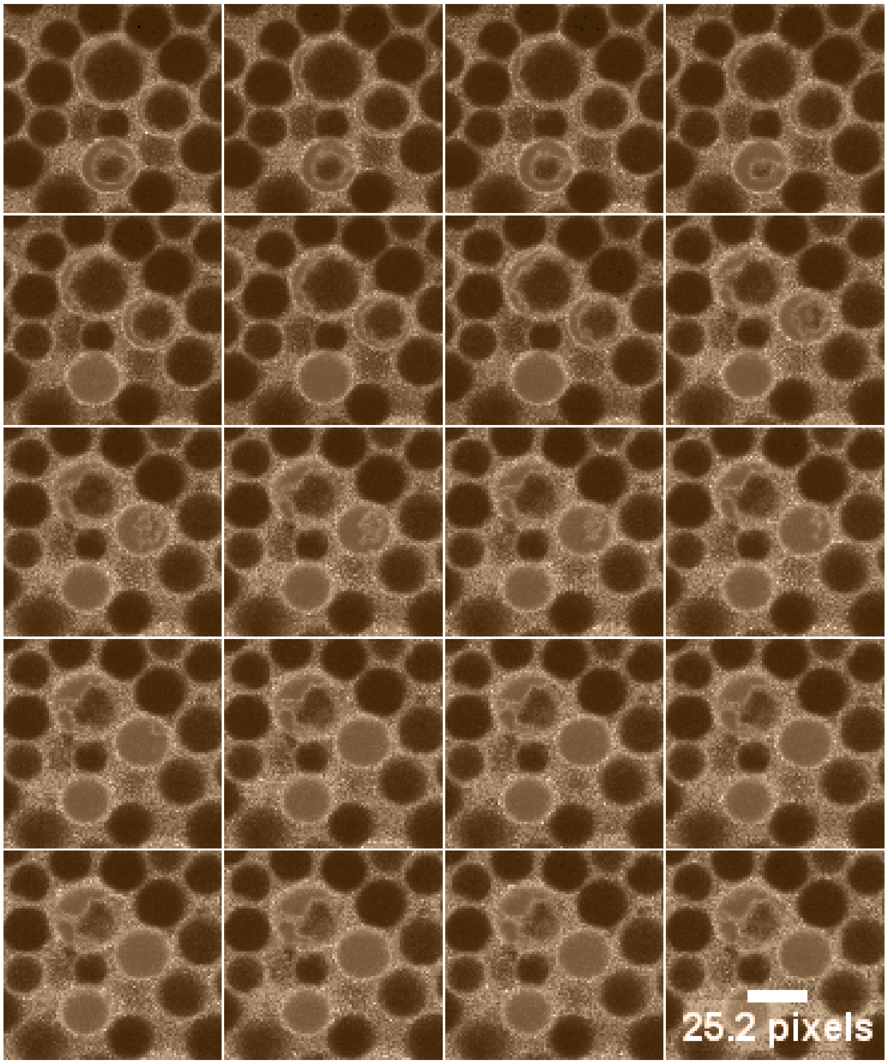

Figure 7.22. Montage of the time-sequence capturing three hydrophobic nanoporous silica particles in the process of wetting with 50 mM SDS solution containing 10 μM Prodan. Time between images was 3 s; scale bar of 25.2 pixels corresponds to 10 microns in the image field; sepia color-scheme was used for better contrast.

There are two possible scenarios for the Prodan's redistribution into the more non-polar environment of SDS-C18 construct once it is delivered inside the hydrophobic nanopores. (1) Upon arrival into the core of the silica particle, SDS micelles disintegrate into individual molecules due to the thermodynamically favorable opportunity of interaction with more non-polar C18 chains on the surface of the pores; released Prodan follows SDS molecules to the C18-derivatized surface. (2) Micelles stay intact throughout the wetting process, but Prodan molecules redistribute from the micelles into the more non-polar C18-surfactant construct, because of Prodan's large octanol/water partition coefficient and preference toward more non-polar environment. Mobility of Prodan in the system does not allow us to make the judgment on the preferential feasibility of one of the scenarios vs. the other. Nevertheless, we can envision that the question of the micelle fate upon the migration into the hydrophobic pore of C18 silica particle can be answered by covalently tagging surfactant molecules with a solvatochromic fluorescent probe.

7.4. Conclusions

Two-channel ratiometric two-photon excitation imaging with a polarity-sensitive fluorescent dye, Prodan, provided polarity-specific information on the dynamics of nanotransport in the pores of silica gel. As was shown in the steady state spectroscopy experiments, when dissolved in increasingly polar media, Prodan exhibits large red shifts in the maximum of its emission wavelength. The polarity of the 50 mM SDS solution, used for the wetting of the hydrophobic nanopores of C18 silica gel, was established to be intermediate between the polarities of ethanol and water. The polarity of the SDS-C18 construct formed on the surfaces of the particles was confirmed to be significantly lower than polarity of SDS micelles. This observation allowed up to optimize the ratiometric imaging system to successfully track nanotransport of intact micelles inside the nanopores derivatized with C18 chains.

On the basis of ratiometric imaging experiments with two-photon excitation, we confirmed with confidence that intact micelles act as carrier vehicles which bring Prodan into the hydrophobic nanopores of the C18 silica particles. In summary of this work, it is noteworthy to remark that the understanding of the polarity trends and the mechanisms of surfactant interaction with C18 silica beads open the opportunities for using these hydrophobic particles as drug delivery vehicles. On the other hand, proven capability to image micellar migration inside the hydrophobic pores in real time promises the applications on this method in nondestructive imaging of micellar and liposome penetration through the biological membranes, which is highly desired in medical and cosmetic research.

CHAPTER 8 FUTURE DIRECTIONS

The original idea to decorate the surface of the hydrophobic nanoporous silica particles with surfactant molecules to effectively solubilize them in aqueous solution was first introduced in the framework of tissue phantom design. The intriguing details of the interaction between the surfactant and the hydrophobic surface of the particles generated a wave of research projects in the area new to our group. By applying confocal imaging, we were able to confirm the wetting of the hydrophobic nanopores with the aqueous surfactant solution – imaging results are presented in Chapter 6 of this thesis. A serendipitous experiment conducted by Claudiu Brumaru generated a method for selective decoration of the particles' outer surface with surfactant molecules without pore wetting. C18-derivatized silica particles prepared in this fashion retain internal dryness and hydrophobicity of the nanopores while displaying a "coat" of surfactant molecules on the outer surface. Polar surfactant head-groups allow solubilization of these particles in the aqueous solution. We envision that such systems can find a variety of applications in separations, drug delivery, and biomedical imaging areas. Electrostatic effects that influence the distribution of the fluorescent probes in the C18-particle-surfactant construct can be employed to optimize the loading potential of the system.

Another aspect of surfactant-induced wetting of the hydrophobic nanopores - the migration of intact micelles through the pores of similar diameter - is a valuable primer for research prospects in the transdermal drug delivery field. Micelles and liposomes have long been known as skin penetration enhancers, but up to date no real-time imaging of the transdermal drug delivery has been done. The conclusions on the intactness of liposomes and micelles during the migration through the skin layers are based on indirect observations. Ratiometric imaging with a solvatochromic fluorescent probe as described in Chapter 7 offers a readily-adaptable methodology for the direct observation of transdermal target delivery.

The wealth of knowledge acquired in the area of tissue phantom preparation, discussed in Chapter 5, is expected to benefit the continued design of the in-house-built confocal system for phase-resolved fluorescence imaging. Generated MatLab programs for the comparison of the diagnostic methods, addressed in Chapters 3 and 4, can be used in the systematic processing of the spectral data once the analysis of real tissue samples in our lab is resumed. It would be especially interesting to test the performance of the diagnostic thresholds established through the analysis of the simulated spectra in discrimination of the real tissues from a substantially large dataset. The potential of the bivariate principal component analysis to differentiate between the spectra from adenomatous and cancerous tissues should be explored as well.

REFERENCES

1. Lichtman, J. W., and J. A. Conchello. "Fluorescence Microscopy." *Nature Methods* 2, no. 12 (2005): 910-919.

2. "Molecular Probes: The Handbook." in Invitrogen [database online]. [Cited 2009]. Available from http://www.invitrogen.com/site/us/en/home/References/Molecular-Probes-The-Handbook.html.

3. Wilson, T. *Confocal Microscopy.* Edited by T. Wilson. San Diego: Academic Press, 1990.

4. Davidovits, P., and M. D. Egger. "Scanning Laser Microscope." *Nature* 223, no. 5208 (1969): 831.

5. White, J. G., W. B. Amos, and M. Fordham. "An Evaluation of Confocal Versus Conventional Imaging of Biological Structures by Fluorescence Light Microscopy." *The Journal of Cell Biology* 105, no. 1 (1987): 41-48.

6. Paddock, S. W. *Confocal Microscopy Methods and Protocols*. Totowa, NJ: Humana Press, 1999.

7. Diaspro, A. and Sheppard,C. "Two-Photon Excitation Fluorescence Microscopy." In *Confocal and Two-Photon Microscopy: Foundations, Applications, and Advances.* Edited by A. Diaspro. New York: Wiley-Liss, 2002, 39-73.

8. Hoheisel, W., W. Jacobsen, B. Luttge, and W. Weiner. "Confocal Microscopy: Applications in Materials Science." *Macromolecular Materials and Engineering* 286, no. 11 (2001): 663-668.

9. Padari, K., P. Saalik, M. Hansen, K. Koppel, R. Raid, I. Langel, and M. Pooga. "Cell Transduction Pathways of Transportans." *Bioconjugate Chemistry* 16, no. 6 (2005): 1399-1410.

10. Aoyagi, H., T. Asami, H. Yoshizawa, C. Wanichanon, and S. Iwasaki. "Newly Developed Technique for Dual Localization of Keratins 13 and 14 by Fluorescence Immunohistochemistry." *Acta Histochemica* 110, no. 4 (2008): 324-332.

11. Singh, A., and K. P. Gopinathan. "Confocal Microscopy: A Powerful Technique for Biological Research." *Current Science* 74, no. 10 (1998): 841-851.

12. Heilker, R., L. Zemanova, M. J. Valler, and G. U. Nienhaus. "Confocal Fluorescence Microscopy for High-Throughput Screening of G-Protein Coupled Receptors." *Current Medicinal Chemistry* 12, no. 22 (2005): 2551-2559.

13. Pygall, S. R., J. Whetstone, P. Timmins, and C. D. Melia. "Pharmaceutical Applications of Confocal Laser Scanning Microscopy: The Physical Characterisation of Pharmaceutical Systems." *Advanced Drug Delivery Reviews* 59, no. 14 (2007): 1434-1452.

14. Chalfie, M., Y. Tu, G. Euskirchen, W. W. Ward, and D. C. Prasher. "Green Fluorescent Protein as a Marker for Gene Expression." *Science* 263, no. 5148 (1994): 802-805.

15. Lippincott-Schwartz, J., and G. H. Patterson. "Development and use of Fluorescent Protein Markers in Living Cells." *Science* 300, no. 5616 (2003): 87-91.

16. Shuman, H., J. M. Murray, and C. Dilullo. "Confocal Microscopy - an Overview." *BioTechniques* 7, no. 2 (1989): 154.

17. Hell, S. W., and E. H. K. Stelzer. "Lens Aberrations in Confocal Fluorescence Microscope." In *Handbook of Biological Confocal Microscopy.* Edited by J. B. Pawley. New York: Plenum Press, 1995, 347-354.

18. Wilke, V. "Optical-Scanning Microscopy - the Laser Scanning Microscope." *Scanning* 7, no. 2 (1985): 88-96.

19. Goldstein, S. R., T. Hubin, S. Rosenthal, and C. Washburn. "A Confocal Video-Rate Laser-Beam Scanning Reflected-Light Microscope with no Moving Parts." *Journal of Microscopy* 157, no. 1 (1990): 29-38.

20. Jiang, G., S. Attiya, G. Ocvirk, W. E. Lee, and D. J. Harrison. "Red Diode Laser Induced Fluorescence Detection with a Confocal Microscope on a Microchip for Capillary Electrophoresis." *Biosensors and Bioelectronics* 14, no. 10-11 (2000): 861-869.

21. Stelzer, E. H. K. "Practical Limits to Resolution in Fluorescence Light Microscopy." In *Imaging Neurons : A Laboratory Manual.* Edited by A. Konnerth, F. Lanni and R. Yuste. New York: Cold Spring Harbor Laboratory Press, 2000, 12.1-12.9.

22. Born, M., E. Wolf, and A. B. Bhatia. *Principles of Optics: Electromagnetic Theory of Propagation, Interference and Diffraction of Light*. 7th expanded ed. Cambridge; New York: Cambridge University Press, 1999.

23. Hell, S., G. Reiner, C. Cremer, and E. H. K. Stelzer. "Aberrations in Confocal Fluorescence Microscopy Induced by Mismatches in Refractive-Index." *Journal of Microscopy-Oxfor*d 169, (1993): 391-405.

24. Inou, S., and K. R. Spring. *Video Microscopy: The Fundamentals*. 2nd ed. New York: Plenum Press, 1997.

25. Jonkman, J. and Stelzer,E. "Resolution and Contrast in Confocal and Two-Photon Microscopy." In *Confocal and Two-Photon Microscopy: Foundations, Applications, and Advances.* Edited by A. Diaspro. New York: Wiley-Liss, 2002, 101-125.

26. Sacek, V. "Telescope Resolution." [Cited 2009]. Available from http://www.telescope-optics.net/telescope_resolution.htm.

27. Stelzer, E. H. K. "Contrast, Resolution, Pixelation, Dynamic Range and Signal-to-Noise Ratio: Fundamental Limits to Resolution in Fluorescence Light Microscopy." *Journal of Microscop*y 189, (1998): 15-24.

28. Pawley, J. B. *Handbook of Biological Confocal Microscopy.* 2nd ed. New York: Plenum Press, 1995.

29. Claxton, N. S., T. J. Fellers, and M. W. Davidson. "Laser Scanning Confocal Microscopy." [Cited 2009]. Available from http://www.olympusconfocal.com/theory/LSCMIntro.pdf.

30. Hecht, E. *Optics*. 3rd ed. Reading, MA: Addison-Wesley Publishing, 1998.

31. Abramowitz, M., K. R. Spring, H. E. Keller, and M. W. Davidson. "Basic Principles of Microscope Objectives." *BioTechnique*s 33, no. 4 (2002): 772.

32. Lakowicz, J. R. *Principles of Fluorescence Spectroscopy.* New York: Kluwer Academic/Plenum Publishers, 1999.

33. Gopalakrishnan, G., I. Rouiller, D. R. Colman, and R. B. Lennox. "Supported Bilayers Formed from Different Phospholipids on Spherical Silica Substrates." *Langmuir: the ACS Journal of Surfaces and Colloid*s 25, no. 10 (2009): 5455-5458.

34. Phair, R. D., and T. Misteli. "Kinetic Modelling Approaches to in Vivo Imaging." *Nature Reviews Molecular Cell Biology* 2, no. 12 (2001): 898-907.

35. Potter, S. M. "Vital Imaging: Two Photons are Better than One." *Current Biology* 6, no. 12 (1996): 1595-1598.

36. So, P. T. C., C. Y. Dong, B. R. Masters, and K. M. Berland. "Two-Photon Excitation Fluorescence Microscopy." *Annual Review of Biomedical Engineering* 2, (2000): 399-429.

37. Stutzmann, G. E., F. M. LaFerla, and I. Parker. "Ca2+ Signaling in Mouse Cortical Neurons Studied by Two-Photon Imaging and Photoreleased Inositol Triphosphate." *The Journal of Neuroscience : the Official Journal of the Society for Neuroscience* 23, no. 3 (2003): 758-765.

38. Svoboda, K., and R. Yasuda. "Principles of Two-Photon Excitation Microscopy and its Applications to Neuroscience." *Neuron* 50, no. 6 (2006): 823-839.

39. Sheppard, C. J. R., and R. Kompfner. "Resonant Scanning Optical Microscope." *Applied Optics* 17, no. 18 (1978): 2879-2882.

40. Gannaway, J. N., and C. J. R. Sheppard. "2nd-Harmonic Imaging in Scanning Optical Microscope." *Optical and Quantum Electronics* 10, no. 5 (1978): 435-439.

41. Spence, D. E., P. N. Kean, and W. Sibbett. "60-fsec Pulse Generation from a Self-Mode-Locked Ti-Sapphire Laser." *Optics Letters* 16, no. 1 (1991): 42-44.

42. Fisher, W. G., E. A. Wachter, M. Armas, and C. Seaton. "Titanium:Sapphire Laser as an Excitation Source in Two-Photon Spectroscopy." *Applied Spectroscopy* 51, no. 2 (1997): 218-226.

43. Wise, F. "Lasers for Two-Photon Microscopy." In *Imaging: A Laboratory Manual.* Edited by R. Yuste, F. Lanni and A. Konnerth. Cold Spring Harbor, NY: Cold Spring Harbor Press, 1999, 18.1-18.9.

44. Diaspro, A., and M. Robello. "Two-Photon Excitation of Fluorescence for Three-Dimensional Optical Imaging of Biological Structures." *Journal of Photochemistry and Photobiology B, Biology* 55, no. 1 (2000): 1-8.

45. Piston, D. W., T. J. Fellers, and M. W. Davidson. "Fundamentals and Applications in Multiphoton Excitation Microscopy." [Cited 2009]. Available from http://www.microscopyu.com/articles/fluorescence/multiphoton/multiphotonintro.html.

46. Oheim, M., D. J. Michael, M. Geisbauer, D. Madsen, and R. H. Chow. "Principles of Two-Photon Excitation Fluorescence Microscopy and Other Nonlinear Imaging Approaches." *Advanced Drug Delivery Reviews* 58, no. 7 (2006): 788-808.

47. Piston, D. W. "Imaging Living Cells and Tissues by Two-Photon Excitation Microscopy." *Trends in Cell Biology* 9, no. 2 (1999): 66-69.

48. Patterson, G. H., and D. W. Piston. "Photobleaching in Two-Photon Excitation Microscopy." *Biophysical Journal* 78, no. 4 (2000): 2159-2162.

49. Straub, M., P. Lodemann, P. Holroyd, R. Jahn, and S. W. Hell. "Live Cell Imaging by Multifocal Multiphoton Microscopy." *European Journal of Cell Biology* 79, no. 10 (2000): 726-734.

50. Mainen, Z. F., M. Maletic-Savatic, S. H. Shi, Y. Hayashi, R. Malinow, and K. Svoboda. "Two-Photon Imaging in Living Brain Slices." *Methods (San Diego, Calif.)* 18, no. 2 (1999): 231-9, 181.

51. Theer, P., M. T. Hasan, and W. Denk. "Two-Photon Imaging to a Depth of 1000 Micron in Living Brains by use of a Ti:Al_2O_3 Regenerative Amplifier." *Optics Letters* 28, no. 12 (2003): 1022-1024.

52. Helmchen, F., and W. Denk. "New Developments in Multiphoton Microscopy." *Current Opinion in Neurobiology* 12, no. 5 (2002): 593-601.

53. Yoder, E. J., and D. Kleinfeld. "Cortical Imaging through the Intact Mouse Skull Using Two-Photon Excitation Laser Scanning Microscopy." *Microscopy research and technique* 56, no. 4 (2002): 304-305.

54. Helmchen, F., M. S. Fee, D. W. Tank, and W. Denk. "A Miniature Head-Mounted Two-Photon Microscope. High-Resolution Brain Imaging in Freely Moving Animals." *Neuron* 31, no. 6 (2001): 903-912.

55. Kalb, J., T. Nielsen, M. Fricke, M. Egelhaaf, and R. Kurtz. "In Vivo Two-Photon Laser-Scanning Microscopy of Ca^{2+} Dynamics in Visual Motion-Sensitive Neurons." *Biochemical and Biophysical Research Communications* 316, no. 2 (2004): 341-347.

56. Konig, K., T. W. Becker, P. Fischer, I. Riemann, and K. J. Halbhuber. "Pulse-Length Dependence of Cellular Response to Intense Near-Infrared Laser Pulses in Multiphoton Microscopes." *Optics Letter*s 24, no. 2 (1999): 113-115.

57. Nguyen, Q. T., N. Callamaras, C. Hsieh, and I. Parker. "Construction of a Two-Photon Microscope for Video-Rate Ca^{2+} Imaging." *Cell Calciu*m 30, no. 6 (2001): 383-393.

58. Denk, W., K. R. Delaney, A. Gelperin, D. Kleinfeld, B. W. Strowbridge, D. W. Tank, and R. Yuste. "Anatomical and Functional Imaging of Neurons Using 2-Photon Laser Scanning Microscopy." *Journal of Neuroscience Methods* 54, no. 2 (1994): 151-162.

59. Pons, T., L. Moreaux, and J. Mertz. "Photoinduced Flip-Flop of Amphiphilic Molecules in Lipid Bilayer Membranes." *Physical Review Letters* 89, no. 28 Pt 1 (2002): 288104.

60. *Cancer Facts and Figures.* Atlanta: American Cancer Society, 2009.

61. Winawer, S. J., R. H. Fletcher, L. Miller, F. Godlee, M. H. Stolar, C. D. Mulrow, S. H. Woolf, S. N. Glick, T. G. Ganiats, J. H. Bond, L. Rosen, J. G. Zapka, S. J. Olsen, F. M. Giardiello, J. E. Sisk, R. van Antwerp, C. BrownDavis, D. A. Marciniak, and R. J. Mayer. "Colorectal Cancer Screening: Clinical Guidelines and Rationale." *Gastroenterology* 112, no. 2 (1997): 594-642.

62. Dacosta, R. S., B. C. Wilson, and N. E. Marcon. "New Optical Technologies for Earlier Endoscopic Diagnosis of Premalignant Gastrointestinal Lesions." *Journal of Gastroenterology and Hepatology* 17, (2002): S85-S104.

63. Richards-Kortum, R., and E. Sevick-Muraca. "Quantitative Optical Spectroscopy for Tissue Diagnosis." *Annual Review of Physical Chemistry* 47, (1996): 555-606.

64. Prosst, R. L., and J. Gahlen. "Fluorescence Diagnosis of Colorectal Neoplasms: A Review of Clinical Applications." *International Journal of Colorectal Disease* 17, (2002): 1-10.

65. Backman, V., M.B. Wallace, I. T. Perelman, J. T. Arendt, R. Gurjar, and M. G. Muller. "Detection of Preinvasive Cancer Cells." *Nature* 406, no. 6791 (2000): 35.

66. Zonios, G., R. Cothren, J. M. Crawford, M. Fitzmaurice, R. Manoharan, J. Van Dam, and M. S. Feld. "Spectral Pathology." *Annals of the New York Academy of Sciences* 838, (1998): 108-115.

67. Schomacker, K. T., J. K. Frisoli, C. C. Compton, T. J. Flotte, J. M. Richter, N. S. Nishioka, and T. F. Deutsch. "Ultraviolet Laser-Induced Fluorescence of Colonic Tissue - Basic Biology and Diagnostic Potential." *Lasers in Surgery and Medicine* 12, no. 1 (1992): 63-78.

68. Cothren, R. M., M. V. Sivak, J. VanDam, R. E. Petras, M. Fitzmaurice, J. M. Crawford, J. Wu, J. F. Brennan, R. P. Rava, R. Manoharan, and M. S. Feld. "Detection of Dysplasia at Colonoscopy Using Laser-Induced Fluorescence: A Blinded Study." *Gastrointestinal Endoscopy* 44, no. 2 (1996): 168-176.

69. Wagnieres, G. A., A. P. Studzinski, and H. E. van den Bergh. "Endoscopic Fluorescence Imaging System for Simultaneous Visual Examination and Photodetection of Cancers." *Review of Scientific Instruments* 68, no. 1 (1997): 203-212.

70. Haringsma, J., and G. N. J. Tytgat. "Fluorescence and Autofluorescence." *Best Practice & Research in Clinical Gastroenterology* 13, no. 1 (1999): 1-10.

71. Wagnieres, G. A., W. M. Star, and B. C. Wilson. "In Vivo Fluorescence Spectroscopy and Imaging for Oncological Applications." *Photochemistry and Photobiology* 68, no. 5 (1998): 603-632.

72. Sokolov, K., M. Follen, and R. Richards-Kortum. "Optical Spectroscopy for Detection of Neoplasia." *Current Opinion in Chemical Biology* 6, no. 5 (2002): 651-658.

73. Gill, E. M., G. M. Palmer, and N. Ramanujam. "Steady-State Fluorescence Imaging of Neoplasia." *Methods in Enzymology* 361, (2003): 452-481.

74. Crowell, E., J. Cox, and L. Geng. "Potential of Fluorescence Spectroscopy for Cancer Diagnosis." *Abstracts of Papers of the American Chemical Society* 222, (2001): U98-U98.

75. Crowell, E., G. F. Wang, J. Cox, C. P. Platz, and L. Geng. "Correlation Coefficient Mapping in Fluorescence Spectroscopy: Tissue Classification for Cancer Detection." *Analytical Chemistry* 77, no. 5 (2005): 1368-1375.

76. Wang, G. F., C. P. Platz, and M. L. Geng. "Probability-Based Differential Normalized Fluorescence Bivariate Analysis for the Classification of Tissue Autofluorescence Spectra." *Applied Spectroscopy* 60, no. 5 (2006): 545-550.

77. Kapadia, C. R., F. W. Cutruzzola, K. M. O'Brien, M. L. Stetz, R. Enriquez, and L. I. Deckelbaum. "Laser-Induced Fluorescence Spectroscopy of Human Colonic Mucosa-Detection of Adenomatous Transformation." *Gastroenterology* 99, (1990): 150-157.

78. Bottiroli, G., A. C. Croce, D. Locatelli, R. Marchesini, E. Pignoli, S. Tomatis, C. Cuzzoni, S. Dipalma, M. Dalfante, and P. Spinelli. "Natural Fluorescence of Normal and Neoplastic Human Colon - a Comprehensive Ex-Vivo Study." *Lasers in Surgery and Medicine* 16, no. 1 (1995): 48-60.

79. Fiarman, G. S., M. H. Nathanson, A. B. West, L. I. Deckelbaum, L. Kelly, and C. R. Kapadia. "Differences in Laser-Induced Autofluorescence between Adenomatous and Hyperplastic Polyps and Normal Colonic Mucosa by Confocal Microscopy." *Digestive Diseases and Sciences* 40, no. 6 (1995): 1261-1268.

80. Izuishi, K., H. Tajiri, T. Fujii, N. Boku, A. Ohtsu, T. Ohnishi, M. Ryu, T. Kinoshita, and S. Yoshida. "The Histological Basis of Detection of Adenoma and Cancer in the Colon by Autofluorescence Endoscopic Imaging." *Endoscopy* 31, no. 7 (1999): 511-516.

81. Marchesini, R., M. Brambilla, E. Pignoli, G. Bottiroli, A. C. Croce, M. Dalfante, P. Spinelli, and S. Dipalma. "Light-Induced Fluorescence Spectroscopy of Adenomas, Adenocarcinomas and Nonneoplastic Mucosa in Human Colon. 1. In Vitro Measurements." *Journal of Photochemistry and Photobiology B, Biology* 14, no. 3 (1992): 219-230.

82. VoDinh, T., M. Panjehpour, B. F. Overholt, C. Farris, P. Buckley, and R. Sneed. "In Vivo Cancer Diagnosis of the Esophagus Using Differential Normalized Fluorescence (DNF) Indices." *Lasers in Surgery and Medicine* 16, no. 1 (1995): 41-47.

83. Ramanujam, N., M. Follen-Mitchell, A. Mahadevan-Jansen, S. Thomson, G. Staerkel, A. Malpica, T. Wright, N. Atkinson, and R. Richards-Kortum. "Cervical Precancer Detection Using Multivariate Statistical Algorithm Based on Laser-Induced Fluorescence Spectra at Multiple Excitation Wavelengths." *Photochemistry and Photobiology* 64, (1996): 720-735.

84. Wang, C. Y., J. K. Lin, B. F. Chen, and H. H. K. Chiang. "Autofluorescence Spectroscopic Differentiation between Normal and Cancerous Colorectal Tissues by Means of a Two-Peak Ratio Algorithm." *Journal of the Formosan Medical Association* 98, (1999): 837-843.

85. Eker, C., S. Montan, E. Jaramillo, K. Koizumi, C. Rubio, S. Andersson-Engels, K. Svanberg, S. Svanberg, and P. Slezak. "Clinical Spectral Characterisation of Colonic Mucosal Lesions Using Autofluorescence and Delta Aminolevulinic Acid Sensitisation." *Gut* 44, no. 4 (1999): 511-518.

86. Haringsma, J., G. N. J. Tytgat, H. Yano, H. Iishi, M. Tatsuta, T. Ogihara, H. Watanabe, N. Sato, N. Marcon, B. C. Wilson, and R. W. Cline. "Autofluorescence Endoscopy: Feasibility of Detection of GI Neoplasms Unapparent to White Light Endoscopy with an Evolving Technology." *Gastrointestinal Endoscopy* 53, no. 6 (2001): 642-650.

87. Majumder, S. K., N. Ghosh, S. Kataria, and P. K. Gupta. "Nonlinear Pattern Recognition for Laser-Induced Fluorescence Diagnosis of Cancer." *Lasers in Surgery and Medicine* 33, (2003): 48-56.

88. Mayinger, B., M. Jordan, P. Horner, C. Gerlach, S. Muehldorfer, B. R. Bittorf, K. E. Matzel, W. Hohenberger, E. G. Hahn, and K. Guenther. "Endoscopic Light-Induced Autofluorescence Spectroscopy for the Diagnosis of Colorectal Cancer and Adenoma." *Journal of Photochemistry and Photobiology B-Biology* 70, no. 1 (2003): 13-20.

89. O'Brien, K. M., A. F. Gmitro, G. R. Gindi, M. L. Stetz, F. W. Cutruzzola, L. I. Laifer, and L. I. Deckelbaum. "Development and Evaluation of Spectral Classification Algorithms for Fluorescence Guided Laser Angioplasty." *IEEE Transactions on Biomedical Engineering* 36, no. 4 (1989): 424-431.

90. Li, Y., P. G. de Silva, L. Xi, A. van Winkle, J. J. Lin, S. Ahmed, and M. L. Geng. "Separation of Flavins and Nicotinamide Cofactors in Chinese Hamster Ovary Cells by Capillary Electrophoresis." *Biomedical Chromatography* 22, no. 12 (2008): 1374-1384.

91. Wang, G., E. Crowell, J. Cox, C. P. Platz, and M. L. Geng. "Comparison of Spectral Analysis Methods for Autofluorescence Cancer Diagnosis." *Lasers in Surgery and Medicine* (Submitted for publication).

92. Duda, R. O., and P. E. Hart. *Pattern Classification and Scene Analysis.* New York: Wiley, 1973.

93. VoDinh, T., M. Panjehpour, B. F. Overholt, and P. Buckley. "Laser-Induced Differential Fluorescence for Cancer Diagnosis without Biopsy." *Applied Spectroscopy* 51, (1997): 58-63.

94. Barton, F. E., D. S. Himmelsbach, J. H. Duckworth, and M. J. Smith. "2-Dimensional Vibration Spectroscopy - Correlation of Midinfrared and Near-Infrared Regions." *Applied Spectroscopy* 46, (1992): 420-429.

95. Sasic, S., and Y. Ozaki. "Statistical Two-Dimensional Correlation Spectroscopy: Its Theory and Applications to Sets of Vibrational Spectra." *Analytical Chemistry* 73, (2001): 2294-2301.

96. Wang, G., and M. L. Geng. "Statistical and Generalized Two-Dimensional Correlation Spectroscopy of Multiple Ionization States. Fluorescence of Neurotransmitter Serotonin." *Analytical Chemistry, no.* 77 (2005): 20-29.

97. Noda, I. "Generalized Two-Dimensional Correlation Method Application to Infrared, Raman, and Other Types of Spectroscopy." *Applied Spectroscopy* 47, (1993): 1329-1336.

98. Paquet, E., M. Y. Hou, and S. L. Chin. "Correlation and Covariance Mapping Applied to Tunnel Ionization of Heavy Water." *Journal of Physics B: Atomic, Molecular and Optical Physics* 25, (1992): L95-L100.

99. Fisher, R. A. "Frequency Distribution of the Values of the Correlation Coefficient in Samples of an Indefinitely Large Population." *Biometrika,* no. 10, (1915): 507-521.

100. Hawkins, D. L. "Using U Statistics to Derive the Asymptotic Distribution of Fisher's Z Statistic." *The American Statistician* 43, (1989): 235-237.

101. Mourant, J. R., T. Fuselier, J. Boyer, T. M. Johnson, and I. J. Bigio. "Predictions and Measurements of Scattering and Absorption Over Broad Wavelength Ranges in Tissue Phantoms." *Applied Optics* 36, no. 4 (1997): 949-957.

102. Wagnieres, G., S. G. Cheng, M. Zellweger, N. Utke, D. Braichotte, J. P. Ballini, and H. vandenBergh. "An Optical Phantom with Tissue-Like Properties in the Visible for Use in PDT and Fluorescence Spectroscopy." *Physics in Medicine and Biology* 42, no. 7 (1997): 1415-1426.

103. Zhang, Q. G., M. G. Muller, J. Wu, and M. S. Feld. "Turbidity-Free Fluorescence Spectroscopy of Biological Tissue." *Optics Letters* 25, no. 19 (2000): 1451-1453.

104. Drezek, R., K. Sokolov, U. Utzinger, I. Boiko, A. Malpica, M. Follen, and R. Richards-Kortum. "Understanding the Contributions of NADH and Collagen to Cervical Tissue Fluorescence Spectra: Modeling, Measurements, and Implications." *Journal of Biomedical Optics* 6, no. 4 (2001): 385-396.

105. Sokolov, K., J. Galvan, A. Myakov, A. Lacy, R. Lotan, and R. Richards-Kortum. "Realistic Three-Dimensional Epithelial Tissue Phantoms for Biomedical Optics." *Journal of Biomedical Optics* 7, no. 1 (2002): 148-156.

106. Zonios, G. I., R. M. Cothren, J. T. Arendt, J. Wu, J. VanDam, J. M. Crawford, R. Manoharan, and M. S. Feld. "Morphological Model of Human Colon Tissue Fluorescence." *IEEE Transactions on Biomedical Engineering* 43, no. 2 (1996): 113-122.

107. Watmough, D. J. "Trans-Illumination of Breast Tissues - Factors Governing Optimal Imaging of Lesions." *Radiology* 147, no. 1 (1983): 89-92.

108. Linford, J., S. Shalev, J. Bews, R. Brown, and H. Schipper. "Development of a Tissue-Equivalent Phantom for Diaphanography." *Medical Physics* 13, no. 6 (1986): 869-875.

109. Grossweiner, L. I., J. H. Hill, and R. V. Lobraico. "Photodynamic Therapy of Head and Neck Squamous-Cell Carcinoma - Optical Dosimetry and Clinical-Trial." *Photochemistry and Photobiology* 46, no. 5 (1987): 911-917.

110. Jacques, S. L., and S. A. Prahl. "Modeling Optical and Thermal Distributions in Tissue during Laser Irradiation." *Lasers in Surgery and Medicine* 6, no. 6 (1987): 494-503.

111. Flock, S. T., B. C. Wilson, and M. S. Patterson. "Total Attenuation Coefficients and Scattering Phase Functions of Tissues and Phantom Materials at 633-nm." *Medical Physics* 14, no. 5 (1987): 835-841.

112. Nauta, J. M., H. L. L. M. van Leengoed, W. M. Star, J. L. N. Roodenburg, M. J. H. Witjes, and A. Vermey. "Photodynamic Therapy of Oral Cancer - A Review of Basic Mechanisms and Clinical Applications." *European Journal of Oral Sciences* 104, no. 2 (1996): 69-81.

113. Star, W. M. "Light Dosimetry in Vivo." *Physics in Medicine and Biology* 42, no. 5 (1997): 763-787.

114. Wilson, B. C., and S. L. Jacques. "Optical Reflectance and Transmittance of Tissues - Principles and Applications." *IEEE Journal of Quantum Electronics* 26, no. 12 (1990): 2186-2199.

115. Firbank, M., and D. T. Delpy. "A Design for a Stable and Reproducible Phantom for Use in Near-Infrared Imaging and Spectroscopy." *Physics in Medicine and Biology* 38, no. 6 (1993): 847-853.

116. Fujimoto, J. G., C. Pitris, S. A. Boppart, and M. E. Brezinski. "Optical Coherence Tomography: An Emerging Technology for Biomedical Imaging and Optical Biopsy." *Neoplasia* 2, no. 1-2 (2000): 9-25.

117. Dennis, T., S. D. Dyer, A. Dienstfrey, G. Singh, and P. Rice. "Analyzing Quantitative Light Scattering Spectra of Phantoms Measured with Optical Coherence Tomography." *Journal of Biomedical Optics* 13, no. 2 (2008).

118. Tomlins, P. H., and R. K. Wang. "Theory, Developments and Applications of Optical Coherence Tomography." *Journal of Physics D - Applied Physics* 38, (2005): 2519-2535.

119. Storen, T., A. Royset, L. O. Svaasand, and T. Lindmo. "Functional Imaging of Dye Concentration in Tissue Phantoms by Spectroscopic Optical Coherence Tomography." *Journal of Biomedical Optics* 10, no. 2 (2005).

120. Sun, J. T., K. Fu, M. Q. Zhu, L. Bickford, E. Post, and R. Drezek. "Near-Infrared Quantum Dot Contrast Agents for Fluorescence Tissue Imaging: A Phantom Study." *Current Nanoscience* 5, no. 2 (2009): 160-166.

121. Sevick-Muraca, E. M., J. P. Houston, and M. Gurfinkel. "Fluorescence-Enhanced, Near Infrared Diagnostic Imaging with Contrast Agents." *Current Opinion in Chemical Biology* 6, no. 5 (2002): 642-650.

122. Pan, M. C., C. H. Chen, M. C. Pan, and Y. M. Shyr. "Near Infrared Tomographic System Based on High Angular Resolution Mechanism - Design, Calibration, and Performance." *Measurement* 42, no. 3 (2009): 377-389.

123. Stasic, D., T. J. Farrell, and M. S. Patterson. "The use of Spatially Resolved Fluorescence and Reflectance to Determine Interface Depth in Layered Fluorophore Distributions." *Physics in Medicine and Biology* 48, no. 21 (2003): 3459-3474.

124. Pogue, B. W., and M. S. Patterson. "Review of Tissue Simulating Phantoms for Optical Spectroscopy, Imaging and Dosimetry." *Journal of Biomedical Optics* 11, no. 4 (2006): 041102-1-041102-16.

125. Streuli, C. "Extracellular Matrix Remodelling and Cellular Differentiation." *Current Opinion in Cell Biology* 11, no. 5 (1999): 634-640.

126. Durkin, A. J., S. Jaikumar, and R. Richards-Kortum. "Optically Dilute, Absorbing, and Turbid Phantoms for Fluorescence Spectroscopy of Homogeneous and Inhomogeneous Samples." *Applied Spectroscopy* 47, no. 12 (1993): 2114-2121.

127. Nieman, L., A. Myakov, J. Aaron, and K. Sokolov. "Optical Sectioning Using a Fiber Probe with an Angled Illumination-Collection Geometry: Evaluation in Engineered Tissue Phantoms." *Applied Optics* 43, no. 6 (2004): 1308-1319.

128. Cubeddu, R., A. Pifferi, P. Taroni, A. Torricelli, and G. Valentini. "A Solid Tissue Phantom for Photon Migration Studies." *Physics in Medicine and Biology* 42, no. 10 (1997): 1971-1979.

129. Manohar, S., A. Kharine, J. C. G. van Hespen, W. Steenbergen, and T. G. van Leeuwen. "Photoacoustic Mammography Laboratory Prototype: Imaging of Breast Tissue Phantoms." *Journal of Biomedical Optics* 9, no. 6 (2004): 1172-1181.

130. Spirou, G. M., A. A. Oraevsky, I. A. Vitkin, and W. M. Whelan. "Optical and Acoustic Properties at 1064 nm of Polyvinyl Chloride-Plastisol for use as a Tissue Phantom in Biomedical Optoacoustics." *Physics in Medicine and Biology* 50, no. 14 (2005): N141-N153.

131. Chandrasekharan, N., B. Gonzales, and B. M. Cullum. "Non-Resonant Multiphoton Photoacoustic Spectroscopy for Noninvasive Subsurface Chemical Diagnostics." *Applied Spectroscopy* 58, no. 11 (2004): 1325-1333.

132. Ghosh, N., S. K. Majumder, and P. K. Gupta. "Polarized Fluorescence Spectroscopy of Human Tissues." *Optics Letters* 27, no. 22 (2002): 2007-2009.

133. Biswal, N. C., S. Gupta, N. Ghosh, and A. Pradhan. "Recovery of Turbidity Free Fluorescence from Measured Fluorescence: an Experimental Approach." *Optics Express* 11, (2003): 3320-3331.

134. Gardner, C. M., S. L. Jacques, and A. J. Welch. "Fluorescence Spectroscopy of Tissue: Recovery of Intrinsic Fluorescence from Measured Fluorescence." *Applied Optics* 35, no. 10 (1996): 1780-1792.

135. Bohren, C. F., and D. R. Huffman. *Absorption and Scattering of Light by Small Particles.* New York: John Wiley and Sons, 1983.

136. Buranda, T., J. Huang, G. V. Ramarao, L. K. Ista, R. S. Larson, T. L. Ward, L. A. Sklar, and G. P. Lopez. "Biomimetic Molecular Assemblies on Glass and Mesoporous Silica Microbeads for Biotechnology." *Langmuir* 19, no. 5 (2003): 1654-1663.

137. Barbe, C., J. Bartlett, L. G. Kong, K. Finnie, H. Q. Lin, M. Larkin, S. Calleja, A. Bush, and G. Calleja. "Silica Particles: A Novel Drug-Delivery System." *Advanced Materials* 16, no. 21 (2004): 1959-1966.

138. Rosenholm, J. M., and M. Linden. "Towards Establishing Structure-Activity Relationships for Mesoporous Silica in Drug Delivery Applications." *Journal of Controlled Release: Official Journal of the Controlled Release Society* 128, no. 2 (2008): 157-164.

139. Freeney, R. M., and M. L. Geng. *Manuscript in preparation.*

140. Zhong, Z., M. Lowry, G. F. Wang, and M. L. Geng. "Probing Strong Adsorption of Solute onto C18-Silica Gel by Fluorescence Correlation Imaging and Single-Molecule Spectroscopy under RPLC Conditions." *Analytical Chemistry* 77, no. 8 (2005): 2303-2310.

141. Zhong, Z., and M. L. Geng. "Microscopic Origins of Band Broadening in Chromatography. Polarity Distribution in C18 Stationary Phase Probed by Confocal Ratiometric Imaging of Nile Red." *Analytical Chemistry* 79, no. 17 (2007): 6709-6717.

142. Sing, K. S. W., D. H. Everett, R. A. W. Haul, L. Moscou, R. A. Pierotti, J. Rouquerol, and T. Siemieniewska. "Reporting Physisorption Data for Gas Solid Systems with Special Reference to the Determination of Surface-Area and Porosity (Recommendations 1984)." *Pure and Applied Chemistry* 57, no. 4 (1985): 603-619.

143. Logar, N. Z., and V. Kaucic. "Nanoporous Materials: From Catalysis and Hydrogen Storage to Wastewater Treatment." *Acta Chimica Slovenica* 53, no. 2 (2006): 117-135.

144. Thomas, J. M., and R. Raja. "Exploiting Nanospace for Asymmetric Catalysis: Confinement of Immobilized, Single-Site Chiral Catalysts Enhances Enantioselectivity." *Accounts of Chemical Research* (2008).

145. Yuan, J., X. Liu, O. Akbulut, J. Hu, S. L. Suib, J. Kong, and F. Stellacci. "Superwetting Nanowire Membranes for Selective Absorption." *Nature Nanotechnology* 3, no. 6 (2008): 332-336.

146. Allen, D., and Z. El Rassi. "Silica-Based Monoliths for Capillary Electrochromatography: Methods of Fabrication and their Applications in Analytical Separations." *Electrophoresis* 24, no. 22-23 (2003): 3962-3976.

147. Unger, K. K., R. Skudas, and M. M. Schulte. "Particle Packed Columns and Monolithic Columns in High-Performance Liquid Chromatography-Comparison and Critical Appraisal." *Journal of Chromatography A* 1184, no. 1-2 (2008): 393-415.

148. Berkland, C., M. J. Kipper, B. Narasimhan, K. K. Kim, and D. W. Pack. "Microsphere Size, Precipitation Kinetics and Drug Distribution Control Drug Release from Biodegradable Polyanhydride Microspheres." *Journal of Controlled Release: Official Journal of the Controlled Release Society* 94, no. 1 (2004): 129-141.

149. Claessens, H. A., and M. A. van Straten. "Review on the Chemical and Thermal Stability of Stationary Phases for Reversed-Phase Liquid Chromatography." *Journal of Chromatography a* 1060, no. 1-2 (2004): 23-41.

150. Wang, H. J., W. H. Zhou, X. F. Yin, Z. X. Zhuang, H. H. Yang, and X. R. Wang. "Template Synthesized Molecularly Imprinted Polymer Nanotube Membranes for Chemical Separations." *Journal of the American Chemical Society* 128, no. 50 (2006): 15954-15955.

151. Wirnsberger, G., P. Yang, B. J. Scott, B. F. Chmelka, and G. D. Stucky. "Mesostructured Materials for Optical Applications: From Low-k Dielectrics to Sensors and Lasers." *Spectrochimica Acta Part A - Molecular and Biomolecular Spectroscopy* 57, no. 10 (2001): 2049-2060.

152. Son, S. J., J. Reichel, B. He, M. Schuchman, and S. B. Lee. "Magnetic Nanotubes for Magnetic-Field-Assisted Bioseparation, Biointeraction, and Drug Delivery." *Journal of the American Chemical Society* 127, no. 20 (2005): 7316-7317.

153. Tang, Q., Y. Xu, D. Wu, Y. Sun, J. Wang, J. Xu, and F. Deng. "Studies on a New Carrier of Trimethylsilyl-Modified Mesoporous Material for Controlled Drug Delivery." *Journal of Controlled Release: Official Journal of the Controlled Release Society* 114, no. 1 (2006): 41-46.

154. Wang, S. B. "Ordered Mesoporous Materials for Drug Delivery." *Microporous and Mesoporous Materials* 117, no. 1-2 (2009): 1-9.

155. Skvortsova, Y. A., Z. Zhong, and M. Lei Geng. "Tissue Phantoms Constructed with Hydrophobic Nanoporous Particles." *Manuscript in preparation.*

156. Butler, J. A. V. "The Energy and Entropy of Hydration of Organic Compounds." *Transactions of the Faraday Society* 33, no. 1 (1937): 0229-0236.

157. Hoeft, C. E., and R. L. Zollars. "Adsorption of Single Anionic Surfactants on Hydrophobic Surfaces." *Journal of Colloid and Interface Science* 177, no. 1 (1996): 171-178.

158. Hiemenz, P. C., and R. Rajagopalan. *Principles of Colloid and Surface Chemistry.* 3rd, illustrated, revised ed. New York, NJ: Marcel Dekker Inc, 1997.

159. Paria, S., and K. C. Khilar. "A Review on Experimental Studies of Surfactant Adsorption at the Hydrophilic Solid-Water Interface." *Advances in Colloid and Interface Science* 110, no. 3 (2004): 75-95.

160. Wolf, D. E., M. Edidin, and P. R. Dragsten. "Effect of Bleaching Light on Measurements of Lateral Diffusion in Cell Membranes by the Fluorescence Photobleaching Recovery Method." *Proceedings of the National Academy of Sciences of the United States of America* 77, no. 4 (1980): 2043-2045.

161. Lowry, M., Y. He, and L. Geng. "Imaging Solute Distribution in Capillary Electrochromatography with Laser Scanning Confocal Microscopy." *Analytical Chemistry* 74, no. 8 (2002): 1811-1818.

162. Lu, S., R. J. Pugh, and E. K. S. Forssberg. *Intefacial Separation of Particles.* Edited by D. Mobius and R. Miller. Elsevier, 2005.

163. Brumaru, C. S., and M. Lei Geng. *Manuscript in preparation.*

164. Geng, M. L. *Unpublished Results.* The University of Iowa: 2009.

165. Lahnstein, K., T. Schmehl, U. Rusch, M. Rieger, W. Seeger, and T. Gessler. "Pulmonary Absorption of Aerosolized Fluorescent Markers in the Isolated Rabbit Lung." *International Journal of Pharmaceutics* 351, (2008): 158-164.

166. Salonen, J., L. Laitinen, A. M. Kaukonen, J. Tuura, M. Bjorkqvist, T. Heikkila, K. Vaha-Heikkila, J. Hirvonen, and V. P. Lehto. "Mesoporous Silicon Microparticles for Oral Drug Delivery: Loading and Release of Five Model Drugs." *Journal of Controlled Release: Official Journal of the Controlled Release Society* 108, no. 2-3 (2005): 362-374.

167. Vallet-Regi, M., F. Balas, and D. Arcos. "Mesoporous Materials for Drug Delivery." *Angewandte Chemie (International Edition in English)* 46, no. 40 (2007): 7548-7558.

168. Ng, J. B. S., P. Kamali-Zare, H. Brismar, and L. Bergstrom. "Release and Molecular Transport of Cationic and Anionic Fluorescent Molecules in Mesoporous Silica Spheres." *Langmuir* 24, no. 19 (2008): 11096-11102.

169. Torchilin, V. P. "Fluorescence Microscopy to Follow the Targeting of Liposomes and Micelles to Cells and their Intracellular Fate." *Advanced Drug Delivery Reviews* 57, no. 1 (2005): 95-109.

170. Yoon, X. A., and D. J. Burgess. "Effect of Cationic Surfactant on Transport of Model Drugs in Emulsion Systems." *The Journal of Pharmacy and Pharmacology* 49, no. 5 (1997): 478-484.

171. Wang, Y., L. V. Allen Jr., and L. C. Li. "Effect of Sodium Dodecyl Sulfate on Iontophoresis of Hydrocortisone across Hairless Mouse Skin." *Pharmaceutical Development and Technology* 5, no. 4 (2000): 533-542.

172. Bhown, A. S., and P. Stroeve. "Micelle-Mediated Transport of a Sparingly Soluble Drug through Nanoporous Membranes." *Industrial & Engineering Chemistry Research* 46, no. 19 (2007): 6118-6125.

173. Burkey, T. J., D. Griller, D. A. Lindsay, and J. C. Scaiano. "Simple Method for Quantifying the Distribution of Organic Substrates between the Micellar and Aqueous Phases of Sodium Dodecyl-Sulfate Solution." *Journal of the American Chemical Society* 106, no. 7 (1984): 1983-1985.

174. Johnson, K. A., G. B. Westermann-Clark, and D. O. Shah. "Controlled Release of Steroids through Microporous Membranes with Sodium Dodecyl Sulfate Micelles." *Pharmaceutical Research* 6, no. 3 (1989): 239-243.

175. Gumbleton, M., and D. J. Stephens. "Coming Out of the Dark: The Evolving Role of Fluorescence Imaging in Drug Delivery Research." *Advanced Drug Delivery Reviews* 57, no. 1 (2005): 5-15.

176. Brumaru, C. S. *Unpublished results.* The University of Iowa: 2009.

177. Tanford, C. "Micelle Shape and Size." *Journal of Physical Chemistry* 76, no. 21 (1972): 3020.

178. Bruce, C. D., S. Senapati, M. L. Berkowitz, L. Perera, and M. D. E. Forbes. "Molecular Dynamics Simulations of Sodium Dodecyl Sulfate Micelle in Water: The Behavior of Water." *Journal of Physical Chemistry B* 106, no. 42 (2002): 10902-10907.

179. Itri, R., and L. Q. Amaral. "Distance Distribution Function of Sodium Dodecyl-Sulfate Micelles by X-Ray-Scattering." *Journal of Physical Chemistry* 95, no. 1 (1991): 423-427.

180. Cheng, K., and C. C. Landry. "Diffusion-Based Deprotection in Mesoporous Materials: A Strategy for Differential Functionalization of Porous Silica Particles." *Journal of the American Chemical Society* 129, no. 31 (2007): 9674-9685.

181. Kushner, J., 4th, D. Kim, P. T. So, D. Blankschtein, and R. S. Langer. "Dual-Channel Two-Photon Microscopy Study of Transdermal Transport in Skin Treated with Low-Frequency Ultrasound and a Chemical Enhancer." *The Journal of Investigative Dermatology* 127, no. 12 (2007): 2832-2846.

182. Tyle, P. "Iontophoretic Devices for Drug Delivery." *Pharmaceutical Research* 3, no. 6 (1986): 318-326.

183. Srinivasan, V., M. H. Su, W. I. Higuchi, and C. R. Behl. "Iontophoresis of Polypeptides - Effect of Ethanol Pretreatment of Human Skin." *Journal of Pharmaceutical Sciences* 79, no. 7 (1990): 588-591.

184. Bettley, F. R. "The Influence of Detergents and Surfactants on Epidermal Permeability." *The British Journal of Dermatology* 77, (1965): 98-100.

185. Tsai, J. C., L. C. Shen, H. M. Sheu, and C. C. Lu. "Tape Stripping and Sodium Dodecyl Sulfate Treatment Increase the Molecular Weight Cutoff of Polyethylene Glycol Penetration across Murine Skin." *Archives of Dermatological Research* 295, no. 4 (2003): 169-174.

186. Moore, P. N., S. Puvvada, and D. Blankschtein. "Challenging the Surfactant Monomer Skin Penetration Model: Penetration of Sodium Dodecyl Sulfate Micelles into the Epidermis." *Journal of Cosmetic Science* 54, no. 1 (2003): 29-46.

187. Ghosh, S., and D. Blankschtein. "The Role of Sodium Dodecyl Sulfate (SDS) Micelles in Inducing Skin Barrier Perturbation in the Presence of Glycerol." *Journal of Cosmetic Science* 58, no. 2 (2007): 109-133.

188. Essa, E. A., M. C. Bonner, and B. W. Barry. "Human Skin Sandwich for Assessing Shunt Route Penetration during Passive and Iontophoretic Drug and Liposome Delivery." *Journal of Pharmacy and Pharmacology* 54, no. 11 (2002): 1481-1490.

189. Lasch, J., R. Laub, and W. Wohlrab. "How Deep do Intact Liposomes Penetrate into Human Skin." *Journal of Controlled Release* 18, no. 1 (1992): 55-58.

190. Cevc, G. "Lipid Vesicles and Other Colloids as Drug Carriers on the Skin." *Advanced Drug Delivery Reviews* 56, no. 5 (2004): 675-711.

191. Schatzlein, A., and G. Cevc. "Non-Uniform Cellular Packing of the Stratum Corneum and Permeability Barrier Function of Intact Skin: A High-Resolution Confocal Laser Scanning Microscopy Study Using Highly Deformable Vesicles (Transfersomes)." *British Journal of Dermatology* 138, no. 4 (1998): 583-592.

192. Alvarez-Roman, R., A. Naik, Y. N. Kalia, H. Fessi, and R. H. Guy. "Visualization of Skin Penetration Using Confocal Laser Scanning Microscopy." *European Journal of Pharmaceutics and Biopharmaceutics* 58, no. 2 (2004): 301-316.

193. Van den Bergh, B. A. I., J. Vroom, H. Gerritsen, H. E. Junginger, and J. A. Bouwstra. "Interactions of Elastic and Rigid Vesicles with Human Skin in Vitro: Electron Microscopy and Two-Photon Excitation Microscopy." *Biochimica et Biophysica Acta-Biomembranes* 1461, no. 1 (1999): 155-173.

194. Dubey, V., D. Mishra, A. Asthana, and N. K. Jain. "Transdermal Delivery of a Pineal Hormone: Melatonin via Elastic Liposomes." *Biomaterials* 27, no. 18 (2006): 3491-3496.

195. Van Kuijk-Meuwissen, M. E., H. E. Junginger, and J. A. Bouwstra. "Interactions between Liposomes and Human Skin in Vitro, a Confocal Laser Scanning Microscopy Study." *Biochimica et Biophysica Acta* 1371, no. 1 (1998): 31-39.

196. Cevc, G., A. Schatzlein, and H. Richardsen. "Ultradeformable Lipid Vesicles can Penetrate the Skin and Other Semi-Permeable Barriers Unfragmented. Evidence from Double Label CLSM Experiments and Direct Size Measurements." *Biochimica et Biophysica Acta-Biomembranes* 1564, no. 1 (2002): 21-30.

197. Rai, K., Y. Gupta, A. Jain, and S. K. Jain. "Transfersomes: Self-Optimizing Carriers for Bioactives." *PDA Journal of Pharmaceutical Science and Technology* 62, no. 5 (2008): 362-379.

198. Georges, J. "Molecular Fluorescence in Micelles and Microemulsions - Micellar Effects and Analytical Applications." *Spectrochimica Acta Reviews* 13, no. 1 (1990): 27-45.

199. Shirota, H., Y. Tamoto, and H. Segawa. "Dynamic Fluorescence Probing of the Microenvironment of Sodium Dodecyl Sulfate Micelle Solutions: Surfactant Concentration Dependence and Solvent Isotope Effect." *Journal of Physical Chemistry A* 108, no. 16 (2004): 3244-3252.

200. Kalyanasundaram, K., and J. K. Thomas. "Environmental Effects on Vibronic Band Intensities in Pyrene Monomer Fluorescence and their Application in Studies of Micellar Systems." *Journal of the American Chemical Society* 99, no. 7 (1977): 2039-2044.

201. Nakajima, A. "Solvent Effect on Vibrational Structures of Fluorescence and Absorption-Spectra of Pyrene." *Bulletin of the Chemical Society of Japan* 44, no. 12 (1971): 3272.

202. Nakajima, A. "Solvent Enhancement in First Singlet-Singlet Transition of Pyrene-D10." *Spectrochimica Acta Part A - Molecular and Biomolecular Spectroscopy* A 30, no. 3 (1974): 860-862.

203. Nakajima, A. "Effects of Isomeric Solvents on Vibronic Band Intensities in Fluorescence-Spectrum of Pyrene." *Journal of Molecular Spectroscopy* 61, no. 3 (1976): 467-469.

204. Wilhelm, M., C. L. Zhao, Y. C. Wang, R. L. Xu, M. A. Winnik, J. L. Mura, G. Riess, and M. D. Croucher. "Polymer Micelle Formation. 3. Poly(Styrene-Ethylene Oxide) Block Copolymer Micelle Formation in Water - a Fluorescence Probe Study." *Macromolecules* 24, no. 5 (1991): 1033-1040.

205. Yekta, A., J. Duhamel, P. Brochard, H. Adiwidjaja, and M. A. Winnik. "A Fluorescent-Probe Study of Micelle-Like Cluster Formation in Aqueous-Solutions of Hydrophobically Modified Poly(Ethylene Oxide)." *Macromolecules* 26, no. 8 (1993): 1829-1836.

206. Anthony, O., and R. Zana. "Fluorescence Investigation of the Binding of Pyrene to Hydrophobic Microdomains in Aqueous-Solutions of Polysoaps." *Macromolecules* 27, no. 14 (1994): 3885-3891.

207. Weber, G., and F. J. Farris. "Synthesis and Spectral Properties of a Hydrophobic Fluorescent Probe: 6-Propionyl-2-(Dimethylamino)-Naphthalene." *Biochemistry* 18, no. 14 (1979): 3075-3078.

208. Chong, P. L. "Effects of Hydrostatic Pressure on the Location of PRODAN in Lipid Bilayers and Cellular Membranes." *Biochemistry* 27, no. 1 (1988): 399-404.

209. Sommer, A., F. Paltauf, and A. Hermetter. "Dipolar Solvent Relaxation on a Nanosecond Time Scale in Ether Phospholipid Membranes as Determined by Multifrequency Phase and Modulation Fluorometry." *Biochemistry* 29, no. 50 (1990): 11134-11140.

210. Rottenberg, H. "Probing the Interactions of Alcohols with Biological Membranes with the Fluorescent Probe Prodan." *Biochemistry* 31, no. 39 (1992): 9473-9481.

211. Krasnowska, E. K., L. A. Bagatolli, E. Gratton, and T. Parasassi. "Surface Properties of Cholesterol-Containing Membranes Detected by Prodan Fluorescence." *Biochimica et Biophysica Acta* 1511, no. 2 (2001): 330-340.

212. Wilson-Ashworth, H. A., Q. Bahm, J. Erickson, A. Shinkle, M. P. Vu, D. Woodbury, and J. D. Bell. "Differential Detection of Phospholipid Fluidity, Order, and Spacing by Fluorescence Spectroscopy of Bis-Pyrene, Prodan, Nystatin, and Merocyanine 540." *Biophysical Journal* 91, no. 11 (2006): 4091-4101.

213. Cowley, D. J. "Protein-Structure - Polar Pocket with Nonpolar Lining." *Nature* 319, no. 6048 (1986): 14-14.

214. Chapman, C. F., and M. Maroncelli. "Fluorescence Studies of Solvation and Solvation Dynamics in Ionic-Solutions." *Journal of Physical Chemistry* 95, no. 23 (1991): 9095-9114.

215. Karukstis, K. K., S. W. Suljak, P. J. Waller, J. A. Whiles, and E. H. Z. Thompson. "Fluorescence Analysis of Single and Mixed Micelle Systems of SDS and DTAB." *Journal of Physical Chemistry* 100, no. 26 (1996): 11125-11132.

216. Capek, I. "Fate of Excited Probes in Micellar Systems." *Advances in Colloid and Interface Science* 97, no. 1-3 (2002): 91-149.

217. Gaudin, A. M., and D. W. Fuerstenau. "Quartz Flotation with Cationic Collectors." *Transactions of the American Institute of Mining and Metallurgical Engineers* 202, no. 10 (1955): 958-962.

218. Atkin, R., V. S. J. Craig, E. J. Wanless, and S. Biggs. "Mechanism of Cationic Surfactant Adsorption at the Solid-Aqueous Interface." *Advances in Colloid and Interface Science* 103, no. 3 (2003): 219-304.

219. Zhang, R., and P. Somasundaran. "Advances in Adsorption of Surfactants and their Mixtures at Solid/Solution Interfaces." *Advances in Colloid and Interface Science* 123, (2006): 213-229.

220. Manne, S., J. P. Cleveland, H. E. Gaub, G. D. Stucky, and P. K. Hansma. "Direct Visualization of Surfactant Hemimicelles by Force Microscopy of the Electrical Double-Layer." *Langmuir* 10, no. 12 (1994): 4409-4413.

221. Wanless, E. J., and W. A. Ducker. "Organization of Sodium Dodecyl Sulfate at the Graphite-Solution Interface." *Journal of Physical Chemistry* 100, no. 8 (1996): 3207-3214.

222. Grant, L. M., and W. A. Ducker. "Effect of Substrate Hydrophobicity on Surface-Aggregate Geometry: Zwitterionic and Nonionic Surfactants." *Journal of Physical Chemistry B* 101, no. 27 (1997): 5337-5345.

223. Fleming, B. D., and E. J. Wanless. "Soft-Contact Atomic Force Microscopy Imaging of Adsorbed Surfactant and Polymer Layers." *Microscopy and Microanalysis* 6, no. 2 (2000): 104-112.

224. Sun, S. Y., M. P. Heitz, S. A. Perez, L. A. Colon, S. Bruckenstein, and F. V. Bright. "6-Propionyl-2-(N,N-Dimethylamino)Naphthalene (PRODAN) Revisited." *Applied Spectroscopy* 51, no. 9 (1997): 1316-1322.

225. Bunker, C. E., T. L. Bowen, and Y. P. Sun. "A Photophysical Study of Solvatochromic Probe 6-Propionyl-2-(N,n-Dimethylamino)-Naphthalene (Prodan) in Solution." *Photochemistry and Photobiology* 58, no. 4 (1993): 499-505.